Head Office: Università degli Studi di Padova

Department of Chemical Sciences

Ph.D. COURSE IN: MOLECULAR SCIENCES

CURRICULUM: CHEMICAL SCIENCES

SERIES: THIRTY-SIX CYCLE

DESIGN OF NOVEL POLYOXOMETALATE-PEPTIDE HYBRID CONJUGATES

Coordinator: Prof. Stefano Corni

Supervisor: Prof. Mauro Carraro

Ph.D. student: Haihong Yu

Table of Content

Chapter 1: General introduction

1.1 Polyoxometalates

1.11 The development of polyoxometalate

POMs consist of an immense class of polynuclear metal-oxygen clusters with the metal centers, formed by Mo, W or V and mixtures of these elements. The first polyoxometalate compound, known to be $[PMo_{12}O_{40}]^{3-}$, was reported by Berzelius in 1826. Marignac observed two isomeric forms of $[SiW_{12}O_{40}]^{4-}$. Since then, countless structures have been synthesized and characterized. However, Prior to the introduction of X-ray diffraction techniques by Laue in 1912 and their subsequent development by W. L. Bragg and W. H. Bragg, only theoretical knowledge regarding the potential structural compositions of heteropolyanions could be put forth. Werner's coordination theory was the first to develop a theory regarding heteropolyacids, which was later further developed by Miolati and Rosenheim in 1908. However, Pauling's work in 1929 superseded this theory. It wasn't until 1933, with Keggin's work, that there was definitive evidence for the structural composition of $H_3PW_{12}O_{40}$. Since then, research in POM chemistry has grown rapidly due to advancements in single crystal X-ray diffraction techniques and analysis software. In 1996, Katsoulis recorded over 700 communications, comprising publications and patents, on POMs. The base unit of POMs, MOn, contains different metallic centers, M, surrounded by oxygen atoms. Nonetheless, some S7, F8, Br9, and other p-block elements modifications are also available. The coordination numbers of M in the base unit are typically six, but they may also be four, five or seven. Over the years, standardized methods were developed to replace metal atoms with other metal atoms, adjust the anion size, anion charge and many other aspects. Polyoxometalates can coordinate a wide range of hetero atoms at well-defined geometric sites in the lattice, including up to 75% of elements in the periodic table. POMs are commonly called strong oxidizing agents. This surge in research is now occurring on a global scale. The growing interest in this field can be attributed to the remarkable structural and

electronic diversity exhibited by POM systems, as well as their potential applications in various scientific domains.

1.12 Classification and structure of POMs

The current group of polyoxometalates (POMs) is a versatile type of polynuclear metal-oxygen clusters that have various potential applications in diverse fields such as catalysis, molecular electronics, and medicine. POMs possess exceptional properties and structural configurations, which have held the interest of chemists for many decades. POMs come in a wide variety of constitutions and structures that can be broadly classified into two categories: isopolyoxometalates and heteropolyoxometalates.[1, 2] POMs can adopt diverse classical configurations (such as the Keggin, Lindqvist, and Anderson types) and intriguing topological architectures (such as annular, spherical, and wheel-shaped) through different types of conjunctions between the metal-oxygen coordination blocks (e.g. coplanar, coangle, and coedge linkages).[3] Despite the extensive array of polyoxometalates (POMs) available and the virtually boundless possibilities for octahedral and tetrahedral units to create diverse structures by sharing oxide ligands, the majority of POMs can be categorized into one of four well-defined structural groups: Lindqvist, Keggin, Well-Dawson, or Anderson clusters.[3] Each of these structural motifs has exhibited distinct functions as individual clusters and is frequently chosen for their consistent reproducibility and stability. Consequently, they stand out as strong candidates for serving as building blocks in the assembly of more extensive clusters.

There are several different structures known for polyoxometalates (POMs), and Figure 1 illustrates some of the more common ones. The Lindqvist structure, shown in Figure 1A, is adopted by hexametalates with the formula $[M_6O_{19}]^{n-}$. It consists of an octahedral arrangement of six octahedra, where each octahedron represents a metal ion with its coordination sphere. The octahedra share four edges with neighboring octahedra, resulting in a compact arrangement. The Lindqvist structure can be seen as a fragment of a cubic closed packed metal oxide. Figures 1B and 1C depict the structural diversity of compounds with the general formula $[M_7O_{24}]^{n-}$. The bent structure in Figure 1B is adopted by the isopolymolybdate $[Mo_7O_{24}]^{6-}$, also known as paramolybdate. The

heteropolyoxometalates $[XM_6O_{24}]^{n-}$ exhibit the Anderson structure shown in Figure 1C. In this structure, six edge-sharing octahedra form a planar hexagon around the central heteroatom. Here, the heteroatom denoted as X is octahedrally coordinated. The most common structure featuring tetrahedrally coordinated heteroatoms is the Keggin ion, represented by the general formula $[XM_{12}O_{40}]^{n-}$ (Figure 2d). In this structure, four trimetallic groups are arranged around a central tetrahedron. Lastly, the Dawson structure of $[X_2M_{18}O_{62}]^{n-}$ (Figure 1e) can be considered as a combination of two Keggin ions. In this structure, one trimetallic group is withdrawn from each Keggin ion, and the remaining fragments are associated. Additionally, by selectively removing one or more metal ions through the addition of a base, lacunary structures can be obtained. These structures possess open coordination sites that can be occupied by other metal or non-metal atoms. This strategy is commonly employed to modify the structure and properties of POMs.

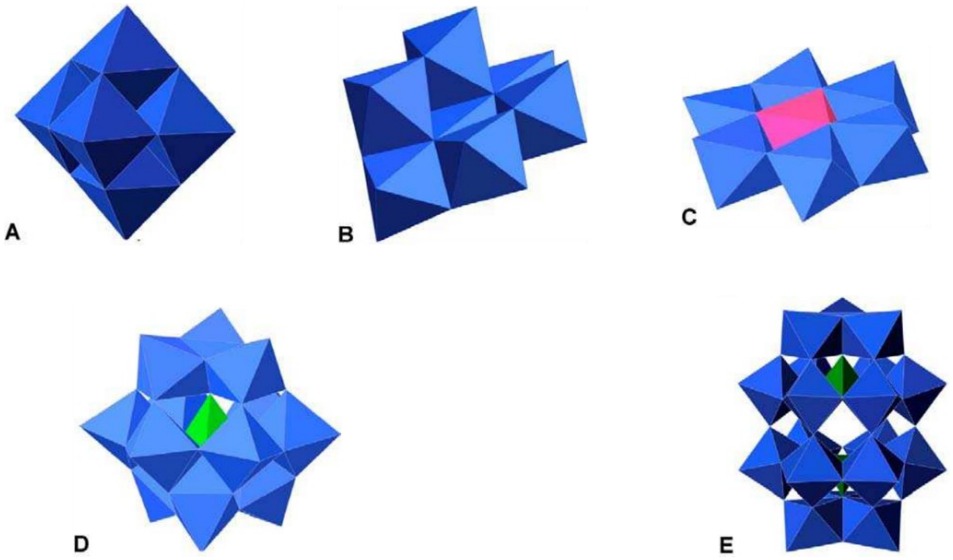

Figure 1. Polyhedral representations of some common polyoxometalate structures. A) $[M_6O_{19}]^{n-}$ (Lindqvist-structure), B)$[Mo_7O_{24}]^{6-}$ (Heptametalate polyoxoanion), C) $[XM_6O_{24}]^{n-}$ (Anderson-structure), D) $[XM_{12}O_{40}]^{n-}$ (Keggin-structure), E) $[X_2M_{18}O_{62}]^{n-}$ (Dawson-structure)[4].

1.2 Isopolyoxometalates [HxMyOz]

Isopolyanions are categorized based on the general formula $[HxMyOz]^{n-}$, where they exclusively consist of a d0 group 5 or 6 metal (M) cation and an oxide anion framework. Isopolyanions exhibit intriguing physical properties such as high charges and strongly basic oxygen surfaces. These

characteristics make them particularly fascinating as foundational building blocks for larger polyoxometalate structures.[5]

1.21 Lindqvist Vanadate

The hexametalate Lindqvist polyoxometalate (POM) stands as one of the most straightforward and compact iso-polyoxometalates, and its discovery dates back to 1950. This cluster follows the general formula $[Mo_6O_{19}]$ (n-) and can be isolated utilizing early transition metals such as Nb, Ta, Mo, and W. Lindqvist structure exhibit approximately high symmetry in their clusters. It should be noted that the $\{V_6O_{19}\}$ cluster core is stabilized by coordinating complementary ligands like metal and organometallic complexes, which are ligated to the $\{V_6O_{19}\}$ core through oxygen bridges to facilitate cluster formation.

Taking a closer look at the structure of a conventional Lindqvist anion such as $[V_6O_{19}]^{2-}$, each fully oxidized (d0) metal center is bonded to one terminal oxygen ligand and shares four additional μ2-bridging oxo ligands with adjacent metal centers. The terminal oxygen ligands have shorter bond lengths, approximately 1.7 Å in $[V_6O_{19}]^{2-}$, compared to the μ2-bridging oxo ligands, which have bond lengths around 1.9 Å in $[V_6O_{19}]$. [2-3] This coordination arrangement suggests that the overall structure is composed of six distorted, edge-sharing octahedra (refer to Figure 2). In the $[V_6O_{19}]^{2-}$ cluster, the weakly basic and highly electronegative terminal oxygen atoms on this fully oxidized POM cluster serve as the binding sites. [6] Organoimido derivatives of $[V_6O_{19}]^{2-}$ polyoxoanions have been synthesized using direct or indirect methods. These derivatizations have been achieved through reactions involving phosphinimines,[7] or aromatic amines with N,N'-dicyclohexylcarbodimide (DCC).[8]

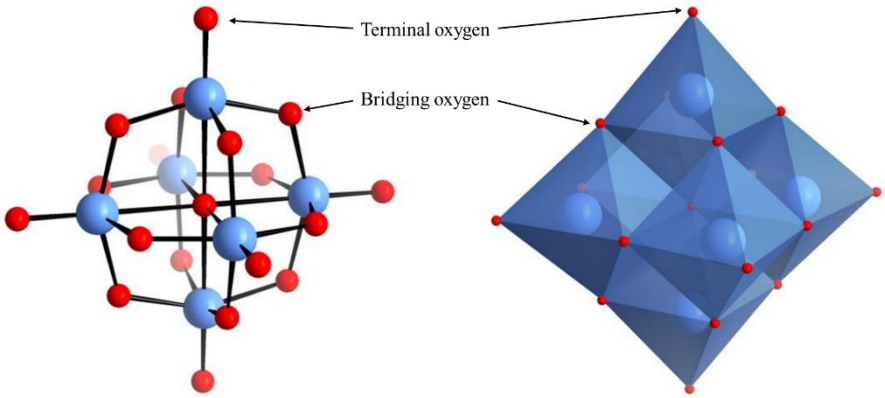

Figure 2: Lindqvist structure $[M_6O_{19}]^{n-}$, where M = V^{5+}, Nb^{5+}, Ta^{5+}, Mo^{6+}, W^{6+}, and n = 8 (group 5 metal centre's) or n = 2 (group 6 metal centres), showing addenda and types of oxygen atoms. Left: balls and sticks; right: polyhedral. Blue, addenda; red, oxygen.[9]

1.22 Decavanadate Polyoxoanion $[V_{10}O_{28}]^{6-}$

By acidifying aqueous solutions containing metavanadate anions $(VO_3)^-$ to a pH of 6 or below, orange solutions can be obtained that contain the decavanadate anion $[V_{10}O_{28}]^{6-}$.[1] Further investigations have revealed that the decavanadate anion can undergo protonation in multiple steps, resulting in the formation of $[HnV_{10}O_{28}]^-$, where n can be 2, 3, or 4, depending on the acidity of the solution.[10]

As is shown in the Figure 3, the structure of the $[V_{10}O_{28}]^{6-}$ anion can be described as a planar rectangular array composed of six edge-sharing $\{VO_6\}$ octahedra, with an additional two pairs of edge-sharing octahedra positioned above and below the plane of the rectangular array.[10] However, these octahedra undergo distortion to maintain an approximate valence balance between the terminal oxo and bridging oxo ligands. Specifically, the approximate V-O (terminal) bond length is 1.60 Å, while the approximate V-O (central) bond length is 2.32 Å.[1] Refer to Figure 3 for visualization.

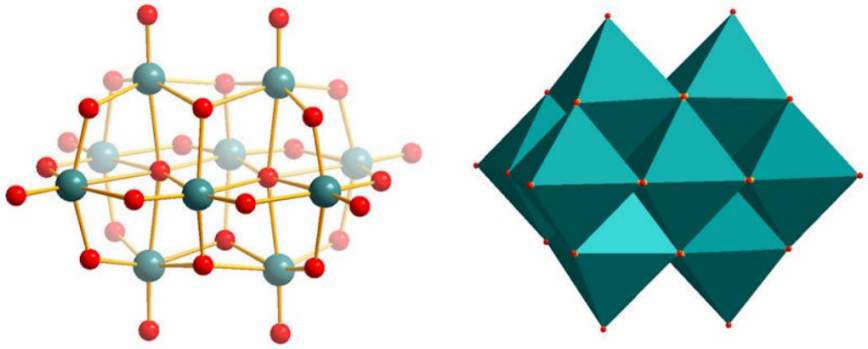

Figure 3. Structural representations of the $[V_{10}O_{28}]^{6-}$ decavanadate anion. Left: Ball-andstick representation where the differences in V-O (terminal) and V-O (bridging) bond lengths can be seen. Right: The polyhedral representation reveals the arrangement of six $\{VO_6\}$ octahedra, sharing edges, that constitute the central rectangular array. Additionally, there are two additional pairs of ed ge-sharing octahedra positioned above and below the central plane, contributing to the coordination. Colour scheme: V, t eal (polyhedra); O, red.

1.23 Heptametalate polyoxoanion $[M_7O_{24}]^{6-}$

The heptametalate $[M_7O_{24}]^{6-}$ structure, (C2v symmetry), is based on the arrangements of seven edge-shared MO6 octahedra (M = Mo, W).The heptamolybdate (paramolybdate) anion can be obtained by crystallization through acidification of aqueous molybdate solutions within the pH range of approximately 3 to 5.5.[1] Similarly, the heptatungstate (paratungstate A) anion is crystallized from acidified aqueous tungstate solutions at a pH of approximately 6.0.[11]

The structures of $[Mo_7O_{24}]^{6-}$ and $[W_7O_{24}]^{6-}$ are isostructural, with similar dimensions. These structures can be described as composed of seven edge-sharing $\{MO_6\}$ octahedra. Each octahedron is distorted as the metal center is displaced towards the periphery of the anion. One can easily visualize the coordination arrangement of these octahedra by examining the $[V_{10}O_{28}]^{6-}$ structure mentioned earlier and eliminating three {MO6} octahedra from the central rectangular array of octahedra (refer to Figure 4). It is worth mentioning that the $[Mo_7O_{24}]^{6-}$ anion has demonstrated its utility as a fundamental component in constructing more extensive polyoxometalate (POM) architectures.

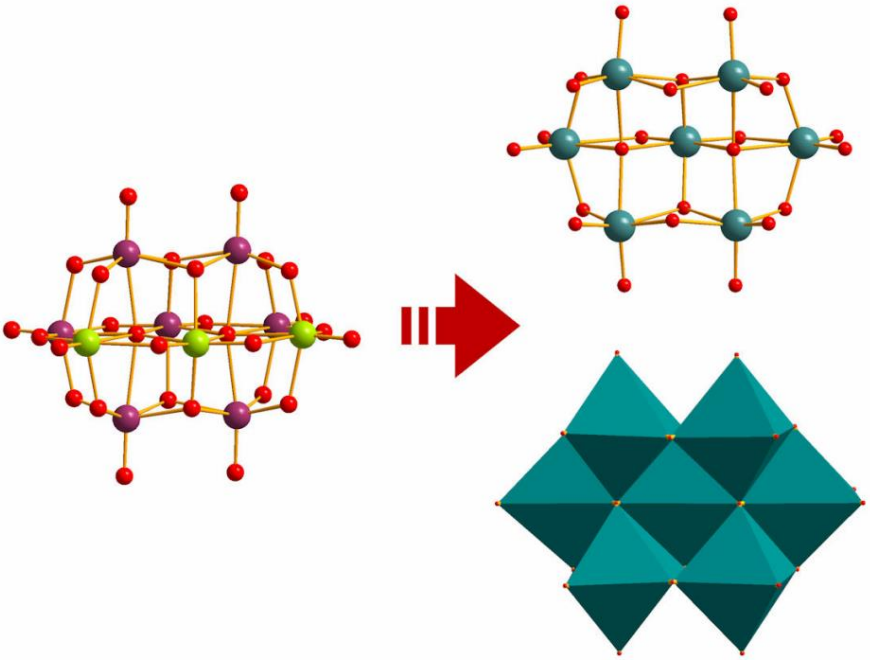

Figure 4. left: the structural characteristics of the $[V_{10}O_{28}]^{6-}$ decavanadate anion. The three metal additions, which can be contemplated for removal in order to generate the $[M_7O_{24}]^{6-}$ framework where M = Mo(VI) or W(VI), are pinpointed in green. Top Right: Ball-andstick representation of the $[Mo_7O_{24}]^{6-}$ anion. Bottom Right: Polyhedral representation showing the seven edge-sharing $\{MoO_6\}$ octahedra of the $[Mo_7O_{24}]^{6-}$ anion. The color scheme employed is as follows: V is depicted in purple and light green, Mo polyhedra are portrayed in teal, and O atoms are represented in red.

1.3 Heteropolyoxometalates [XxMyOz]

Heteropolyanions can be described by the general formula [XxMyOz], where n represents a positive integer, x is less than or equal to y, and they comprise one or more p-, d-, or f-block "heteroatoms" (X), such as TeO^{66-}, IO^{65-}, SO^{42-}, and PO^{43-}.[12] These heteroatoms are incorporated within a fundamental metal-oxide anion framework. The coordination of these heteroatoms can occur either in an environment inaccessible to solvents or on the surface of the POM structure. Due to the wide range of elements capable of functioning as heteroatoms, there exists a larger pool of these structures to synthesize and investigate. Additionally, the structural and electronic properties of heteropolyanions are relatively easier to modify through synthetic means. Consequently, this

particular POM structure has been the subject of extensive research efforts, with the aim of discovering new applications.

1.31 The Anderson polyoxoanion $[Hx(XO_6)M_6O_{18}]^{n-}$

Anderson polyoxoanion exhibit a fundamental topological structure within the POM family, initially hypothesized by Anderson in 1937 and eventually elucidated by Evans in 1948. Additionally, Anderson polyoxoanion characterized by a general formula of $[Hy(XO_6)M_6O_{18}]^{n-}$ (where y ranges from 0 to 6, n ranges from 2 to 8, M represents the addenda atom, and X denotes the heteroatom). This polyoxometalate anion consists of six edge-sharing $\{MoO_6\}$ or $\{WO_6\}$ octahedra surrounding a central heteroatom octahedron, {XO6}, resulting in a planar arrangement as depicted in Figure 5A. The structure contains three different coordination modes for oxygen atoms: six triple-bridged oxygen atoms (μ3-O) connecting the heteroatom and two addenda atoms, six double-bridged oxygen atoms (μ2-O) connecting two addenda atoms, and two terminal oxygen atoms (Ot) connected to each of the six addenda atoms (top view, Figure 5A).

The average dimensions of the Anderson-Evans anion are approximately 8.6 × 8.6 × 2.7 Å (Figure 5B). An isomer of this structure is heptamolybdate ($[Mo_7O_{24}]^{6-}$),[13] which exhibits a "bent" configuration (Figure 5C). Heptamolybdate can be visualized as three edge-shared octahedra aligned with two octahedra on each side, creating a space in between. The two octahedra on each side are shifted by half an octahedron, resulting in the "bent" structure (Figure 5C, bottom). The Anderson-Evans structure can be classified into two types: the non-protonated A-type, featuring central heteroatoms in high oxidation states with the general formula $[X^{n+}M_6O_{24}]^{(12-n)-}$, and the protonated B-type, with heteroatoms in low oxidation states and the general formula $[X^{n+}(OH)_6M_6O_{18}]^{(6-n)-}$. In the B-type, the six protons are situated on the six μ3-O atoms surrounding the heteroatom.

Thus, the overall structure exhibits approximate D3d symmetry. These POMs can undergo various modifications: (1) by altering the central heteroatom; (2) by incorporating inorganic and/or organic cations to construct coordination or supramolecular architectures; and (3) by forming covalent bonds with organic moieties, resulting in functional hybrids. Notably, B-type molybdenum Anderson structures exhibit significant functionalization capabilities through coordination with a wide variety

of tris(alkoxo) ligands, denoted as $RC(CH_2OH)_3$, where R represents a chosen substituent group (e.g., alkyl, aryl, nitro, etc.). This feature has led to the isolation of numerous organic-inorganic hybrid compounds through an indirect synthesis method. These distinctive properties make Anderson-type POMs exceptionally versatile nanoclusters in the field of POM chemistry, offering a wide range of possibilities for exploration and application.

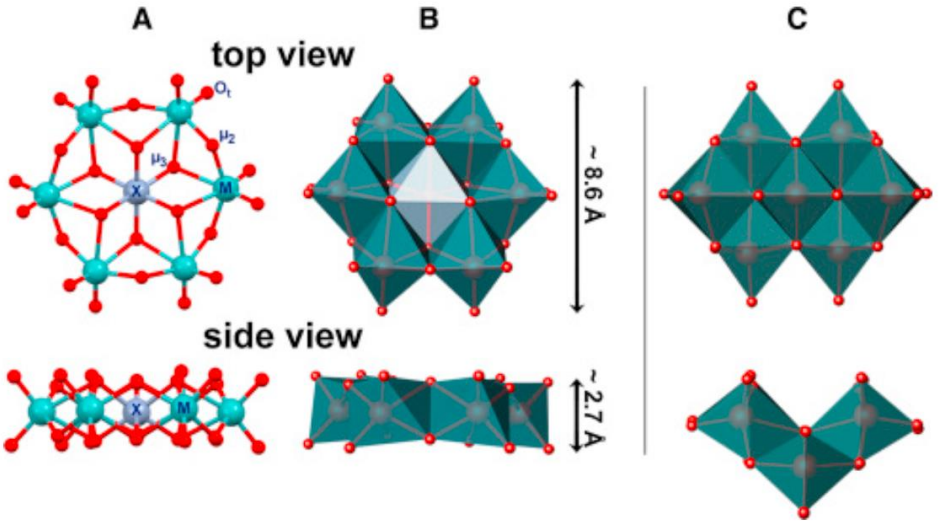

Figure 5. Ball-and-stick (A) and polyhedral (B) representations of the Anderson-Evans POM denoted as $[XM_6O_{24}]^{n-}$. The top and side views showcase the structural components, including the heteroatom (represented by a gray sphere and a gray octahedron, where X signifies a first-row transition metal), the addenda atoms (depicted as green spheres and green octahedra, with M representing W(VI) or Mo(VI)), and three distinct oxygen atom types (illustrated as red spheres) that constitute the structure: triple-bridged (μ3), double-bridged (μ2), and terminal oxygen atoms (Ot). Additionally, the "bent" isomer $[M_7O_{24}]^{6-}$ is also displayed (C).

1.32 The Keggin Anion $[XM_{12}O_{40}]^{n-}$

The Keggin anion was initially proposed by J. F. Keggin in 1933 based on X-ray powder diffraction data. Since then, numerous Keggin structures have been discovered, making it the prototypical polyoxometalate (POM) and a subject of extensive research in the field. The Keggin ion has a general formula of $[XM_{12}O_{40}]^{n-}$, where it consists of a $\{XO_4\}$ tetrahedron surrounded by Mo or W centers. The charge of the Keggin ion can vary from 2- to 7- .[14]

The Keggin anion is composed of a central $\{XO_4\}$ heteroatom tetrahedron, surrounded by twelve $\{MO_6\}$ octahedra, where M represents W or Mo. These twelve $\{MO_6\}$ octahedra are organized into

four groups of three octahedra, known as $\{M_3O_{13}\}$ units. These units share edges, forming connections with each other and with the central heteroatom tetrahedron (refer to Figure 6). As a result, the tungsten Keggin anions exhibit an overall Td symmetry.

It is important to highlight that the majority of heteropolyoxotungstates adopt either the Keggin anion structure or structures derived from it. In contrast, there are fewer heteropolyoxomolybdates based on the Keggin or Keggin-derived building blocks. Common heteroatoms for the Keggin are p-block elements such as B, Si, Ge, P and S.[15]

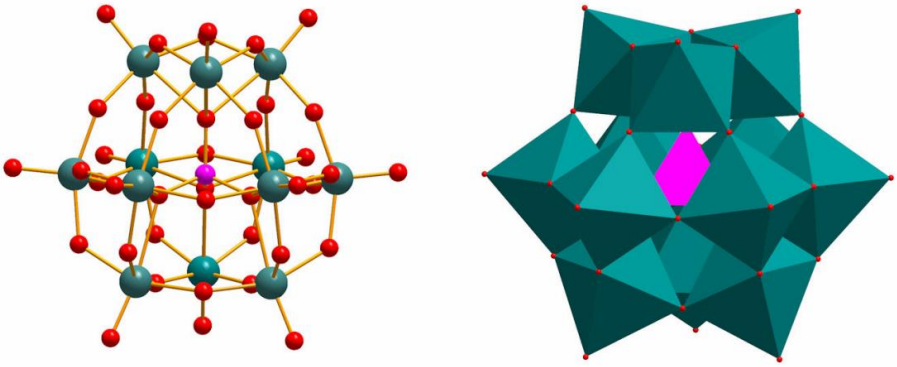

Figure 6: Depiction of the $[\alpha\text{-}PW_{12}O_{40}]^{3-}$ Keggin anion. Left: Ball-and-stick representation illustrating the tetrahedral coordination of the central heteroatom. Right: Polyhedral representation displaying the arrangement of twelve $\{WO_6\}$ octahedra into three edge-sharing $\{W_3O_{13}\}$ units. These $\{W_3O_{13}\}$ units are connected to each other and the central tetrahedron via corner-sharing (highlighted in pink). Color scheme: W, teal (polyhedra); P, pink (central tetrahedron); O, red.

1.33 The Wells-Dawson polyoxoanion $[X_2M_{18}O_{62}]^{n-}$

The Wells-Dawson anion is an example of a structural type derived from the Keggin structure. To obtain the Wells-Dawson anion, three adjacent addenda atoms are removed from the Keggin structure: one from each of three triads. Subsequently, two of the resulting fragments are connected, forming a cluster with the chemical formula $[X_2M_{18}O_{62}]^{n-}$, where addenda atoms exist in two distinct chemical environments. The top and bottom triads are often referred to as the "cap" regions, each consisting of

three addenda atoms. The middle region is known as the "belt" region and contains 12 addenda atoms. Figure 6 is a visual representation of this structure. The Wells-Dawson can be described by the general formula $[X_2M_{18}O_{62}]^{n-}$, where M represents either W or Mo, and X denotes a central heteroatom. This polyoxoanion consists of two tetrahedral heteroanion units, for example, PO^{43-}, within the metal-oxide framework.

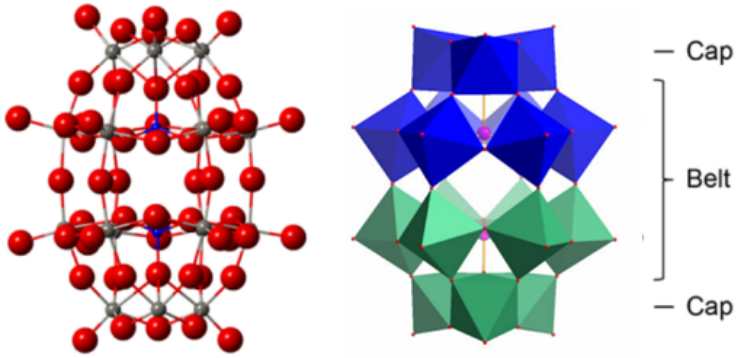

Figure 6. Wells−Dawson structure $[X_2M_{18}O_{62}]^{n-}$. Left: balls and sticks (Gray, addenda; red, oxygen; blue, heteroatom.); right: polyhedral (In this illustration the metal-oxide octahedra of the cluster shell are shown as blue and green polyhedra, the two central heteroatoms are shown in purple, and oxygen ligands in red).

Dawson polyoxoanions can undergo further coordination with transition metals, utilizing their terminal oxo ligands as binding sites, thereby allowing the construction of more complex polyoxoanion architectures.[16] They can also undergo partial hydrolysis, similar to the Keggin anion described earlier, leading to the formation of Dawson-based lacunary structures.[17] The most extensively studied Dawson structure to date is $\{P_2W_{18}\}$, which has been utilized in thin-film fabrication for applications in photochromic, electrochromic, and optoelectronic properties, as well as in heterogeneous catalysis and biomedical applications.[16]

1.34 Lacunary Anion

The controlled hydrolysis of specific constituent units can be achieved through pH manipulation in certain polyoxometalate (POM) clusters, notably the Keggin and Dawson anions. The resultant

entities are referred to as 'lacunary' anions, with 'lacuna' denoting unfilled space or gap, while the original polyoxometalates are termed 'plenary' POMs. The removal of one or more constituent atoms leads to the exposure of anionic oxo-ligands and an increase in the overall charge of the POM. In the case of polyoxotungstates, lacunary species are typically stable and isolable. Conversely, for polyoxomolybdates, these species tend to exhibit high reactivity and often prove challenging to isolate and manipulate without undergoing degradation.[18]

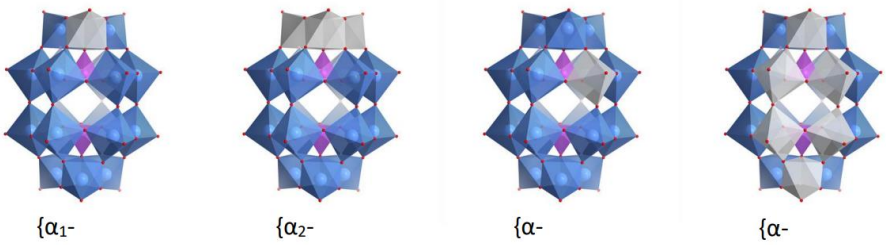

Figure 7. Polyhedral representation of the four possible lacunary species of the Wells-Dawson cluster

Lacunary species play a pivotal role in functionalizing POMs, as the exposed oxo-anions can either coordinate with a variety of metals or engage in covalent organo-functionalization with oxo-philic p-block elements. Within the Keggin anion, three distinct types of lacunary structures are known to exist, achieved through the removal of one to three metal centers, thereby generating mono-lacunary $[XM_{11}O_{39}]^{(n-4)}$, dilacunary $[XM_{10}O_{36}]^{(n-4)}$, and trilacunary $[XM_9O_{34}]^{(n-6)}$ derivatives (where n represents the charge of the parent anion). The increase in the POM's negative charge directly corresponds to the number of oxo-anions formed via the removal of metal center(s). Furthermore, successive hydrolysis events typically occur at the same site on the POM, resulting in a progressively larger lacuna, rather than isolated sites. The destabilization induced by the removal of addenda atoms can lead to structural isomerization as a means of stabilizing the POM.

The formation of lacunary structures from the Wells-Dawson cluster is also a common phenomenon. Unlike the sequential formation of lacuna in the Keggin structure, lacunary species in the Wells-Dawson structure emerge through the removal of a single metal (monolacunary, $[X_2M_{17}O_{61}]^{(n-4)}$), a single cap (trilacunary, $[X_2M_{15}O_{56}]^{(n-6)}$), or a single "face" (hexalacunary, $[X_2M_{12}O_{48}]^{(n-8)}$) from the

structure. Due to the high thermodynamic stability of plenary POMs, the formation of lacunary structures can only be achieved through base-driven hydrolysis. These structures exhibit far less positional isomerism, with stable lacunary structures primarily stemming from the α-Dawson anion.

1.4 Biological application of POMs

POMs are molecular metal oxide anions based on covalently linking transition metal elements (M often Mo, W, V) with oxygen atoms.[19, 20] Their broad structural and chemical tunability, together with their unique properties (acidity, redox-activity, charge, and rigidity, etc.), makes them ideal models to optimize the interaction with biological macromolecules, such as proteins, enzymes and peptides.[21] Polyoxometalates have agelong been studied in a variety of biological applications. Interactions between the highly charged POM molecules and biological molecules frequently occur through covalent-bonding and electrostatic interactions. Moreover, Polyoxometalates (POMs) and POM-based hybrid compounds have shown significant potential as agents for various medical applications, including antitumor, antiviral (such as anti-HIV and anti-HBV), antibacterial, and anti-Alzheimer's disease (AD) therapies, refer to Figure 8.

Currently, clinical development of POMs is still in its early stages, and researchers are actively working on developing POM derivatives with low toxicity, high stability and selectivity, improved biological activity to achieve superior antitumor, anti-infection, and anti-AD effects. The focus of current research is on novel POM-based molecular and composite materials.[22]

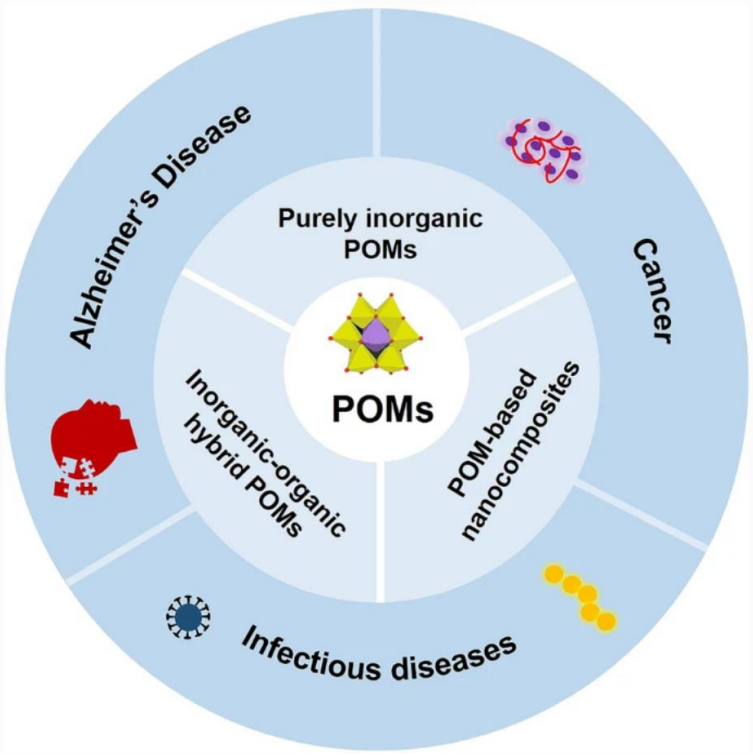

Figure 8. As shown in studies performed in recent decades, polyoxometalates (POMs) have promising biological activities, including antitumor, anti-infectious and anti-Alzheimer's activities.

One approach to mitigating the toxicity of POMs is the conjugation of organic molecules or bioactive compounds to the POM core or skeleton, which can reduce their toxicity. Additionally, POM-based hybrid compounds for cell targeting can significantly decrease the toxicity caused by metal ions and enhance biocompatibility. Moreover, doping anticancer, anti-infection, and anti-AD drugs into POM-based nanocomposites can further enhance their biological properties. POM-based nanocomposites demonstrate superior biological and pharmacokinetic properties compared to organically functionalized POMs. Thus, the development of more POM-based nanocomposites for anticancer, anti-infection, and anti-AD therapies is a key area of future research.

Several potential toxicity mechanisms of POMs have been proposed, including competition with acetylated low-density lipoprotein (LDL) for macrophage scavenger receptors,[23] protein binding through electrostatic interactions, preferential deposition in highly perfused organs such as the liver, spleen, lungs, and kidneys, and limited elimination from the body.[24]

Despite the proposition of these mechanisms, the precise impact of POMs on cellular and systemic processes remains incompletely understood. Future research endeavors will be geared towards the design and synthesis of novel POM hybrids with favorable toxicity profiles, pharmacokinetic attributes, and biological functionalities. The objective is to mitigate the toxicity associated with POMs, thus paving the way for their utilization as the next generation of therapeutic agents for addressing conditions such as tumors, viral infections, bacterial infections, and Alzheimer's disease [25](AD). Among these diverse biological applications, the anticancer potential is particularly paramount and has garnered substantial attention from researchers.

1.5 Development of cancer treatment

In the long history of human diseases, numerous afflictions have been eradicated due to technological advancements. However, there are still several diseases that have evolved over time into formidable threats to human health. One such disease is cancer, which stands as a dreadful killer of human well-being. Cancer encompasses a group of diseases characterized by uncontrolled growth and proliferation of cells. If left untreated, these abnormal cells can lead to high mortality rates. Although the exact causes of cancer development are not entirely understood, numerous factors are known to increase the risk, including modifiable factors like tobacco use and obesity, as well as non-modifiable factors such as inherited genetic mutations.

Statistics from recent years depict the immense toll of cancer on a global scale. In 2018, an estimated 9.6 million people died from cancer worldwide. In 2019, there were 23.6 million new cancer cases and about 10 million deaths. According to the World Health Organization's World Cancer Report 2020, published in February 2020, the number of cancer cases worldwide could surge by 60% in the next two decades, with low- and middle-income countries potentially experiencing an 81% increase.

Globally, one in six people dies from cancer each year, and the cancer burden is increasing. Today, cancer is the second most common cause of death. However, by 2050, it may surpass heart disease to become the leading cause of mortality worldwide. Therefore, it is necessary to develop efficacious treatment strategies for patients with cancer.

In the battle against cancer, treatment methods have undergone significant revolutions. These include surgery, radiotherapy and chemotherapy, molecular targeted drugs. The driving force behind these significant advancements in treatment stems from our increasingly profound comprehension of the dynamic and progressive characteristics of cancer.

The term "cancer" itself originates from the Latin word and in Latin, it means crab - rampant is the way crabs walk, and it is also the most intuitive feeling of cancer at first: overbearing cancer. The earliest understanding of cancer comes from Hippocrates, ancient Greece, who first described malignant tumors - cancer is a lump, or tumor. This perception did not change much until the 19th century. If you think of it as a lump, then cutting it off is undoubtedly a good option. The first recorded cancer surgery was in 1809, when Americans surgically removed ovarian tumors. Since then, surgery has become an important way to treat cancer, with the development of aseptic technology and anesthesia technology, until now, surgery is still the most important and effective treatment for early cancer.

During surgical interventions, however, it remains challenging for doctors to predict the long-term survival outcomes for cancer patients. Some individuals may live for several decades post-surgery, while others may survive for only a few months. The growth patterns of tumors also vary, with some large tumors showing slower progression and smaller tumors exhibiting rapid growth. The reasons for these discrepancies remained unknown during this period, as the understanding of tumors was primarily limited to visual observation.

It was not until 1836 that the microscopic examination of cancer revealed its composition of "abnormal cells." This realization led to the understanding that cancer is not merely a lump but is composed of cells. Consequently, the concept emerged that inhibiting cell growth could potentially impede cancer progression. This led to the emergence of the second line of cancer treatment: radiotherapy and chemotherapy, collectively known as chemoradiotherapy. Radiotherapy, which involves using radiation to kill cancer cells, traces its origins back to 1895 when X-rays and radium were first utilized for cancer treatment. Early radiotherapy techniques had significant drawbacks,

harming normal cells along with cancer cells. However, advancements in radiotherapy technology have greatly improved the accuracy and precision of treatment, resulting in reduced side effects

Chemotherapy, on the other hand, arrived on the scene later than radiotherapy. It was not until the 1940s, with the successful clinical trial of nitrogen mustard for treating lymphoma in the United States, that chemotherapy gained recognition as a viable cancer treatment. Researchers discovered that fast-growing cancer cells could be specifically targeted by chemotherapy drugs, as they exhibited accelerated growth compared to normal cells. However, this approach also had drawbacks, as the drugs not only killed cancer cells but also affected fast-growing healthy cells, leading to side effects such as hair loss due to damage to hair follicle cells. Over time, the side effects of chemoradiotherapy have been significantly reduced as technology has advanced.

Following its initial clinical approval in the late 1990s and the subsequent impressive efficacy demonstrated against specific cancer types, molecular targeted therapy employing small molecule agents or therapeutic monoclonal antibodies as inhibitors of signal transduction pathways has emerged as a cornerstone in the field of precision medicine for cancer treatment. These strategies have now become standard first-line therapies for diverse human malignancies. In contrast to conventional chemotherapy, targeted therapeutic agents offer enhanced antitumor effects while minimizing adverse side effects.

The limitations of chemotherapy, such as its nonselective effects on normal cells leading to side effects and toxicity, have prompted the development of innovative "targeted" cancer treatments with enhanced specificity for cancer cells. Targeted therapy encompasses various approaches, including conventional molecular targeted agents like small molecule inhibitors or antibodies that specifically hinder signal transduction pathways involved in growth, proliferation, and survival, refer to Figure 9. Hormonal agents, such as estrogen receptor antagonists and aromatase inhibitors, have been employed for treating hormone receptor-dependent breast cancer as well as reproductive cancers in both males and females. Additional targeted therapy is Immune checkpoint inhibitors, such as antibodies against programmed cell death protein 1 (PD-1), programmed death-ligand 1 (PD-L1), or cytotoxic T-lymphocyte-associated protein 4 (CTLA-4), activate the host's anti-tumor immune

response either directly or indirectly.[26] Targeted cytotoxic therapy, such as methotrexate (a dihydrofolate reductase inhibitor), interferes with specific cellular targets. Although these targeted therapies exhibit effectiveness against cancer, they are limited to patients harboring specific driver mutations or aberrations that can be targeted. Moreover, side effects, toxicity resulting from unexpected interactions with normal cells, and the emergence of intrinsic or acquired drug resistance pose challenges to their efficacy. Despite these limitations, targeted therapy has demonstrated significant survival benefits in certain cancer types, revolutionizing the fundamental concept of cancer treatment and providing the basis for the progression towards precision or personalized medicine in cancer.

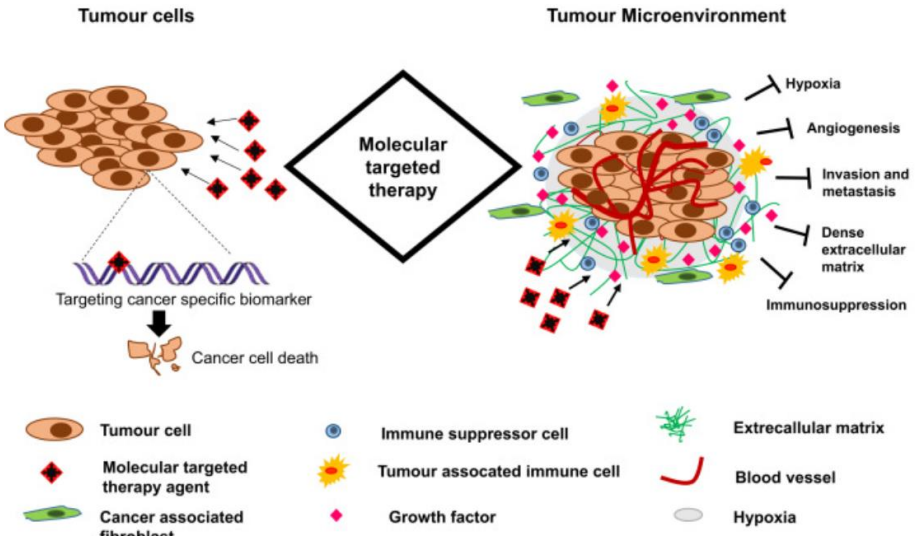

Figure 9. Overview of molecular targeted therapy mechanism. Molecular targeted therapy on cancer focuses on targeting specific cancer associated molecules that are highly expressed in cancer cells or by modulating the tumor microenvironment related to tumor vasculature, metastasis or hypoxia.[27]

1.6 The concept of drug targeting

In modern medicine, drugs are typically distributed within the body evenly and proportionally to the regional blood flow after administration. However, to reach their intended site of action, drugs must overcome various biological barriers, including other organs, cells, and intracellular compartments. These barriers can potentially lead to drug inactivation or undesired effects on organs and tissues not

involved in the disease process. To address this challenge, drug targeting has emerged as a strategy to selectively and quantitatively accumulate active pharmaceutical ingredients (APIs) in specific organs or tissues, regardless of the method of administration.[28]

The concept of drug targeting, initially proposed by Paul Ehrlich in the early 20th century as the "magic bullet," involves the coordinated action of three components: the drug itself, a targeting moiety, and a carrier.[29] **the drug component** represents the active pharmaceutical ingredient responsible for the therapeutic effect on the target cells or tissues. Typically, drugs are designed to interact with specific molecular targets involved in the disease process, such as receptors or enzymes, to exert their desired therapeutic effects. **the targeting moiety**, also known as a ligand or targeting agent, is the second component. It plays a crucial role in recognizing and binding to specific molecules or receptors present on the surface of the target cells. By attaching the targeting moiety to the drug, the magic bullet can selectively deliver the drug to the desired cells while minimizing exposure to non-target cells. Antibodies, peptides, aptamers, or other molecules with high affinity and specificity for the target can serve as targeting moieties. **the third component is a carrier or delivery system**, which acts as a protective vehicle for the drug and targeting moiety during transport to the target site. The carrier enhances the drug's stability, solubility, and bioavailability while providing a means for controlled release. Various carrier systems are employed, including liposomes, nanoparticles, micelles, and polymer-based systems.

The combination and interaction of these three components enable the magic bullet to effectively deliver the drug to the intended target cells or tissues. The targeting moiety guides the magic bullet to the specific cells of interest, while the carrier safeguards the drug during circulation and facilitates its release at the target site.

The concept of "magic bullets" holds immense potential within the realm of medicine, particularly in the context of targeted therapies for conditions like cancer, infectious diseases, and other intricate disorders. By precisely directing therapeutic agents to afflicted cells or tissues, these "magic bullets" offer the promise of heightened treatment effectiveness, minimized side effects, and enhanced patient outcomes. Ongoing research and advancements in drug delivery systems continually refine the design

and efficiency of these targeted therapies, thus paving the way for a more personalized approach to medicine. Emerging from the groundbreaking strides made in nanotechnology, nanomaterials have emerged as an innovative category of drug delivery vehicles. These colloidal systems, notable for their diminutive size (less than 1 μm), can be fashioned from a diverse array of materials and compositions (as illustrated in Figure 10). A variety of nanoparticle types are frequently employed as carriers, encompassing liposomes, micelles, dendrimers, nanotubes, hydrogels, solid lipid nanoparticles, metallic nanoparticles, semiconductor nanoparticles, and polymeric nanoparticles.

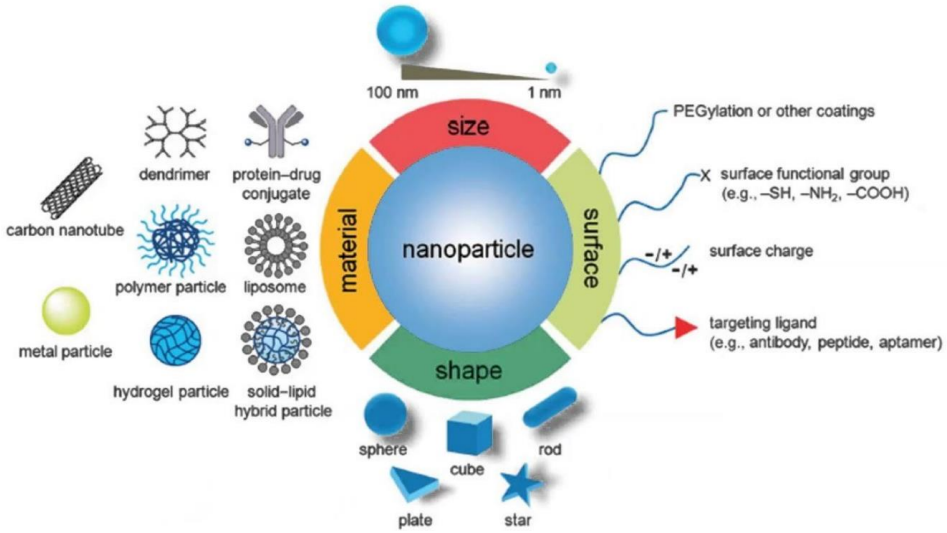

Figure 10. An overview of the methodologies employed in attaining drug targeting with nanomaterials. [30]

1.7 Targeting Ligands

Despite the tremendous potential of nanoparticle systems for drug delivery, the translation of targeted nanoparticles into clinical trials has encountered significant challenges, with only a few candidates successfully advancing. The limited success of targeted nanoparticles in clinical development stems from a complex array of factors that may be multifaceted. Among these factors, the selection of appropriate targeting ligands plays a vital role in achieving successful development. Various variables should be considered, such as ligand biocompatibility, cell specificity, binding affinity, and ligand purity.[31] Additionally, crucial factors to be taken into account include the size and charge of the ligand molecule, as well as its ease of modification and conjugation to the nanoparticles. Practical

considerations for ligand selection also involve production cost, scalability, and stability (e.g., stability in organic solvents and at high temperatures) during mass production. Five distinct classes of targeting ligands were used in biological application, encompassing antibodies and antibody fragments, aptamers, peptides, sugars, and small molecules.[32]

1.71 Peptide ligands

Peptide ligands have exhibited remarkable potential for targeting due to their small size, high stability, and ease of large-scale synthesis with excellent quality control. Moreover, they are easily synthesized by using solid-phase peptide synthesis (SPPS) and can be easily tailored. Furthermore, it can be expressed in situ or chemically synthesized, allowing for straightforward production and scalable manufacturing. Advancements in phage display techniques[33] and other screening methods have facilitated the discovery of novel peptide-targeting domains and the identification of cell-specific peptide ligands.[34] Peptide-conjugated nanoparticles have found extensive use in targeting cancer cells and tumor vasculature. peptide-drug conjugates (PDCs) consist of three components: a tumor-homing peptide, a linker, and a cytotoxic agent (Figure 10).[35] The molecule has a relatively small weight (2-20 kDa), which facilitates its penetration into the tumor stroma and entry into tumor cells. It is quickly eliminated by the kidneys, reducing its toxicity to the bone marrow and liver.[36] Notwithstanding, small molecule-based cytotoxic agents offer advantages such as high oral availability, metabolic stability, and good membrane permeability. They also have drawbacks including high toxicity, poor solubility, and lower selectivity compared to alternative options. By delivering PDCs into tumor cells using tumor-homing peptides, a tumoricidal effect can be achieved within the intracellular compartments where tumor-specific pH or enzymes can break the linkers, thereby releasing the drugs. The use of PDCs increases the local concentration of cytotoxic agents in tumor tissues, reducing the cytotoxic effects on normal tissues and enhancing therapeutic efficacy. Antibody-drug conjugates (ADCs) are predicted to exceed 16 billion dollars in the market size by 2026. While , most ADCs do not penetrate into tumors. With a molecular weight of about 150 kDa, they are too big to diffuse efficiently into malignant tissue. However, PDCs offer several advantages over ADCs.[37] Due to their small molecular weight, PDCs exhibit better tumor penetration. They also have lower systemic

exposure as they are rapidly cleared from the body, resulting in a lower risk of immunogenicity and liver damage. Additionally, PDCs can be produced more easily and at a lower cost.

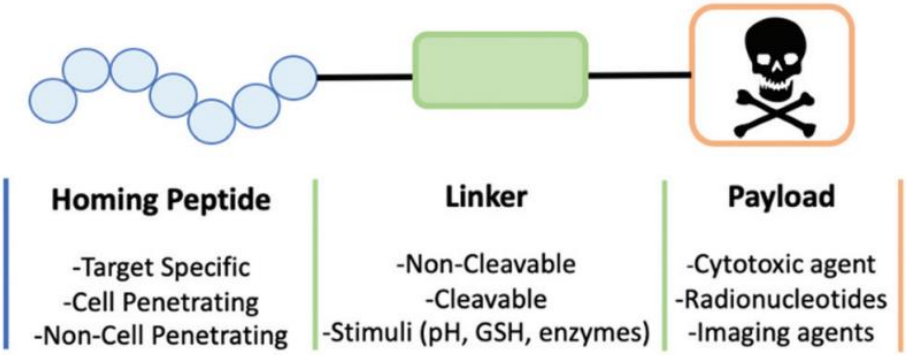

Figure 10. A schematic of a PDC, comprising a combination of a homing peptide, a linker, and a payload. [35]

Various linkers have been developed to conjugate drugs or cytotoxic agents with tumor-homing peptides. The selection of an appropriate linker is crucial for the design of PDCs. Moreover, the microenvironment in which PDCs function should be taken into consideration, as different linkers can impact drug efficacy or binding affinity depending on their structural characteristics. For instance, certain peptide linkers are designed to be cleaved by enzymes that are abundant in tumor cells, enabling the selective release of drugs within these cells. Examples of such linkers include the GFLG peptide, which is cleaved by cathepsin B, the PLGLAG peptide, which is cleaved by matrix metalloprotease (MMP)-2/9, and the oxime-hydrazone bond, which is hydrolyzed under acidic pH conditions.[38] Simultaneously, a number of PDCs are currently under consideration for approval by the Food and Drug Administration (FDA) for commercial use. One such example is BT8009, which consists of a bicyclic peptide (CP(1Nal)dCM(hArg)DWSTP(HyP)WC) as the targeting component and monomethyl auristatin (MMAE) as the cargo.[39] BT8009 specifically targets Nectin-4, a protein present on tumor cells.[40] This PDC is currently in phase I/II clinical trials, evaluating its efficacy in the treatment of patients with metastatic non-small cell lung cancer. The PDCs currently under clinical/preclinical trials are summarized in Table 1.

Table 1. Peptide–drug conjugates in clinical/preclinical trials for Food and Drug Administration approval.[37]

PDC name (Manufacturer)	Sequence	Drug	Target	Target disease	Status
ANG1005 (AngioChem)	TFFYGGSRGKRNNFKTEEY (Angiopep-2)	Paclitaxel	LRP-1	Breast cancer with brain metastasis	Phase III
BT1718 (Bicycle Therapeutics)	-	Mertansine (DM1)	Membrane type 1-matrix metalloprotease	Esophageal tumor	Phase II
BT8009 (Bicycle Therapeutics)	CP(1Nal)dCM(hArg)DWSTP(HyP)WC	MMAE	Nectin-4	Metastatic non-small cell cancer	Phase I/II
CBX-12 (Cybrexa Therapeutics)	ACEQNPIYWARYADWLFTTPLLLLDLALLVDADEGTG (pHLIP®)	Exatecan	Low pH	Advanced solid tumors	Phase I/II
OPD5 (Oncopeptides AB)	-	Melflufen	Aminopeptidase	Relapsed multiple myeloma	Phase I
SBI-1301 (Soricimed Biopharma)	-	Paclitaxel	Transient receptor potential vanilloid subfamily member 6	Solid tumors	Preclinical
SG3299 (Spirogen)	NAVPNLRGDLQVLAQKVARTC	Tesirine	αvβ6 integrin	Pancreatic tumor	Preclinical
TH1902 (Theratechnologies)	GVRAKAGVRN(Nle)FKSESY	Docetaxel	Sortilin	Triple-negative breast cancer	Phase I

1.72 Agonists and antagonist peptides

Peptides are short chains of amino acids that play important roles in biological processes. When used as ligands in active drug targeting, peptides can act as agonists or antagonists for the targeted receptor depending on their specific sequence and structure. Peptides designed as agonists mimic the natural ligands that bind to a specific receptor. They interact with the receptor and activate downstream signaling pathways, leading to a physiological response. Agonistic peptides can induce receptor activation and promote biological effects such as cell growth, differentiation, or the release of specific signaling molecules. On the other hands, when peptides designed as antagonists, it competes with the endogenous ligands for binding to the receptor but do not activate downstream pathway. Instead, the peptide antagonist blocks or inhibits the binding of the endogenous ligand or other agonists to the receptor, preventing their activation and subsequent downstream signaling. Peptide antagonists can effectively compete with the natural ligand for binding to the receptor, thereby interfering with its function and suppressing the biological response that would be induced by receptor activation.[41]

1.73 Bombesin:

Bombesin (Bn) (Figure 11) is originally extracted from the skin of two European aquatic toads belonging to the Bombinatoridae family, namely Bombina bombina and Bombina variegata. Bn is a bioactive tetradecapeptide with potent regulatory properties. It exhibits excellent cellular permeability and biocompatibility.[42]

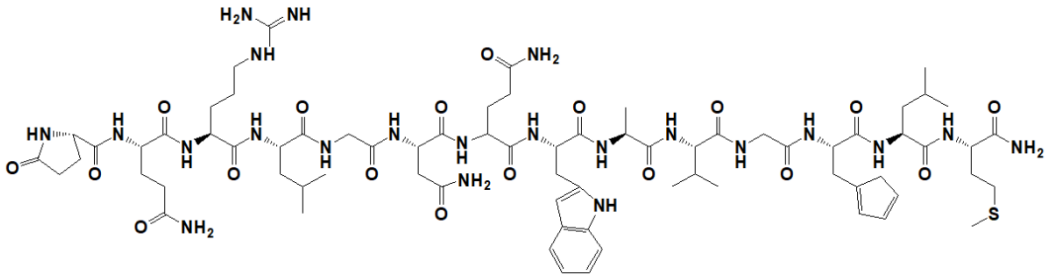

Figure 11. the structure of Bombesin

Bn, a hydrophilic tetra-decapeptide, exhibits high permeability in peripheral cells but lacks significant ability to cross the blood-brain barrier. Previous research indicates the involvement of Bn and Bn receptors in various intricate physiological pathways and neuroendocrine signaling. The Bn receptors consist of three subtypes found in mammals: the neuromedin B (NMB) receptor (NMBR or BB1 receptor), the gastrin-releasing peptide (GRP) receptor (GRPR or BB2 receptor), and the orphan bombesin receptor subtype 3 (BRS-3 or BB3 receptor).[43] Among these receptors, BB2 has been extensively investigated and found to be overexpressed in various human cancers, including breast, colon, non-small cell lung cancer, gliomas, meningiomas, head/neck squamous cell, ovarian, pancreatic, prostate cancers, and neuroblastomas.[44] These receptor subtypes share over 50% of a common amino acid sequence. The C-terminal region of BB2 shows homology with the mammalian gastrin-releasing peptide (GRP), which functions as a modulatory neurotransmitter and an endocrine factor promoting cancer cell growth in normal and neoplastic tissues of diverse origins. GRP stimulates various physiological processes, including exocrine secretion, smooth muscle contraction, and exhibits trophic effects. GPCRs employ a classic seven-transmembrane-segment motif and initiate various downstream signal transduction pathways. These pathways involve phospholipase C (PLC), which leads to the release of inositol triphosphate (IP3) and subsequent activation of the

calcium cascade. Additionally, protein kinase C (PKC) plays a crucial role in phosphorylating other key signaling molecules, thereby mediating the effects of Bn through GPCR activation.[45]

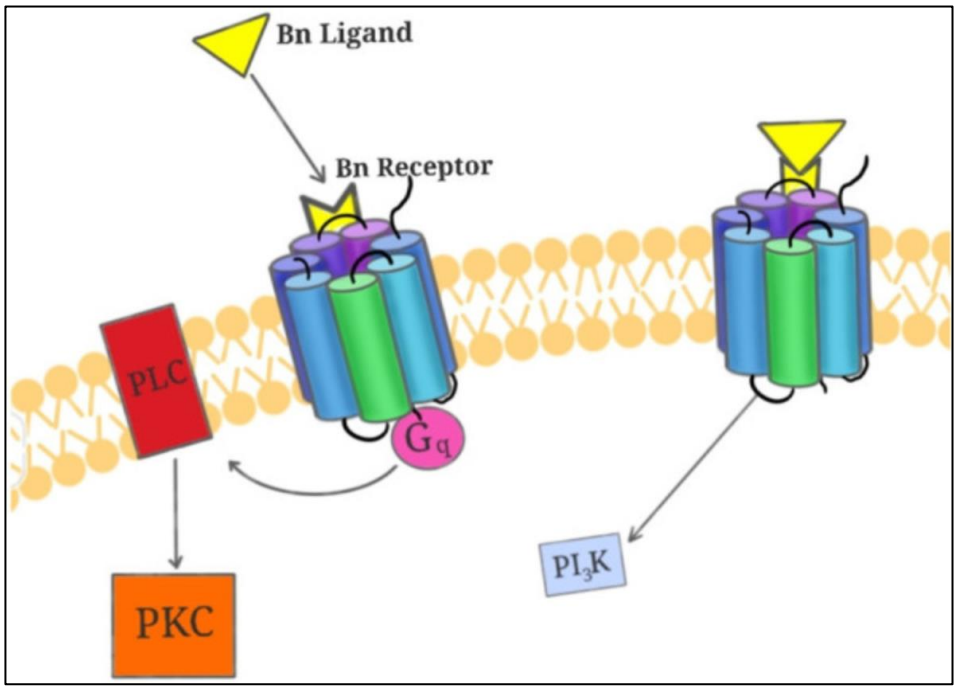

Figure 12. Targeting of gastrin-releasing peptide receptor.[46]

The bombesin (Bn) functions as an antagonist for the GRPR (gastrin-releasing peptide receptor). The natural ligand for GRPR is bombesin, which activates the receptor to stimulate various cellular responses. However, the bombesin analogue is designed to competitively bind to the GRPR receptor without activating it. By occupying the receptor's binding site, the bombesin analogue prevents the binding of the endogenous bombesin ligand, thereby blocking receptor activation. This inhibition of receptor activation classifies the bombesin analogue as an antagonist peptide.

1.74 RGD

The RGD sequence (Arg-Gly-Asp) (Figure 13A) was initially identified in the 1970s by E. Ruoslahti as a cell attachment site in fibronectin. Subsequently, this sequence was found to be a key integrin-binding motif present in various natural ligands that interact with the αvβ3 receptor, including fibrinogen, fibronectin, vitronectin, plasminogen, thrombospondin, prothrombin, MMP-2, laminin, osteopontin, and others.[47] The RGD sequence serves as the fundamental building block for the design

of molecules that selectively bind to the αvβ3 integrin and other integrins. The binding affinity of RGD peptides to their ligands can be influenced by the steric conformation of the peptide. In addition to direct interactions between flanking groups and their receptors, the conformational characteristics of the RGD motif can also be modulated. Cyclization, for instance, is commonly employed to enhance the binding properties of RGD peptides by imparting structural rigidity. (Figure 13B)

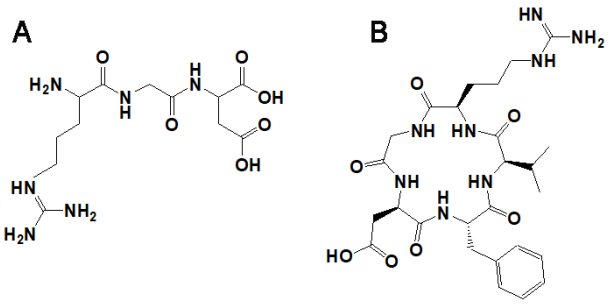

Figure 13. The chemical structures, A) is the sequence of RGD and B) is the cyclization of RGD.

Integrins, a family of heterodimeric transmembrane glycoproteins, play crucial regulatory roles in cell adhesion, migration/invasion, proliferation, survival, and apoptosis. It is widely acknowledged that integrins exhibit "on" and "off" states. In the "off" state, the extracellular domain of αvβ3 integrin is folded or bent, concealing the RGD-binding site and preventing ligand binding. Conversely, when αvβ3 integrin is bound to RGD, its extracellular domain becomes unbent or straighter (Figure14). Although the cytoplasmic tails of integrins are much smaller compared to their extracellular domains, they play crucial roles in integrin signaling.[48] Mechanisms such as separation, twisting, and hinging of the cytoplasmic tails are considered essential for enabling activation.[49]

The integrin αvβ3 plays a critical role in angiogenesis, being expressed in both tumoral endothelial cells and certain tumor cells. RGD peptides have been widely recognized for their selective binding to the αvβ3 integrin. Consequently, targeting tumor cells or tumor vasculature using RGD-based approaches holds significant promise for delivering anticancer drugs or contrast agents in cancer therapy and diagnosis. RGD-based strategies encompass various approaches such as RGD sequence antagonists (peptidic or peptidomimetic), RGD-conjugates, and the surface grafting of RGD peptides or peptidomimetics onto nanocarriers as targeting ligands.[50]

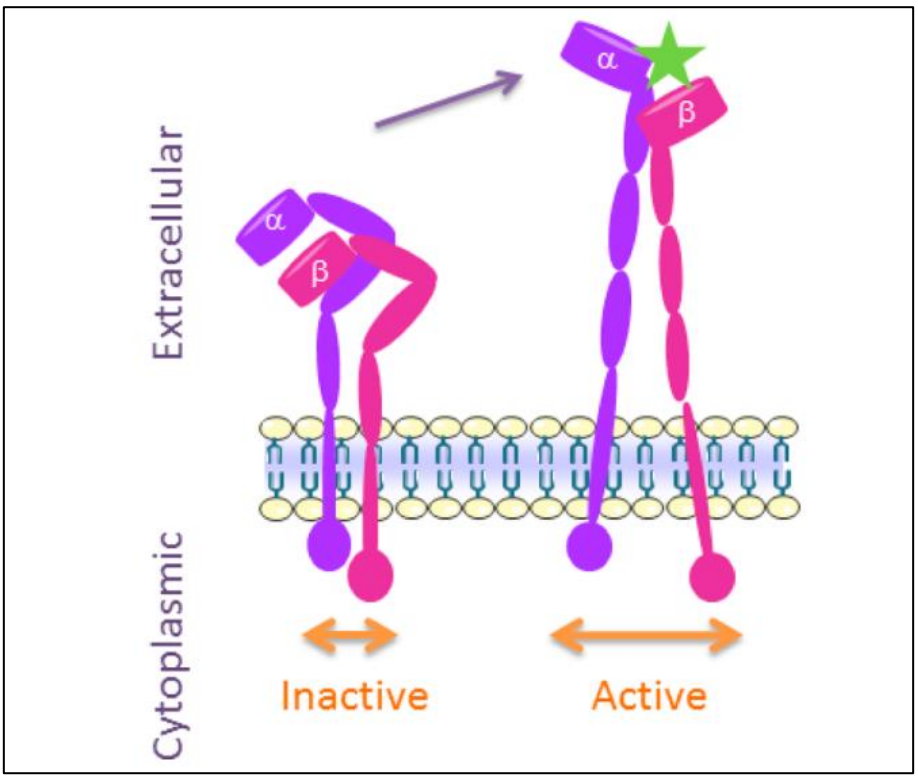

Figure 14. Conformational changes in αvβ3 integrin. Upon activation the extracellular domains extend and straighten, exposing the RGD binding domain (star).[48]

The RGD (Arg-Gly-Asp) analogue acts as an antagonist for integrins. Integrins are cell surface receptors involved in cell adhesion, migration, and signaling processes, and the RGD motif is commonly found in extracellular matrix proteins and serves as a recognition sequence for integrins. The RGD analogue is designed to competitively bind to integrins, specifically targeting the RGD binding site. By occupying this site, the RGD analogue prevents the interaction of endogenous ligands (such as fibronectin or vitronectin) with integrins, thereby inhibiting integrin activation and downstream signaling. This competitive inhibition of integrin binding categorizes the RGD analogue as an antagonist peptide. The cyclic version of the RGD motif has demonstrated effective binding to integrins and has been extensively investigated for targeting nanoparticles to disrupt tumor angiogenesis.

In both cases, the antagonist peptides (bombesin analogue and RGD analogue) are designed to block the activation of their respective receptors without initiating downstream signaling pathways. Instead

of promoting cellular responses, these peptides interfere with the binding of the natural ligands to the receptors, thereby exerting inhibitory effects and functioning as antagonists.

1.8 Alzheimer's Disease (AD)

Alzheimer's disease (AD) is a progressive brain disorder characterized by the accumulation of specific proteins, leading to brain changes. This disease results in brain shrinkage and eventual cell death. It is the most common cause of dementia, a condition marked by a continuous decline in memory, cognitive abilities, behavior, and social skills, impairing a person's ability to care for themselves. In the United States, approximately 6.5 million individuals aged 65 and older are affected by Alzheimer's disease, with more than 70% of cases occurring in those aged 75 and above. Globally, out of the approximately 55 million people living with dementia, around 60% to 70% have Alzheimer's disease.

Early signs of the disease include recent memory loss and difficulties in communication. As the condition progresses, severe memory problems develop, accompanied by an inability to perform daily tasks. While medications can alleviate symptoms or slow down their progression, there is currently no cure for Alzheimer's disease. Advanced stages of the disease may lead to severe brain function loss, causing complications such as dehydration, malnutrition, or infections, which can ultimately result in death. To support individuals with Alzheimer's disease and their caregivers, various programs and services are available. However, addressing the underlying cause and finding a definitive cure for the disease remain ongoing challenges.

1.81 Amyloid-β and Neurofibrillary Tangles Involvement in Alzheimer's Diseases

In 1907, the first report of Alzheimer's disease (AD) was reported by Dr. Alois Alzheimer, a German psychiatrist and neuropathologist. He encountered a middle-aged woman with acute memory loss and linguistic difficulties. Dr. Alzheimer conducted a postmortem examination of her brain, employing the silver staining technique, and observed the presence of thick fibrillar materials distributed throughout the cerebral cortex region.[51] These deposited materials were subsequently identified as

plaques (refer to (Figure 15A) and tangles.[51, 52] Histopathological investigations of AD brains have revealed the major pathological hallmarks in the AD brain are extracellular deposition of amyloid-β (Aβ) and intracellular neurofibrillary tangles (NTF) formed by hyperphosphorylated tau,[53] as depicted in the Figure 15B.

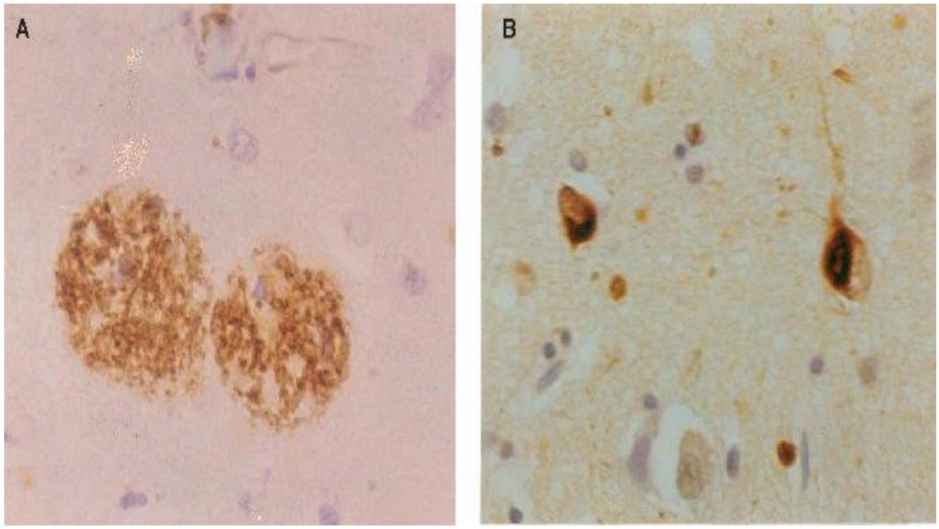

Figure 15. The cerebral cortex region of AD brain displaying (A) neuritic plaques and (B) neurofibrillary tangles. Neuritic p laques are extracellular deposition of Aβ and neurofibrillary tangles are inner deposition of microtubule-associated tau proteins of neuron.[54] Both of these phenomena constitute the principal hallmark features of Alzheimer's disease (AD).

In 1985, the amyloid-β protein (Aβ) was identified as the main component of these plaques. Monomeric Aβ, approximately 4 kDa in size, is generated through the intramembrane proteolytic cleavage of a larger protein called amyloid-β precursor protein (APP).[55] APP is sequentially cleaved by the aspartyl proteases β-secretase and γ-secretase and results in the production of Aβ peptides of lengths varying from 38 to 43 residues depending on the position of the cleavage by γ-secretase (Figure 16). The Aβ peptides predominantly found in AD-associated plaques are Aβ40 and Aβ42, spanning residues 1-40 and 1-42, respectively. It is noteworthy that Aβ42 is considered to be the more harmful form of Aβ. Despite differing by only two amino acids, Aβ42 exhibits a significantly higher propensity for aggregation than Aβ40 in vitro. Moreover, genetic mutations in presenilin 1 and 2, which encode enzymes involved in APP cleavage, lead to an aggressive early-onset form of AD and an increased ratio of Aβ42 to Aβ40 production.[56]

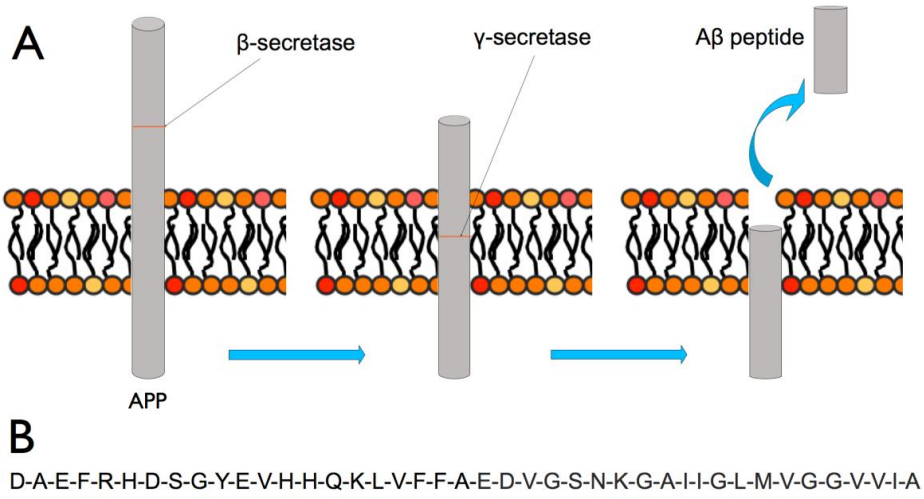

Figure 16. A schematic of the production of Aβ via the proteolytic processing of amyloid precursor protein is depicted in (A). The peptide sequence of Aβ42 is shown in (B)

While amyloid involvement is a prominent feature of Alzheimer's disease, it's essential to note that the exact relationship between amyloid plaques and the development of the disease is still under investigation. The amyloid cascade hypothesis, proposed based on the widespread presence of amyloid plaque deposits in the brains of deceased dementia patients, suggests that the amyloidogenesis of Aβ plays a crucial role in initiating AD, leading to dementia symptoms. Genetic evidence strongly supports this hypothesis. Individuals with trisomy 21 (Down's syndrome), where the chromosome responsible for encoding APP is triplicated, experience early-onset dementia with AD-like plaque accumulation.[57] Moreover, genetic mutations in APP in individuals with early-onset familial AD contribute to the production of Aβ peptides with an increased propensity for aggregation.

In addition to amyloid plaques, another characteristic feature of AD is the presence of intracellular neurofibrillary tangles (NFTs), which contribute to neuronal dysfunction and damage. These tangles consist of aggregated and hyperphosphorylated forms of the tau protein, which is a microtubule-associated protein. The exact role of tau and its interactions with amyloid in the pathogenesis of AD are still under investigation. Studies using mouse models suggest that NFTs may develop downstream of amyloid-beta (Aβ) pathology. Genetic and pathological evidence indicates that the accumulation of Aβ is the initial event in AD pathogenesis, triggering a series of pathological changes, including

the formation of intracellular neurofibrillary tangles, neuronal death, cholinergic deficiency, and inflammation.[58]

1.82 Versatile nanomaterials for Alzheimer's disease

Alzheimer's disease (AD) is a complex neurodegenerative disorder characterized by various pathological features, including abnormal amyloid deposits, tauopathy, neuroinflammation, and abnormal microglia. The pathogenesis of AD is multifaceted, leading to the proposal of several hypotheses, such as the Aβ cascade hypothesis, tau hypothesis, cholinergic hypothesis, and neuroinflammation hypothesis.[59] Among these, the Aβ cascade hypothesis has gained significant attention in pharmaceutical development for AD.

Amyloid-β (Aβ) peptides, specifically Aβ1–40 and Aβ1–42, are generated from β-amyloid precursor protein (APP) through a series of enzymatic cleavages by β- and γ-secretase within endosomes. These peptides are subsequently released from neurons, a process that is regulated by synaptic activity.[60] In the context of AD pathology, Figure 18. demonstrates that the protease β-site APP-cleaving enzyme 1 (BACE1) aberrantly cleaves the amyloid precursor protein (APP), leading to the abnormal production of amyloid-β (Aβ). These newly generated Aβ peptides, also known as Aβ monomers, have a tendency to self-assemble and form various Aβ species with increasing degrees of aggregation. This aggregation process occurs through hydrophobic interactions at the C-terminus, resulting in the formation of initial oligomers, irregular protofibrils, and mature fibrils.[61] Notably, Aβ1–42, which exhibits enhanced hydrophobicity, has been identified as more toxic and has a greater propensity to aggregate compared to Aβ1–40. Consequently, Aβ1–42 is recognized as the primary component of amyloid plaques.

Aβ oligomers, known as the primary neurotoxic agents, have the ability to interact with cell membranes, leading to the disruption of membrane integrity. This process results in synaptic damage, neuronal death, an inflammatory response, increased tau hyperphosphorylation, and oxidative stress. Consequently, Aβ, particularly in its oligomeric form, represents a crucial upstream target for the

treatment of AD. Therapeutic interventions targeting Aβ hold significant potential in modulating the pathological processes associated with AD.

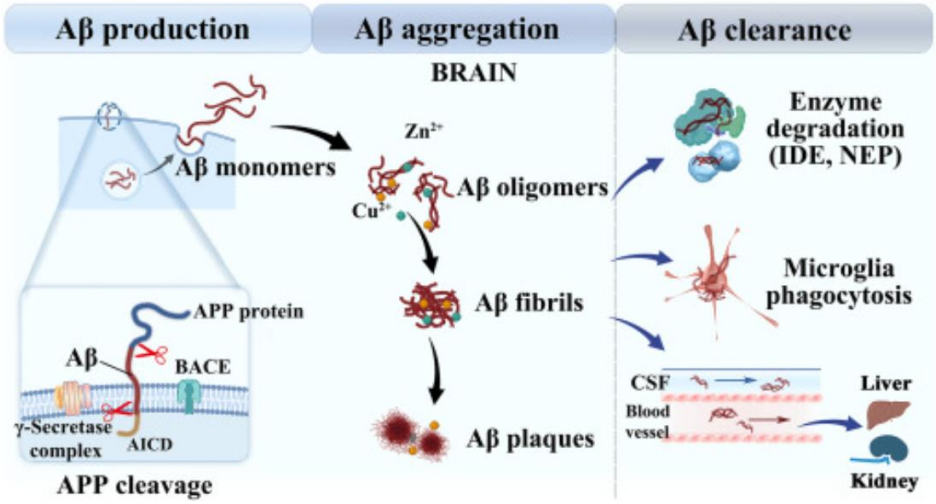

Figure 18. The displaying is the process of Aβ production, aggregation, and clearance in AD brain. Cleaved by β- and γ-secretase, Aβ is released from the APP on neuron cells, and self-aggregated into oligomers and fibrils to form plaques.[58] The amassed Aβ can undergo degradation within the brain through enzymatic processes and microglial phagocytosis. Alternatively, it can be transp orted out of the brain for degradation mediated by the liver and kidneys.

In addition to the complex pathology, overcoming the blood-brain barrier (BBB) is a crucial strategy for combating AD. As the most tightly regulated interface in the body, the BBB restricts the entry of most macromolecule drugs and over 98% of small molecule drugs.[62] Although the integrity of the BBB may be compromised to some extent in AD progression, it still presents a formidable obstacle for drug delivery into the brain. As one of nanomaterial, Polyoxometalate offer potential solutions to overcome these challenges and have garnered significant interest in the field of biomedical research.[63] Additionally, certain bioactive nanomaterials themselves show promise in intervening in AD progression, including Aβ depolymerization, Aβ clearance, tau clearance, and more. The biomedical applications of nanomaterials have the potential to overcome the current treatment dilemma in AD and explore novel disease-modifying strategies for AD therapy in the future.

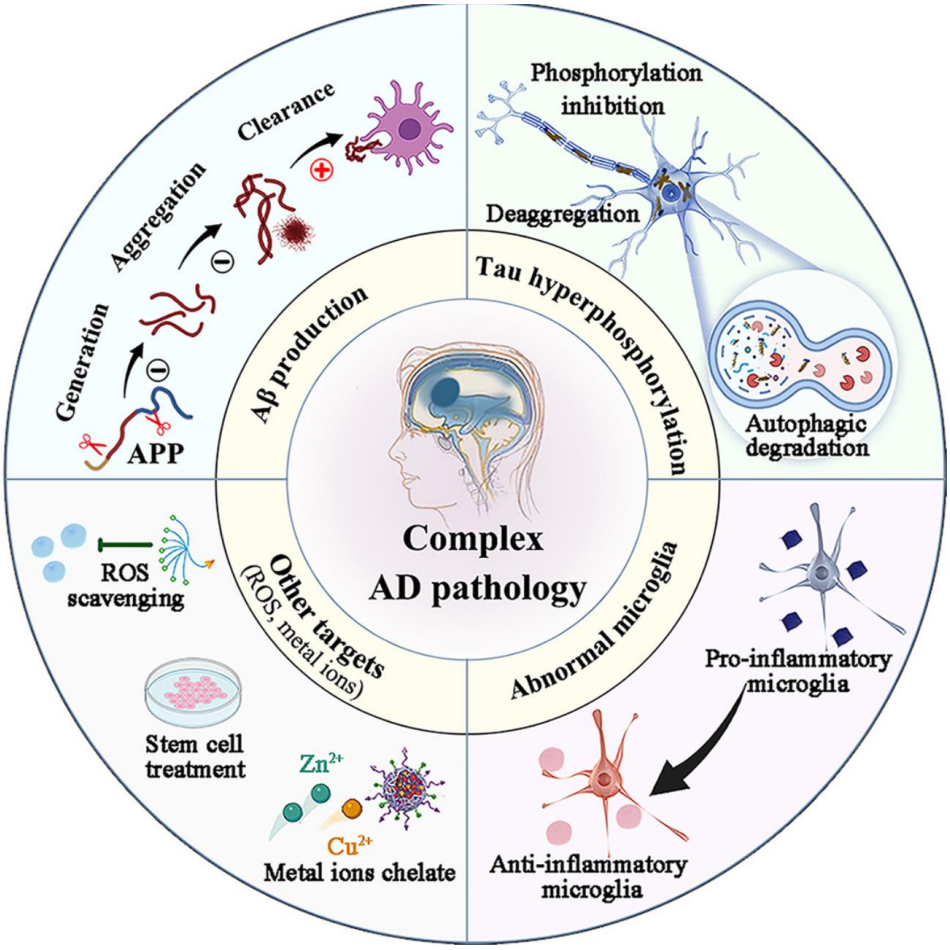

Figure 17. An overview of different pathogenesis of AD, such as the Aβ cascade hypothesis, tau hypothesis, cholinergic hypoth esis, and neuroinflammation hypothesis, leading to different methodology.[58]

1.83 Overview of Aβ-targeting therapies in clinical trials

Initially, early research efforts in Aβ intervention strategies focused primarily on small organic molecules that aimed to modulate Aβ production by inhibiting β−/γ-secretase. However, progress in the development of secretase inhibitors has been limited, largely due to reported adverse effects resulting from excessive secretase inhibition and disruptions to the physiological function of active substances. Consequently, attention has shifted towards addressing the impaired Aβ clearance pathway, which plays a crucial role in the imbalance of Aβ metabolism and catabolism. Multiple Aβ clearance strategies have emerged as a result.

Aβ remains a major focus in drug development for AD treatment, comprising a significant portion of disease-modifying therapeutic pipelines. Currently, the majority of active clinical trials in phase III are centered around monoclonal antibodies, highlighting the prominent position of target Aβ therapy in AD treatment. Passive immunotherapy involves the binding of antibodies' Fc fragments to pathological Aβ forms, facilitating Aβ clearance through microglia-mediated phagocytosis or complement-dependent cytotoxicity. Notably, less than 0.1% of antibodies can permeate into lesion, indicating that treatment benefits may also simultaneously arise from peripheral Aβ clearance, enhancing Aβ efflux from the brain. Active immunotherapy, including vaccines, has also been explored, but satisfactory clinical treatment benefits have not been achieved due to serious adverse effects such as acute meningitis.

Additionally, comprehensive modulation strategies targeting different stages of Aβ pathology, including Aβ production, aggregation, and clearance, have been pursued. Table 2 provides a concise overview of Aβ-targeting therapies currently undergoing phase III clinical trials, facilitating easy comparison between different approaches.

Table 2. Aβ-targeted therapies in phase III clinical trials.[58]

Drugs	Mechanism	Recruitment status	NCT No.	Start date	Sponsor
Azeliragon	- Small-molecule inhibitor of RAGE for alleviating Aβ transport to brain	- Terminated	- NCT02916056	- Jun 2016,	- vTv Therapeutics
		- Terminated	- NCT02080364	- Apr 2015	
Gantenerumab	- Monoclonal antibody binding with aggregated Aβ in brain	- Active, not recruiting	- NCT03443973	- Aug 2018	- Hoffmann-La Roche
		- Active, not recruiting	- NCT04339413	- May 2020	
		- Recruiting	- NCT03444870	- Jun 2018	
		- Recruiting	- NCT04374253	- Feb 2021	
		- Completed	- NCT02051608	- Mar 2014	
		- Completed	- NCT01224106	- Nov 2010	
Solanezumab	- Monoclonal antibody binding with soluble Aβ monomeric	- Terminated	- NCT02760602	- Jun 2016	- Eli Lilly and Company
		- Terminated	- NCT01900665	- Jul 2013	
		- Terminated	- NCT01127633	- Dec 2010	
		- Active, not recruiting	- NCT02008357	- Feb 2014	
		- Completed	- NCT00905372	- May 2009	
		- Completed	- NCT00904683	- May 2009	
Gantenerumab& solanezumab	- Monoclonal antibodies binding with aggregated Aβ and soluble Aβ monomeric respectively	- Completed	- NCT04623242	- Dec 2012	- Washington University
		- Recruiting	- NCT01760005	- Dec 2012	
Lecanemab (BAN2401)	- Monoclonal antibody binding with soluble Aβ protofibrils.	- Recruiting	- NCT04468659	- Jul 2020	- Eisai Inc.
		- Active, not recruiting	- NCT04468659	- Mar 2019	
Umibecestat (CNP520)	- Small molecule BACE inhibitor	- Terminated	- NCT03131453	- Aug 2017	- Novartis Pharmaceuticals
Amilomotide & Umibecestat	- Aβ Vaccine & Small molecule BACE inhibitor	- Terminated	- NCT02565511	- Nov 2015	- Novartis Pharmaceuticals
Simufilam	- Small molecule inhibiting binding of Aβ with α7nAChR	- Recruiting	- NCT04994483	- Oct 2021	- Cassava Sciences, Inc.
		- Not yet recruiting	- NCT05026177	- Oct 2021	

1.84 The amyloid-inhibiting function of KLVFF

Multiple lines of evidence from molecular, genetic, animal transgenic modeling, and biochemical experiments strongly support the notion that the peptide Aβ is the primary contributor to the formation of amyloid plaques, playing a crucial role in the pathophysiology of AD. Consequently, a key objective is to develop therapies that target Aβ by reducing its production.

One particular peptide sequence, Lys-Leu-Val-Phe-Phe (KLVFF), which shares structural similarities with β-conformation regions of Aβ involved in Aβ peptide-peptide interactions, has attracted attention. Tjernberg et al. (1996) synthesized a small Aβ fragment, KLVFF (Aβ16-20), and found

that it bound to Aβ, and is a key driver of Aβ fibrillation.[64] Further in vitro studies revealed that this fragment has shown potential in targeting Aβ and inhibiting its fibrillation process through strong H-bond co-assembly. Additionally, this is a model reported by Riek's group that shows KLVFF is the similar with the Aβ25-35 sequence. Interactions may occur between Ala (30) of Aβ25-35 and Val (18) of KLVFF and Asn (27) of Aβ25-35 and Phe (20) of KLVFF. These interactions may lead to inhibition of fibril formation of Aβ25-35.[65]

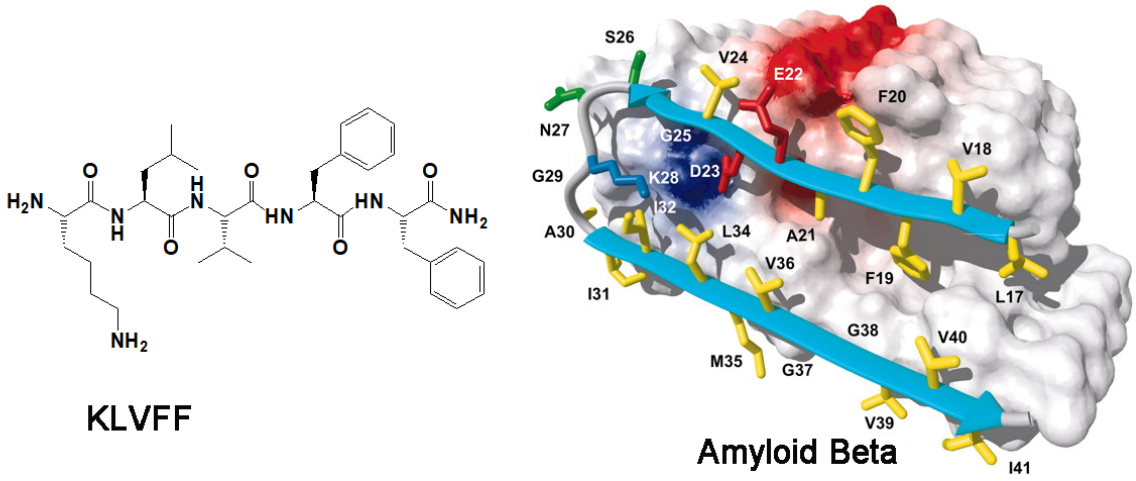

Figure 19. This is a model of KLVFF Interactions may occur between Ala (30) of Aβ25-35 and Val (18) of KLVFF and Asn (27) of Aβ25-35 and Phe (20) of KLVFF.[66]

1.85 Amyloid inhibition by Ala(N_3)-KLVFF-NH_2

Ala(N_3)-KLVFF-NH_2 is a modified peptide sequence derived from the amyloid-beta (Aβ) peptide, specifically targeting the aggregation and inhibition of Aβ. The peptide sequence KLVFF corresponds to a region within Aβ that is known for its propensity to form beta-sheet structures, which are involved in Aβ aggregation.

The addition of the Ala(N_3) modification introduces an azide group (N_3) at the N-terminus of the peptide. This modification can potentially enhance the peptide's stability and solubility, allowing for better experimental control and delivery.

Studies have investigated the inhibitory effects of Ala(N_3)-KLVFF-NH_2 on Aβ aggregation and toxicity. Research has suggested that this modified peptide can interfere with the aggregation of Aβ, thereby reducing the formation of toxic Aβ aggregates, such as oligomers and fibrils. By inhibiting Aβ aggregation, it may help mitigate the neurotoxicity associated with Alzheimer's disease.

It's important to note that while Ala(N_3)-KLVFF-NH_2 and related peptides show promise as potential inhibitors of Aβ aggregation, their development and application are still in the experimental stage. Further research and preclinical studies are needed to evaluate their efficacy, safety, and potential as therapeutic agents for Alzheimer's disease.

1.9 POM-peptide hybrids

Polyoxometalate (POM)–peptide hybrids have been categorized based on the connection between the POM and the peptide, specifically, whether the linkage is ionic (Class I) or covalent (Class II), as illustrated in Figure 20. Both of these synthetic strategies offer opportunities to create synergistic materials that amalgamate and enhance the properties of their individual constituents. Class I hybrids, involving ionic connections, present a straightforward yet versatile approach to crafting materials using relatively uncomplicated and readily available POM and peptide building blocks. In designing these hybrids, critical considerations encompass the dimensions and geometry of the components, along with their stoichiometry. Conversely, the covalent organo-functionalization approach employed in the fabrication of Class II hybrids affords greater precision in tailoring the physicochemical attributes of the resulting materials. This approach enables the precise development of functional molecules.

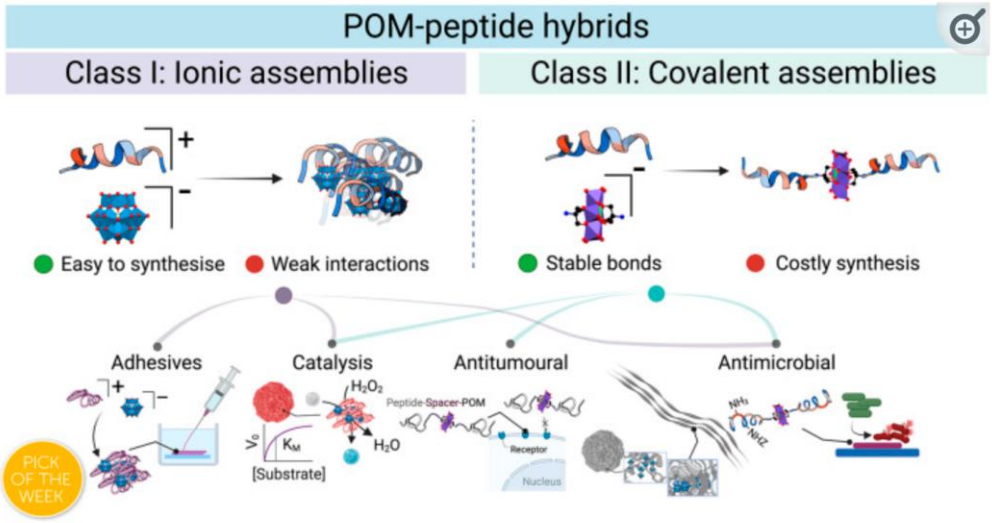

Figure 20. Formation of POM–peptide hybrids via ionic interaction (left) and covalent binding (right), which has various applications, including adhesives, catalysts, antitumor, antimicrobe.[67]

The proliferation of publications on POM–peptide hybrids in recent years underscores the steady expansion of this subfield within POM-hybrid research. For instance, peptides create confined environments conducive to catalysis; therefore, the incorporation and encapsulation of POMs within these environments enhance their catalytic properties. Additionally, both POMs and peptides possess antimicrobial characteristics, prompting investigations into the combination of these materials to yield high-performance antimicrobials. POM hybrids hold significance across various applications, including their utility as catalysts, adhesives, bioactive materials, and more.[67]

Additionally, POM-peptide assemblies offer a synergy of advantages from both peptides and POMs, encompassing superior biocompatibility and optical properties compared to POMs, as well as heightened water solubility and ease of detection relative to peptides. In the context of actively targeting drug delivery to tumor cells, our previous investigations involved functionalizing the Mn-Anderson POM with DB.[68] However, these studies revealed no substantial differences in cytotoxicity between the POM on its own and the POM-peptide hybrid. This outcome is likely attributable to the excessively close proximity between the peptide and the negatively charged POM, leading to structural phenomena such as foldings (as illustrated in Figure 21). These foldings, in turn, prompt the self-assembly of spherical vesicles, impeding the targeting potential.[69]

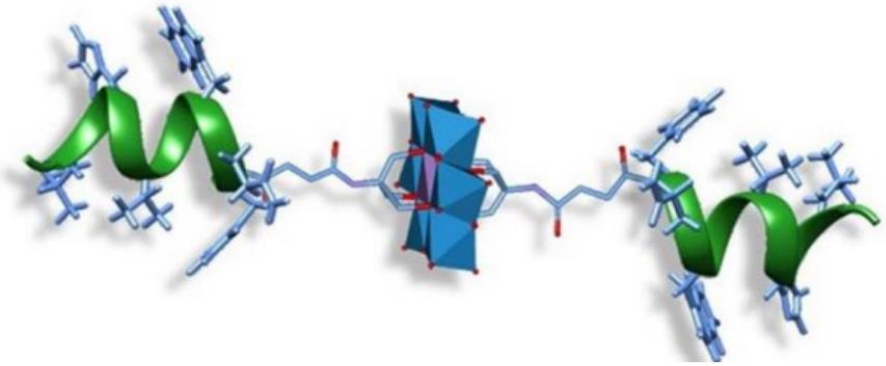

Figure 21. Proposed structure of the Mn-Anderson POM-(Demobensin-1)2 [68]

To address this challenge, a lengthy spacer, comprising two distinct units, was subsequently introduced (as shown in Figure 22) between the POM and the peptide.[69] The first unit adopts a PEG-like trioxatridecan-succinamic acid (Ttds) structure, while the second unit consists of a pentapeptide composed of four glutamic acid residues and one β-Alanine (EEEE-βA). Consequently, this innovative hybrid exhibits a moderate alteration in secondary structure, reduces the folding of chains onto the POM, thereby enhancing the accessibility of the receptor-binding region. Importantly, it no longer exhibits a propensity to self-assemble into spherical vesicles but instead forms a fibrous, pliable material. Ultimately, this modification led to an enhancement in cytotoxicity towards cancer cells compared to the original POM precursor.

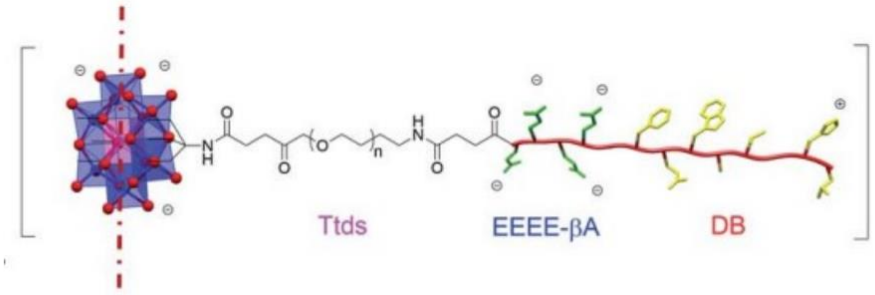

Figure 22. Structure of the Mn-Anderson POM-(DB)2 with spacer. [69]

2.0 Thesis Concept:

The objective of this thesis revolves around two main directions. The first one involves the development of novel POM-peptide hybrids capable of selectively targeting tumor cells by binding to integrins or the GPRP receptor. The initial investigation was aimed to determine if using the EEEE-βA spacer, Ttds spacer, or the Ttds-EEEE-βA spacer is sufficient to prevent Mn Anderson-Evans POM-peptide (DB) interactions, which were shown to hinder peptide's ability to interact with its receptor. Additionally, the impact of covalently binding the cyclic peptide c(RGDfK) to molybdate was explored to assess if the POM affected its ability to target integrin receptors.

The reactivity of vanadate hybrids was also thoroughly investigated to identify potential similarities or differences compared to the Mn-Anderson molybdates. The selection of these clusters among various POMs was based on the double negative charge of the anionic core, which differs from the triple negative charge of molybdates. This choice aimed to minimize the cluster's influence on the peptide structure, thus avoiding undesired interactions even without the presence of spacers.

The second direction focuses on the creation of POM-peptide hybrids with the potential to target Aβ and inhibit its fibrillation process, thus mitigating the progression of Alzheimer's Disease (AD). The peptide Ala(N_3)-KLVFF-NH_2 was successfully designed and synthesized to target Aβ, with the aim of inhibiting its fibrillation and increase penetration ability by conjugating it to Mn Anderson-Evans molybdate, to potentially mitigate the development of Alzheimer's Disease (AD).

Reference:

1. Pope, M. T.; Jeannin, Y.; Fournier, M., *Heteropoly and isopoly oxometalates*. Springer: 1983; Vol. 8.

2. Long, D. L.; Burkholder, E.; Cronin, L., Polyoxometalate clusters, nanostructures and materials: From self assembly to designer materials and devices. *Chemical Society Reviews* **2007,** *36* (1), 105-121.

3. Wilson, E. F. Synthesis, structure and mechanism of polyoxometalate self-assembly: Towards designed nanoscale architectures. University of Glasgow, 2009.

4. Hasenknopf, B., Polyoxometalates: Introduction to a class of inorganic compounds and their biomedical applications. *Frontiers in Bioscience-Landmark* **2005,** *10*, 275-287.

5. Rakovský, E., *Isopolyoxometalate Functionalisation Facilitated by Transition Metal Complexes*. 2015.

6. Hagrman, D.; Haushalter, R. C.; Zubieta, J., Three-dimensional organic/inorganic hybrid materials constructed from one-dimensional copper diamine coordination polymers linked by bridging oxoanion tetrahedra:[Cu (dpe)(MoO4)] and [Cu (dpe)(SO4)(H2O)](dpe= 1, 2-trans-(4-pyridyl) ethene). *Chemistry of materials* **1998,** *10* (1), 361-365.

7. Proust, A.; Thouvenot, R.; Chaussade, M.; Robert, F.; Gouzerh, P., Phenylimido derivatives of [Mo6O19] 2−: syntheses, X-ray structures, vibrational, electrochemical, 95Mo and 14N NMR studies. *Inorganica chimica acta* **1994,** *224* (1-2), 81-95.

8. Xu, L.; Lu, M.; Xu, B.; Wei, Y.; Peng, Z.; Powell, D. R., Towards Main-Chain-Polyoxometalate-Containing Hybrid Polymers: A Highly Efficient Approach to Bifunctionalized Organoimido Derivatives of Hexamolybdates. *Angewandte Chemie* **2002,** *114* (21), 4303-4306.

9. Damian, H. A. Polyoxometalates and peptides: hybridisation and disulfide detection. University of Nottingham, 2022.

10. Nakamura, S.; Ozeki, T., Hydrogen-bonded aggregates of protonated decavanadate anions in their tetraalkylammonium salts. *Journal of the Chemical Society, Dalton Transactions* **2001,** (4),

472-480.

11. Paulat-Böschen, I., X-Ray crystallographic determination of the structure of the isopolyanion [Mo 36 O 112 (H 2 O) 16] 8–in the compound K 8 [Mo 36 O 112 (H 2 O) 16]· 36H 2 O. *Journal of the Chemical Society, Chemical Communications* **1979,** (17), 780-782.

12. Neumann, R.; Levin, M., Aerobic oxidative dehydrogenations catalyzed by the mixed-addenda heteropolyanion PV2Mo10O405-: a kinetic and mechanistic study. *Journal of the American Chemical Society* **1992,** *114* (18), 7278-7286.

13. Blazevic, A.; Rompel, A., The Anderson–Evans polyoxometalate: From inorganic building blocks via hybrid organic–inorganic structures to tomorrows "Bio-POM". *Coordination chemistry reviews* **2016,** *307*, 42-64.

14. Maestre, J. M.; Lopez, X.; Bo, C.; Poblet, J.-M.; Casan-Pastor, N., Electronic and magnetic properties of α-keggin anions: A DFT Study of [XM12O40] n-,(M= W, Mo; X= AlIII, SiIV, PV, FeIII, CoII, CoIII) and [SiM11VO40] m-(M= Mo and W). *Journal of the American Chemical Society* **2001,** *123* (16), 3749-3758.

15. Lahnsteiner, M.; Kastner, A.; Mayr, J.; Roller, A.; Keppler, B. K.; Kowol, C. R., Improving the stability of maleimide–thiol conjugation for drug targeting. *Chemistry–A European Journal* **2020,** *26* (68), 15867-15870.

16. Fan, L.; Wang, E.; Li, Y.; An, H.; Xiao, D.; Wang, X., Wells–Dawson anion, a useful building block to construct one-dimensional chain as a chelate ligand coordinating with transition metal cations. *Journal of Molecular Structure* **2007,** *841* (1-3), 28-33.

17. Dablemont, C.; Hamaker, C. G.; Thouvenot, R.; Sojka, Z.; Che, M.; Maatta, E. A.; Proust, A., Functionalization of Heteropolyanions—Osmium and Rhenium Nitrido Derivatives of Keggin-and Dawson-Type Polyoxotungstates: Synthesis, Characterization and Multinuclear (183W, 15N) NMR, EPR, IR, and UV/Vis Fingerprints. *Chemistry–A European Journal* **2006,** *12* (36), 9150-9160.

18. Kibler, A. J.; Newton, G. N., Tuning the electronic structure of organic–inorganic hybrid polyoxometalates: The crucial role of the covalent linkage. *Polyhedron* **2018,** *154*, 1-20.

19. Anyushin, A. V.; Kondinski, A.; Parac-Vogt, T. N., Hybrid polyoxometalates as post-functionalization platforms: from fundamentals to emerging applications. *Chemical Society Reviews*

2020, *49* (2), 382-432.

20. Cherevan, A. S.; Nandan, S. P.; Roger, I.; Liu, R.; Streb, C.; Eder, D., Polyoxometalates on functional substrates: concepts, synergies, and future perspectives. *Advanced Science* **2020,** *7* (8), 1903511.

21. Arefian, M.; Mirzaei, M.; Eshtiagh-Hosseini, H.; Frontera, A., A survey of the different roles of polyoxometalates in their interaction with amino acids, peptides and proteins. *Dalton Transactions* **2017,** *46* (21), 6812-6829.

22. Wang, X.; Wei, S.; Zhao, C.; Li, X.; Jin, J.; Shi, X.; Su, Z.; Li, J.; Wang, J., Promising application of polyoxometalates in the treatment of cancer, infectious diseases and Alzheimer's disease. *JBIC Journal of Biological Inorganic Chemistry* **2022,** *27* (4-5), 405-419.

23. Galani, A.; Tsitsias, V.; Stellas, D.; Psycharis, V.; Raptopoulou, C. P.; Karaliota, A., Two novel compounds of vanadium and molybdenum with carnitine exhibiting potential pharmacological use. *Journal of Inorganic Biochemistry* **2015,** *142*, 109-117.

24. Fraqueza, G.; Fuentes, J.; Krivosudský, L.; Dutta, S.; Mal, S. S.; Roller, A.; Giester, G.; Rompel, A.; Aureliano, M., Inhibition of Na+/K+-and Ca2+-ATPase activities by phosphotetradecavanadate. *Journal of Inorganic Biochemistry* **2019,** *197*, 110700.

25. Gao, N.; Sun, H.; Dong, K.; Ren, J.; Duan, T.; Xu, C.; Qu, X., Transition-metal-substituted polyoxometalate derivatives as functional anti-amyloid agents for Alzheimer's disease. *Nat Commun* **2014,** *5*, 3422.

26. Kareva, I., *Understanding Cancer from a Systems Biology Point of View: From Observation to Theory and Back*. Academic Press: 2018.

27. Lee, Y. T.; Tan, Y. J.; Oon, C. E., Molecular targeted therapy: Treating cancer with specificity. *European journal of pharmacology* **2018,** *834*, 188-196.

28. Torchilin, V. P., Passive and active drug targeting: drug delivery to tumors as an example. *Drug delivery* **2010**, 3-53.

29. Schwartz, R. S., Paul Ehrlich's magic bullets. *New England Journal of Medicine* **2004,** *350* (11), 1079-1080.

30. Svenson, S.; Prud'homme, R. K., *Multifunctional nanoparticles for drug delivery applications:*

imaging, targeting, and delivery. Springer Science & Business Media: 2012.

31. Srinivasarao, M.; Low, P. S., Ligand-targeted drug delivery. *Chemical reviews* **2017,** *117* (19), 12133-12164.

32. Cerwenka, A.; Lanier, L. L., Ligands for natural killer cell receptors: redundancy or specificity. *Immunological reviews* **2001,** *181* (1), 158-169.

33. Wu, C.-H.; Liu, I. J.; Lu, R.-M.; Wu, H.-C., Advancement and applications of peptide phage display technology in biomedical science. *Journal of Biomedical Science* **2016,** *23* (1), 8.

34. Saw, P. E.; Song, E.-W., Phage display screening of therapeutic peptide for cancer targeting and therapy. *Protein & cell* **2019,** *10* (11), 787-807.

35. Cooper, B. M.; Iegre, J.; O'Donovan, D. H.; Halvarsson, M. Ö.; Spring, D. R., Peptides as a platform for targeted therapeutics for cancer: Peptide–drug conjugates (PDCs). *Chemical society reviews* **2021,** *50* (3), 1480-1494.

36. Vrettos, E. I.; Mező, G.; Tzakos, A. G., On the design principles of peptide–drug conjugates for targeted drug delivery to the malignant tumor site. *Beilstein journal of organic chemistry* **2018,** *14* (1), 930-954.

37. Fu, C.; Yu, L.; Miao, Y.; Liu, X.; Yu, Z.; Wei, M., Peptide–drug conjugates (PDCs): a novel trend of research and development on targeted therapy, hype or hope? *Acta Pharmaceutica Sinica B* **2023,** *13* (2), 498-516.

38. Poreba, M., Protease-activated prodrugs: strategies, challenges, and future directions. *The FEBS Journal* **2020,** *287* (10), 1936-1969.

39. Vadevoo, S. M. P.; Gurung, S.; Lee, H.-S.; Gunassekaran, G. R.; Lee, S.-M.; Yoon, J.-W.; Lee, Y.-K.; Lee, B., Peptides as multifunctional players in cancer therapy. *Experimental & Molecular Medicine* **2023**, 1-11.

40. Rigby, M.; Bennett, G.; Chen, L.; Mudd, G. E.; Harrison, H.; Beswick, P. J.; Van Rietschoten, K.; Watcham, S. M.; Scott, H. S.; Brown, A. N., BT8009; A Nectin-4 Targeting Bicycle Toxin Conjugate for Treatment of Solid Tumors. *Molecular Cancer Therapeutics* **2022,** *21* (12), 1747-1756.

41. Hruby, V. J., Designing peptide receptor agonists and antagonists. *Nature reviews Drug discovery* **2002,** *1* (11), 847-858.

42. Anastasi, A.; Erspamer, V.; Bucci, M., Isolation and structure of bombesin and alytesin, two analogous active peptides from the skin of the European amphibians Bombina and Alytes. *Experientia* **1971,** *27* (2), 166-167.

43. Reubi, J. C., Peptide receptors as molecular targets for cancer diagnosis and therapy. *Endocrine reviews* **2003,** *24* (4), 389-427.

44. Jensen, R.; Battey, J.; Spindel, E.; Benya, R., International Union of Pharmacology. LXVIII. Mammalian bombesin receptors: nomenclature, distribution, pharmacology, signaling, and functions in normal and disease states. *Pharmacological reviews* **2008,** *60* (1), 1-42.

45. Okarvi, S.; Al-Jammaz, I., Synthesis, radiolabelling and biological characteristics of a bombesin peptide analog as a tumor imaging agent. *Anticancer research* **2003,** *23* (3), 2745-2750.

46. Zhang, Y.; Holland, E.; Dinh, A.; Au, D.; Sun, L., Bombesin-drug conjugates in targeted therapy for small cell lung cancer. *American Journal of Cancer Research* **2022,** *12* (3), 927.

47. Eble, J. A.; Haier, J., Integrins in cancer treatment. *Current cancer drug targets* **2006,** *6* (2), 89-105.

48. Danhier, F.; Le Breton, A.; Préat, V. r., RGD-based strategies to target alpha (v) beta (3) integrin in cancer therapy and diagnosis. *Molecular pharmaceutics* **2012,** *9* (11), 2961-2973.

49. Sani, S.; Messe, M.; Fuchs, Q.; Pierrevelcin, M.; Laquerriere, P.; Entz-Werle, N.; Reita, D.; Etienne-Selloum, N.; Bruban, V.; Choulier, L., Biological relevance of RGD-integrin subtype-specific ligands in cancer. *ChemBioChem* **2021,** *22* (7), 1151-1160.

50. Fu, S.; Xu, X.; Ma, Y.; Zhang, S.; Zhang, S., RGD peptide-based non-viral gene delivery vectors targeting integrin αvβ3 for cancer therapy. *Journal of drug targeting* **2019,** *27* (1), 1-11.

51. Selkoe, D. J.; Schenk, D., Alzheimer's disease: molecular understanding predicts amyloid-based therapeutics. *Annual review of pharmacology and toxicology* **2003,** *43* (1), 545-584.

52. Hippius, H.; Neundörfer, G., The discovery of Alzheimer's disease. *Dialogues in clinical neuroscience* **2022**.

53. Crowther, R.; Goedert, M., Abnormal tau-containing filaments in neurodegenerative diseases. *Journal of structural biology* **2000,** *130* (2-3), 271-279.

54. Armstrong, R. A., Alzheimer's disease and the eye. *Journal of Optometry* **2009,** *2* (3), 103-111.

55. Chow, V. W.; Mattson, M. P.; Wong, P. C.; Gleichmann, M., An overview of APP processing enzymes and products. *Neuromolecular medicine* **2010,** *12*, 1-12.

56. Zhang, Y.-w.; Thompson, R.; Zhang, H.; Xu, H., APP processing in Alzheimer's disease. *Molecular brain* **2011,** *4*, 1-13.

57. Lott, I. T.; Head, E., Dementia in Down syndrome: unique insights for Alzheimer disease research. *Nature Reviews Neurology* **2019,** *15* (3), 135-147.

58. Xi, Y.; Chen, Y.; Jin, Y.; Han, G.; Song, M.; Song, T.; Shi, Y.; Tao, L.; Huang, Z.; Zhou, J., Versatile nanomaterials for Alzheimer's disease: Pathogenesis inspired disease-modifying therapy. *Journal of Controlled Release* **2022,** *345*, 38-61.

59. Long, J. M.; Holtzman, D. M., Alzheimer disease: an update on pathobiology and treatment strategies. *Cell* **2019,** *179* (2), 312-339.

60. Kamenetz, F.; Tomita, T.; Hsieh, H.; Seabrook, G.; Borchelt, D.; Iwatsubo, T.; Sisodia, S.; Malinow, R., APP processing and synaptic function. *Neuron* **2003,** *37* (6), 925-937.

61. Reiss, A. B.; Arain, H. A.; Stecker, M. M.; Siegart, N. M.; Kasselman, L. J., Amyloid toxicity in Alzheimer's disease. *Reviews in the Neurosciences* **2018,** *29* (6), 613-627.

62. Furtado, D.; Björnmalm, M.; Ayton, S.; Bush, A. I.; Kempe, K.; Caruso, F., Overcoming the blood–brain barrier: the role of nanomaterials in treating neurological diseases. *Advanced materials* **2018,** *30* (46), 1801362.

63. Tjernberg, L. O.; Näslund, J.; Lindqvist, F.; Johansson, J.; Karlström, A. R.; Thyberg, J.; Terenius, L.; Nordstedt, C., Arrest of-Amyloid Fibril Formation by a Pentapeptide Ligand (∗). *Journal of Biological Chemistry* **1996,** *271* (15), 8545-8548.

64. Pallitto, M. M.; Ghanta, J.; Heinzelman, P.; Kiessling, L. L.; Murphy, R. M., Recognition sequence design for peptidyl modulators of β-amyloid aggregation and toxicity. *Biochemistry* **1999,** *38* (12), 3570-3578.

65. Lührs, T.; Ritter, C.; Adrian, M.; Riek-Loher, D.; Bohrmann, B.; Döbeli, H.; Schubert, D.; Riek, R., 3D structure of Alzheimer's amyloid-β (1–42) fibrils. *Proceedings of the National Academy of Sciences* **2005,** *102* (48), 17342-17347.

66. Soria-Carrera, H.; Atrián-Blasco, E.; Martín-Rapún, R.; Mitchell, S. G., Polyoxometalate–

peptide hybrid materials: from structure–property relationships to applications. *Chemical science* **2023,** *14* (1), 10-28.

67. Ventura, D.; Calderan, A.; Honisch, C.; Krol, S.; Serrati, S.; Bonchio, M.; Carraro, M.; Ruzza, P., Synthesis and biological activity of an Anderson polyoxometalate bis-functionalized with a Bombesin-analog peptide. *Peptide Science* **2018,** *110* (5).

68. Tagliavini, V.; Honisch, C.; Serratì, S.; Azzariti, A.; Bonchio, M.; Ruzza, P.; Carraro, M., Enhancing the biological activity of polyoxometalate–peptide nano-fibrils by spacer design. *RSC advances* **2021,** *11* (9), 4952-4957.

Chapter 2: Structural study of POM-bombesin conjugates

Polyoxometalates (POMs), are a class of polynuclear oxo-bridged transition metal complexes and have many applications in multidisciplinary fields, including biomedicine. Indeed, they display antitumor, antiviral and antibacterial activity.[13] Their main advantage is that shape, acidity, surface charge distribution and redox potentials can be easily tuned to optimize the interaction with biological targets as macromolecules (peptides, proteins and enzymes leading to their misfolding or inhibition) or to affect cellular redox process. Despite the negative charge, POMs were proven to cross cell membranes.

Polyoxometalates (POMs) possess biological activity but suffer from limited selectivity. To enhance the selectivity of POMs, targeting molecules and peptides have been conjugated to them.[13, 18] However, the strong interactions between the POM and peptide can induce the peptide's folding and restrict its biological efficacy. To address this challenge, POMs were modified with a bombesin analog peptide and optimized by incorporating a specially designed hydrophilic and anionic spacer between the two components. This modification facilitated improved accessibility of the targeting sequence, resulting in an improved ability to recognize cancer cells. This strategy is thus promising, but the activity is still too low for practical applications and needs further engineering of the POM bio-conjugate.

Mn-Anderson Evans polyoxomolybdates (A)

Polyoxomolybdates (MnPOMs) -peptide (Bombesin) conjugation with spacer design

The Anderson-Evans polyoxometalates (MnPOMs) with general formula $[XM_6O_{24}]^{n-}$ (n=2-8) are constituted by six edge-sharing octahedra, MO_6 (M = W or Mo), surrounding a central edge-sharing XO_6 octahedron containing the heteroatom (X = Mn, Cr, I, etc). The Mn-centered polyoxomolybdate

(MnPOM) functionalized with tris(hydroxymethyl) aminomethane (TRIS), $[(C_4H_9)_4N]_3[MnMo_6O_{18}\{(OCH_2)_3CNH_2\}]$ and its derivatives have a proven cytotoxic effect on cancer cells. The functionalization of such POMs by peptides and biomolecules can be promising to increase bioactivity and impart recognition capability towards specific substructure of the target systems.

Bombesin-1 (DB) displays a high affinity to gastrin-releasing peptide receptors (GRPr), which are highly overexpressed in various types of cancers, including breast cancer, prostate cancer, and gastrointestinal stromal tumors to benefit for the proliferation and growth of these malignancies. Blocking these pathways indirectly could inhibit the recruitment toward GRPr, not only hampering the growth of tumor but also decreasing the adverse reaction.[46]

In this section, the peptides Demobesin-1, having distinct spacers (EEEEβAlaDB and Ttds-DB), are individually linked with POM to investigate whether the peptide's structure is inherent and undergoes unfolding upon spatial alteration. the preparation of the hybrid POMs has been performed by following our group published procedures, involving the synthesis of the Anderson-Evans POM-TRIS, followed by the condensation of amino groups with spacers containing carboxylic groups. The last ones are then activated by insertion of N-hydroxy succinimide (NHS) before the last conjugation step with a peptide (as shown in Figure 2.1.). In the next paragraph, the synthetic steps leading to the NHS-activated POM will be described.

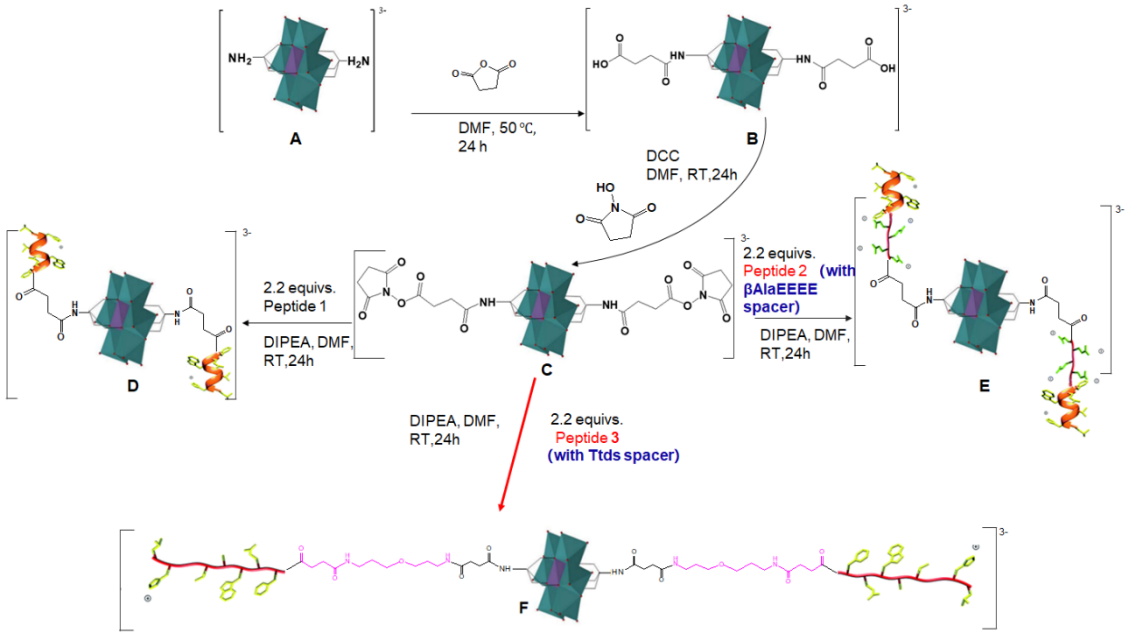

Figure 2.1. The scheme of the synthesis of POM-hybrids.

Mn-Anderson TRIS: $[(C_4H_9)_4N]_3[MnMo_6O_{18}((OCH_2)_3CNH_2)_2]$

This starting POM is prepared in two steps: the first one involves the condensation of molybdate anions in acidic conditions, to give a polyoxomolybdate, as tetrabutylammonium (TBA) salt, with formula $[(C_4H_9)_4N]_4[Mo_8O_{26}]$. To this aim, sodium molybdate dihydrate ($Na_2MoO_4{\cdot}2H_2O$, 0.0209 mol) is dissolved in milliQ water and acidified with HCl, then a tetrabutylammonium bromide, $(C_4H_9)_4NBr$, (0.010 mol) solution was added to obtain a white solid (Yield: 6.43 g, 14%).

In the second step, the inorganic isopolyanion is converted to the hybrid Anderson-Evans structure by mixing, at 80 °C for 24h, $[(C_4H_9)_4N]_4[Mo_8O_{26}]$ (1.4 mmol), Mn $(CH_3COO)_3{\cdot}2H_2O$ (2.0 mmol) and $(HOCH_2)_3CNH_2$ (5.0 mmol) in acetonitrile. After removal of insoluble by-products, orange crystals can be obtained (yield 53.6%). The identity of the product has been confirmed by FT-IR, ^{1}H-NMR and ESI-MS (Figure 2.2.). FT-IR (KBr) allows to confirm the expected pattern of signals due to the Mo-O vibrations, in the range 600-1200 cm^{-1} and to C-H bands, 2800-3000 cm^{-1}. By ^{1}H-NMR (300 MHz, CD_3CN) it is possible to recognize the TBA signals 0.95 (t, 36 H, CH_3), 1.34 (m, 24 H, CH_2), 1.58 (m, 24 H, CH_2), 3.17 (m, 24 H, CH_2), together with a broad peak for the amino group. The signal

of the CH_2 groups can be found at around 65 ppm (not shown), as a result of the deshielding by the paramagnetic POM, in agreement with literature data. ESI-MS (-) (CH3CN) shows the presence of mono-charged species, with one or two TBA cations 1398.5 $[M-2TBA+H]^-$, 1155.2 $[M-3TBA+2H]^-$.

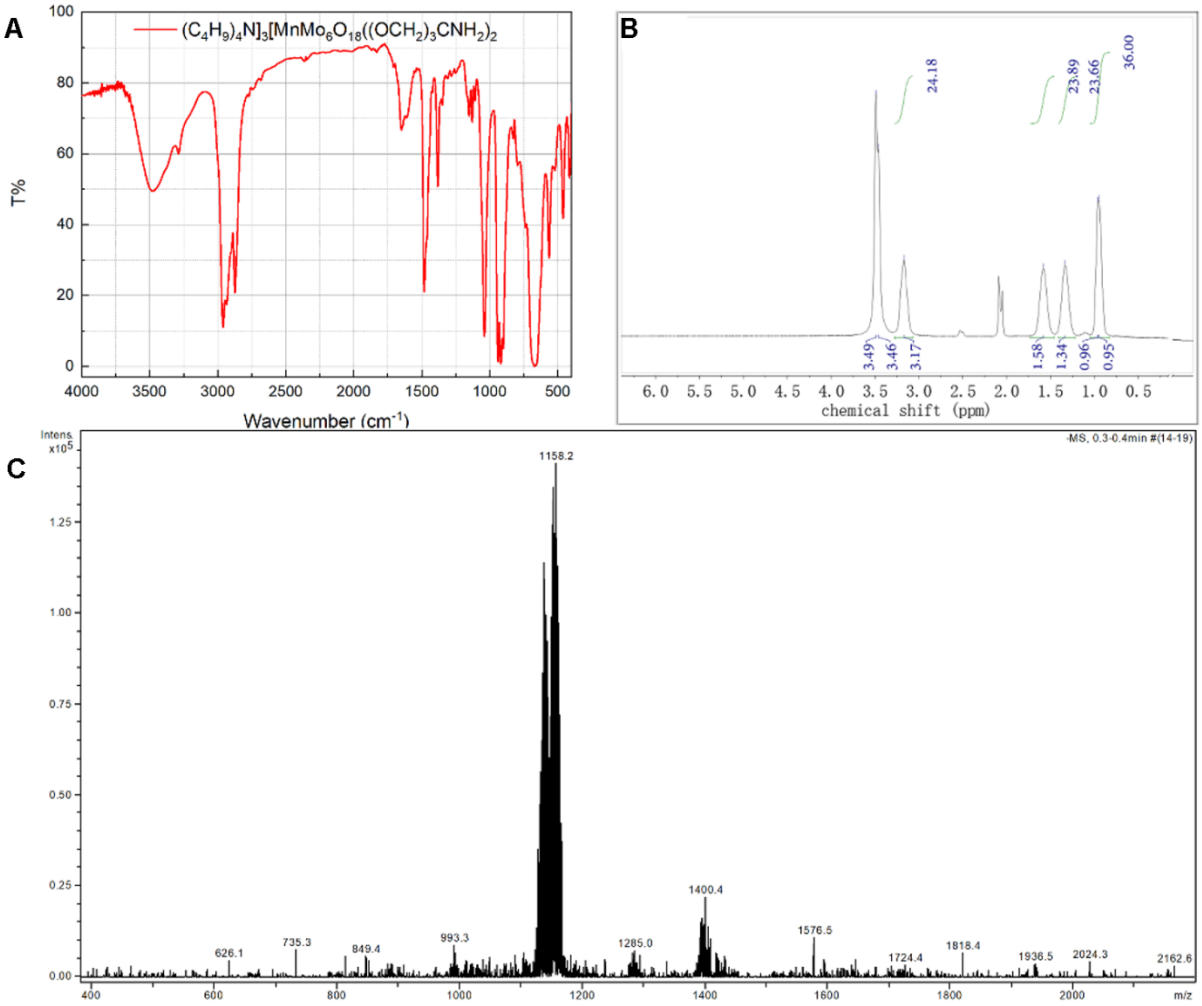

Figure 2.2. The characterization of Mn-Anderson-Evans POM-TRIS. A) FT IR (KBr), ^{1}H-NMR (300 MHz, CD_3CN) C) ESI-MS (-) (CH_3CN).

Mn-Anderson Evans POM-succinate

The previously obtained $[(C_4H_9)_4N]_3[MnMo_6O_{18}((OCH_2)_3CNH_2)_2]$ (Compound 1) (0.142 mmol) is reacted with succinic anhydride (2.875 mmol), in DMF at 50ºC for 24 h. Orange crystals of $[(C_4H_9)_4N]_3[MnMo_6O_{18}\{(OCH_2)_3CNHCO(CH_2)_2COOH\}_2]$ were finally collected (yield: 64.2%).

FT-IR allows to observe the appearance of the signal belonging to carboxylic groups at 1750-1670 cm^{-1}. ^{1}H NMR (200 MHz, d6-DMSO), shows additional signals at 2.36 and 2.72, due to two C*H*2 groups of the new spacer, together with the amide and carboxyl signals at 7.49 (s, N*H*, 2 H) and 10.04 (s, O*H*, 2 H). ESI-MS (-) (CH_3CN) shows the main signal at m/z = 1841.6, ascribed to $[M\text{-}TBA]^-$ (calculated 1839.8) together with other unidentified signals.

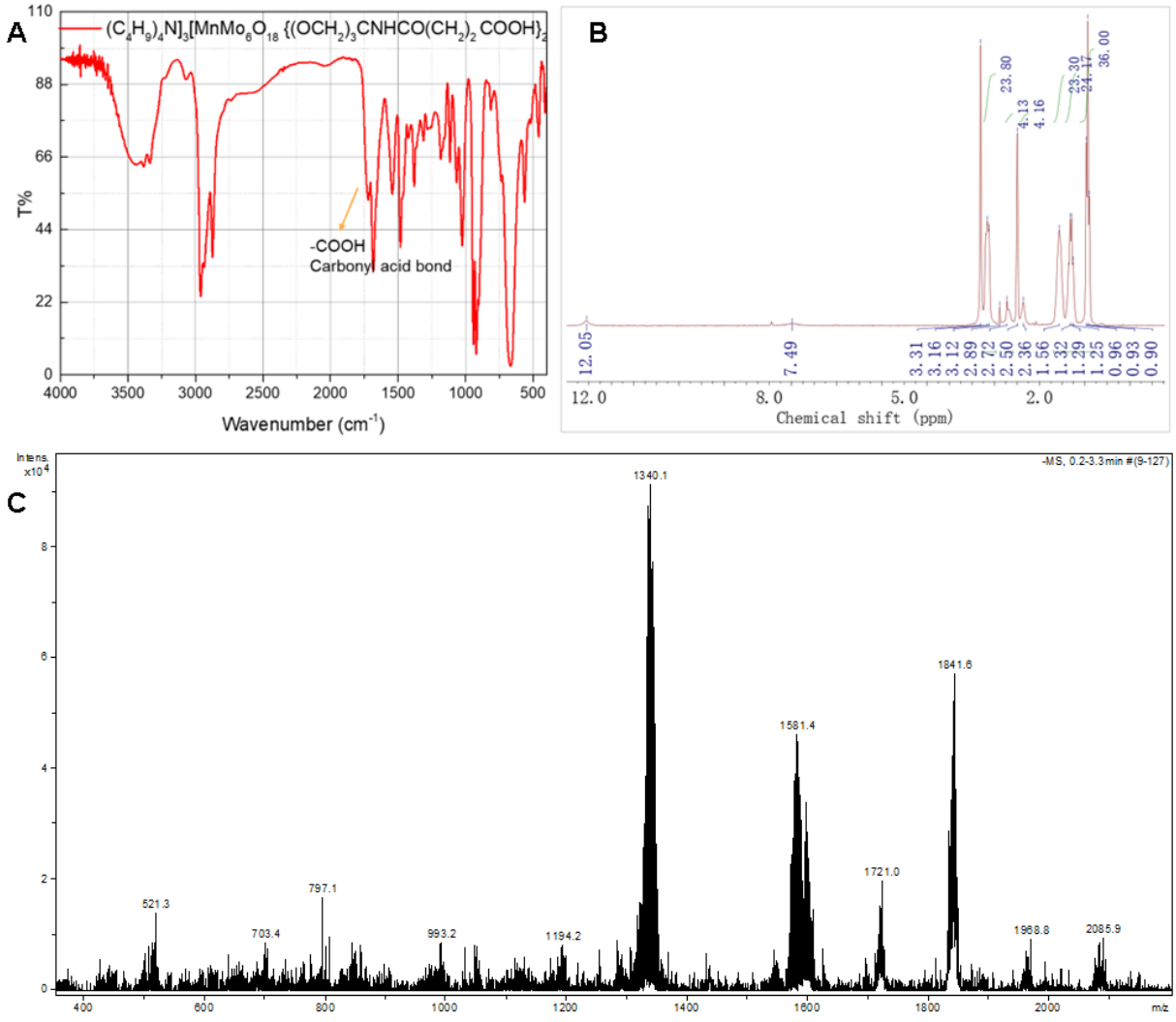

Figure 2.3. The characterization of Mn-Anderson Evans POM-succinate. A) FT IR (KBr), ^{1}H-NMR (200 MHz, d6-DMSO) C) ESI-MS (-) (CH_3CN).

Mn-Anderson-Evans POM-NHS

$[(C_4H_9)_4N]_3[MnMo_6O_{18}\{(OCH_2)_3CNHCO(CH_2)_2COOH\}_2]$ (Compound 2) (0.063 mmol) is then converted into a more active species containing the NHS group. To this aim, DCC (N, N'-dicyclohexylcarbodiimmide) (0.374 mmol) and NHS (N-Hydroxysuccinimide) (0.255 mmol) were dissolved in DMF and reacted with POM under stirring at room temperature for 24 h. After removal of by-products, orange solid crystals of $[(C_4H_9)_4N]_3[MnMo_6O_{18}\{(OCH_2)_3CNHCO(CH_2)_2CO(C_4H_4NO_3)\}_2]$ were collected. Yield: 71.1%. in this case (Figure 5), the FT-IR shows a different signal in the region 1750-1660, owing to the conversion of carboxylic group into the cyclic imide ester. ^{1}H NMR (300 MHz, CD_3CN) shows a strong signal ascribed to all CH_2 groups of the pendant (succinate and NHS) at 2.75 (m, 16 H). ESI-MS (-) (CH_3CN) shows signals of the monocharged species with variable content of TBA counter ions, at 2035.7 (m/z calc. for $[M\text{-}TBA]^-$=2034.7), 1793.4 (m/z calc. for $[M\text{-}2TBA+H]^-$=1793.6), 1552.2 (m/z calc. for $[M\text{-}3TBA+2H]^-$=1552.3).

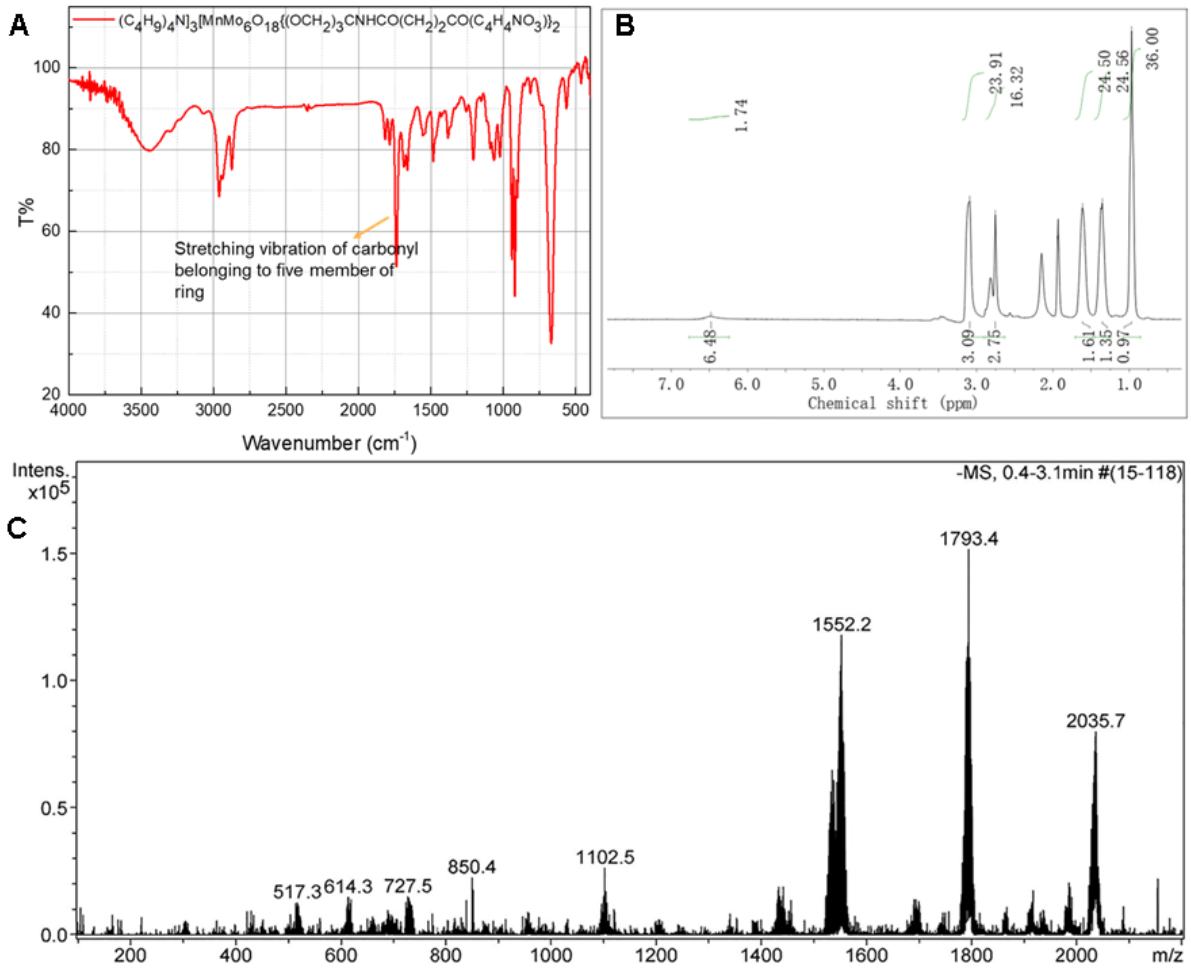

Figure 2.4. The characterization of Mn-Anderson NHS. A) FT IR (KBr), ^{1}H-NMR (300 MHz, CD3CN) C) ESI-MS (-) (CH_3CN).

Conjugation of Mn-Anderson-Evans POM-NHS

Before using a peptide, however, it was tested with a single amino acid. As displayed in the Figure 2.5, Phenylalanine was used to find optimal reaction condition. The reaction was thus performed successfully in DMF. In the Figure 2.5A, C-H stretching vibrations from the alkyl groups (CH_2 and CH_3) and aryl groups can be observed around 3000 cm^{-1}. At 1680 and 1620 cm^{-1}, C=C benzene ring stretching vibrations are also present. Other aryl C-H bending vibration absorptions occur at wavenumbers 770 to 690 cm^{-1}. ^{1}H-NMR (300 MHz, CD_3CN) spectroscopy (in Figure 2.5B) shows the signals of the amino acids at 3.65 (s, 6H, CH_3) 4.63 (m, 2H, CH), 6.84 (d,2H, NH) and the integral of the signals ascribed to CH benzene ring (7.29, m, 10 H)) is in agreement with the introduction of

two residues. In Figure 2.5C, ESI-MS (-) (CH_3CN) shows the expected signals at 1921.8 (m/z calc. for $[M\text{-}3TBA+2H]^-$=1921.42), 2161.9 (m/z calc. for $[M\text{-}2TBA+1]^-$=2163.66), and 1681.6 (m/z calc. for $[M\text{-}2TBA+1]^-$=1680.18).

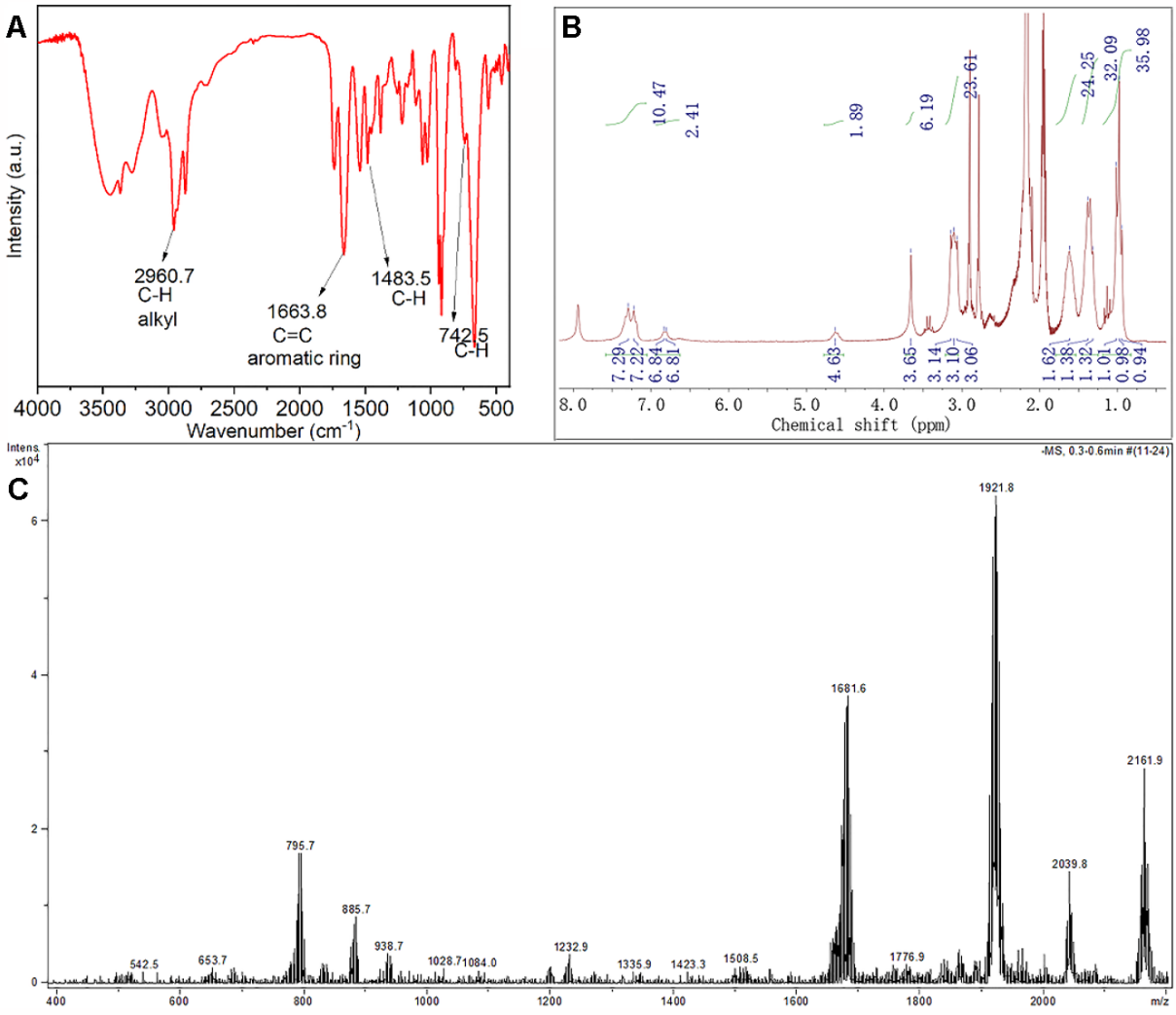

Figure 2.5. A) FT IR (KBr), ^{1}H-NMR (300 MHz, CD^3CN) C) ESI-MS (-) (CH_3CN).

The synthesis of Mn-Anderson-Evans POM-peptides

The method, same as with POM-Phenylalanine, was performed to synthesize POM-peptides. POM-NHS (1 equivs) has been dissolved in 0.8 mL of DMF in a vial. In order peptides (2.2 equivs) and DIPEA were added to the reaction mixture, and the orange solution was stirred for 24 hours at room temperature. The day after the vial was put under diethyl ether atmosphere to promote the crystallization. After a few hours, however, a greasy light orange product was recovered. This was

washed with approximately 1.5 mL of diethyl ether for three times and then dried under vacuum. FT-IR spectroscopy, NMR and ESI, CD, UV-vis were the first tools applied for determining the success in the synthesis of the POM hybrids.

As illustrated in Figure 2.6., the FT-IR (KBr) spectra of $MnMO_6$-NHS and $MnMO_6$-spacer(s)-peptide exhibit no structural alterations in the region characteristic of the polyoxometalate framework (between 1000 cm^{-1} and 500 cm^{-1}). A moderately intense band at 1534 cm^{-1} could be attributed to -N-H bending, and the signals associated with the C=O of the -NHS group (at 1783 and 1814 cm^{-1}) are absent, replaced by novel signals related to peptide bond stretching around 1640 cm^{-1}.

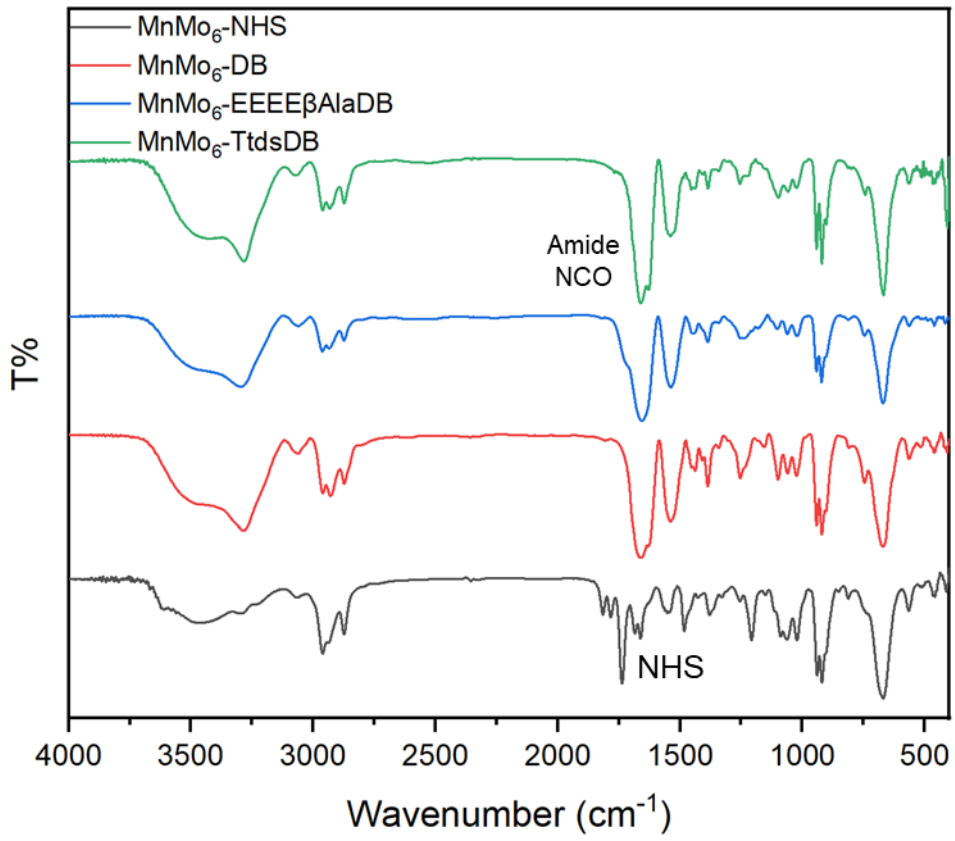

Figure 2.6. FT-IR spectrum of MnMO6-peptide.

Insightful details regarding the structure of the peptides bound to the POMs were acquired through the ROESY spectra. As depicted in Figure 2.7A, the molybdenum hybrid ($MnMo_6$-DB) displays coupling between Trp and Val (i, i+2), indicating the presence of a γ-turn. Additionally, Figure 2.7 B illustrates the CHα-NH crosspeak region of the ROESY spectrum for $MnMo_6$-EEEEβAla-DB in d6-

DMSO. The highlighted red circle signifies the connectivity between the His and Gln residues, implying the folding of peptide. Meantime, CHα-NH crosspeak region of the ROESY spectrum there isn't any coupling between two amino acids that are not adjacent to each other.

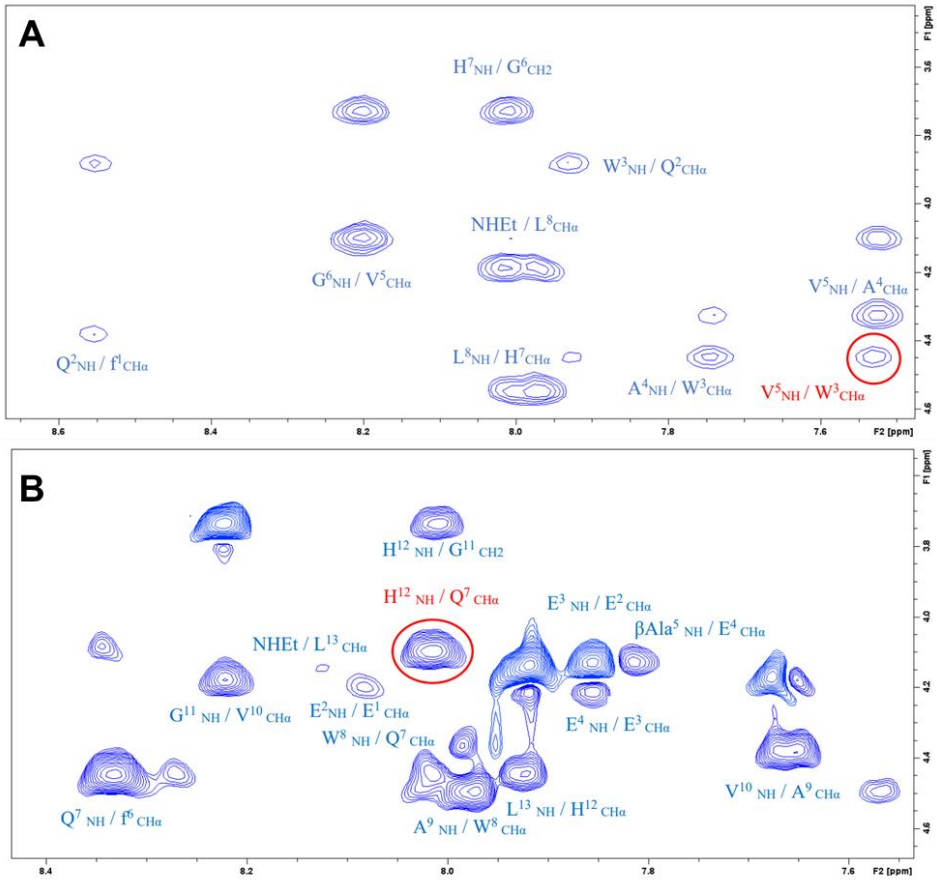

Figure 2.7. A) CHα-NH crosspeak region of ROESY for MnMo6-DB in d6-DMSO. B) CHα-NH crosspeak region of ROESY for MnMo6-EEEEβAlaDB in d6-DMSO. The red circle highlights the connectivity between His and Gln residues. The spectrum was acquired on a Bruker DMX-400 instrument operating at 399.92 MHz for 1H at 298 K. The red circle highlights the connectivity between Val and Trp residues.

To explore the influence of $MnMo_6$ and spacers on Demobensin-1 peptide, secondary chemical shift values were obtained by subtracting the CHα and NH resonance values of spacer-Demobensin-1 constructs (peptides 2 and 3) from those of Demobensin-1. In Figure 2.8A, following the addition of spacers to the peptide, NH resonance values in those residues exhibited slight upfield shifts, with the exception of the Gly residue in peptide 2. As depicted in Figure 2.8B, CHα resonance values in these residues also experienced slight upfield shifts, except for Phe. Furthermore, the presence of the spacer induced shifts towards lower frequencies in other resonances. This effect was most pronounced in the N-terminal region of the peptides, gradually diminishing towards the C-terminal region. When comparing peptide 2 and 3 to the parent peptide 1, it's evident that they display upfield shifts in NH and CHα resonances, suggesting that the negative spacer may indeed influence the peptide's conformation. Additionally, the shielding effect of the two spacers is quite similar.

To investigate the impact of the POM cluster on Demobensin-1 in POM-peptide hybrid constructs, secondary chemical shift values were determined by subtracting NH and CHα resonance values of POM-spacer-Demobensin-1 constructs from those of Demobensin-1-spacer. As illustrated in Figure 2.8C, it's evident that most residues shifted to lower frequencies. Notably, the minimum shift in Mo-hybrids was $MnMo_6$-Ttds-DB (with Ttds spacers). Furthermore, differences in the CHα chemical shift are depicted in Figure 2.8D. The CHα resonance in the D-Phe residue was shifted downfield in the presence of the POM. The paramagnetic polyoxygenic anions containing Mo, indeed, predominantly shielded most CHα resonances, causing them to undergo a downfield shift relative to the peptide. Upon comparing NH and CHα resonances, it became apparent that the POM-spacer in compound $MnMo_6$-Ttds-DB had a minimal impact on observed chemical shifts, suggesting that Ttds spacers added to the POM could reduce interactions between the POM and peptide.

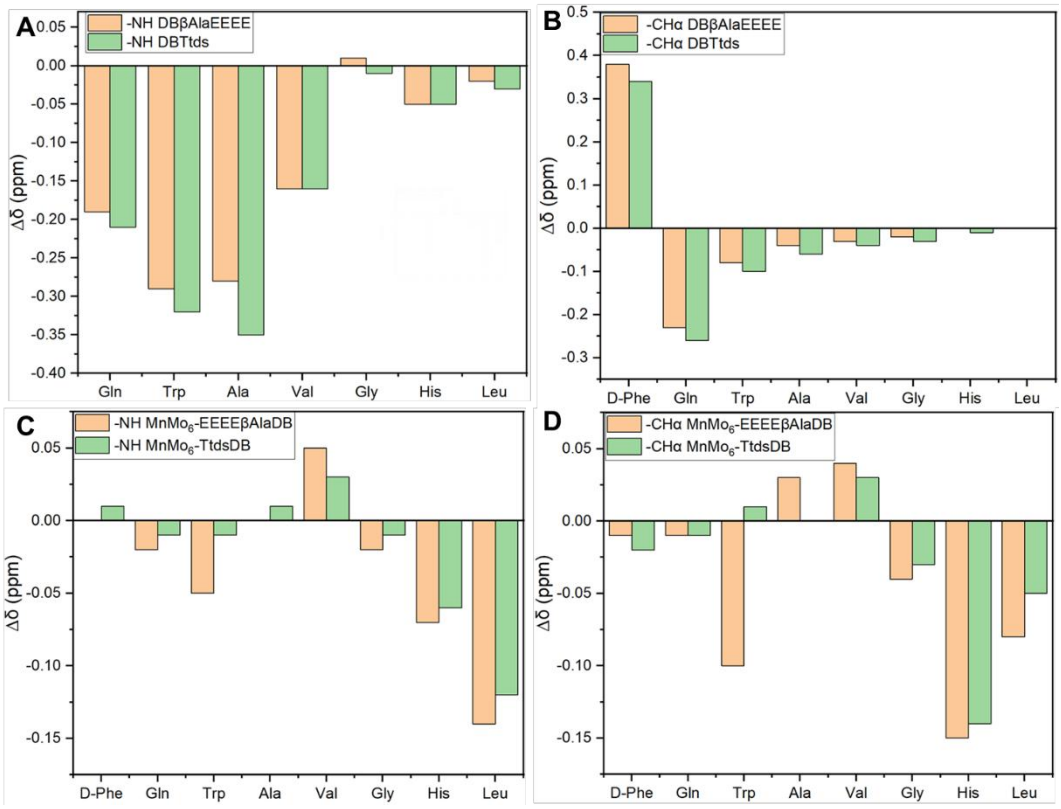

Figure 2.8. Influence of the POM-spacers on chemical shift of peptide. Δδ values were determined by subtracting the resonances of DB-spacer or POM spacer-DB hybrids from the resonances of DB/ DB-spacer constructs. A) and B) are the chemical shift of DB-spacers, C) and D) are the chemical shift of POM-spacers-DB.

The initial recording of Circular Dichroism spectra occurred at 185 nm, a region where characteristic signals associated with secondary structures in proteins are observed. These signals are intricately linked to the local environment, a consequence of chain folding.

Trifluoroethanol (TFE) to water ratios were systematically chosen as solvents to examine the developmental changes in secondary structure. TFE is frequently utilized as a co-solvent in such analyses due to its proficiency in structuring and solubilizing peptides and proteins. Moreover, TFE's minimal adsorption within the specified spectral range renders it a preferred option over many organic solvents, where the UV-vis cutoff impedes their suitability for Circular Dichroism (CD) measurements.

CD spectroscopy was employed to evaluate the secondary structure of peptides and their POM hybrids across a range of trifluoroethanol (TFE) concentrations, spanning from 10% to 100% (v/v), as depicted in Figure 2.9., the utilization of TFE, with displays a comparatively lower polarity, allows for an exploration of how a more hydrophobic environment, resembling a membrane milieu, could impact the peptide's conformation. This investigation offers valuable insights into the bioactive conformation when the peptide engages with a cell surface receptor. In an 80% TFE solution, the general CD shape remains relatively unchanged in the presence of the POM, but a substantial 80% increase, in intensity, with respect to CD of the peptide, is observed. Similarly, at a 10% TFE concentration, there is an increase in intensity, although not as pronounced as in the previous case.

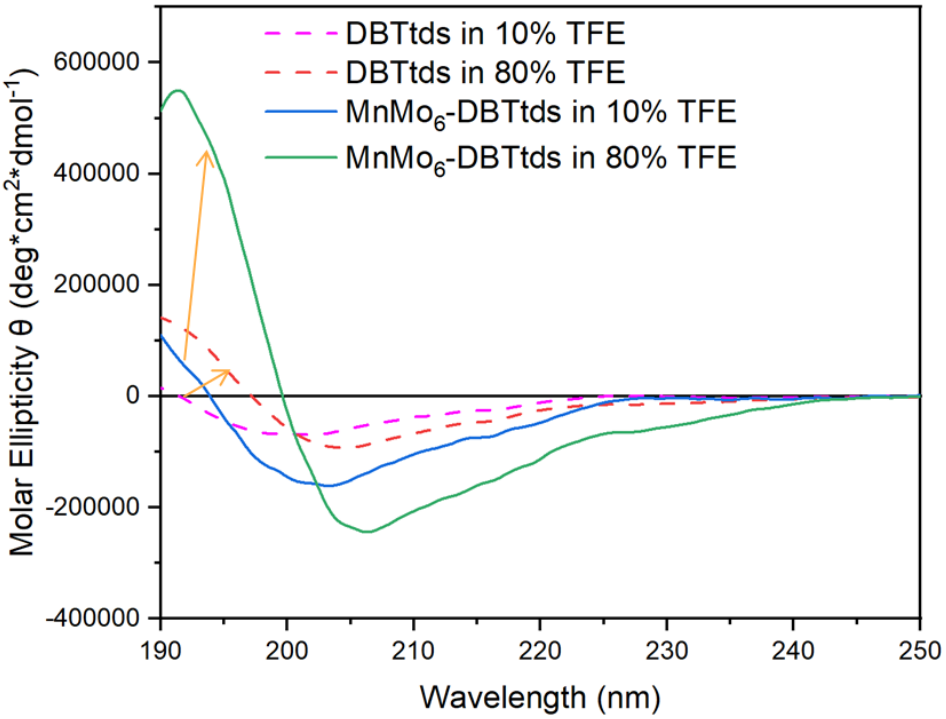

Figure 2.9. Far-UV CD spectra of DBTtds (12.5 μM, solid) and MnMO6-TtdsDB (12.5 μM, dot line) at different TFE : water percentage.

Conclusion:

Peptides Demobesin-1, each with distinct spacers (EEEEβAlaDB and Ttds-DB), were individually linked with the POM. The peptide's structure remains inherent and does not adopt an α-helix due to spatial alterations. The addition of spacers effectively reduces the influence from the POM cluster. Among the two spacers, EEEEAla and Ttds, the latter proves more practical in minimizing molecular interactions. This preliminary study guided the design of analogous spacers for Lindqvist type polyoxovanadates, as detailed in the following section.

Lindqvist type polyoxovanadates (B)

Polyoxovanadates (POVs) -peptide (Bombesin) conjugation with spacer design

Among different POMs, the Lindqvist-type POMs are composed of six transition metals with the anion formula $\{X_6O_{19}\}$ (where X represents V, Mo, or W) and are known for their compact architectures, high symmetry, low molecular charge, and stability.[3] Lindqvist-type polyoxovanadates, in particular, (POVs) are characterized by a central octahedral $[V_6O_{19}]$ core, with six vanadium atoms forming a hexagonal ring and oxygen atoms bridging the vanadium ions. POVs can be functionalized with two tris (hydroxymethyl) aminomethane (TRIS) molecules to allow further functionalization via their amino groups. Therefore, modified with organic pendants, POVs are oxidatively and hydrolytically stable to broad their applications in the biological field. Moreover, Vanadium is an important element that exists in many living organisms, in a wide range of biological processes. The mechanism of action of Lindqvist-type POVs in cancer-killing is believed to involve interactions with cellular components and disruption of critical pathways involved in cell proliferation and survival. Additionally, these compounds may induce oxidative stress and DNA damage in cancer cells, leading to their destruction. POVs have been proven to be efficient against leukemia, breast cancer, lung cancer and ovarian cancer.

Owing to their versatility, POVs are an arising field with applications in biology and medicine. Nevertheless, their selectivity is still too low for practical use. Among the possible solution, is the introduction of targeting moieties for the recognition of cancer cells. For example, the conjugation with peptides may offer some advantages.

With this scenario, the POVs are decorated with a bombesin-1 (DB) derivative, and engineered by adding one or two tailored spacers between the two moieties (the tetraglutamic acid and Ttds chain reported in Figure 2.10-2.11). Beside introducing a longer distance, the spacers should guarantee electrostatic repulsion between POM and the peptide chains, thus allowing the peptide to retain its initial conformation, with no POM-induced misfolding. The strategy to obtain the final hybrid involves similar strategies as mentioned before, however, the pentaerythritol was used instead of the TRIS. This procedure requires the generation of an activated NHS moiety in the POV form to achieve the following steps. The first reaction consists in the synthesis of the polyoxovanadate starting from inorganic $NaVO_3$, $C_{16}H_{36}BrN$, stoichiometric amount of HCl and $(HOCH_2)_3CCH_2OH$, to obtain $[(C_4H_9)_4N]_2[V_6O_{13}\{(OCH_2)_3CCH_2OH\}_2]$ (V_6OH). the second step allows further functionalization with succinic anhydride to generate $[(C_4H_9)_4N]_2[V_6O_{13}\{(OCH_2)_3CCH_2OOCCH_2CH_2COOH\}_2]$ (V_6O-succinate). and the final step, which is the reaction with n-hydroxysuccinimide (NHS) in the presence of dicyclohexylcarbodiimide (DCC) finally generates $[(C_4H_9)_4N]_2[V_6O_{13}\{(OCH_2)_3CCH_2OOCCH_2CH_2CO(C_4H_4NO_3)\}_2]$ (V_6O-NHS).

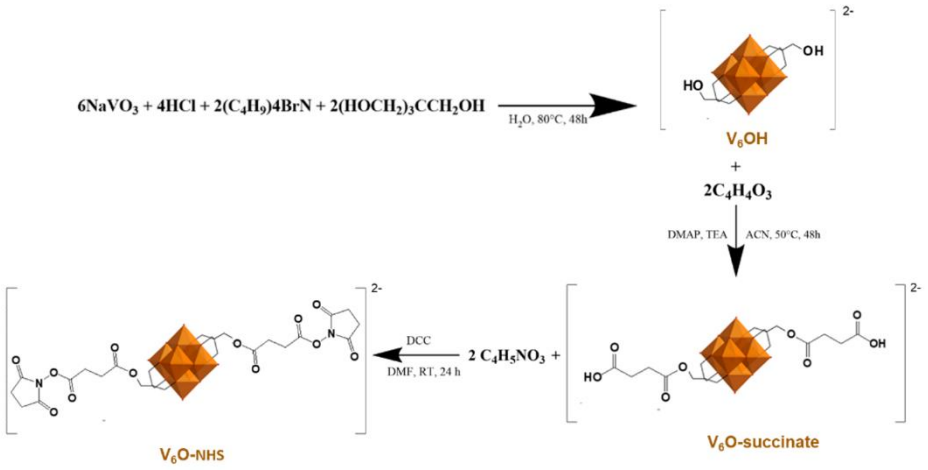

Figure 2.10. the scheme of the synthesis of V_6O-NHS.

Following the step, the peptides Demobesin-1 (peptide 1), with different spacers: DB-βAlaEEEE (peptide 2), DB-Ttds (peptide 3), DB-βAlaEEEE-Ttds (peptide 4) are combined with POVs separately to study whether the function of the peptide is increased after spatial modification and enhance the biological function of POV.

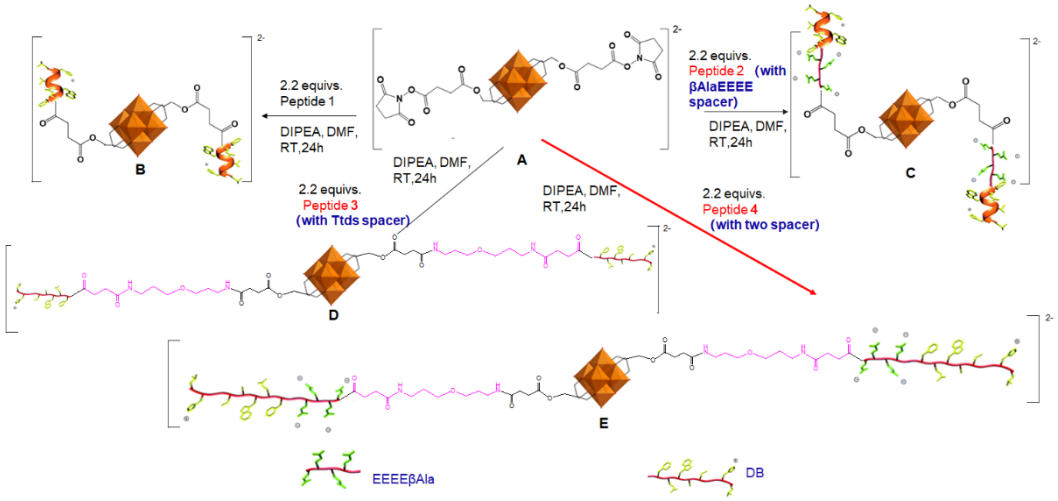

Figure 2.11 the scheme of the synthesis of V_6-Hybrids.

The characterization and analysis of POVs-Hybrids

In this section, POVs undergo decoration using a peptide DB derivative. The process involves engineering by introducing one or two specifically designed spacers between the two components: the tetraglutamic acid and Ttds chain. As depicted in Figure 2.12, the FT-IR (KBr) spectra of the V_6O-NHS and V_6O-spacer(s)-peptide show no structural changes in the region typical of the polyoxometalate framework (between 1000 cm^{-1} and 500 cm^{-1}). An intense absorption band at 1668 cm^{-1} is observed, indicating the successful synthesis of the hybrid between the peptide and the polyoxometalate, with the characteristic N-C=O amide bond. Additionally, a medium-intensity band at 1534 cm^{-1} may be assigned to -N-H bending. The loss of -NHS group signals (at 1783 cm^{-1} and 1814 cm^{-1}) are obvious, together with the new peptide bond stretching around 1640 cm^{-1}. Following the reaction with peptides, it is crucial to observe the disappearance of the NHS group signal.

Simultaneously, a new peak appears, corresponding to the C=O carbonyl signal, which serves as confirmation of the correct progression of the reaction, as evidenced at 1737 cm^{-1}.

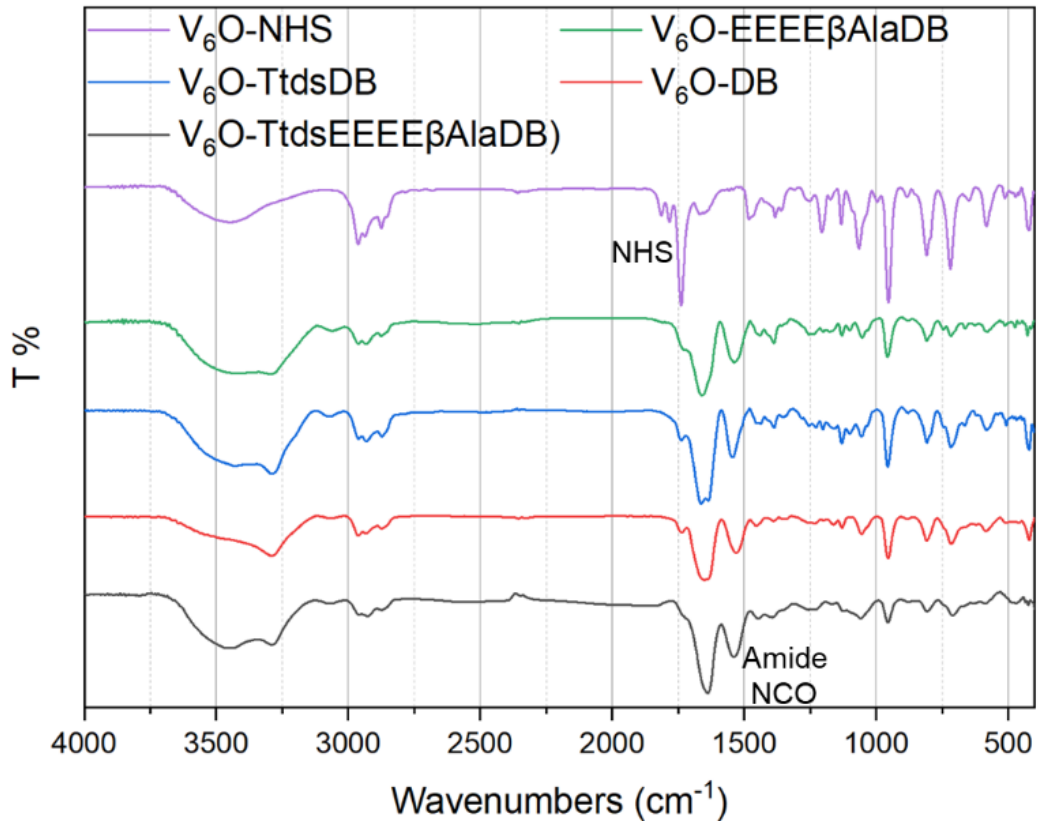

Figure 2.12. FTIR comparison between V6O-NHS (purple), V6O-EEEEβAlaDB (green), V6O-TtdsDB (blue), V6O-DB (red) and V6O-TtdsEEEEβAlaDB (black).

The objective of this study was to investigate the influence of the spacer on the interactions between POV and peptides. To achieve this, 2D 1H NMR were used. Figure 2.13 displays the overlapping COSY NMR spectra in the NH amide and CHα resonance region for peptide DB, V_6O-DB, and V_6O-TtdsEEEEβAla-DB. Notably, the presence of βAla, NH-Ttds, and NH-POV can be observed, along with a higher intensity of NHEt in V_6O-TtdsEEEEβAla-DB. Additionally, it is of significance to observe that without spacers, Gln on V_6O-DB experiences the most significant shift to the right, and the shift of Gln on V_6O-TtdsEEEEβAla-DB is less pronounced. Likewise, comparable alterations are noted in other amino acid residues, including His, Trp, Ala, and Val. These observations from the

COSY analysis suggest that the spacers may mitigate the effect of POV, in terms of chemical shifts, on the peptide.

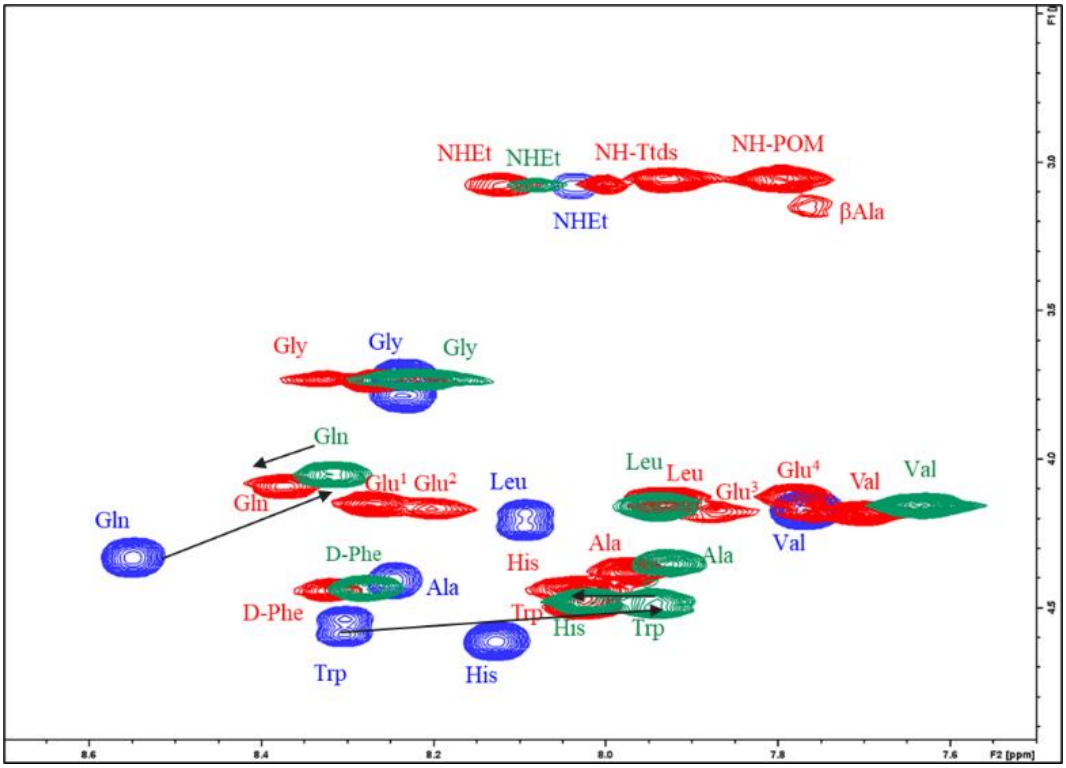

Figure 2.13. Comparison of chemical shift (600 MHz COSY spectra in d6-DMSO) for NH–CHα cross peaks belonging to free and V₆O-grafted DB. (peptide DB (blue), (V₆O-DB, green) and V₆O-TtdsEEEEβAlaDB, (red).

In an effort to scrutinize the influence of spacers on the peptide Demobensin-1, secondary chemical shift values were calculated by subtracting the CHα resonance values of spacers-Demobensin-spacers (peptides 2, 3, and 4) from Demobensin-1. The distinctions in the CHα chemical shift between DB and the three corresponding spacers-DB are outlined in Figure 2.14A. The CHα resonance of the D-Phe residue displays an upfield shift owing to the presence of the link with the spacer, resulting in a new amide group proximate to CHα in Pept 2-4. Conversely, the three spacers exhibit comparable shielding effects on other residues, notably pronounced in the N-terminal region of the peptides, closer to the spacers, with a gradual decrease towards the C-terminal region. Notably, the C-terminal region of Demobensin-1 exhibits a distinctive inclination to adopt a helical structure.

To explore the impact of the POV cluster and the addition of spacers on Demobensin-1 in POV-peptide hybrid constructs, chemical shift values were computed by subtracting CHα resonance values of POV-spacer-Demobensin-1 constructs from Demobensin-1. The paramagnetic polyoxygenic anions containing vanadium (V) induce a downfield shift in most CHα resonances relative to the peptide, as illustrated in Figure 2.14B, with the exception of the Leu residue, which experiences an upfield shift. In comparison to other hybrids, the shifts of V_6O-TtdsEEEEβAla-DB and V_6O-EEEEβAla-DB are smaller. Importantly, these findings are corroborated by the ROESY spectra, where the characteristic connectivity indicative of the helical structure remains detectable in V_6O-EEEEβAla-DB (see in the figure S.5.75). In contrast, no similar characteristic detection is observed in V_6O-TtdsEEEEβAla-DB.

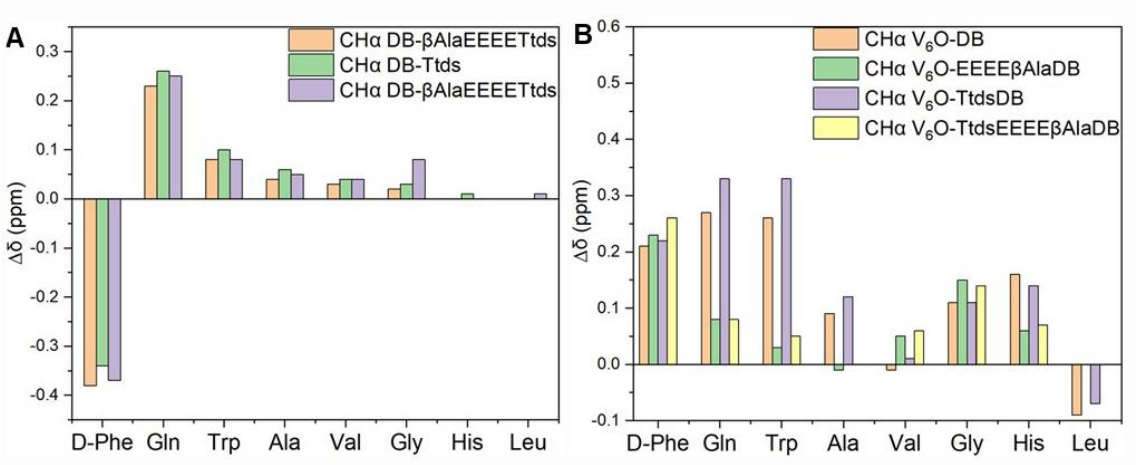

Figure 2.14. Influence of the POV-spacers on chemical shift of peptide. Δδ values were determined by subtracting the resonances of DB-spacer or POV-spacers-DB hybrids to the resonances of DB constructs. A) is the chemical shift of DB-spacers and B) is the chemical shift of POV-spacers-DB.

As depicted in Figure 2.15, UV spectra were measured for the following coupling products in 10% TFE solution: V_6O-NHS, V_6O-DB, V_6O-EEEEβAlaTtdsDB, and Demobesin peptide individually, each at concentrations of 12.5 μM, 12.5 μM, 12.5 μM and 25 μM. The UV spectrum of the V_6-hybrids mirrors the shape of Demobesin-1 alone. A distinct peak, likely below 191.5 nm, and a shoulder around 218 nm are visible in V_6O-EEEEβAlaTtdsDB. Additionally, in comparison the remaining three, it is notice that a increase of the baseline is observable in Demobesin peptide, which is not clear. A potential factor may be the inconsistency of the light source of the instrument.

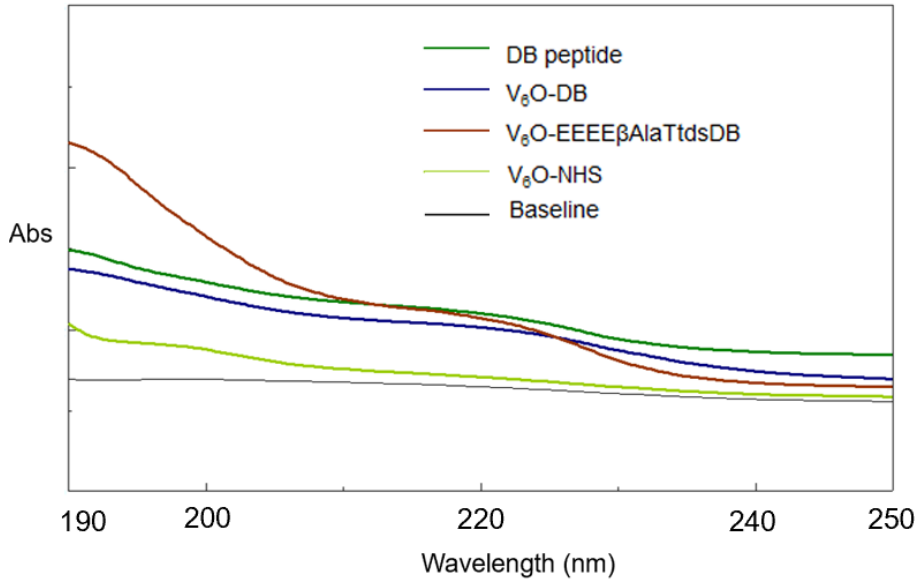

Figure 2.15. UV-Vis absorption spectra of peptide Demobesin-1 alone and its hybrids.

Consequently, CD spectroscopy was applied to evaluate the secondary structure of peptides and their POV hybrids as the proportion of trifluoroethanol (TFE) escalated from 10% to 100% (v/v), as illustrated in Figure 2.16, the relatively lower polarity of TFE allowed for the examination of how a more hydrophobic medium (mimicking the membrane environment) may affect the peptide's conformation, providing valuable insights into the bioactive conformation when the peptide interacts with a receptor on the cell surface. Figure 2.16 illustrates that in an 80% TFE solution, the shape of the CD is not significantly altered by the POV, while a marked (80%) increased intensity is observed.

In a 10% TFE solution, there was also an intensity increase, although not as pronounced as in the previous case.

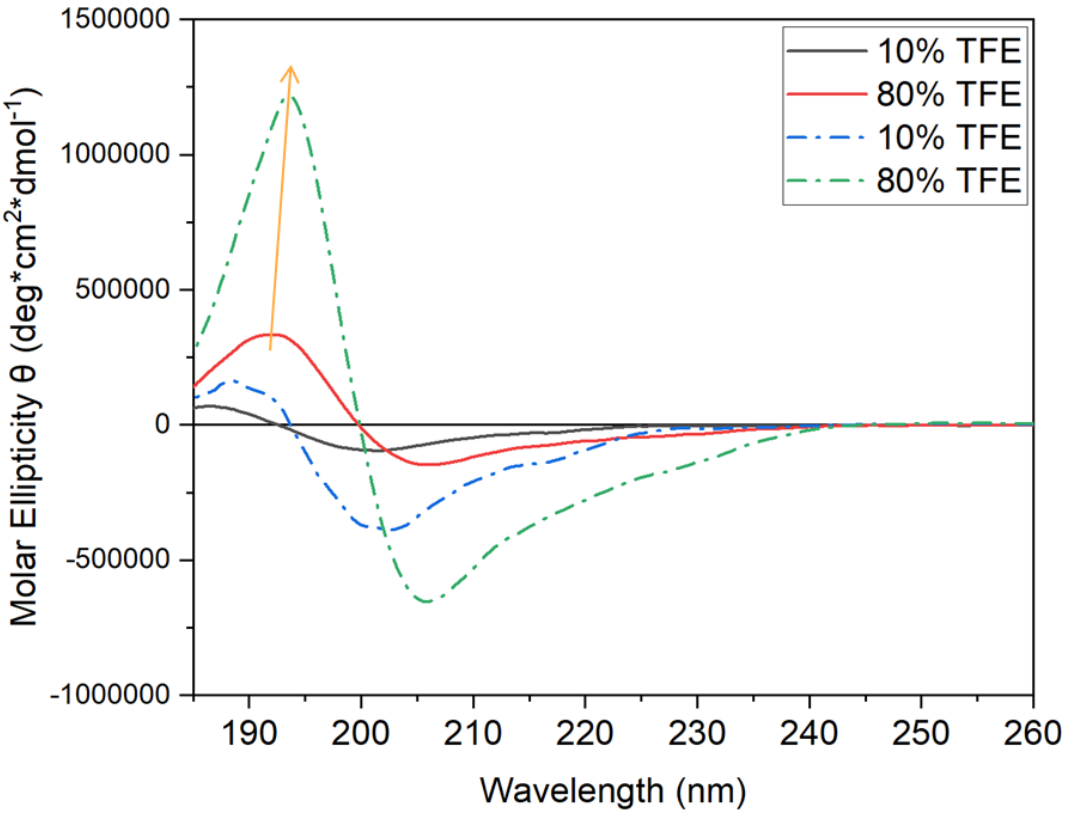

Figure 2.16. Far-UV CD spectra of DBβAlaEEEETtds (12.5 μM, solid) and V6O-TtdsEEEEβAlaDB (12.5 μM, dot line) at different TFE : water percentage.

For a more thorough comprehension of the distinctions in Circular Dichroism (CD) spectra, additional analysis was conducted using B23 CD Apps at Diamond Light Source. This secondary structure simulator utilizes an X-ray protein database, generating various graphs for interpretation of possible secondary structures. The histogram presented in Figure 2.17 delineates the distribution of secondary structures in different compounds across varying percentages of trifluoroethanol (TFE). As TFE concentrations increase, the structural tendency leans towards an α-helix, whereas in an aqueous environment, the peptide demonstrates a heightened affinity for a β-sheet structure. Notably, the α-helix of V_6O-TtdsEEEEβAlaDB exhibits sensitivity to TFE, particularly between 10% and 20% TFE.

This suggests that in lower TFE solutions, the peptides on V_6O-TtdsEEEEβAlaDB tend to unfold to a greater extent.

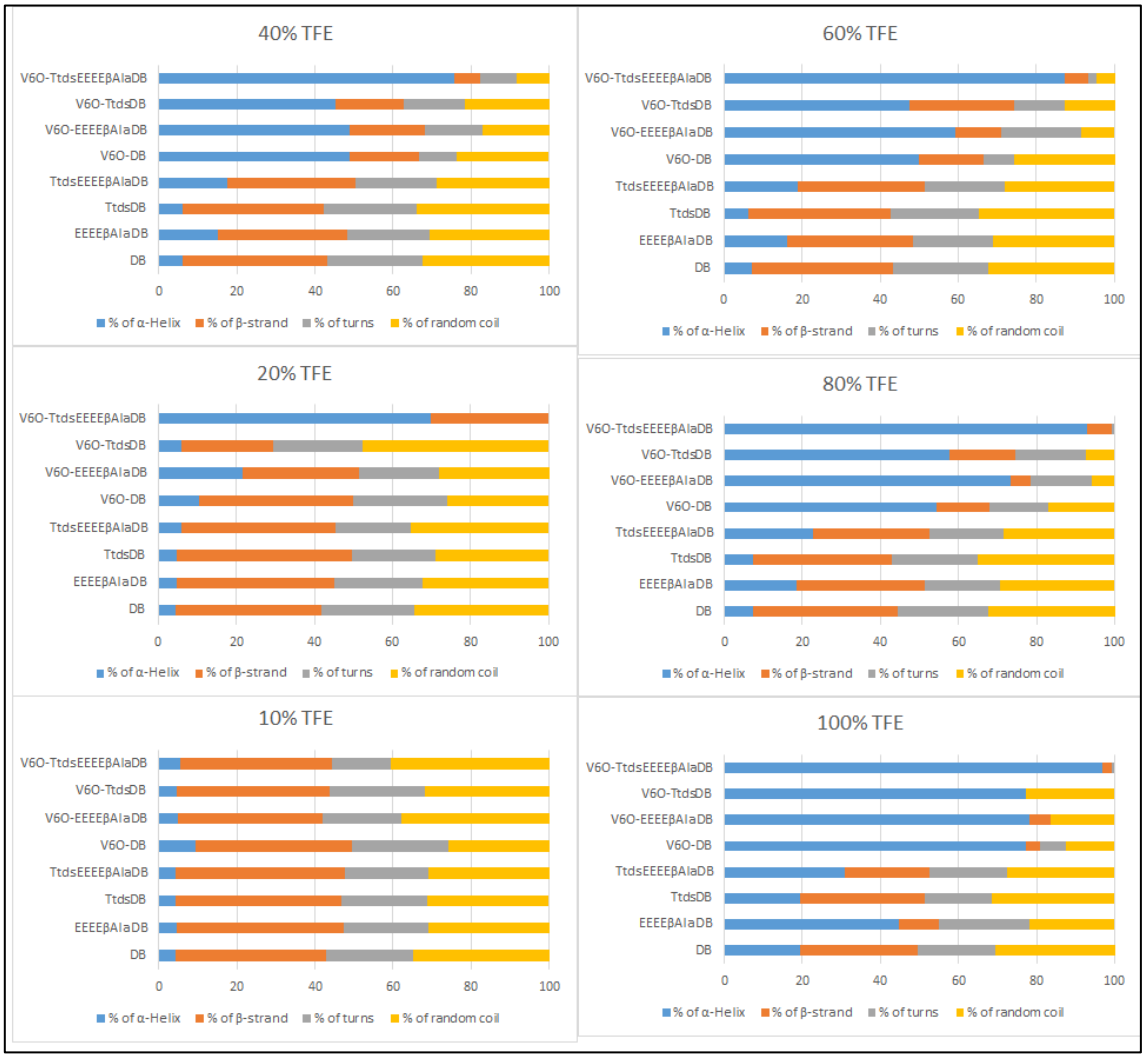

Figure 2.17. Percentage of α-helix, β-strand, turns and random coil for V_6O-hybirds in 10% and 80 % TFE solution.

With the intention of studying on structure and morphology of our compounds, Transmission electron microscopy (TEM) technique has been used to follow the structure changes in different compounds. Specifically, Figure 2.18A illustrates that the V_6O-DB compounds are formed in clustering without a defined shape (V_6-OH size is around 2-3 nm). Similarly, Figure 2.18B depicts the clustering of V_6O-EEEEβAlaDB, with the additional presence of small, dispersed nano-sized dots within the cluster. Figure 2.18 C displays that V_6O-TtdsDB forms bigger elongated structures

with fiber-like shape. Figure 2.18 D demonstrates nano-sized particles without any noticeable aggregation. This change in behavior suggests that thehybrid POV is scarcely aggregated in the presence of the two spacers.

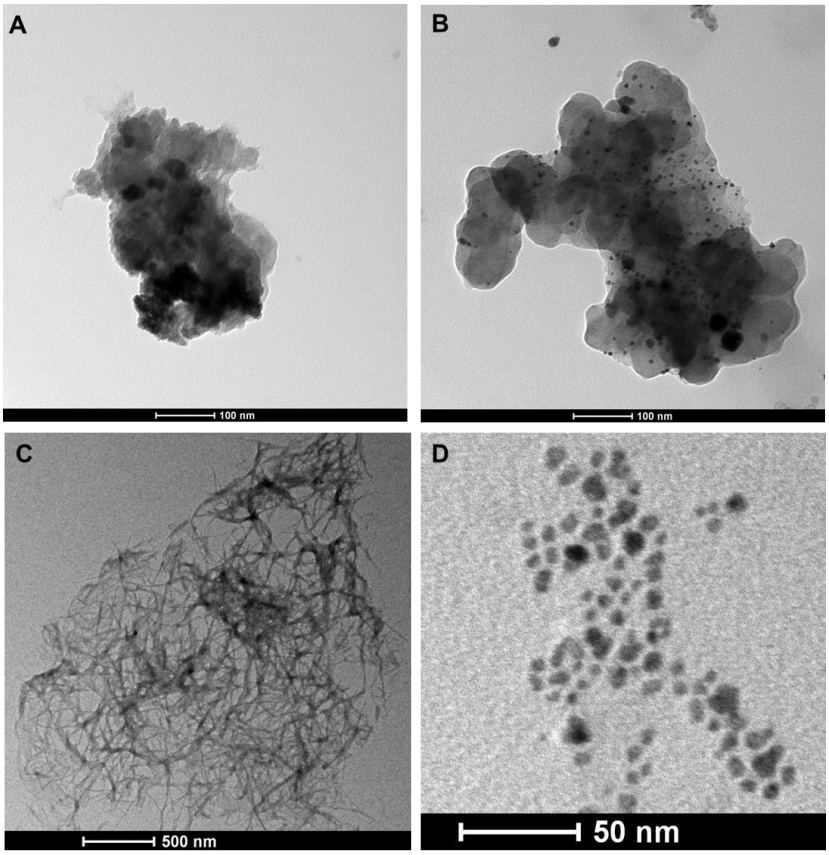

Figure 2.18. TEM measurements, 10^{-4} M solutions of A) V_6O-DB, bar: 100 nm B) V_6O-EEEEβAlaDB, bar: 100 nm C) V_6O-TtdsDB, bar: 500 nm D) V_6O-TtdsEEEEβAlaDB in DMSO/water.

Conclusions

In this project, NMR, ESI, CD, UV-vis and FT-IR spectroscopy were the first tools applied on determining the success in the synthesis of the POV hybrids. (i)The 2D NMR results indicate that the presence of POVs causes a shift towards higher fields in the peptides DB, the adding of spacers may be able to reduce the shift, especially for what concerns TtdsEEEEβAla spacer. (ii) Based on CD and the calculated secondary structure, in lower TFE solutions, the peptides on hybrids tend to unfold to a greater extent. (iii) Furthermore, in the TEM, the use of two spacers leads to lower aggregation, favoring the formation of spherical nano-particles.

Chapter 3: The design of nano POM-RGD

Mn-Anderson Evans polyoxomolybdates with RGD (A)

In this section, the Anderson-Evans POM was decorated with a peptide containing the RGD motif, known as an antagonist of natural peptides, integrated into the structure of the cyclic pentapeptide c(fKRGD).[48, 50] The objective is to design a functional polyoxomolybdate-RGD ($MnMO_6$-c(RGDfK)) conjugate in which the targeting sequence is easily accessible, enabling effective recognition of cancer cells.To this aim, this process entails the introduction of a spacer unit between the two respective components. As shown in Figure 3.1. The small spacer serves to introduce a longer distance between the POM and the peptide chains.

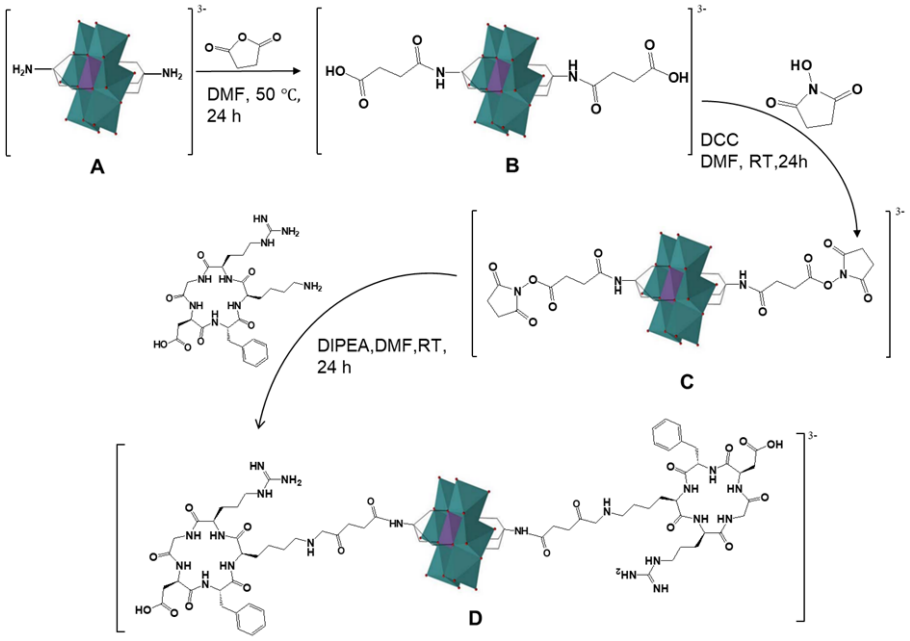

Figure 3.1. the scheme of the synthesis of MnPOM- c(fKRGD)

The employed reaction procedure in this instance has been adapted from prior reactions, using N-hydroxysuccinimide (NHS) ester for the activation of the POM, leading to a product yield of 76%. The resultant solid powder exhibited a faint orange tint. The $MnMO_6$-c(RGDfK) underwent thorough

characterization using ESI-MS (-), which revealed two primary ionizations. The first one was noted at m/z 1386, corresponding to $[M-2TBA]^{2-}$ (m/z 1384.4), while the second appeared at m/z 1261.9, consistent with $[M-3TBA+H]^{+}$ (m/z 1263.6). The FTIR spectrum of $MnMo_6$-c(RGDfK) displayed signals that were in perfect agreement with those observed in previous syntheses, providing robust evidence of the successful reaction outcome without causing any disruption to the inorganic framework.

The UV spectra of $MnMO_6$-c(RGDfK) hybrid exhibited a peak with maximum absorbance below 190 nm (ε190=241600 $cm^{-1}M^{-1}$) and a shoulder at 214 nm (ε214=110400 $cm^{-1}M^{-1}$). These two features were also discernible in the c(RGDfK) peptide, albeit with lower absorbance: a maximum absorbance below 190 nm (ε190=63200 cm-1M-1) and a shoulder around 217 nm (ε217=83200 $cm^{-1}M^{-1}$).

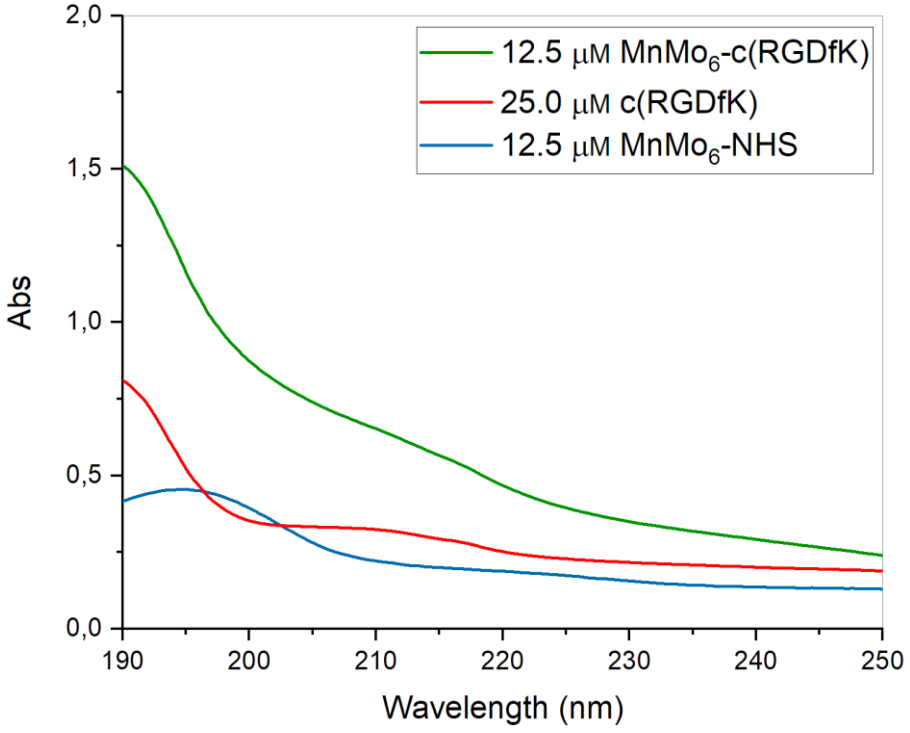

Figure 3.2. UV absorption spectra of the MnMO6-c(RGDfK) hybrid, the peptide alone and MnMO6-NHS.

The molar ellipticity patterns at various TFE/H_2O ratios exhibit strikingly similar shapes for both the $MnMo_6$-c(RGDfK) complex and the cyclic peptide in isolation. This suggests that there are no significant alterations in conformation. As the TFE concentration increases, the molar ellipticity

values on the graphs also increase (showing in Figure 3.3). Notably, in pure TFE, the $MnMo_6$-c(RGDfK) complex reaches its minimum at 206 nm ([θ] = -82397 $degcm^2dmol^{-1}$), while in TFE/H_2O 1:10 (TFE 10%), a similar wavelength yields a value of [θ] = -162564 $degcm^2dmol^{-1}$. This consistent trend is mirrored in the cyclic peptide when dissolved in pure TFE. Importantly, the extreme values (maximum and minimum) in the final hybrid complex are approximately four times more intense than those observed in c(RGDfK) alone. This serves as confirmation of the influence of a chiral center on the polyoxometalate metal-oxygen transitions, which also acquire chirality.

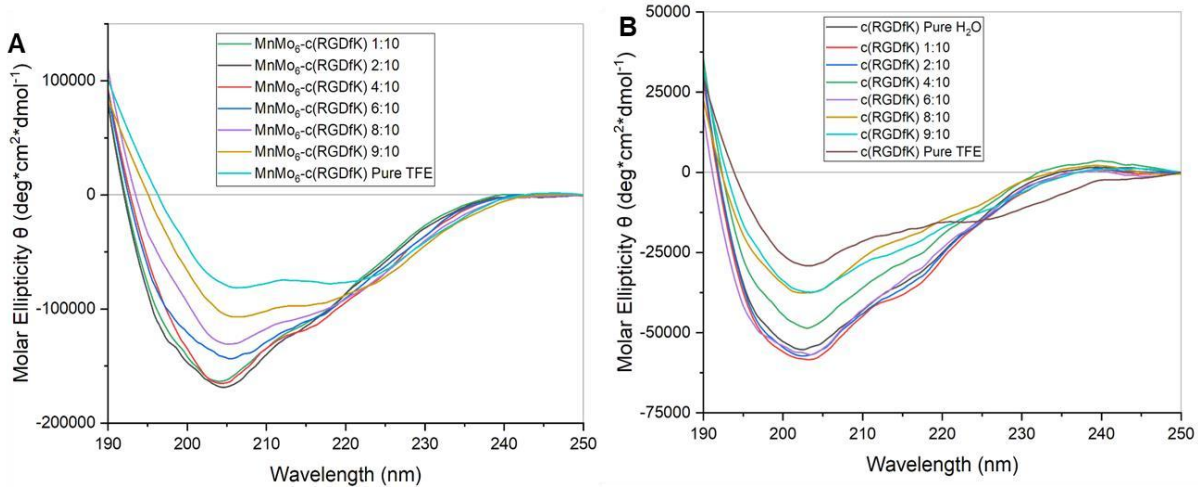

Figure 3.3. A) Molar ellipticity trends for MnMo6-c(RGDfK) at different TFE/H2O ratios: 1:10, 2:10, 4:10, 6:10, 8:10, 9:10, pure TFE. B) Molar ellipticity trends for c(RGDfK) at different TFE/H2O ratios: pure water, 1:10, 2:10, 4:10, 6:10, 8:10, 9:10, pure TFE.

Simultaneously, as depicted in Figure 3.4, it is evident that, in a TFE/H_2O 1:10 solution, the conjugation with POM does not induce substantial alterations in the shape of the peptide. However, an increase in the intensity of the peptide signal is observed. The comparison results implied the successful synthesis of POM-hybrids as well.

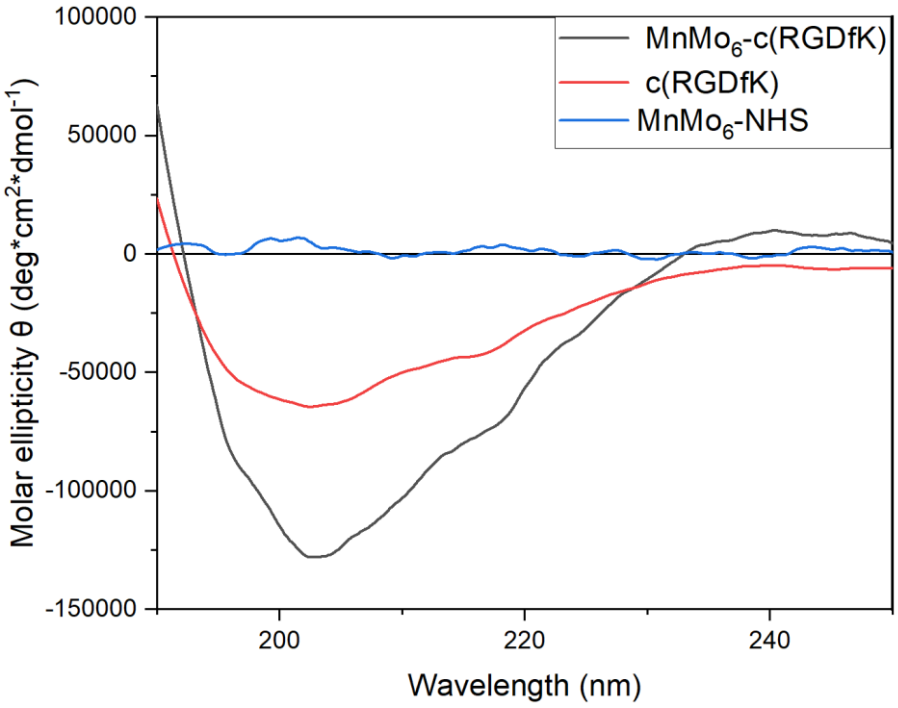

Figure 3.4 Molar ellipticity of c(RGDfK), MnMo6-RGD and MnMo6 at 1:10 TFE/H2O.

Given that the peptide exhibits cyclic structure and experiences negligible conformational alterations, no additional secondary structure simulations was performed. To elucidate the peptide sequence and assess the influence of the inorganic framework, the hybrid structure underwent analysis using COSY, TOCSY, and ROESY 2D NMR techniques. While chemical shift values for certain amino acids exhibited resemblance and minor shielding, others, such as arginine, displayed notable alterations, with an up-shielding effect of 1.2 ppm. This phenomenon could potentially be attributed to the elongated structure of the arginine amino acid side chain, which likely engages in interactions, possibly folding, with the polyoxometalate framework. The absence of the NH^{3+} signal from lysine can be construed as evidence supporting the creation of the $MnMo_6$-peptide bond. The peptide sequence's validation was corroborated through ROESY analysis, even though no coupling signals between arginine and other amino acids were detected.

Table 3.1 The chemical shift of individual amino acids was determined both in the c(RGDfK) peptide alone and when it was conjugated to the POM. Furthermore, the side chains of each amino acid within the peptide, when linked to the POM, were identified.

	$MnMo_6$-c(RGDfK)			c(RGDfK)	
AA	NH (ppm)	CH_α (ppm)	Rest of the chain (ppm)	NH (ppm)	CH_α (ppm)
Arg	7.81	2.97	$-CH_{2\gamma}$ 1.33 $-CH_{2\beta}$ 1.11	7.62	4.16
δ-Arg	-	-	-	7.58	$-CH_\delta$ 3.09
NH_3^+ Arg	8.21	3.28	/	8.48	3.25
D-Phe	7.83	4.55	$-CH_{2\beta}$ (diastereotopic) 2.72, 3.09 Aromatics not assigned	8.08	4.42
Gly	8.21	$-CH_{2\alpha}$ 4.10	/	8.48	$-CH_{2\alpha}$ 4.05
Asp	8.11	4.43	$-CH_{2\beta}$ 2.51	8.10	4.64
Lys	8.07	4.07	$-CH_{2\beta}$ (diastereotopic) 1.47, 1.58 $-CH_{2\gamma}$ 1.33 $-CH_{2\delta}$ 1.10	8.09	3.95
NH_3^+ Lys	-	-	-	7.69	$-CH_{2\varepsilon}$ 2.67

Lindqvist type polyoxovanadates with RGD (B)

Using a parallel method, Lindqvist-type POMs were also investigated, to establish the influence of different POMs structure and charge. As is shown in the Figure 3.5, reactions are designed to obtain V_6O-c(RGDfK). The reaction procedure employed in this case mirrored the mechanisms and conditions of previous reactions.

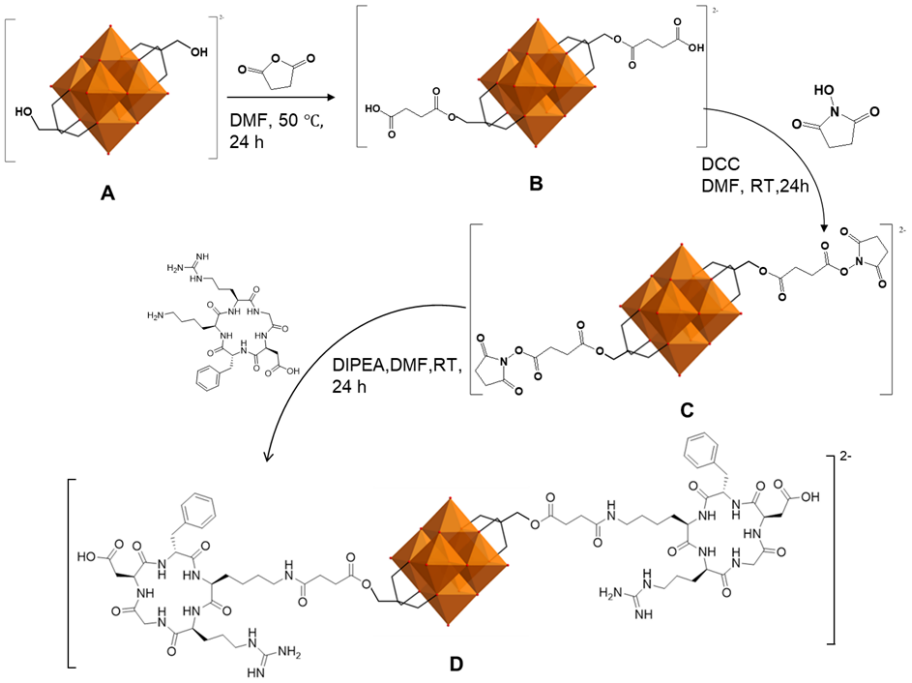

Figure 3.5., the scheme of the synthesis of V_6O-c(RGDfK).

The ESI-MS(-) analysis in acetonitrile was used to characterize the V_6O-c(RGDfK). An evident peak at m/z 1075.1, attributed to $[M\text{-}2TBA]^{2-}$ (calculated m/z 1075.7), and another at m/z 2152.2, corresponding to $[M\text{-}2TBA+H]^{-}$ (calculated m/z 2152.0), were observed. The FT-IR (KBr) spectrum closely resembles previously examined samples. The UV spectrum of V_6O-c(RGDfK) reveals a typical peak below 190 nm (ε_{190}=211200 $cm^{-1}M^{-1}$) and a secondary peak at 211 nm (ε_{211}=164000 $cm^{-1}M^{-1}$), mirroring the peptide c(RGDfK) spectrum. Compared to V_6O-NHS, the significant increase of the baseline is observed in V_6O-c(RGDfK) and c(RGDfK), the reason for this is still not so clear, one possible reason is that the light source of the instrument is not very stable.

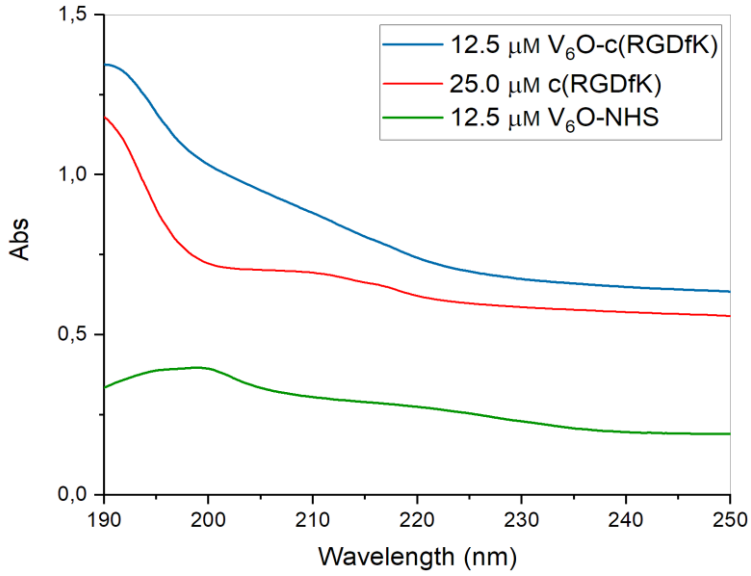

Figure 3.6. UV-spectra of V6O-c(RGDfK), V6OH-NHS and c(RGDfK) with respective concentrations 12.5 μM, 12.5 μM, and 25 μM. The solvent used was a mixture of TFE/H2O 1:10

Molar ellipticity analysis was conducted across different TFE/H_2O ratios within the 190-250 nm range for both V_6O-c(RGDfK) and c(RGDfK). The limited water solubility of V_6O-c(RGDfK) posed challenges for recording the corresponding CD, potentially accounting for the unusual pattern observed at TFE 10% and 20%. Conversely, c(RGDfK) displayed markedly low molar ellipticity minima in water, TFE 10%, and TFE 20%. Moreover, the minimum for V_6O-c(RGDfK) when dissolved in pure TFE was noted at 207 nm ([θ]=-79633 deg cm^2 $dmol^{-1}$), whereas for the peptide, it was positioned at 203 nm ([θ]=-29513 deg cm^2 $dmol^{-1}$). The application of CDApps for analysis was excluded due to the inherent cyclic structure of the peptide, which imparts reduced flexibility compared to peptides utilized in earlier syntheses.

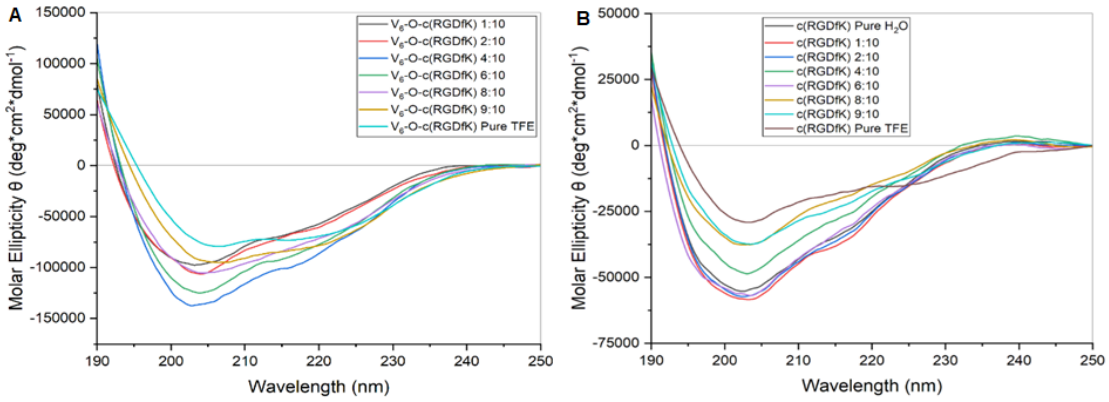

Figure 3.7. Molar ellipticity trends of A) V6O-c(RGDfK) and B) c(RGDfK) at different of TFE/H2O ratios: 1:10, 2:10, 4:10, 6:10, 8:10, 9:10, pure TFE.

Concurrently, as illustrated in Figure 3.8, it becomes apparent that, in a TFE/H_2O 1:10 solution, the conjugation of the peptide with POM does not bring about significant changes in the peptide's overall conformation. Nevertheless, there is a noticeable augmentation in the intensity of the peptide signal towards negative values. Conversely, the molar ellipticity of the POM closely aligns with the baseline. These comparative findings suggest the successful synthesis of POM-hybrids.

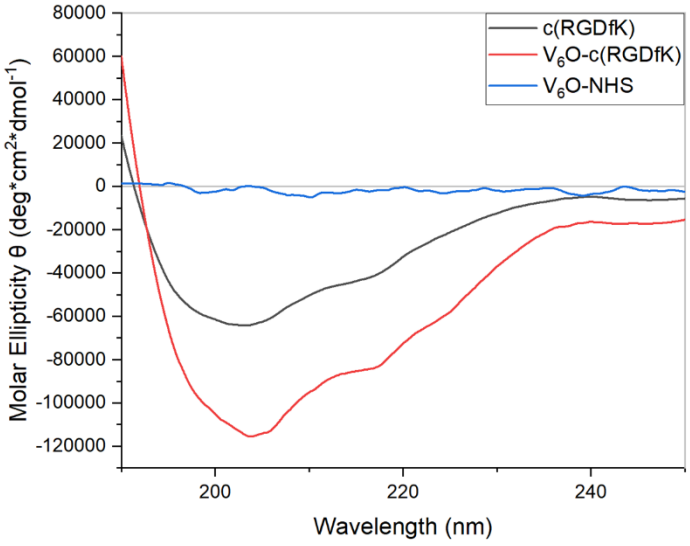

Figure 3.8. Molar ellipticity trends of A) V6O-c(RGDfK) and B) c(RGDfK) at different of TFE/H2O ratios: 1:10, 2:10, 4:10, 6:10, 8:10, 9:10, pure TFE.

Table 3.2 displayed the chemical shift of individual amino acids of peptide and its hybrids. Furthermore, the side chains of each amino acid within the peptide, when linked to the POM, were identified. The 2D NMR spectra closely resembled those of the corresponding V_6O-hybrid, with only marginal shifts in chemical charges. A subtle interaction between the POM and the peptide potentially contributes to a more pronounced shift in the Arg CHα signal.

Table 3.2 The chemical shift of individual amino acids in c(RGDfK) and its hybrids.

	V_6O-c(RGDfK)			c(RGDfK)	
AA	NH (ppm)	CH_α (ppm)	Rest of the chain (ppm)	NH (ppm)	CH_α (ppm)
Arg	7.82	2.95	$-CH_{2\gamma}$ 1.32 $-CH_{2\beta}$ 1.11	7.62	4.16
δ-Arg	-	-	-	7.58	$-CH_\delta$ 3.09
NH_3^+ Arg	8.23	3.30	/	8.48	3.25 (?)
D-Phe	7.83	4.57	$-CH_{2\beta}$ 2.72 Aromatics not assigned	8.08	4.42
Gly	8.24	$-CH_{2\alpha}$ 4.11	/	8.48	$-CH_{2\alpha}$ 4.05
Asp	8.16	4.39	$-CH_{2\beta}$ (diastereotopic) 2.38, 2.54	8.10	4.64
Lys	8.15	4.12	$-CH_{2\beta}$ (diastereotopic) 1.49, 1.58	8.09	3.95

			$-CH_{2\gamma}$ 1.32 $-CH_{2\delta}$ 1.11		
NH_3^+ Lys	-	-	-	7.69	$-CH_{2\varepsilon}$ 2.67

The comparison of Mn-Anderson Evans polyoxomolybdates hybrids and Lindqvist type polyoxovanadates hybrids (C)

In order to research the difference between Mn-Anderson Evans polyoxomolybdates hybrids and Lindqvist type polyoxovanadates hybrids, Molar ellipticity 220/208 ratios were calculated for both the peptide alone and the hybrids. In relation to the spectra of the c(RGDfK)-POM hybrids, a trough initially observed at 203 nm experiences a redshift to higher wavelengths (208 nm) as the TFE concentration increases. Additionally, an additional peak emerges at 222 nm with elevated TFE concentrations. As anticipated, due to the peptide's inherent structural characteristics, no isodichroic points are discernible in either the molybdenum or vanadium hybrids. For the c(RGDfK), $MnMo_6$-c(RGDfK), and V_6-c(RGDfK) variants, the molar ellipticity 220/208 ratios were calculated for both the isolated peptide and the hybrids (as depicted in Figure 3.9.). The behavior of the hybrids displays significant divergence from that of the unmodified peptide as the TFE concentration rises. The molybdenum and vanadium hybrids exhibit distinctive features at lower TFE concentrations, gradually converging as the TFE/H_2O ratios increase.

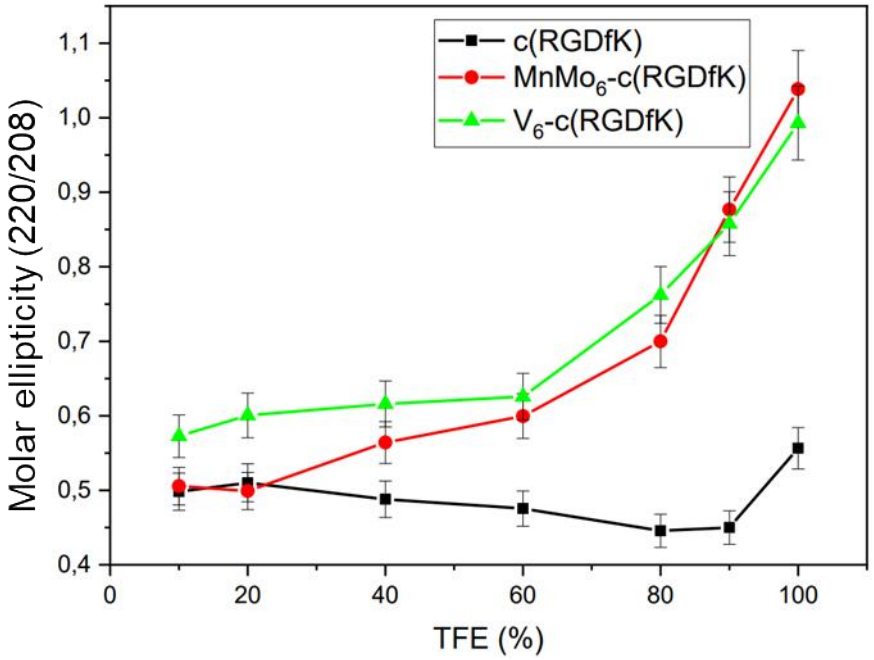

Figure 3.9. Plot of Molar ellipticity 220/208 as a function of the percentage of TFE for c(RGDfK), MnMo6-c(RGDfK) and V6-c(RGDfK).

The NMR examination of the POM-c(RGDfK) hybrids (refer to Figure 3.10) reveals alterations in the NH-CHα diagnostic zone due to the POM's presence. Several amino acids experience upfield shifts, while others encounter downfield shifts. However, no significant discrepancies are observed when the metal's nature is altered.

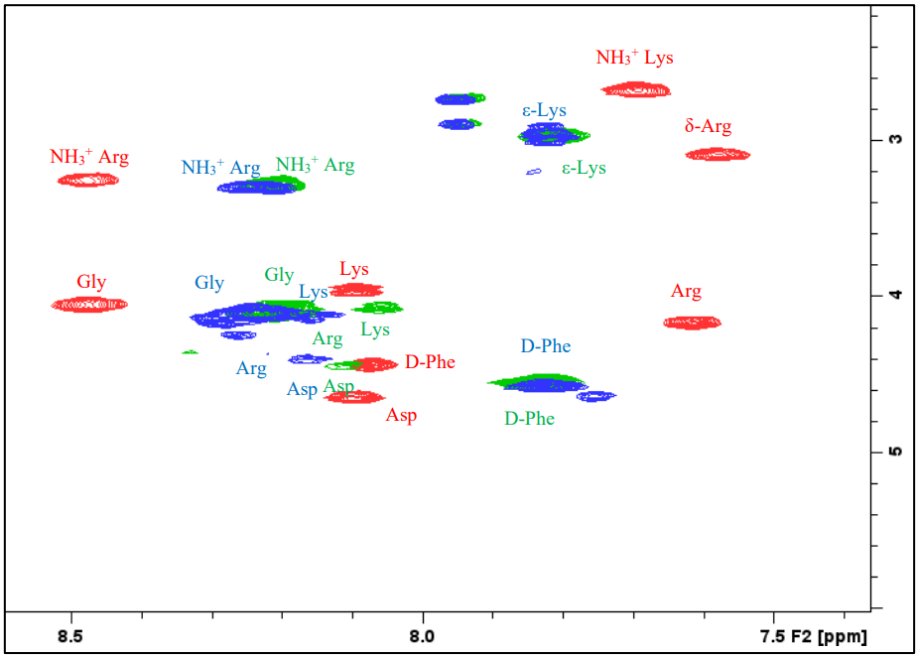

Figure 3.10. Comparison of chemical shifts for NH-CHα crosspeaks belonging to compound c(RGDfK) (red), MnMo6-c(RGDfK) (green) and V6-c(RGDfK) (blue) in d6-DMSO. The spectra were acquired on a Bruker DMX-600 instrument operating at 599.90 MHz for 1H at 298 K.

In this specific context, focusing on biological activity *in vitro*, Mn-Anderson Evans polyoxomolybdates and Lindqvist type polyoxovanadates were linked to Phenylalanine. All the compounds are dissolved in 5% DMSO- Buffer solution. The Figure 3.11 depicted that the standalone V_6-Phe exhibited a moderate level of cytotoxicity effectiveness, retaining 70% viability of HeLa cells after 24 hours (at a concentration of 10 µM). A noticeable enhancement in cell viability inhibition was observed, instead, for V_6-c(RGDfK), which demonstrated significant inhibition of cell growth, resulting in a residual viability of 70% at a concentration of 1 µM after 24 hours (with an IC50 value 3.5 µM). When considering $MnMo_6$-Phe on its own, it displayed limited anticancer efficacy even at a higher concentration (100 µM). In contrast, $MnMo_6$-c(RGDfK) exhibited visibly improved cell viability inhibition, whose IC50 value is 4.5 µM. Moreover, upon comparing the outcomes of V_6-c(RGDfK) and $MnMo_6$-c(RGDfK), the former demonstrates higher efficiency (with a steeper decline in viability) when the concentration surpasses 5 µM.

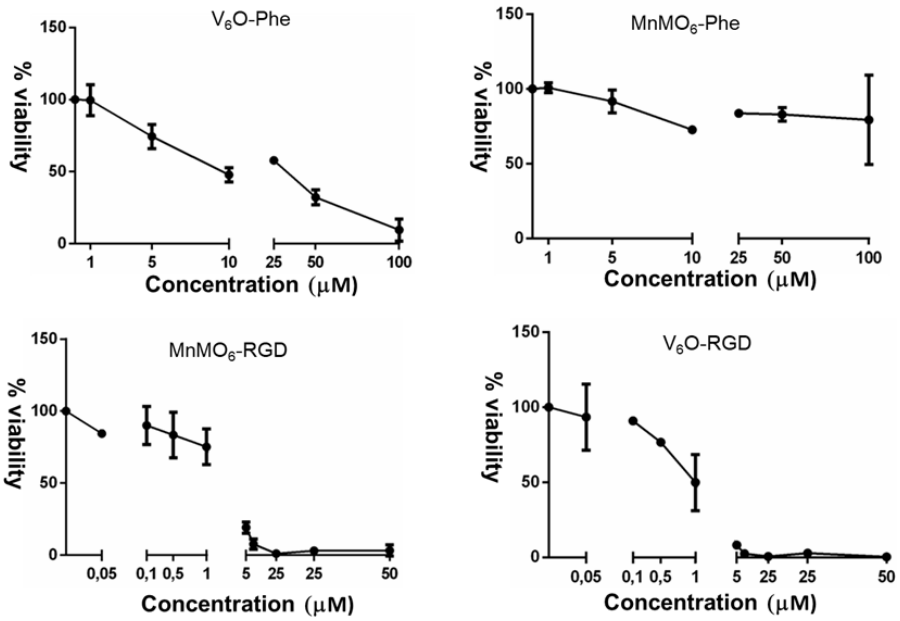

Figure 3.11. MTT test on HeLa cells after24h incubation.

Conclusion

Hybrid compounds possess distinctive attributes. Additionally, the discrimination between vanadate and molybdate becomes more pronounced when the concentration of TFE is low, although their differences are less conspicuous in a more hydrophobic environment. NMR analysis indicated that modifying the metal core within the hybrid does not lead to substantial changes in the chemical shifts of individual amino acids in c(RGDfK). Presently, ongoing cytotoxicity assessments of POM-RGD are promising results (IC_{50} < 5 μM) and are underway to evaluate their selectivity effects on cells with different overexpressing the targeted receptors.

Chapter 4: The study on nano POM-KLVFF for Alzheimer's Disease

Aβ plays a key role in Alzheimer's disease (AD), which is an increasingly common disease and a major global healthy challenge in the aging population. Aggregated β-amyloid (Aβ) is widely considered to be a key factor leading to the progressive loss of neuron functions. Therefore, targeting and inhibiting Aβ aggregation has been regarded as an effective therapeutic strategy for the treatment of AD. The key sequence that drives aggregation of Aβ is the central sequence KLVFF, which contains a di-phenylalanine motif and plays an important role in the tendency to aggregate via β-sheet staking. [63]The polymerization of isolated KLVFF has extensively studied before, and many variants have been prepared to examine their effects on Aβ.[52, 72, 73]

On the other hand, KLVFF peptide can interact with its homologous sequence to prevents amyloid aggregation,[66] acting as β-sheet breaker. In this chapter, MnPOM was functionalized with a short peptide able to recognize Amyloid β (Aβ) peptides. KLVFF peptide-modified polyoxometalates have been synthesized by following a different synthetic scheme, involving click-chemistry between a targeting peptide and the POM (Figure 4.1). In this way, the competition between amino group of the side chain and terminal amino group, for the conjugation of the POM's carboxyl group can be avoided.

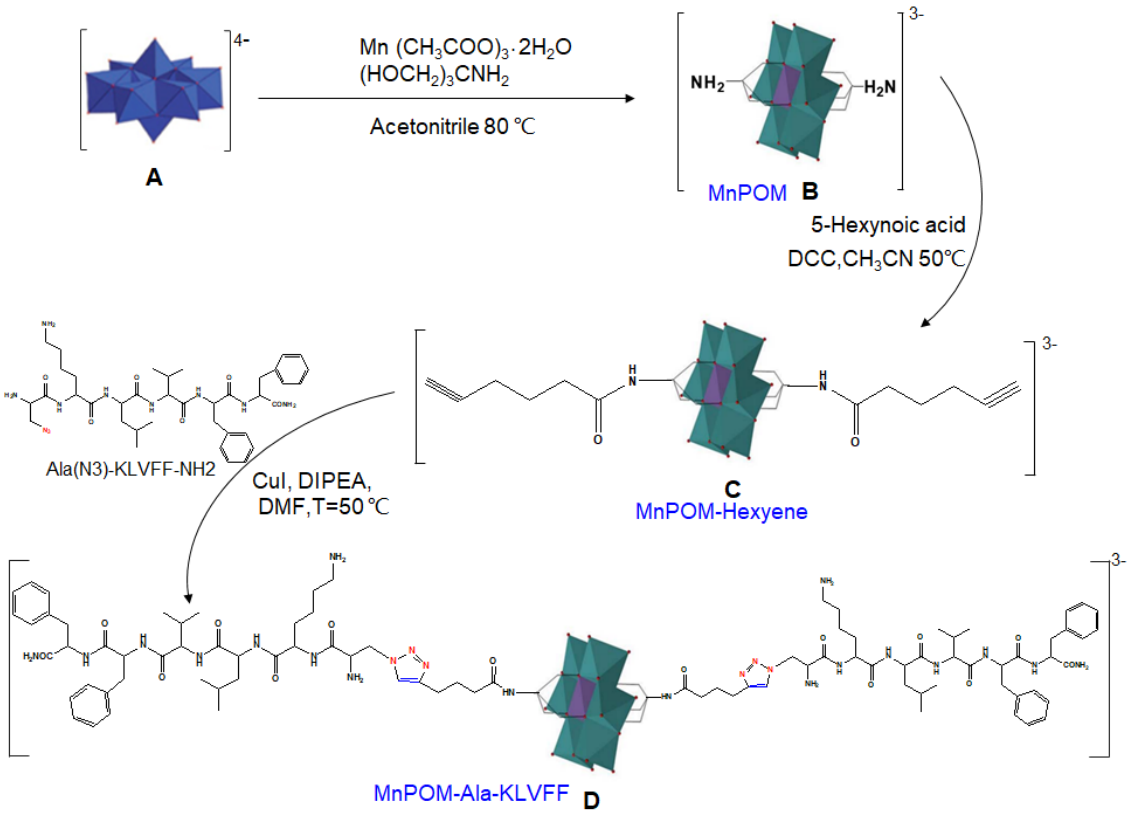

Figure 4.1. The synthetic scheme to obtain the POM-KLVFF conjugate.

Mn-Anderson-Evans POM-Hexyne

A different reaction pathway was also planned to allow the selective grafting of KLVFF peptide. A "clickable" POM has thus been prepared, by reacting 5-hexynoic acid with compound 2 (0.106mmol) in the presence of DCC in CH_3CN at 50°C. An orange solid was collected (yield 85.5%, Compound POM-Hexyne) and characterized by FT-IR, ^{1}H-NMR and ESI-MS (-) (CD_3CN). In the Figure 4.2, the stretching of typical peaks of terminal alkynes, -C≡C- and C≡C-H signals, can be recognized at 2148 cm^{-1}, 3315 cm^{-1} . ^{1}H-NMR (300 MHz, d_6-DMSO) also shows additional signals at 1.65, 2.14 and 2.73, attributed of three C*H*2 groups and terminal alkyne of the new spacer, together with the new amide and carboxyl signals signals at 7.46 (s, 2H, NH). ESI-MS (-) in CH_3CN Confirms the bis-

functionalization with the two signals at m/z =1828.0 (m/z calcd. for $[M\text{-}TBA]^-$ = 1828.14) and 1585.8 (m/z calc. for $[M\text{-}2TBA]^{2-}$ = 1587.72).

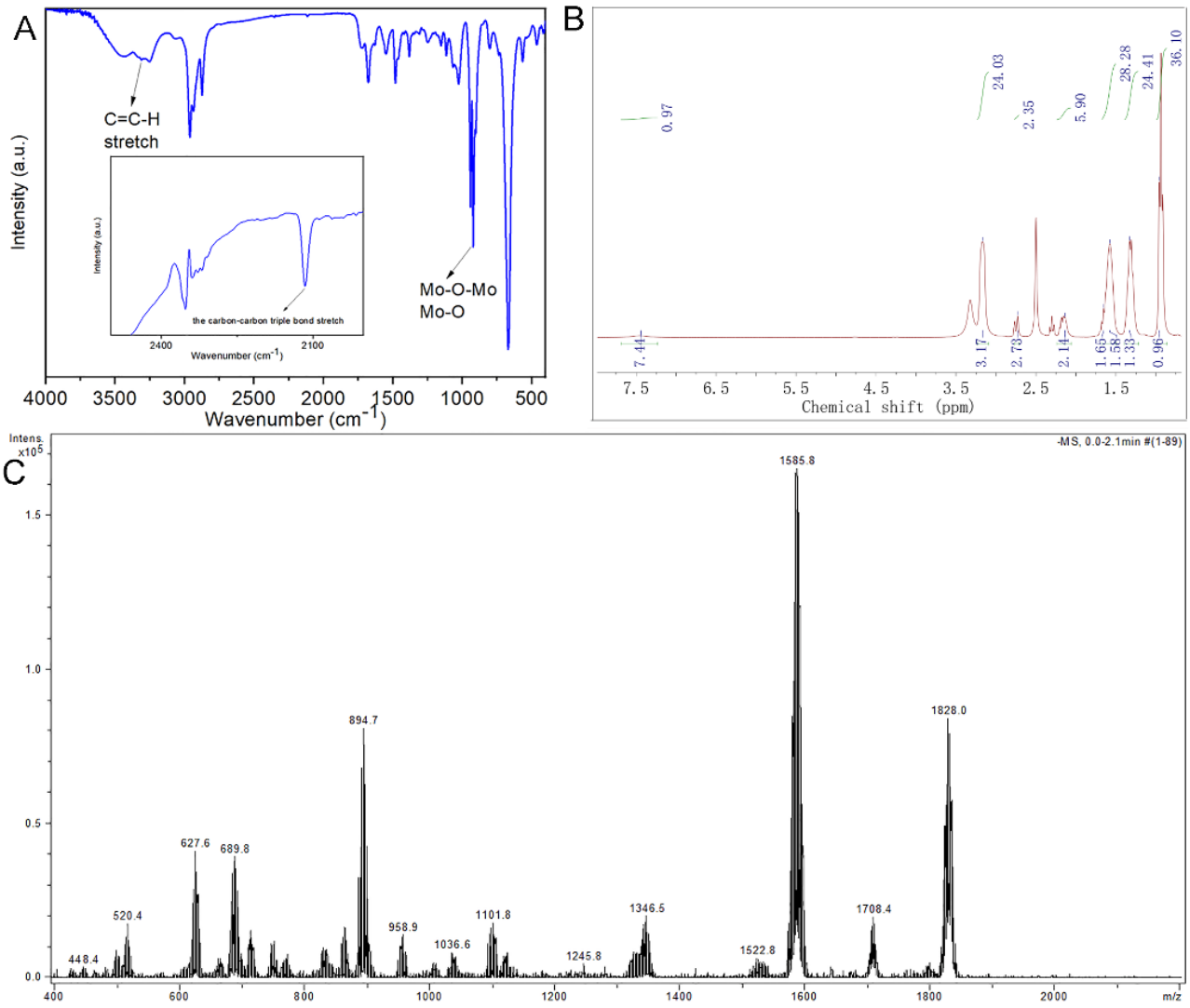

Figure 4.2. The characterization of Mn-Anderson-Hexyne. A) FT IR (KBr), 1H-NMR (300 MHz, CD_3CN) C) ESI-MS (-) (CH3CN).

Conjugation of Mn-Anderson-Evans POM-Hexyne with the peptide

The compound MnPOM-β-azido-Ala was supposed to be coupled with a peptide (Ala(N_3)-KLVFF-NH_2). Before that, meanwhile, it was also tested with a single amino acid. POM-hexyne (0.038mmol) and 0.2% CuI and DIPEA (0.07mmol) were dissolved in anhydrous acetonitrile and DMF (14:1).

After stirring under N_2 flow for 30 min, Fmoc-β-azido-Ala-OH (0.114mmol) was added in the mixture system. After 24h, the transparent orange solution was obtained upon centrifugation, then transferred into diethyl ether atmosphere for one day (repeating the latter step 3 times) and finally washing with water and ether. The Figure 4.3 illustrates that the reaction was implemented successfully. In Figure 4.3A, the signals ascribed to triazole ring are close to wavenumbers 2100 and 1000 cm^{-1}. Benzene ring bands occur at wavenumbers 800 to 700 cm^{-1} and 1790 to 1700 cm^{-1}. ^{1}H-NMR (300 MHz, CD_3CN) spectroscopy is shown in Figure 4.3B, with new signals at 4.36 (m, 12H, CH_2) and 7.66 (m, 16H, CH Fmoc ring). In Figure 4.3D, ESI-MS (-) (CH_3CN) shows signals at m/z =1144.5 (m/z calcd. $(M\text{-}2TBA)^{2-}$=1145.6) and 1014.9 (m/z calc. for $[M\text{-}3TBA+Na]^{2-}+H_2O$=1017.76). Figure 4.3D and Figure 4.3E are UV-Vis spectroscopy and circular dichroism (CD) spectroscopy, as further proofs that the Fmoc-β-azido-Ala-OH was successfully linked. The maximum wavelength of absorbance of the free Fmoc-β-azido-Ala-OH and of its POM conjugate can be found in the near-ultraviolet spectral region, from 250 to 300 nm, where the bands are mainly due to $\pi \rightarrow \pi^*$ transitions of side chain aromatic groups. The CD spectra of the POM coupling with Fmoc-β-azido-Ala-OH shows a strong signal due to the induction of chirality by the amino acid at 222 nm, while very small signals are observed for the achiral POM and Fmoc-β-azido-Ala-OH.[31]

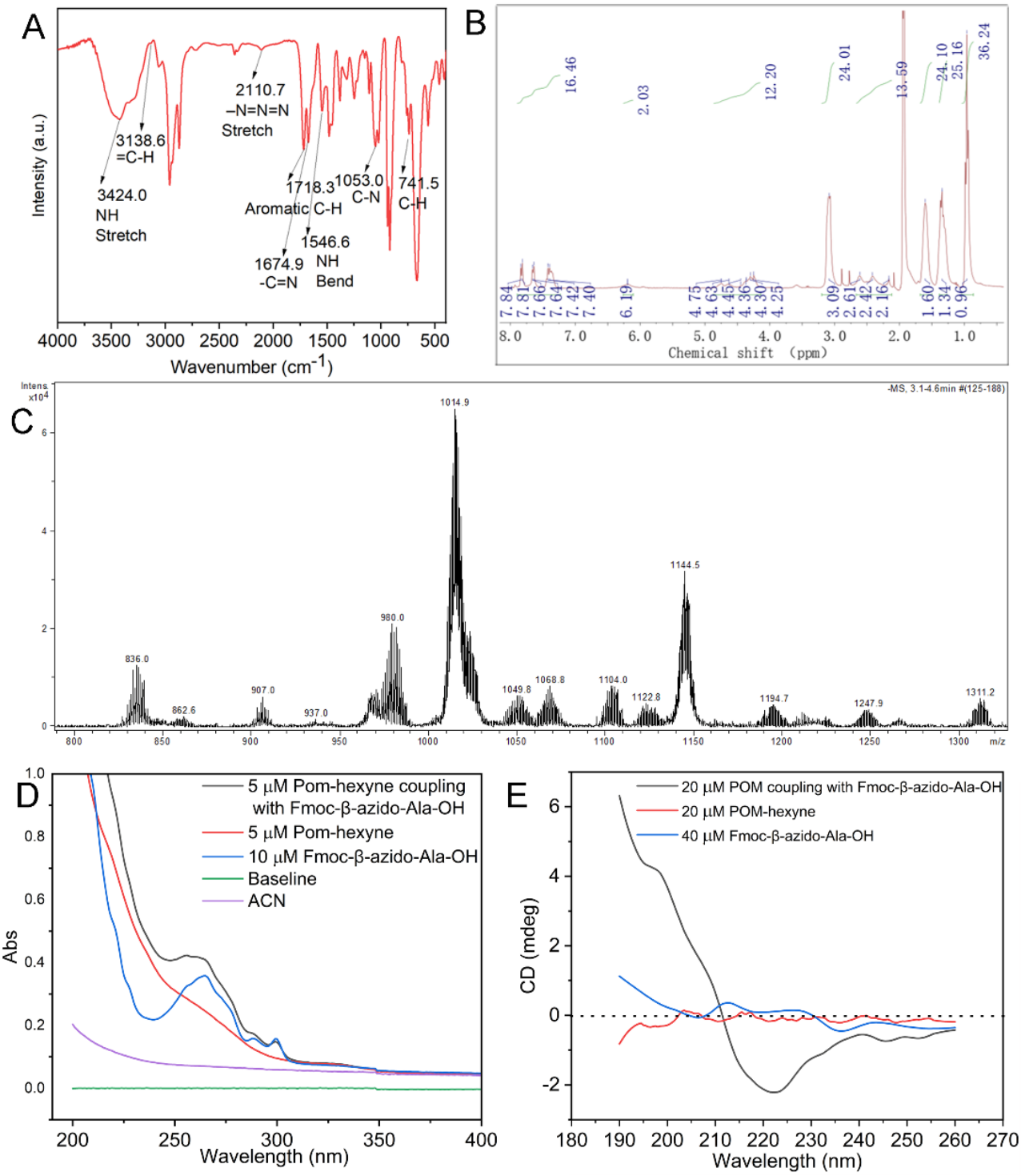

Figure 4.3. The characterization of Mn-Anderson-Hexyne. A) FT IR (KBr), B) 1H-NMR (300 MHz, CD3CN) C) ESI-MS (-) (CH3CN). D) UV-Vis spectroscopy E) Circular Dichroism spectroscopy

The synthesis of peptide Ala(N_3)-KLVFF-NH_2 and POM conjugation

The 5% piperidine/DMF and 2% DBU induced Fmoc deprotection. the peptide Ala(N_3)-KLVFF-NH_2 was synthesized by conjugating of Fmoc-Phe-OH, Fmoc-Phe-OH, Fmoc-Val-OH and Fmoc-Leu-OH, Fmoc-Lys (Boc)-OH and Fmoc-*β*-azido-Ala-OH sequentially. Ala(N_3)-KLVFF-NH_2 was characterized by LC-MS. As it is displayed in Figure 4.4, the Mol. Weight number of Ala(N_3)-KLVFF-NH_2 was obtained at retention time 14.13 min. Therefore, Ala(N_3)-KLVFF-NH_2 was successfully synthesized.

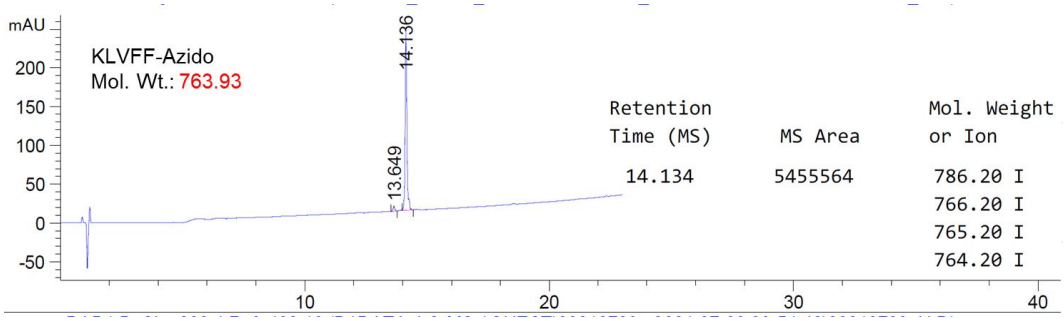

Figure 4.4. The LC-MS of peptide KLVFF-azido.

The Figure 4.5A displays the characteristic peaks of TBA on Anderson POM, which are located at 0.96, 1.33, 1.58, and 3.17 ppm. In Figure 4.5B, the aromatic peaks corresponding to the Ala(N3)-KLVFF-NH_2 moiety were observed at 7.43 and 8.04 ppm. Additionally, Figure 4.5C demonstrates the presence of both the aromatic peaks and TBA peaks. The NMR results strongly suggest the successful synthesis of POM-hybrids

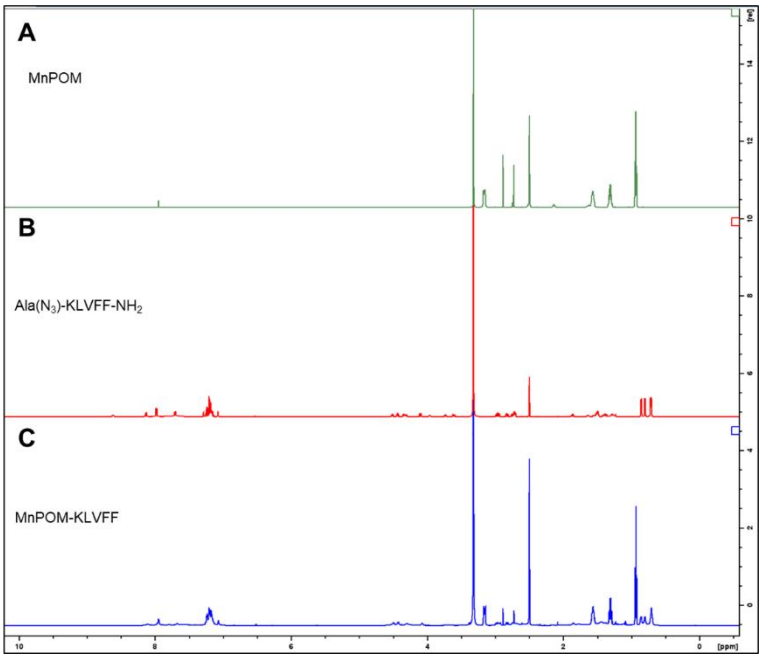

Figure 4.5. The comparison of ^{1}H 2D-NMR of A) MnPOM, MnPOM-Ala-KLVFF and Ala(N_3)-KLVFF-NH_2 in d6-DMSO.

In the Figure 4.6, The analysis of the COSY spectrum reveals that when comparing MnPOM-KLVFF with Ala(N_3)-KLVFF-NH_2, there is evidence suggesting that Mn-POMs caused a lower chemical shift for peptides, particularly noticeable in the case of lysine.

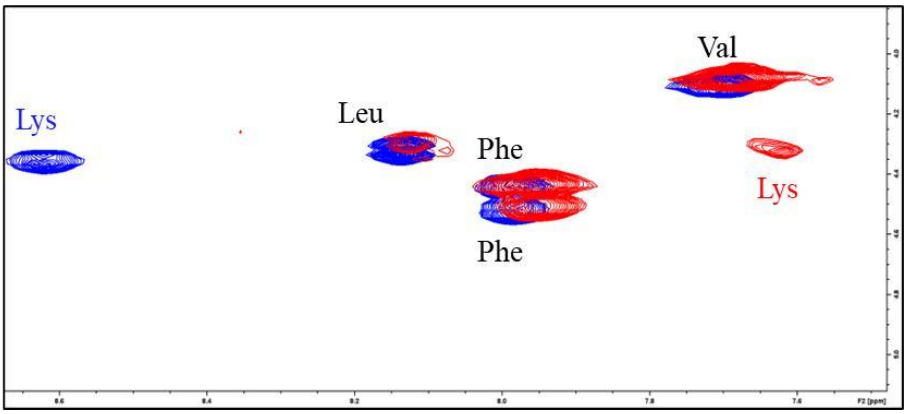

Figure 4.6. COSY spectrum of MnPOM-KLVFF and Ala(N_3)-KLVFF-NH_2

FTIR and ESI-MS analysis were utilized to characterized POM-hybrid. In the Figure 4.7A, the stretching bonds of Ar-C=C, C=N, and N=N were obtained at 1652, 1540 and 1455 cm^{-1}, separately, which are the typical peak of MnPOM-KLVFF as well. ESI-MS (-) (CH_3CN) shows the presence of mono-charged species, without TBA cations signals at m/z =1435.1 (m/z calcd. for $[M-3TBA]^-$= 1436).

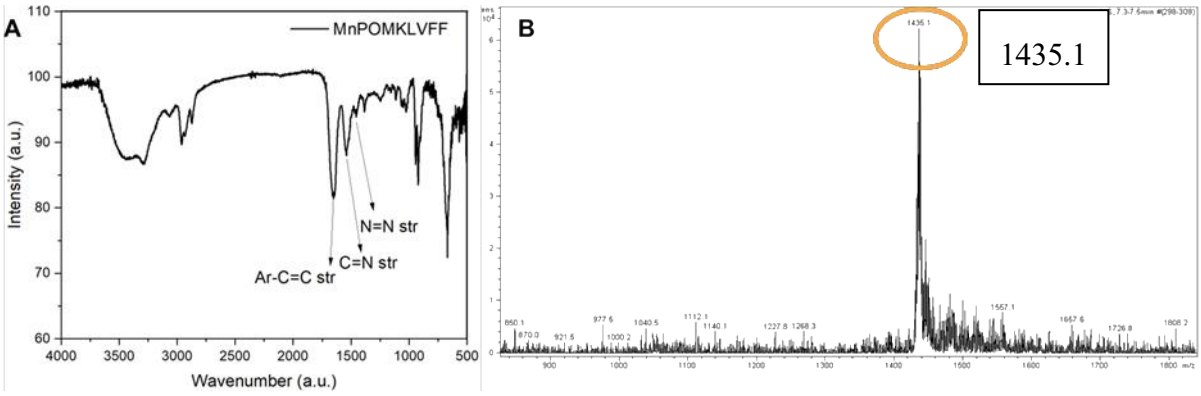

Figure 4.7. FTIR and ESI-MS analysis of MnPOM-KLVFF.

Figure 4.8A shows that the pure peptide Ala(N_3)-KLVFFNH_2 forms net-like aggregations of a significant size. However, after conjugation with MnPOM, Figure 4.8B reveals the presence of fiber-like structures along with some nano-sized spherical particles dispersed within. This indicates that the involvement of POM alters the initial structure of the peptide, which may offer a further evidence of the successful synthesis of MnPOM-hybrids.

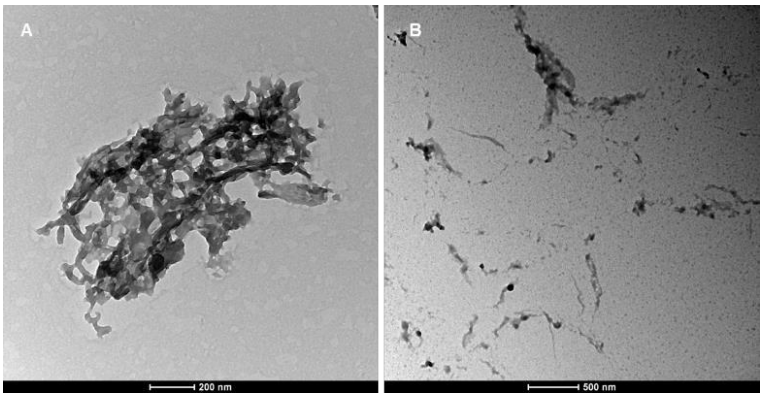

Figure 4.8. Transmission electron microscopy (TEM) technique of (A) Ala(N_3)-KLVFF-NH_2, bar:200nm and (B)MnPOM-KLVFF, bar: 500 nm.

Conclusion

POM was functionalized with a short peptide KLVFF that can recognize Amyloid β (Aβ) peptides, which play a key role in Alzheimer's disease (AD). From all data, (i) Ala(N_3)-KLVFF-NH_2 was synthesized by solid phase peptide synthesis method, and purified by HPLC. (ii) Chemical bonds between MnPOMs and Ala(N_3)-KLVFF-NH_2 were confirmed by NMR, ESI, CD, UV-vis and FT-IR. (iii) In order to study the biological effects of the hybrid POM, in vitro experiments are ongoing on drosophila, as a model animal for neurodegenerative disorders.

Chapter 5: INSTRUMENTS AND METHODS

5.1 INSTRUMENTS AND MATERIALS

Circular Dichroism:

Instruments Circular Dichroism For the CD analysis a concentrated TFE solution (250 μM for the peptides and 125 μM for the hybrids) of each compound was prepared in a 2 mL flask. Eventually, the solution was diluted in the cuvette with different TFE/H2O ratios until a concentration of either 25 μM (peptides) or 12.5 μM (hybrids) was obtained. The measurements were carried out using a Jasco J-1500 instrument at 25°C in a cuvette and performing 16 accumulations per sample. The chosen wavelength range is 250-190 nm, the data pitch is 0.2 nm, the D.I.T. 1 sec and the scanning speed is 50 nm/min. The obtained spectra were processed with Spectra Manager software supplied by Jasco. The software CDApps (Diamond Light Source) was used to evaluate of secondary structure.

NMR Spectroscopy:

Two-dimensional 1H NMR data were acquired using a Bruker Avance DMX 600 and 400 MHz spectrometers, while monodimensional 1H NMR and 51V NMR (78.9 MHz) data were collected with a Bruker 300 MHz UltraShield instrument. Deuterated DMSO and acetonitrile served as the solvents for the analyses. The analysis of NMR spectra was conducted using MestReNova and TopSpin software.

Electrospray Ionization Mass Spectroscopy:

Mass spectrometry (MS) measurements were conducted employing an LC/MSD Trap SL instrument, which was equipped with an Agilent Technologies electrospray (ESI) source. The samples were

dissolved in acetonitrile (ACN) and analyzed in negative ionization mode. Subsequent analysis of the MS spectra was performed using the Data Analysis software provided by Bruker.

Infrared Spectroscopy:

Infrared Spectroscopy IR measurements (400-4000 cm^{-1}) were performed on a Jasco FT/IR-4100 spectrophotometer, with samples prepared as KBr pellets. The spectra executed using Jasco Spectra Manager 2.00.07.

UV-vis measurements:

UV-visible (UV-vis) measurements were conducted using two instruments: simultaneously on the CD Jasco J-1500 instrument, employing the same parameters as the CD analysis, and the Varian Cary® 50 – Agilent instrument with a 1 cm path quartz cuvette. The data obtained from the latter instrument were processed using the Cary WinUV Application Software.

The peptides' purity was assessed through an analytical HPLC system from Shimadzu, comprising two LC-10-ΔD UP pumps, an SCL-10A VP controller, an SPD-10A Shimadzu UV-Vis detector, a Gastorr 154 degasser, and an SIL-9A Shimadzu autoinjector. ChromNAV software (Jasco) was employed for data acquisition and processing. Elution was performed on a Phenomenex Jupiter C18 column with a 300Å pore size, 10 μm particle size, and dimensions of 250x4.60 mm, utilizing a linear gradient between two solvents: (A) 0.05% TFA in H2O and (B) 0.05% TFA in a 9:1 v/v ACN:H2O mixture.

Purification and characterization of peptides

The peptides' purity was assessed through an analytical HPLC system from Shimadzu, comprising two LC-10-ΔD UP pumps, an SCL-10A VP controller, an SPD-10A Shimadzu UV-Vis detector, a Gastorr 154 degasser, and an SIL-9A Shimadzu autoinjector. ChromNAV software (Jasco) was employed for data acquisition and processing. Elution was performed on a Phenomenex Jupiter C18/C5 column with a 300Å pore size, 10 μm particle size, and dimensions of 250x4.60 mm, utilizing

a linear gradient between two solvents: (A) 0.05% TFA in H2O and (B) 0.05% TFA in a 9:1 v/v ACN:H2O mixture.

Purification of the synthesized peptides was carried out using a Shimadzu preparative HPLC system equipped with two LC-8A pumps, a UV-SPD-6A spectrophotometric detector, an ERC 3562 ERMA degasser, and a recorder. Separation was accomplished on a VYDAC C18/C5 column with a 300 Å pore size, 10 μm particle size, and dimensions of 250x22 mm. The eluent system was identical to that employed in the analytical HPLC. Fractions containing the desired product were subsequently freeze-dried using an Edwards Freeze Dryer Modulyo freeze-drier.

Mass analysis was conducted on an Agilent Technologies 1260 Infinity II LC-MS spectrometer equipped with a 6130 Quadrupole and an ESI ionization system.

Electron microscope

TEM images were recorded on a Jeol 300 PX electron microscope.

MATERIALS

If not specified, all reagents and solvents were obtained from commercial sources and were used without further purification. For all the syntheses and solution, only MilliQ water has been used.

5.2 METHODS AND CHARACTERIZATIONS

Synthesis 1A

H-fQWAVGHLNHEt peptide 1

The Fmoc-based synthetic strategy was utilized for manual solid-phase synthesis of the peptide. Loading was achieved on Fmoc-deprotected ethyl-indole AM resin using equimolar HATU as the coupling reagent in the presence of a two-fold molar excess of DIPEA, with Fmoc-Leu-OH (0.24 mmol). For each coupling step, a three-fold molar excess (0.24 mmol) of Fmoc-amino acids was used, with HBTU/HOBt as the coupling reagents, and the reaction time was 40 min. The Fmoc group was

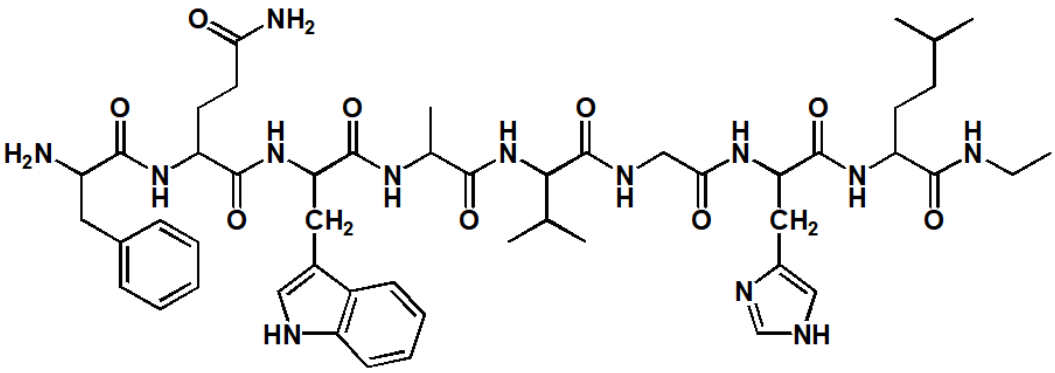

Figure 5.1 The structure of peptide 1.

(D-)Phe-Gln-Trp-Ala-Val-Gly-His-Leu-NHEt

removed using 20% piperidine in DMF. The peptide was then detached from the resin and all the side-chain protecting groups of the amino acid residues were removed using TFA/anisole/triisopropylsilane/H_2O (95:2.5:2.0:0.5 v/v) for 45 min. The crude product was purified using preparative HPLC with a Vydac C18 column (300Å, 10µ, 250 x 22 mm) and a linear gradient elution (eluent A: 0.05% TFA in H_2O; eluent B: 0.05% TFA in 9:1 v/v CH_3CN/H_2O). The yield was 51%. ESI MS (+) in MeOH. m/z =984.5 is the peak of peptide. ($[M+H]^+$calculated = 984.5.)

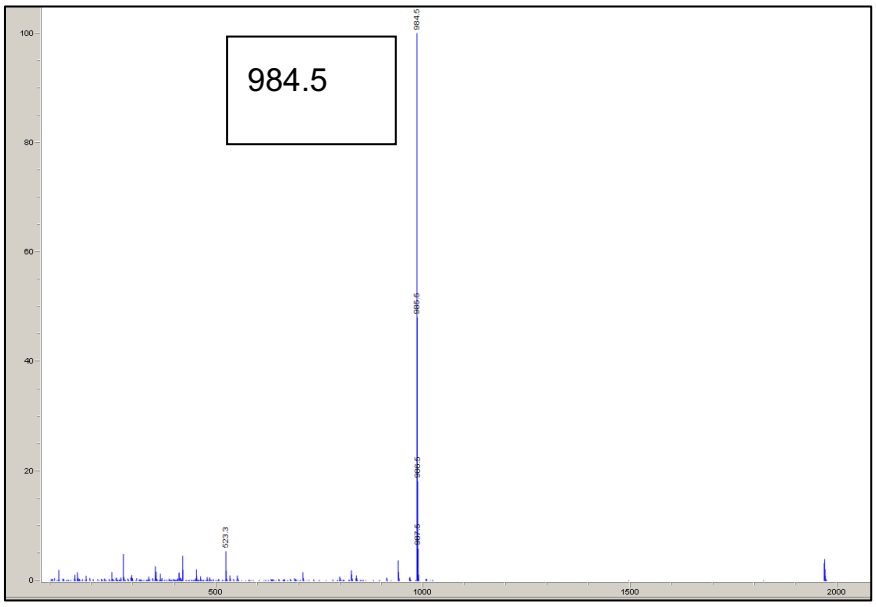

Figure 5.2 ESI-MS (+) spectrum of peptide 1 in MeOH

Table 5.1 Proton resonances of fQWAVGHL-NHEt (0.6 μM d6-DMSO solution).

AA	NH (ppm)	CHα (ppm)	Rest of the chain(ppm)
Phe	/	4.07	-CH2β 2.97 Aromatics 7.27
Gln	8.55	4.33	-CH2β (diastereotopic) 1.78 1.62 -CH2γ 1.95 -NH2 not detected
Trp	8.30	4.56	-CH2β (diastereotopic) 3.11, 2.91 Unassigned aromatics
Ala	8.25	4.41	-CH3 1.20
Val	7.77	4.17	-CHβ 1.97 (-CH3γ)2 0.85
Gly	8.23	-CH2α 3.72, 3.79	/
His	8.13	4.61	-CH2β 3.03 -NH aromatics not detected -CH Unassigned aromatics
Leu	8.09	4.20	-CH2β 1.48 -CHγ 0.86 (-CH3δ)2 not detected
NHEt	8.04	-CH2α 3.08	-CH3β 1.01

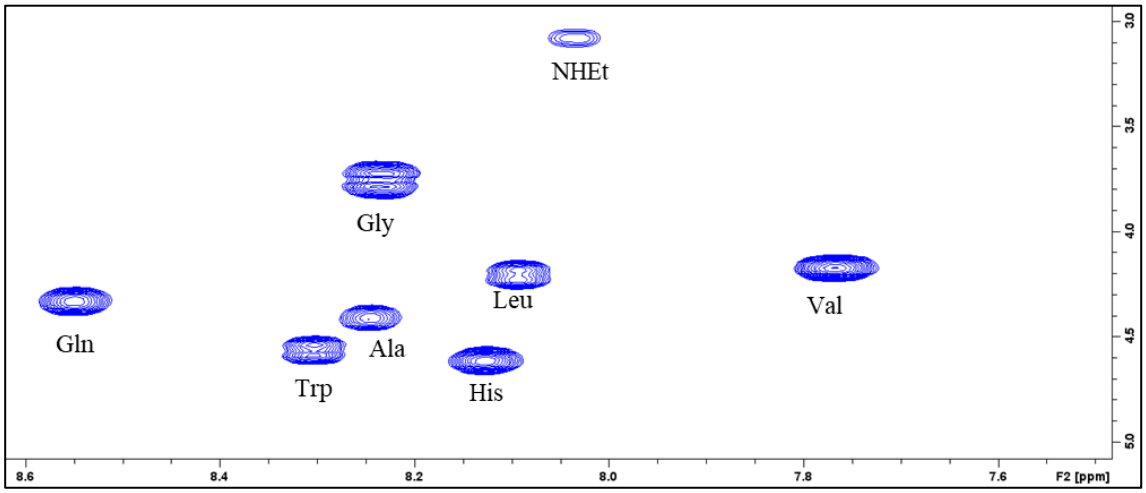

Figure 5.3 2D-1H-NMR spectrum of peptide1 (150 µM) in d6-DMSO. COSY spectra of peptide 1.

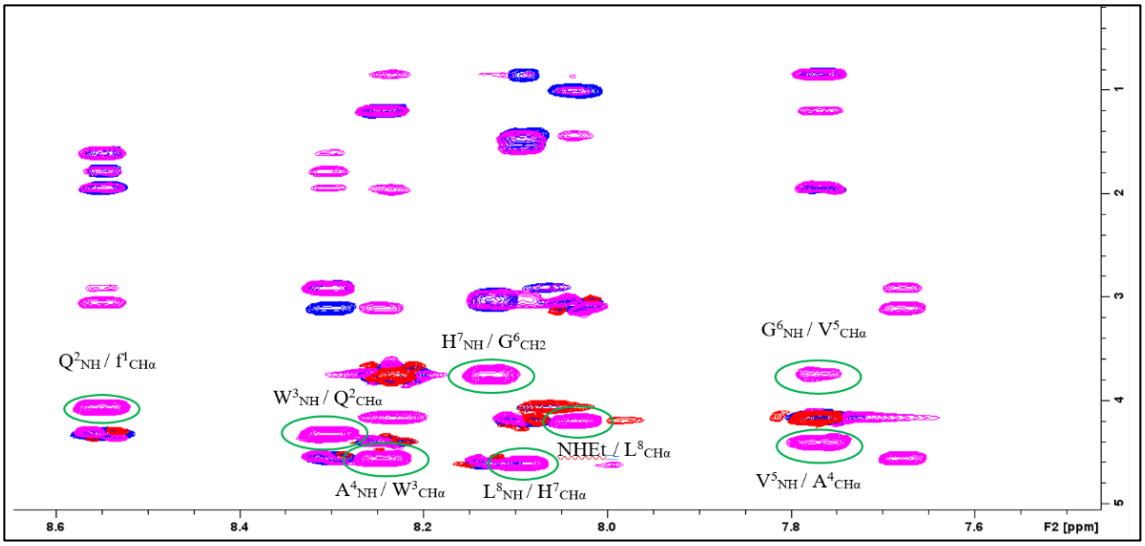

Figure 5.4 2D-^{1}H-NMR spectrum of peptide1 (150 µM) in d6-DMSO. TOCSY spectra (blue) and ROESY (pink), cross peak region.

Synthesis 2A:

H- EEEEA-fQWAVGHL-NHEt peptide 2

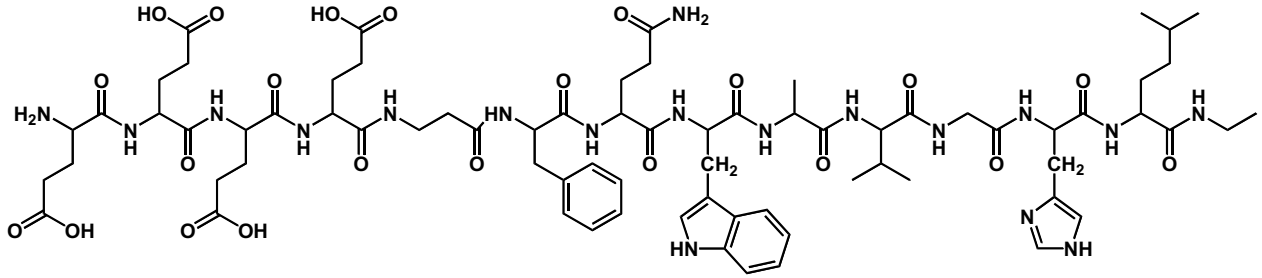

H-Glu-Glu-Glu-Glu-βAla-D-Phe-Gln-Trp-Ala-Val-Gly-His-Leu-NH-Et

Figure 5.5 The structure of peptide 2.

To mitigate peptide-POM interaction, a polyanionic spacer composed of four glutamic acid residues was added to a second DB analogue. This linker creates charge repulsion with the negatively charged POM. Additionally, an extra β-alanine residue was introduced to enhance flexibility. Compound 2 was synthesized according to the procedure previously described. The peptide was then detached from the resin, cleavage solution was then evaporated under nitrogen flow, and the desired peptide was precipitated by adding diethyl ether to the solid residue and centrifuging the mixture (5000 rpm for 10 minutes). The supernatant was removed, and the peptide was dissolved in water, filtered to remove any insoluble resin, and freeze-dried. The crude product was then purified by preparative HPLC system (Shimadzu, Tokyo, Japan) equipped with LC-8A pumps, SCL-8A controller and SPD-6A spectrophotometric detector, using a linear gradient (eluent A: 0.05% TFA in H_2O; eluent B: 0.05% TFA in 9:1 v/v CH_3CN-H_2O; 22% B for 3 min; flow 12 mL/min), and a Vydac C18 column (300Å, 10μ, 250 x 22 mm). The yield is 79%

ESI MS (+) in MeOH, the peaks of peptide are present. ($[M+H]^+$calculated = 1571.7, [M+H]+ found = 1571.7 m/z; $[M+3H]^{3+}$calculated = 524.6 Da, $[M+3H]^{3+}$found = 523.3 m/z

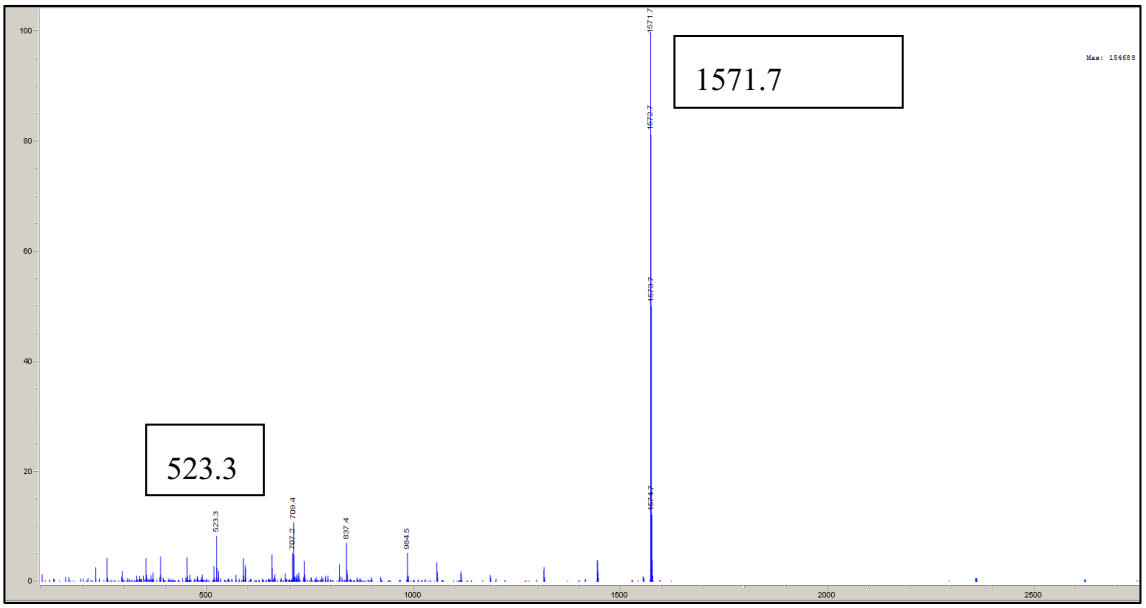

Figure 5.6 ESI-MS (+) spectrum of peptide 2 in MeOH.

Table 5.2 Proton resonances of H- EEEEA-fQWAVGHL-NHEt peptide (0.6 µM d6-DMSO solution).

AA	NH (ppm)	CHα (ppm)	Rest of the chain(ppm)
Glu2	8.62	4.35	-CH2β 2.30 -CH2γ 1.77
Glu3	8.21	4.25	-CH2β 2.25 -CH2γ 1.74
Glu4	8.01	4.15	-CH2β 2.19 -CH2γ 1.72
βAla	7.93	-CH2α 3.11, 3.21	-CH2β 2.26
			-CH2β (diastereotopico)

D-Phe	8.27	4.45	2.93, 2.78 Aromatics not observed
Gln	8.36	4.10	-CH2β 1.89 -CH2γ 1.58
Trp	8.01	4.48	-CH2β (diastereotopico) 3.07 Unassigned aromatics
Ala	7.97	4.37	-CH3 1.21
Val	7.61	4.14	-CHβ 1.97 (-CH3γ)2 0.85
Gly	8.24	-CH2α 3.70, 3.77	/
His	8.08	4.61	-CH2β 3.00 -NH aromatic not detected -CH Unassigned aromatics
Leu	8.07	4.20	-CH2β 1.47 -CHγ 0.85 (-CH3δ)2 not detected
NHEt	8.04	-CH2α 3.08	-CH3β 1.00

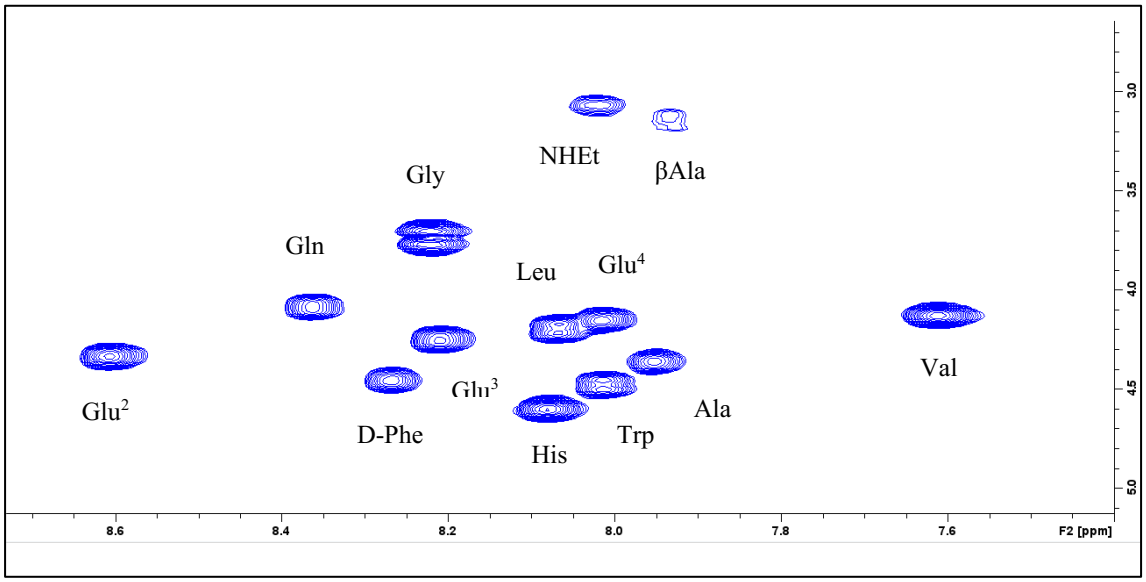

Figure 5.7 2D-^{1}H-NMR spectrum of peptide2 (150 µM) in d6-DMSO. COSY spectra of peptide 2.

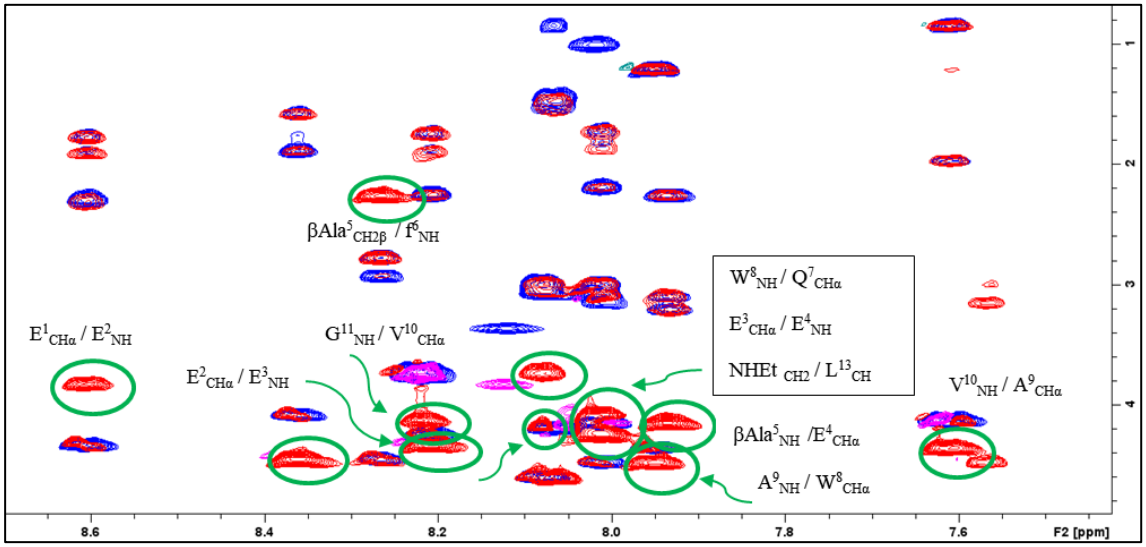

Figure 5.8 2D-^{1}H-NMR spectrum of peptide 2 (150 µM) in d6-DMSO. ROESY of DB-βAlaEEEE (in red) overlapped with TOCSY (in blue), cross peak region.

Synthesis 3A

Ttds-fQWAVGHL-NHEt peptide 3

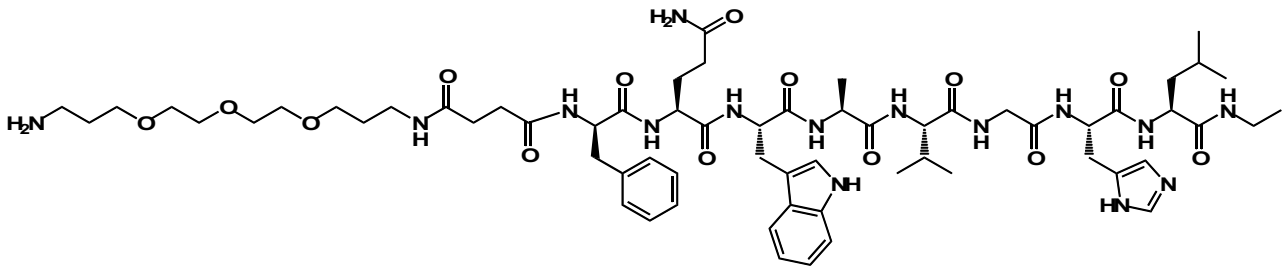

H-Ttds-D-Phe-Gln-Trp-Ala-Val-Gly-His-Leu-NH-Et

Figure 5.9 The structure of peptide 3.

The addition of the customized PEG-like linker, trioxatridecan-succinamic acid (Ttds), resulted in the synthesis of an analog of the DB (3) compound. Ttds is a biocompatible and non-toxic substance that enhances water solubility, increases stability, and elicits minimal immune response. Compound 3 was synthesized according to the procedure previously described. The crude product as then purified by preparative HPLC system. The yield is 32%. ESI MS (+) in MeOH, at m/z =1286.7 and 644.3, the peaks of peptide are present ($[M+H]^+$ calculated= m/z =1286.7 and $[M+2H]^{2+}$ calculated = 643.8).

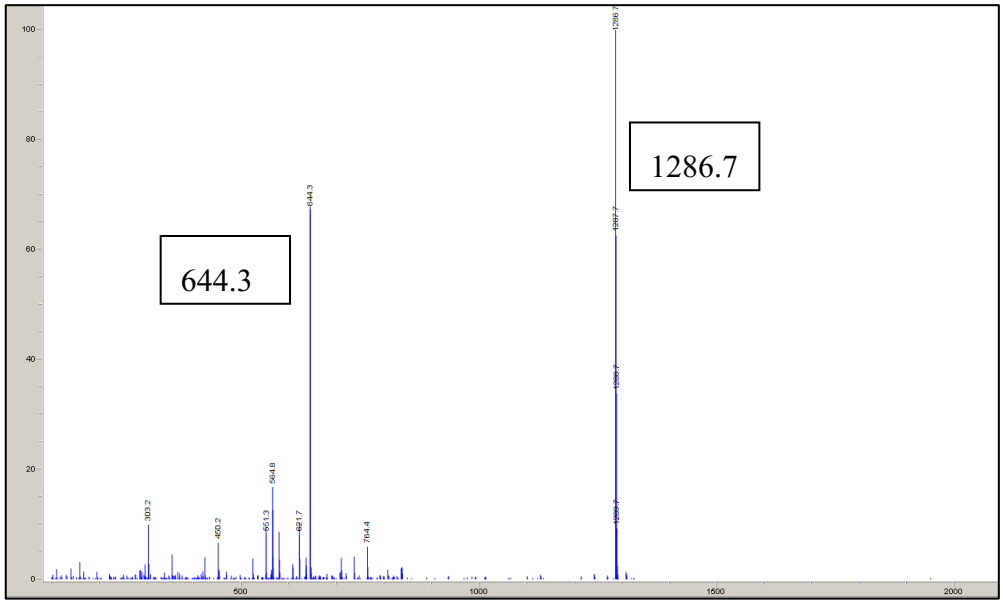

Figure 5.10 ESI-MS (+) spectrum of peptide 3 in MeOH.

Table 5.3 Proton resonances of Ttds-fQWAVGHL-NHEt peptide (0.6 μM d6-DMSO solution).

AA	NH (ppm)	CHα (ppm)	Rest of the chain(ppm)
D-Phe	8.25	4.41	-CH2β (diastereotopico) 2.78, 2.95 Aromatics not observed
Gln	8.34	4.07	-CH2β (diastereotopico) 1.90, 1.77 -CH2γ 1.59
Trp	7.98	4.46	-CH2β (diastereotopico) 3.00, 3.16 Unassigned aromatics
Ala	7.90	4.35	-CH3 1.21
Val	7.61	4.13	-CHβ 1.98

			(-CH3γ)2 0.85
Gly	8.22	-CH2α 3.70, 3.76	/
His	8.08	4.60	-CH2β 3.02 -NH aromatic not detected -CH Unassigned aromatics
Leu	8.06	4.20	-CH2β 1.47 -CHγ 0.85 (-CH3δ)2 not detected
NH-Ttds	7.79	-CH2α 3.03	-CH2β 1.58 -CH2γ 3.35
NHEt	8.02	-CH2α 3.06	-CH3β 1.01
NH3+ term	7.64	-CH2α 2.84	-CH2β 1.76 -CH2γ 3.46

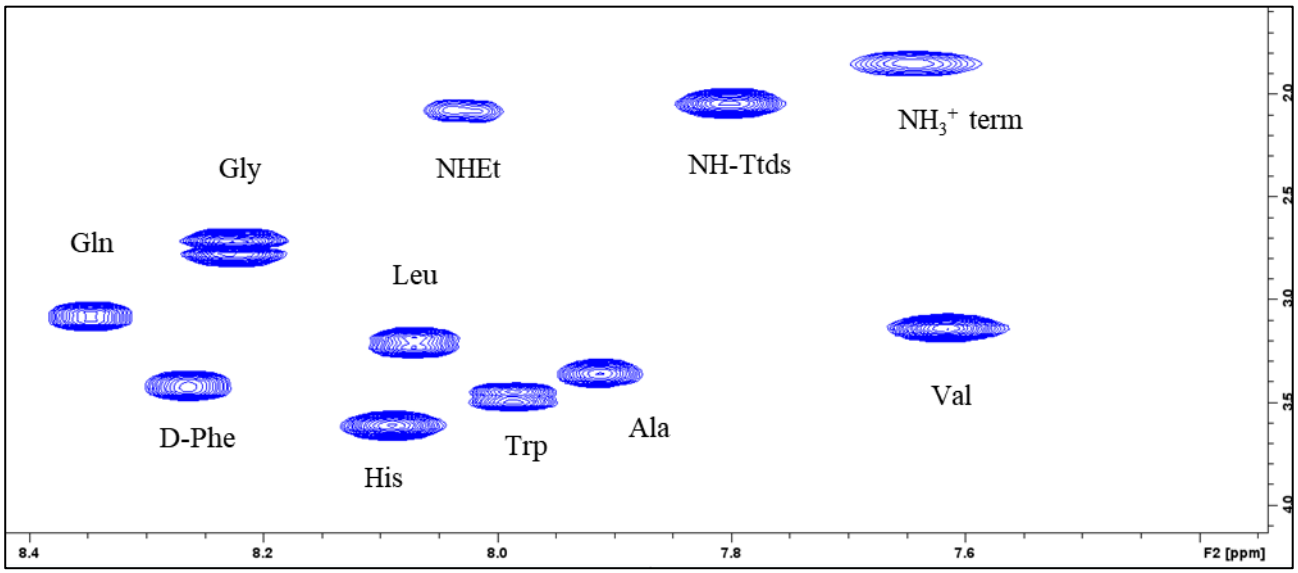

Figure 5.11 2D-^{1}H-NMR spectrum of peptide3 (150 µM) in d6-DMSO. COSY spectra of peptide 3.

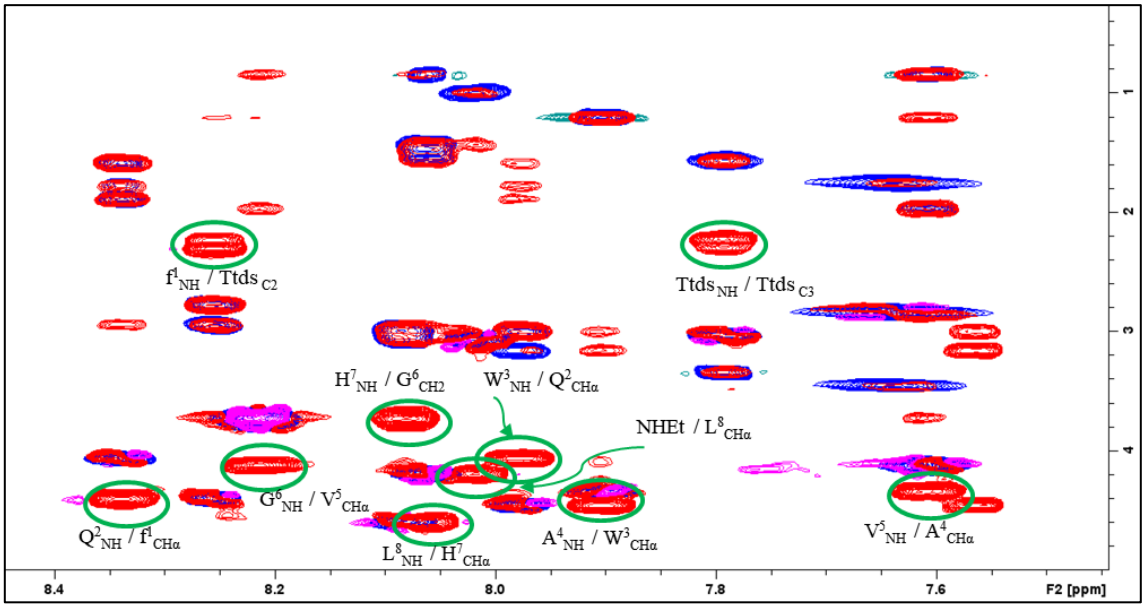

Figure 5.12 2D-^{1}H-NMR spectrum of peptide 3 (150 µM) in d6-DMSO. ROESY of 3 (in red) overlapped with TOCSY (in blue), cross peak region.

Synthesis 4A

Ttds- EEEEA-fQWAVGHL-NHEt peptide 4

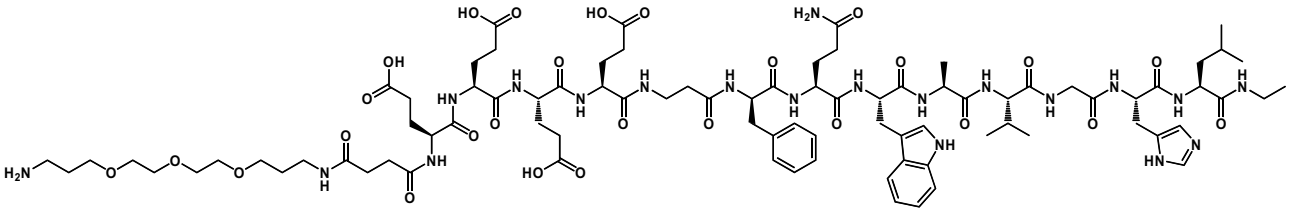

H-Ttds- Glu-Glu-Glu-Glu-βAla-D-Phe-Gln-Trp-Ala-Val-Gly-His-Leu-NH-Et

Figure 5.13 the structure of peptide 4.

To mitigate peptide-POM interaction and improve water solubility, A DB analogue (4) was synthesized by adding four glutamic acid residues and the tailored PEG-like spacer trioxatridecan-succinamic acid (Ttds). The yield is 46%. At m/z =1873.2 the peak of charged peptide is present (m/z =1874.1 calc. for $[M+H]^{+}$ and At m/z= 937.3(m/z =938.0 calc. for $[M+2H]^{2+}$)

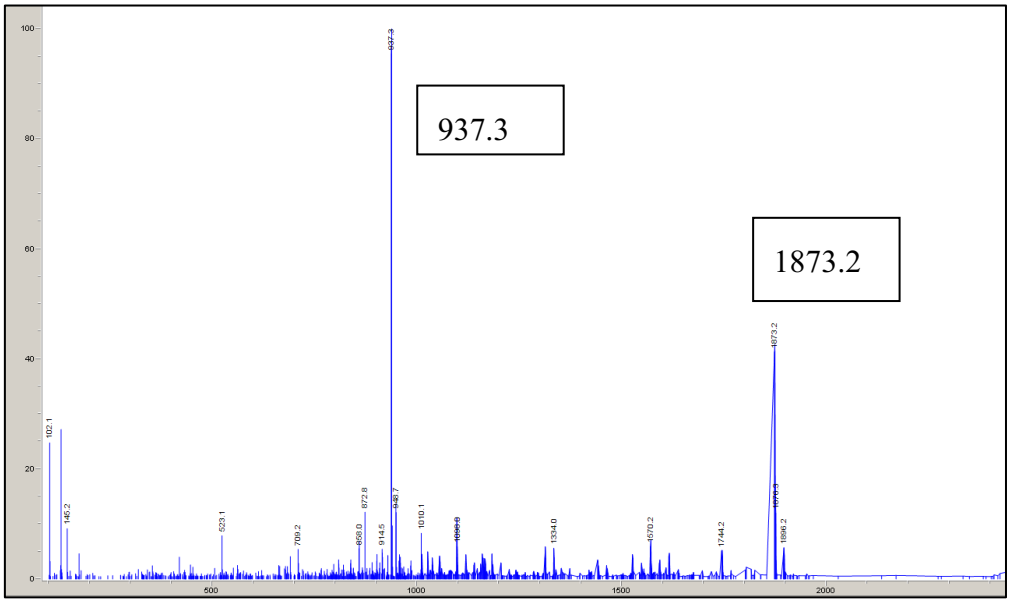

Figure 5.14 ESI-MS (+) spectrum of peptide 4 in MeOH.

Table 5.4 Proton resonances of Ttds- EEEEβAla-fQWAVGHL-NHEt peptide

AA	NH (ppm)	CHα (ppm)	Rest of the chain(ppm)
Glu1	8.18	4.17	-CH2β 2.26 -CH2γ 1.82
Glu2	8.09	4.19	-CH2β 2.27 -CH2γ 1.87
Glu3	7.83	4.20	-CH2β 2.25 -CH2γ 1.83
Glu4	7.79	4.13	-CH2β 2.20 -CH2γ 1.79
βAla	7.83	-CH2α 3.11, 3.21	-CH2β 2.26
			-CH2β (diastereotopico)

D-Phe	8.28	4.44	2.93, 2.78 Aromatics not observed
Gln	8.37	4.08	-CH2β 1.82 -CH2γ 1.57
Trp	8.01	4.48	-CH2β (diastereotopico) 3.01, 3.16 Unassigned aromatics
Ala	7.95	4.36	-CH3 1.21
Val	7.61	4.13	-CHβ 1.98 (-CH3γ)2 0.86
Gly	8.23	-CH2α 3.71, 3.75	/
His	8.07	4.61	-CH2β 3.03 -NH aromatic not detected -CH Unassigned aromatics
Leu	8.06	4.19	-CH2β 1.49 -CHγ 0.86 (-CH3δ)2 not detected
NH-Ttds	7.90	3.06	-CH2β 1.60 -CH2γ 3.37
NH3+ term	7.61	-CH2α 2.85	-CH2β 1.77 -CH2γ 3.47
NHEt	8.03	-CH2α 3.08	-CH3β 1.00

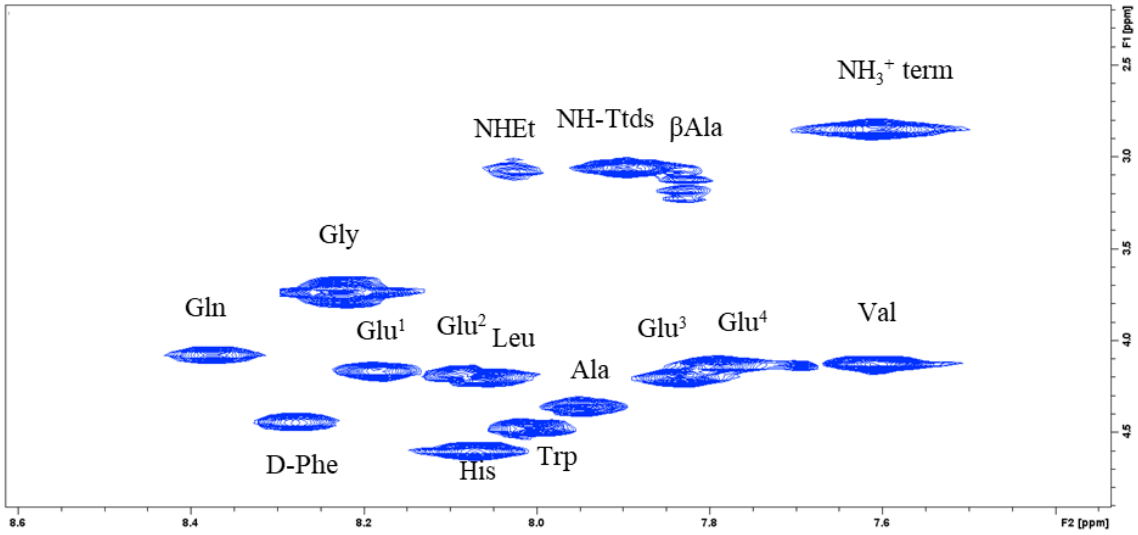

Figure 5.15 2D-^{1}H-NMR spectrum of peptide 4 (150 µM) in d6-DMSO. COSY spectra of peptide 4

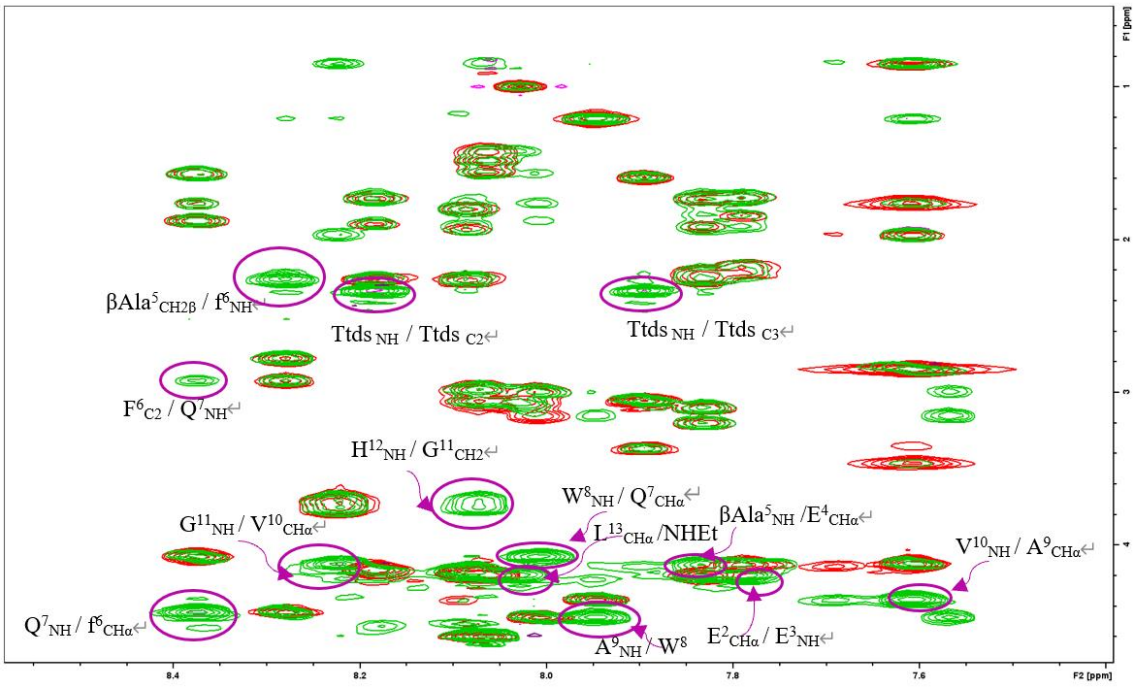

Figure 5.16 2D-1H-NMR spectrum of peptide 4 (150 µM) in d6-DMSO. ROESY of 4 (in green) overlapped with TOCSY (red), cross peak region.

SYNTHESIS 5A:

Synthesis of "TBA-Mo_8O_{26}" Compounds 1

$[(C_4H_9)_4N]_4[Mo_8O_{26}]$

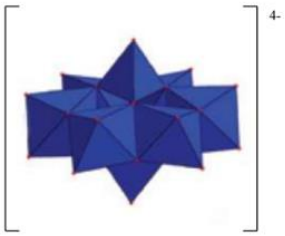

Reaction:

$$12HCl + MoNa_2O_4 \cdot 2H_2O + 4C_{16}H_{36}BrN \rightarrow [(C_4H_9)_4N]_4[Mo_8O_{26}] + 12NaCl + 4NaBr + 6H_2O$$

Procedure:

$MoNa_2O_4 \cdot 2H_2O$ (4.20g, 0.017mol) was dissolved in 10 mL of H_2O in a flask, and TBA-Br (2.8515g, $8.85x10^{-3}$ mol) was dissolved in 8 mL of H_2O in a beaker. 6.8 mL of HCl 3.8375M were added to the colorless solution of $MoNa_2O_4 \cdot 2H_2O$ under stirring, and then the solution of TBA-Br was added dropwise to the mixture under vigorous stirring with the immediate production of a white precipitate. The solid was filtered on a fitted funnel under vacuum and then washed with 30 mL of water, 20 mL of ethanol and 20 mL of diethyl ether. After 10 minutes the white precipitate was transferred in a round-bottom flask, dried under vacuum at first at the rotatory evaporator and finally with high vacuum pump. A white powder solid was obtained (MM = 2153.35 g/mol, 4.6782 g, 90% yield).

Analysis & Characterization:

FTIR (KBr, cm^{-1}): 3443 (w, br), 2963 (s), 2938 (s), 2873 (s), 1634 (w), 1483 (s), 1462 (m), 1381 (m), 1348 (w), 1153 (w), 951 (m), 924 (s), 909 (s), 853 (m), 806 (s), 663 (s), 599 (m), 501 (w).

ESI-MS (-) CH_3CN: 1913.7 ($[M\text{-}TBA]^-$), 1665.5 ($[M\text{-}2TBA+H]^-$), 833.8 ($[M\text{-}2TBA]^{2-}$).

SYNTHESIS 6A:

Synthesis of "Mn-Anderson TRIS" Compounds 2

$[(C_4H_9)_4N]_3[MnMo_6O_{18}\{(OCH_2)_3CNH_2)_2]$

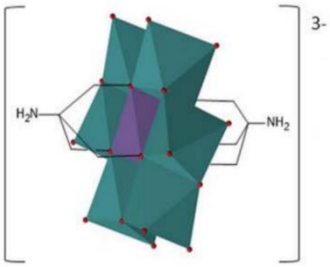

Reaction:

$$3\ [(C_4H_9)_4N]_4[\alpha\text{-}Mo_8O_{26}] + 4Mn(O_2CCH_3)_3 + 8(HOCH_2)_3CNH_2 \xrightarrow[ACN,\ 80°C,\ 22\ hours]{}$$

$$[(C_4H_9)_4N]_3[MnMo_6O_{18}\{(OCH_2)_3CNH_2)_2] + 12CH_3COOH + 6H_2O$$

Procedure:

$[(C_4H_9)_4N]_4[\alpha\text{-}Mo_8O_{26}]$ (3.02g, $1.40x10^{-3}$ mol), $Mn(O_2CCH_3)_3$ (0.56893g, $2.12x10^{-3}$ mol) and $(HOCH_2)_3CNH_2$ (0.62702g, $5.22x10^{-3}$ mol) were dissolved in 75 mL of acetonitrile in a round-bottom flask and heated at 80°C for 22 hours with a reflux condenser attached to it. The day after the brown solution was cooled at room temperature and filtered twice until a red-orange solution was obtained. The solution was put under vacuum on the rotary evaporator until a milk color precipitate was obtained and it was again removed through filtration. The dark orange solution was put under diethyl ether atmosphere for 3 days until an orange solid was obtained. The orange crystals were recovered and washed multiple times with diethyl ether, then dried under vacuum with the rotary evaporator and finally high vacuum pump (MM = 1882.24 g/mol, 1.43 g, 41% yield).

Analysis & Characterization:

FTIR (KBr, cm^{-1}): 3444 (m, br), 2960 (s), 2943 (s), 2873 (s), 2360 (w), 1646 (s), 1480 (s), 1381 (m), 1039 (s), 939 (s), 919 (s), 902 (s), 800 (w), 663 (s), 562 (m), 460 (m), 411 (w).

ESI-MS (-) CH_3CN: 1639.7 ($[M\text{-}TBA]^-$), 1518 ($[2M\text{-}3TBA+H]^{2-}$), 1397.6 ($[M\text{-}2TBA+H)^-$], 698.5 ($[M\text{-}2TBA]^{2-}$).

SYNTHESIS 7A:

Synthesis of "POM-SUCC" Compounds 3

$[(C_4H_9)_4N]_3[MnMo_6O_{18}\{(OCH_2)_3CNHCO(CH_2)_2COOH\}_2]$

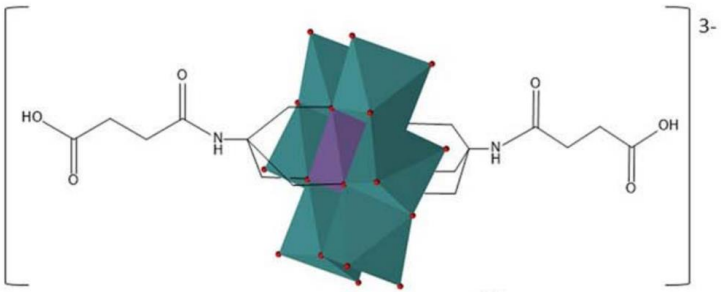

Reaction:

$$[(C_4H_9)_4N]_3[MnMo_6O_{18}\{(OCH_2)_3CNH_2)_2] + 2C_4H_4O_3 \xrightarrow[DMF,\ 50°C,\ 24\ hours]{}$$

$$[(C_4H_9)_4N]_3[MnMo_6O_{18}\{(OCH_2)3CNHCO(CH_2)_2COOH\}_2]$$

Procedure:

POM-TRIS (0.73228g, $3.89x10^{-3}$ mol) was dissolved in 8 mL of DMF in a vial, and succinic anhydride $C_4H_4O_3$ was added (0.78875g, $7.78x10^{-3}$ mol). The orange reaction mixture was stirred at 50°C for one day without any noticeable color change. The solution was then cooled at room

temperature and crystallized under diethyl ether atmosphere. After 1 day, the orange crystals were recovered and washed multiple times with diethyl ether, then dried under vacuum. (MM = 2082,32 g/mol, 0.70440g, 86% yield).

Analysis & Characterization:

FTIR (KBr, cm^{-1}): 3386 (m, br), 3072 (m), 2962 (s), 2943 (s), 2875 (m), 1718 (m), 1684 (s), 1540 (m), 1483 (m), 1382 (w), 1183 (w), 1068 (w), 1025 (m), 942 (s), 920 (s), 814 (w), 665 (s), 564 (w), 460 (w).

ESI-MS (-) CH_3CN: 2082.0 ($[M-H]^-$), 1839.8 ($[M-TBA]^-$), 1717.3 ($[2M-3TBA+H]^{2-}$), 1597.7 ($[M-2TBA+H]^-$), 1148 ($[2M-3TBA]^{3-}$).

SYNTHESIS 8A:

Synthesis of "POM-NHS" Compounds 4

$[(C_4H_9)_4N]_3[MnMo_6O_{18}\{(OCH_2)_3CNHCO(CH_2)_2CO(C_4H_4NO_3)\}_2]$

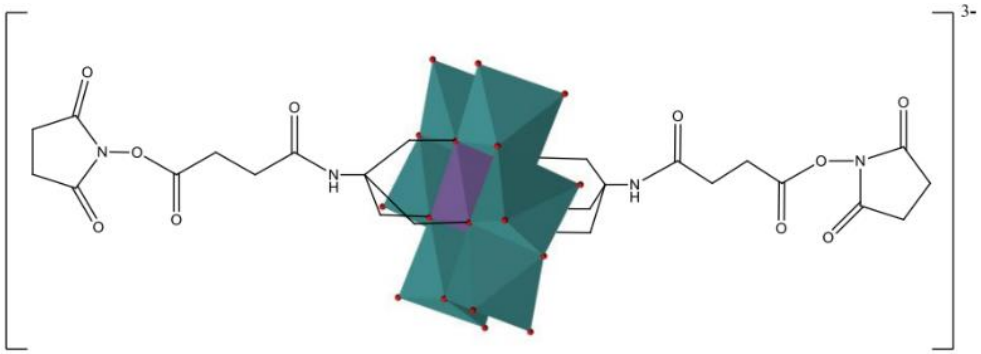

Reaction:

$$[(C_4H_9)_4N]_3[MnMo_6O_{18}\{(OCH_2)_3CNHCO(CH_2)_2COOH\}_2] + 2\ C_4H_5NO_3 \xrightarrow[DMF,\ R.T.,\ 24\ h.]{DCC}$$

$[(C_4H_9)_4N]_3[MnMo_6O_{18}\{(OCH_2)_3CNHCO(CH_2)_2CO(C_4H_4NO_3)\}_2]$

Procedure:

POM-SUCC (70.55 mg; 0,0339 mmol) was dissolved 1.5 mL of DMF in a vial. In order, NHS (18.08 mg, 0.15 mmol) and DCC (44.72 mg, 0.21 mmol) were added to the reaction mixture, and the orange solution was stirred for 24 hours at room temperature. The day after, the orange solution was centrifuged to remove a minor white precipitate and it was put under diethyl ether atmosphere to crystallize. After a few hours the orange needle-shaped crystals were recovered and washed with approximately 1.5 mL of diethyl ether for three times, dried under vacuum, and finally weighted (MM = 2276.55 g/mol, 0,018 mmol, 54% yield).

Analysis & Characterization:

FTIR (KBr, cm^{-1}): 3497 (m, br), 3271 (m), 3224 (m), 3062 (m), 2961 (s), 2935 (s), 2872 (s). 2119 (m), 1814 (m), 1782 (m), 1739 (s), 1660 (s), 1553 (m), 1484 (m), 1414 (w), 1387 (m), 1331 (w), 1225 (w), 1210 (m), 1150 (w), 1098 (s), 1061 (s), 1028 (s), 939 (s), 917 (s), 902 (s), 810 (w), 668 (s), 561 (m), 516 (w), 458 (w), 407 (w).

ESI-MS (-) CH_3CN: 2033.7 ($[M\text{-}TBA]^-$), 1793.6 ($[M\text{-}2TBA+H]^-$), 1553.4 ($[M\text{-}3TBA+2H]^-$), 516.4 ($[M\text{-}3TBA]^{3-}$)

SYNTHESIS 9A:

Synthesis of "$MnMo_6$ POM – L-Phe" Compounds 5

$[(C_4H_9)_4N]_3[MnMo_6O_{18}\{(OCH_2)_3CNHCO(CH_2)_2COPheOMe\}_2]$

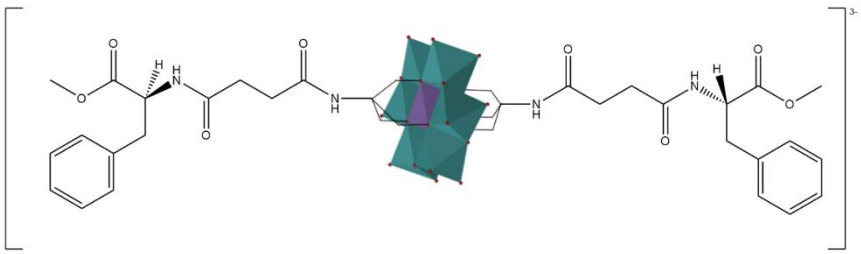

Reaction:

$[(C_4H_9)_4N]_3[MnMo_6O_{18}\{(OCH_2)_3CNHCO(CH_2)_2CO(C_4H_4NO_3)\}_2]$ + 2L-PheOMe·HCl

$\xrightarrow[DMF\ R.T.]{DIPEA}$ $[(C_4H_9)_4N]_3[MnMo_6O_{18}\{(OCH_2)_3CNHCO(CH_2)_2COPheOMe\}_2]$

Procedure:

POM-NHS (42.06 mg; 0.0185 mmol) has been dissolved in 1.5 mL of DMF in a vial. In order, L-PheOMe·HCl (9.50 mg, 0.044 mmol) and DIPEA (33 mg, 44 µL, 0.25 mmol) were added to the reaction mixture, and the orange solution was stirred for 24 hours at room temperature. The day after the vial was put under diethyl ether atmosphere to crystallize. After a few hours the orange greasy product was recovered and washed with approximately 1.5 mL of diethyl ether for three times and then dried under vacuum, and finally weighted (MM = 2404.86 g/mol, 0.034 g, 54% yield).

Analysis & Characterization:

FTIR (KBr, cm^{-1}): 3441 (m, br), 3372 (m), 3279 (m), 2961 (s), 2874 (m), 1738 (m), 1664 (s), 1543 (m), 1483 (m), 1384 (w), 1220 (w), 1064 (m), 1028 (m), 941 (s), 920 (s), 742 (w), 669 (s), 562 (w).

ESI-MS (-) CH_3CN: 2161.0 ($[M\text{-}TBA]^-$), 2042.9 ($[2M\text{-}3TBA+H]^{2-}$), 1919.8 ($[M\text{-}2TBA+H]^-$), 1677.5 ($[M\text{-}3TBA+2H)^-$], 1361.8 ($[2M\text{-}3TBA)^{3-}$].

^1H NMR (300MHz, CD_3CN, δ, ppm): 0.96 (t, $^+N(CH_2CH_2CH_2CH_3)_4$, 36H), 1.33 (m, $^+N(CH_2CH_2CH_2CH_3)_4$, 24H), 1.59 (m, $^+N(CH_2CH_2CH_2CH_3)_4$, 24H), 3.07 (m, $^+N(CH_2CH_2CH_2CH_3)_4$, 24H), 3.64 (s, $-OCH_3$, 6H), 4.59 (s, CH phenylalanine, 2H), 6.78 (m, -(CO)NH-, 2H), 7.1-7.4 (m, aromatic Phe of amino acid, 10H), 7.92 (s, NH TRIS, 2H), 65.89 (s, CH_2 TRIS, 12H).

UV-Vis (CH_3CN): Main band under 190 nm (ε_{190}=215200 $cm^{-1}M^{-1}$). Shoulder between 230 nm (ε_{230}=80000 $cm^{-1}M^{-1}$) and 205 nm (ε_{205}=128000 $cm^{-1}M^{-1}$).

CD (CH_3CN): Positive dichroic signals, with two bands recalling those of L-Phe. The maximums of intensity are located at 196 nm ([θ]=112806 deg*cm^2*dmol^{-1}) and 219 nm ([θ]=42729 deg*cm^2*dmol^{-1}).

Elemental Analysis: Calculated for $C_{84}H_{154}MnMo_6O_{32}N_7$: C 41.95%, H 6.45%, N 4.08%. Found: C 40.81%, H 6.87%, N 4.83%

SYNTHESIS 10A:

Synthesis of "$MnMo_6$ POM-DB" Compounds 6

$[(C_4H_9)_4N]_3[MnMo_6O_{18}\{(OCH_2)_3CNHCO(CH_2)_2CO(C_{49}H_{68}N_{13}O_9)\}_2]$

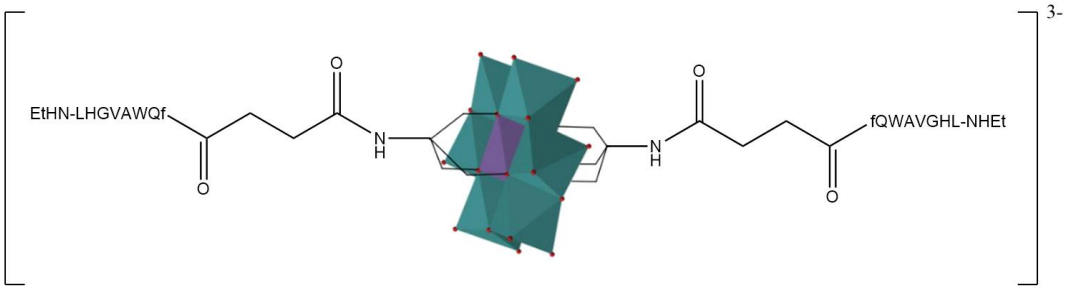

Reaction:

$[(C_4H_9)_4N]_3[MnMo_6O_{18}\{(OCH_2)_3CNHCO(CH_2)_2CO(C_4H_4NO_3)\}_2] + 2\ C_{49}H_{68}N_{13}O_9 \xrightarrow[DMF\ R.T.]{DIPEA} [(C_4H_9)_4N]_3[MnMo_6O_{18}\{(OCH_2)_3CNHCO(CH_2)_2CO(C_{49}H_{68}N_{13}O_9)\}_2]$

Procedure:

POM-NHS (20.25 mg; 0.0089 mmol) has been dissolved in 1.2 mL of DMF in a vial. In order Demobesin-1 (20.28 mg, 0.021 mmol) and DIPEA (18 mg, 24 µL, 0.13 mmol) were added to the reaction mixture, and the slightly orange solution was stirred for 24 hours at room temperature. The day after the vial was put under diethyl ether atmosphere to crystallize. After 24 hours the greasy milk color solid was recovered and washed with approximately 1.5 mL of diethyl ether for three times. The solid was then dissolved in 2 mL of DMF and put in diethyl ether atmosphere to crystallize for a weekend. The spongy product was then washed with diethyl ether and redissolved in DMF to attempt

the crystallization under diethyl ether atmosphere. After two attempts lasting several days, a greasy milk color solid was obtained. The solid was washed with diethyl ether multiple times, put under vacuum, and finally weighted (MM = 4014.76 g/mol, 0.02985 g, 84% yield).

Analysis & Characterization:

FTIR (KBr, cm^{-1}): 3470 (m, br), 3285 (s, br), 3062 (w), 2961 (m), 2929 (m), 2873 (m), 1660 (s, br), 1540 (s, br), 1439 (m), 1409 (w), 1387 (m), 1342 (w), 1254 (m), 1157 (w), 1100 (m), 1061 (m), 1025 (m), 942 (s), 920 (s), 810 (w), 745 (m), 671 (s), 563 (w), 518 (w), 461 (w).

ESI-MS (-) CH_3CN: 1095.0 ($[M-3TBA]^{3-}$),1643.6 ($[M-3TBA+H]^{2-}$), 1763.6 ($[M-2TBA]^{2-}$).

UV (TFE-H_2O 1:10): Maximum at 193 nm (ε_{193}=289600 $cm^{-1}M^{-1}$) and weak shoulder between 215 nm (ε_{215}=120000 $cm^{-1}M^{-1}$) and 198 nm (ε_{193}=248000 $cm^{-1}M^{-1}$).

CD (TFE-H_2O 1:10): Minimum located at 202 nm ([θ]=-109508 $deg*cm^2*dmol^{-1}$) and maximum at 190.5 nm ([θ]=108404 $deg*cm^2*dmol^{-1}$).

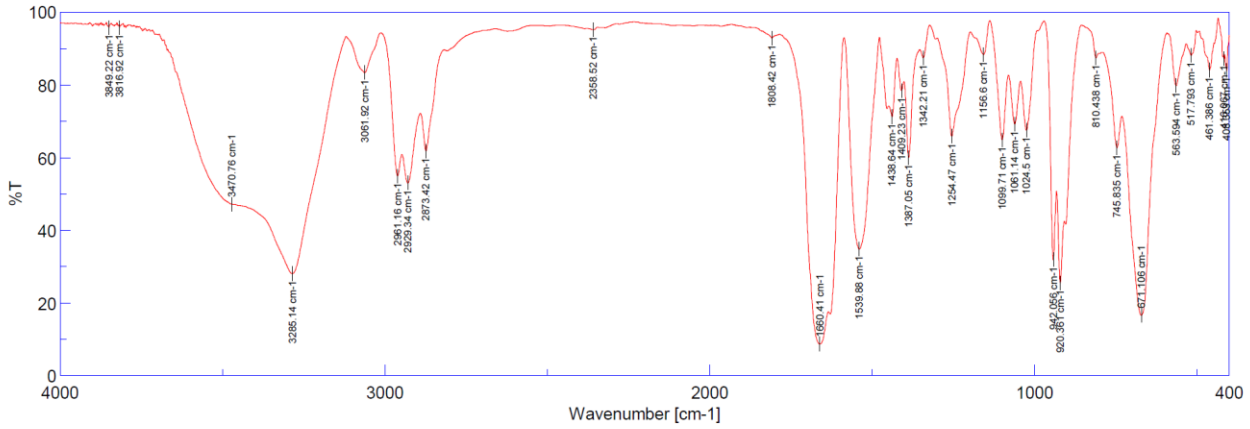

Figure 5.17 FT-IR spectrum of Infrared Spectrum of Coupling Product: MnMo6 POM-DB (Red) and Initial Reagent: MnMo6 POM-NHS (Purple)

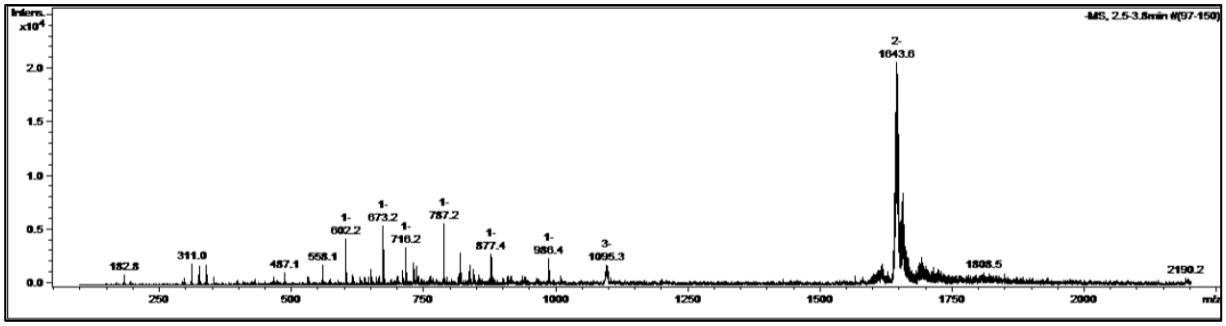

Figure 5.18 ESI-MS (-) (CH3CN) spectra of MnMo6-DB.

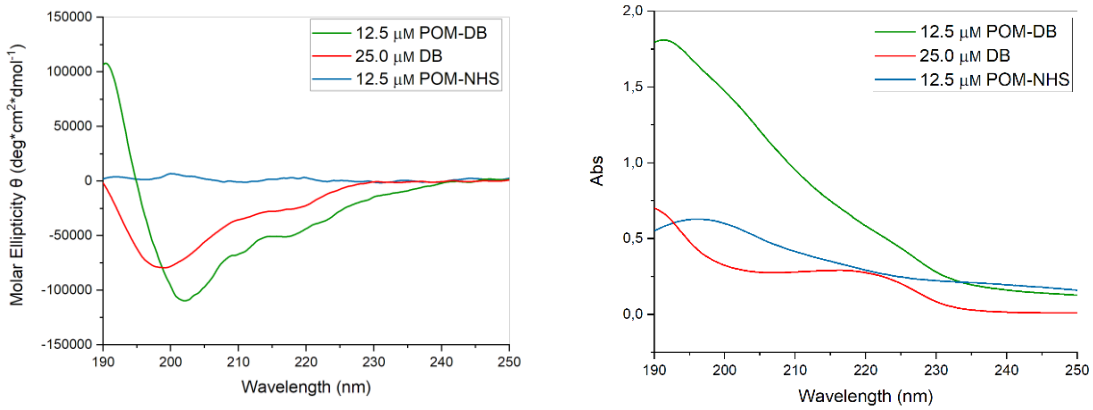

Figure 5.19 In the left, Molar ellipticity of MnMo6 POM-NHS, MnMo6 POM-DB (coupling product), and the peptide DB (Demobesin-1) alone. Solvent: TFE/H2O of MnMo6-DB. In the right, UV spectra of the coupling product MnMo6 POM-DB and the precursors. Solvent: TFE/H2O 1:10.

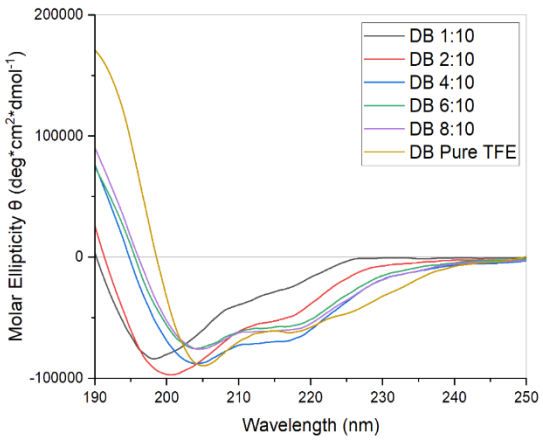

F*igure 5.20 Molar Ellipticity of Demobesin-1 25 µM at different solvent TFE/H2O ratio: 1:10, 2:20, 4:10, 6:10, 8:10, TFE pure.*

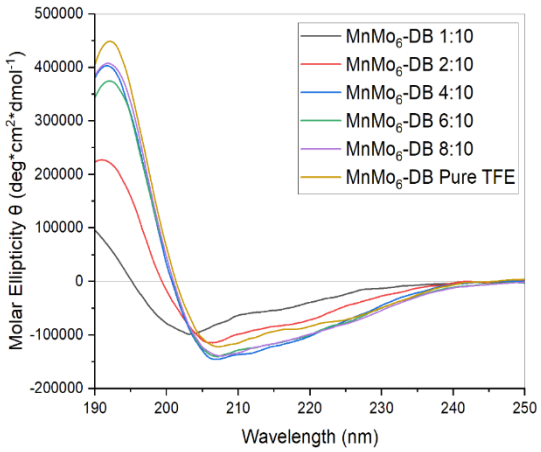

Figure 5.21 Molar Ellipticity of the MnMo6 POM- DB 12.5 µM at different solvent TFE/H2O ratio: 1:10, 2:20, 4:10, 6:10, 8:10, TFE pure.

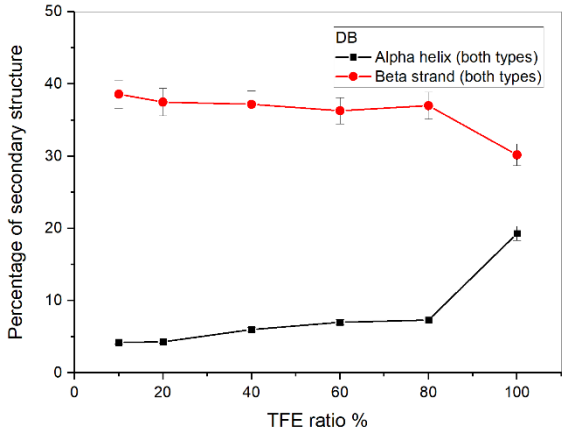

Figure 5.22 Percentage of α-helix and β-strand for Demobesin-1 at different TFE/H2O percentages: 1:10,

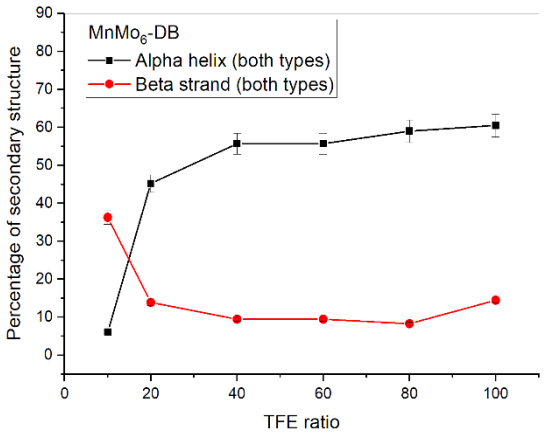

Figure 5.23 Percentage of α-helix and β-strand for the MnMo6 POM-DB at different TFE/H2O percentages: 1:10,

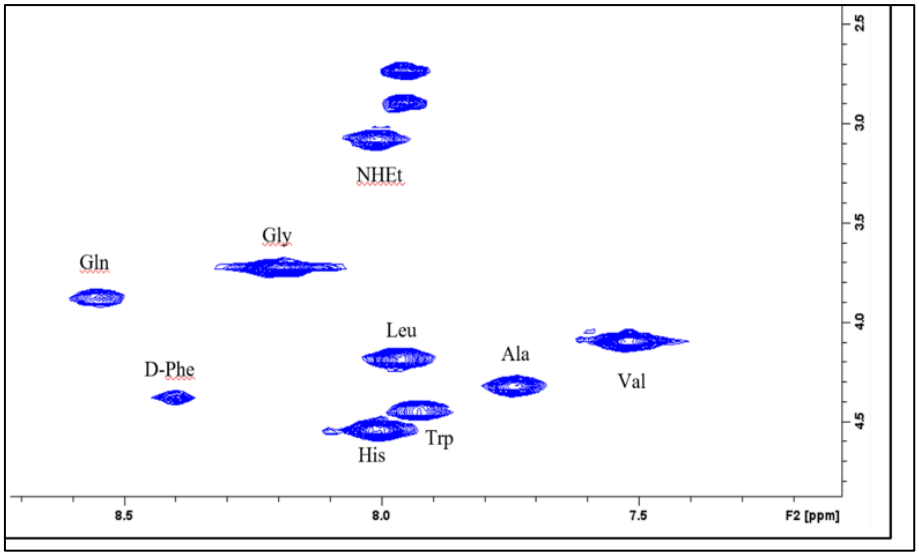

Figure 5.24 2D-1H-NMR COSY spectrum of MnMo6 POM-DB

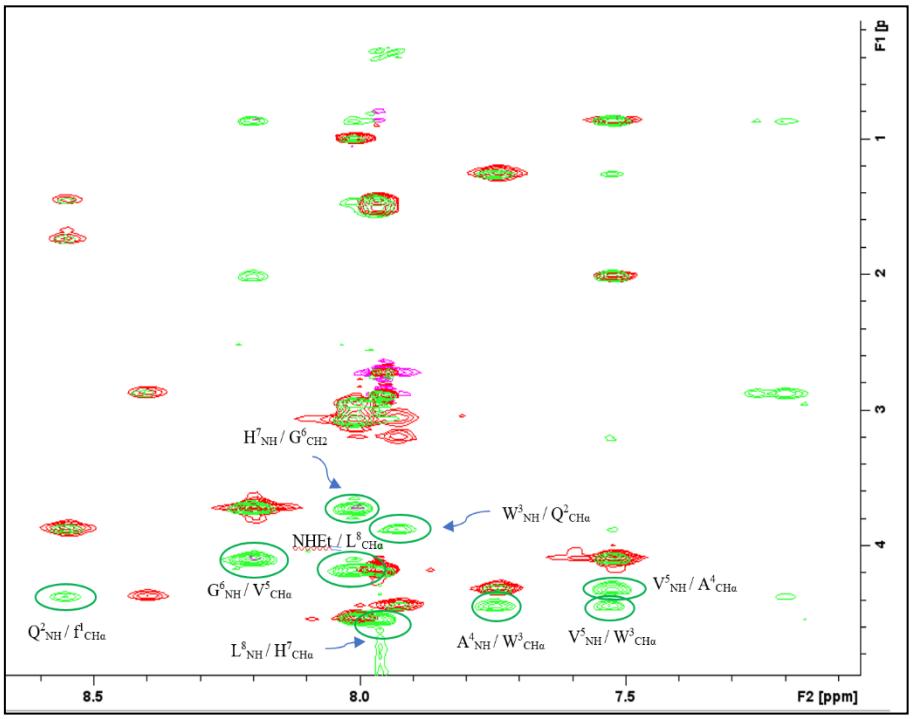

Figure 5.25 2D-1H-NMR TOCSY and ROESY of MnMo6 POM-DB.

Table 5.5 Chemical shift of the Demobesin-1 alone and linked to the POM. Each amino acid in the hybrid were identified.

	MnMo6 POM-DB			DB	
AA	NH (ppm)	CHα (ppm)	Rest of the chain (ppm)	NH (ppm)	CHα (ppm)
D-Phe	8.40	4.37	-CH2β 2.87 Aromatics not assigned	-	-
Gln	8.55	3.87	-CH2β (diastereotopic) 1.68, 1.74 -CH2γ 1.45 -NH2 not observed	8.55	4.33
Trp	7.93	4.45	-CH2β	8.30	4.56

			(diastereotopic) 3.06, 3.20 Aromatics not assigned		
Ala	7.74	4.32	-CH3 1.25	8.25	4.41
Val	7.52	4.09	-CHβ 2.00 (-CH3γ)2 0.87	7.77	4.17
Gly	8.19	-CH2α 3.72	/	8.23	-CH2α 3.72, 3.79
His	8.00	4.54	-CH2β 3.02 -NH aromatics not observed -CH aromatics not assigned	8.13	4.61
Leu	7.96	4.18	-CH2β 1.46 -CHγ 0.83 (-CH3δ)2 not observed	8.09	4.20
NHEt	8.00	-CH2α 3.08	-CH3β 1.00	8.04	-CH2α 3.08

SYNTHESIS 11A:

Synthesis of "$MnMo_6$ POM-EEEEβAla-fQWAVGHL-NHEt" Compounds 7

$[(C_4H_9)_4N]_3[MnMo_6O_{18}\{(OCH_2)_3CNHCO(CH_2)_2CO(C_{72}H_{101}N_{18}O_{22})\}_2]$

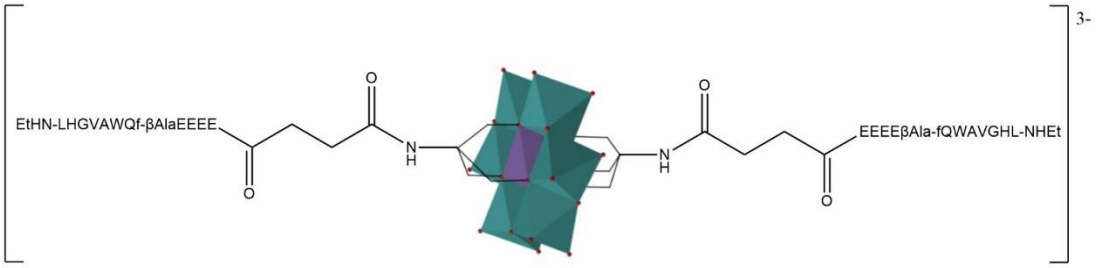

Reaction:

$[(C_4H_9)_4N]_3[MnMo_6O_{18}\{(OCH_2)_3CNHCO(CH_2)_2CO(C_4H_4NO_3)\}_2] + 2\ C_{72}H_{101}N_{18}O_{22}$

$\xrightarrow[DMF\ R.T.]{DIPEA} [(C_4H_9)_4N]_3[MnMo_6O_{18}\{(OCH_2)_3CNHCO(CH_2)_2CO(C_{72}H_{101}N_{18}O_{22})\}_2]$

Procedure:

POM-NHS (10.63 mg; 0.0047 mmol) has been dissolved in 0.8 mL of DMF in a vial. In order EEEEβAla-fQWAVGHL-NHEt (16.50 mg, 0.011 mmol) and DIPEA (9.6 mg, 13 µL, 0.075 mmol) were added to the reaction mixture, and the orange solution was stirred for 24 hours at room temperature. The day after the vial was put under diethyl ether atmosphere to crystallize. After a few hours the greasy light orange product was recovered and washed with approximately 1.5 mL of diethyl ether for three times and then dried under vacuum and finally weighted (MM = 5189.2 g/mol, 0.023 g, 95% yield).

Analysis & Characterization:

FTIR (KBr, cm^{-1}): 3296 (m, br), 3061 (w, br), 2962 (m), 2934 (m), 2874 (m), 1656 (s, br), 1539 (s), 1452 (w), 1388 (m), 1252 (w), 1102 (w), 1062 (w), 1023 (w), 943 (m), 922 (m), 746 (w), 670 (s), 540 (w), 460 (w), 416 (w).

ESI-MS (-) CH_3CN: 1487.0 ($[M-3TBA]^{3-}$), 1503.4 ($[M-3TBA-2H+2Na]^{3-}$), 1574.5 ($[M-2TBA-2H+Na]^{3-}$).

UV (TFE-H_2O 2:10): Maximum at <190 nm (ε_{190}=289600 $cm^{-1}M^{-1}$) and shoulder at 218 nm (ε_{218}=112000 $cm^{-1}M^{-1}$).

CD (TFE-H_2O 2:10): Minimum located at 205 nm ([θ]=-269470 $deg*cm^2*dmol^{-1}$) and maximum under 190 nm ([θ]=404754 $deg*cm^2*dmol^{-1}$ at 190 nm).

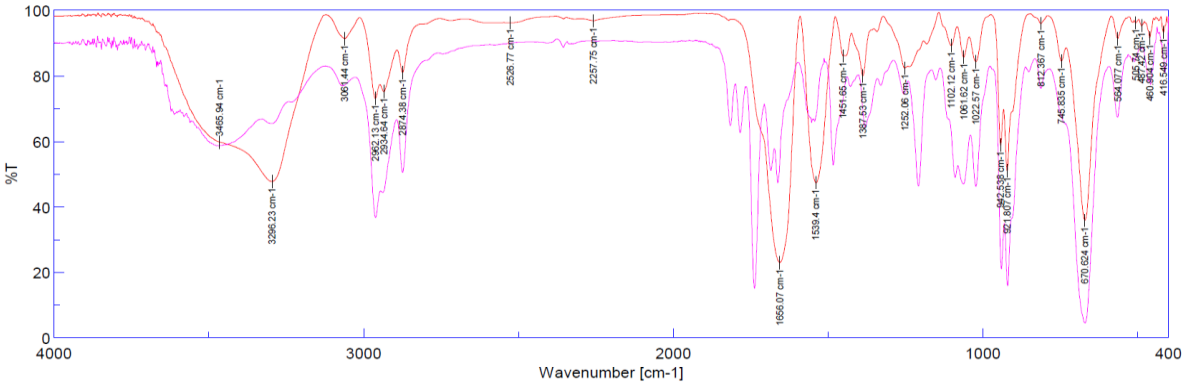

Figure 5.26 FT-IR spectrum of the reagent POM-NHS (in purple) and the final coupling product (in red).

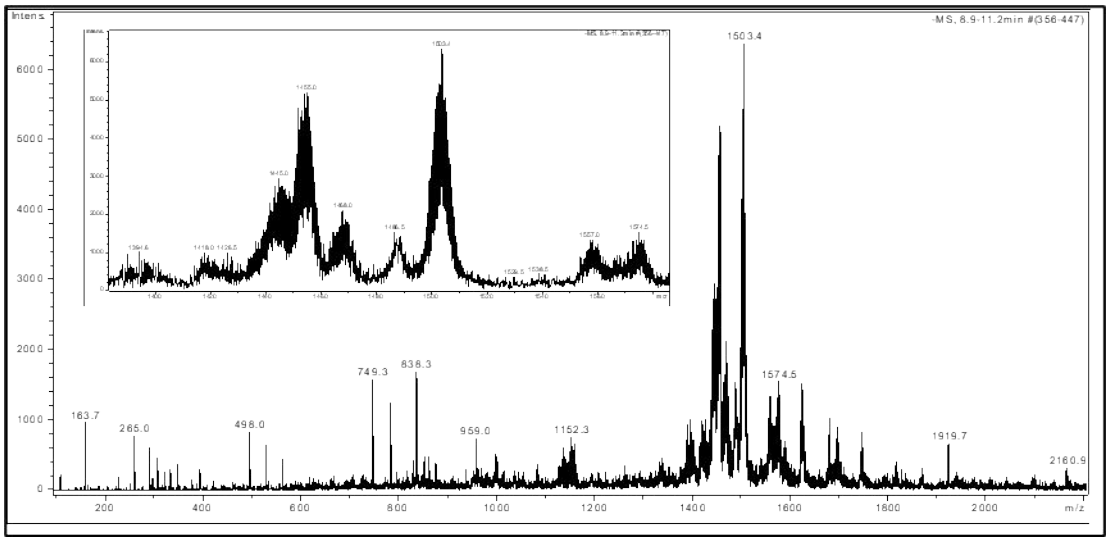

Figure 5.27 ESI-MS (+) spectrum of POM-NHS in CH3CN.

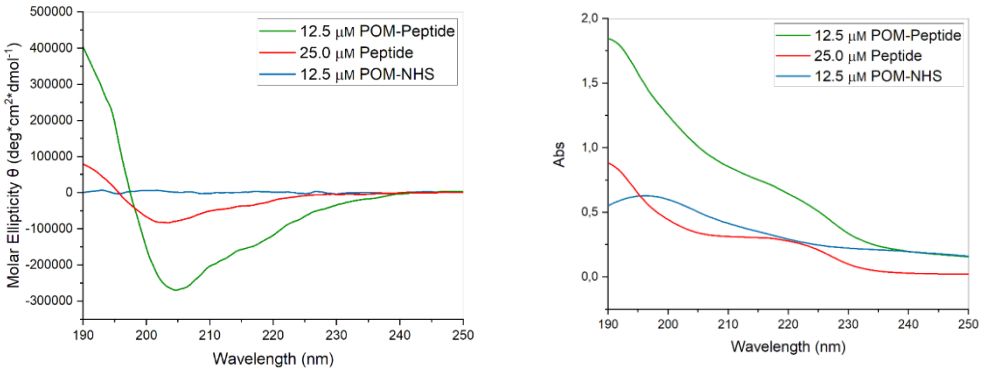

Figure 5.28 Molar Ellipticity graphs and UV spectra of the POM-EEEEβAlaDB and the two reagents POM-NHS and the single peptide. The solvent is TFE-H2O 2:10.

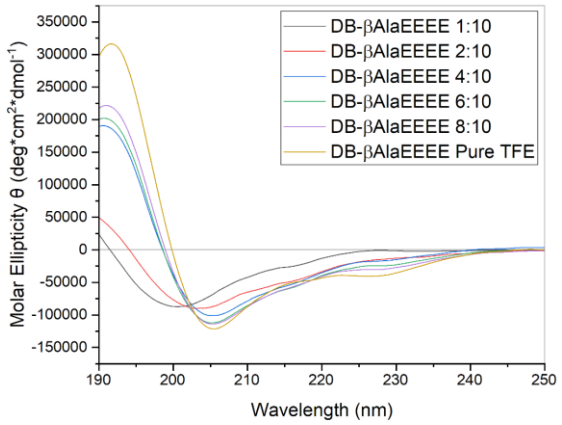

Figure 5.29 Molar Ellipticity of the peptide DB-βAlaEEEE 25 μM at different solvent TFE/H2O ratio: 1:10, 2:20,

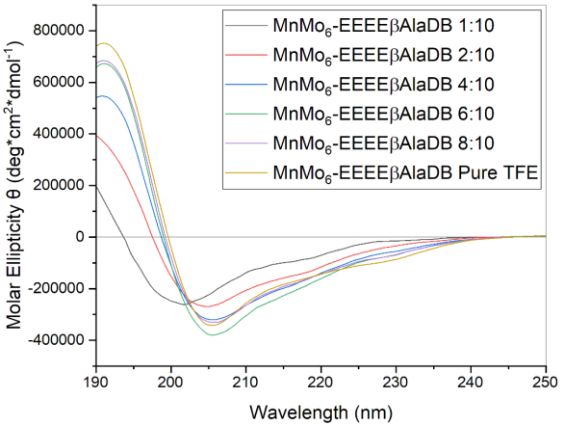

Figure 5.30 Molar Ellipticity of the POM-EEEEβAlaDB 12.5 μM at different solvent TFE/H2O ratio: 1:10, 2:20,

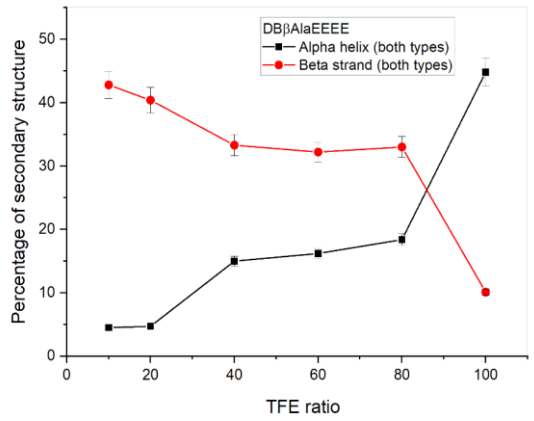

Figure 5.31 Percentage of α-helix and β-strand for the peptide DB-βAlaEEEE at different TFE/H2O percentages: 1:10, 2:20, 4:10, 6:10, 8:10, TFE pure.

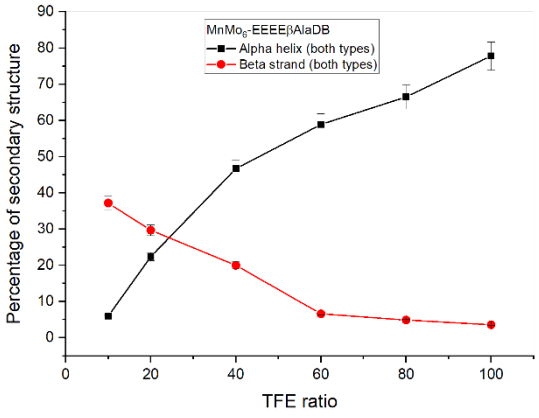

Figure 5.32. Percentage of α-helix and β-strand for the POM-EEEEβAlaDB at different TFE/H2O percentages: 1:10, 2:20, 4:10, 6:10, 8:10, TFE pure.

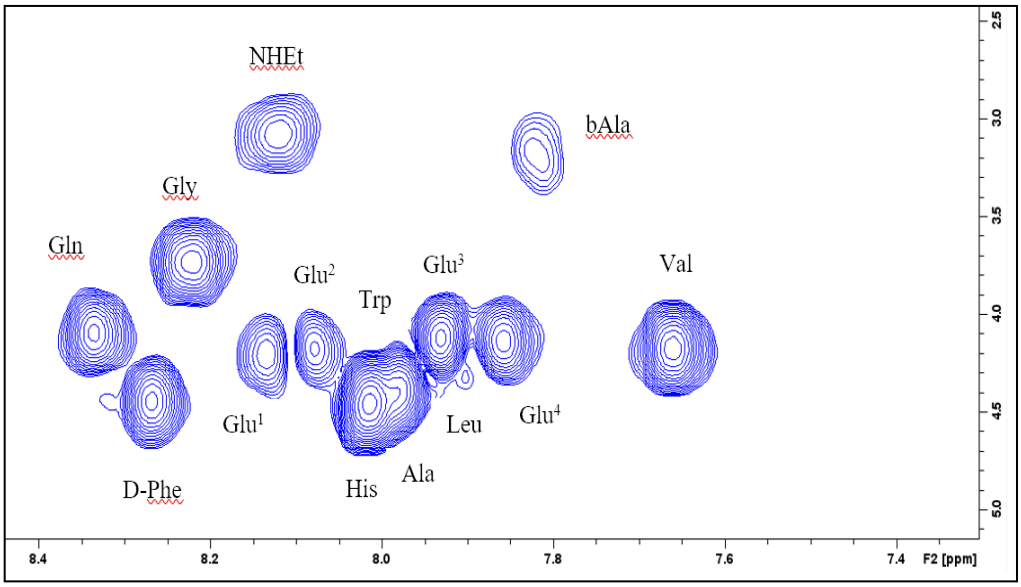

Figure 5.33 2D 1H NMR (COSY)COSY signals for POM-EEEEβAlaDB

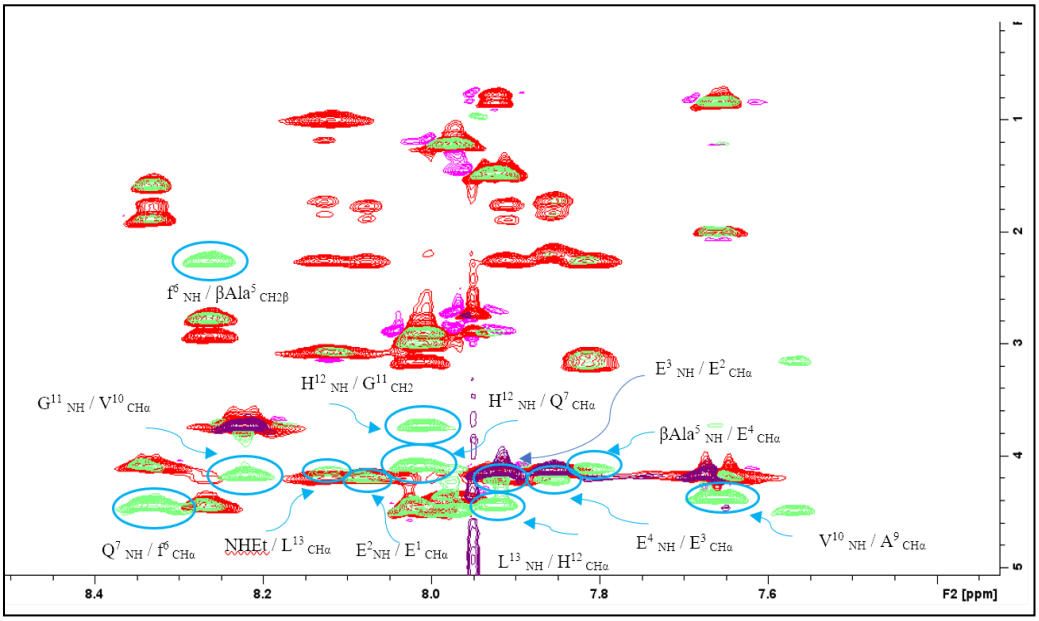

Figure 5.34 [1]H ROESY of POM-EEEEβAlaDB (in green) overlapped with TOCSY (in red). It is possible to notice the match between the amino acids His 12 and Gln 7.

Table 5.6 COSY and TOCSY signals for the amino acids composing the POM-EEEEβAlaDB and the peptide alone.

	POM-EEEEβAlaDB			DBβAlaEEEE	
AA	NH (ppm)	CHα (ppm)	Rest of the chain (ppm)	NH (ppm)	CHα (ppm)
Glu1	8.13	4.20	-CH2β 2.26 -CH2γ (diastereotopic) 1.73, 1.85	-	-
Glu2	8.08	4.17	-CH2β 2.27 -CH2γ (diastereotopic) 1.77, 1.89	8.62	4.35
Glu3	7.93	4.12	-CH2β 2.26 -CH2γ (diastereotopic) 1.76, 1.90	8.21	4.25
Glu4	7.86	4.14	-CH2β 2.20 -CH2γ (diastereotopic) 1.73, 1.84	8.01	4.15
bAla	7.82	-CH2α 3.18	-CH2β 2.27	7.93	-CH2α 3.11, 3.21
D-Phe	8.27	4.44	-CH2β (diastereotopic) 2.94, 2.78 Aromatici non osservati	8.27	4.45
Gln	8.34	4.09	-CH2β (diastereotopic) 1.89, 1.78	8.36	4.10

			-CH2γ 1.59		
Trp	7.96	4.38	-CH2β (diastereotopic) 2.72, 2.88 Aromatics not assigned	8.01	4.48
Ala	7.97	4.40	-CH3 1.21	7.97	4.37
Val	7.66	4.18	-CHβ 2.01 (-CH3γ)2 0.85	7.61	4.14
Gly	8.22	-CH2α 3.73	/	8.24	-CH2α 3.70, 3.77
His	8.01	4.46	-CH2β 2.91 -NH aromatics not observed -CH aromatics not assigned	8.08	4.61
Leu	7.93	4.12	-CH2β 1.48 -CHγ 0.82 (-CH3δ)2 non observed	8.07	4.20
NHEt	8.12	-CH2α 3.08	-CH3β 1.00	8.04	-CH2α 3.08

SYNTHESIS 12A:

Synthesis of "$MnMo_6$-TtdsDB" Compounds 8

$[(C_4H_9)_4N]_3[MnMo_6O_{18}\{(OCH_2)_3CNHCO(CH_2)_2CO(C_{63}H_{94}N_{15}O_{14})\}_2]$

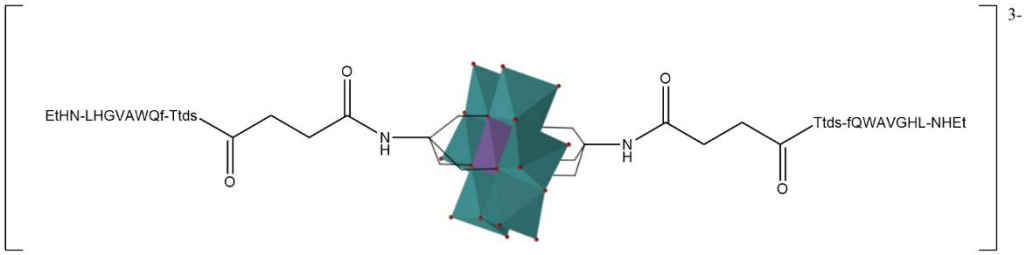

Reaction:

$[(C_4H_9)_4N]_3[MnMo_6O_{18}\{(OCH_2)_3CNHCO(CH_2)_2CO(C_4H_4NO_3)\}_2] + 2\ C_{63}H_{94}N_{15}O_{14} \xrightarrow[DMF\ R.T.]{DIPEA} [(C_4H_9)_4N]_3[MnMo_6O_{18}\{(OCH_2)_3CNHCO(CH_2)_2CO(C_{63}H_{94}N_{15}O_{14})\}_2]$

Procedure:

POM-NHS (9.24 mg; 0.0041 mmol) has been dissolved in 0.8 mL of DMF in a vial. In order Ttds-fQWAVGHL-NHEt (12.46 mg, 0.0097 mmol) and DIPEA (7.42 mg, 10 µL, 0.057 mmol) were added to the reaction mixture, and the yellow-orange solution was stirred for 24 hours at room temperature. The day after the vial was put under diethyl ether atmosphere to crystallize. After 96 hours the milk colour product was recovered and washed with approximately 1.5 mL of diethyl ether for three times and then dried under vacuum for several hours, and finally weighted (MM = 4619.48g/mol, 0.017 g, 90% yield).

Analysis & Characterization:

FTIR (KBr, cm^{-1}): 3429 (m, br), 3284 (s), 3076 (w), 2961 (m), 2926 (m), 2874 (m), 1660 (s), 1629 (s), 1549 (m), 1448 (w), 1386 (w), 1256 (w), 1099 (w), 1017 (w), 943 (s), 920 (s), 742 (w), 669 (s), 566 (w), 406 (m).

ESI-MS (-) CH_3CN: 2067.5 ($[M-2TBA]^{2-}$), 1947.8 ($[M-3TBA+H]^{2-}$), 1299.6 ($[M-3TBA]^{3-}$).

UV (TFE-H_2O 1:10): Maximum at <190 nm (ε_{190}=244800 $cm^{-1}M^{-1}$) and shoulder at 217 nm (ε_{217}=115200 $cm^{-1}M^{-1}$).

CD (TFE-H_2O 1:10): Minimum at 203 nm ([θ]=-160978 $deg*cm^2*dmol^{-1}$) and maximum under 190 nm ([θ]=107838 $deg*cm^2*dmol^{-1}$ at 190 nm).

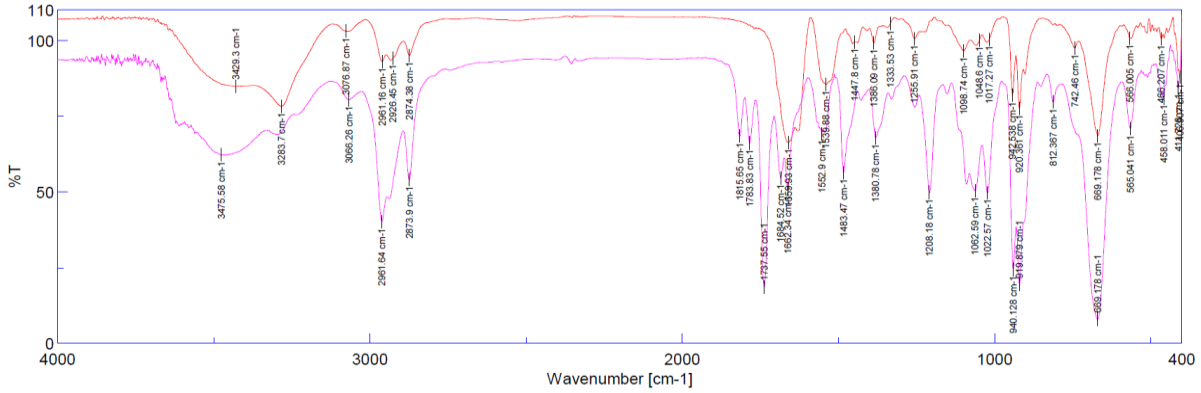

Figure 5.35 FT-IR spectrum of the reagent POM-NHS (in purple) and the final coupling product MnMo6-TtdsDB (in red).

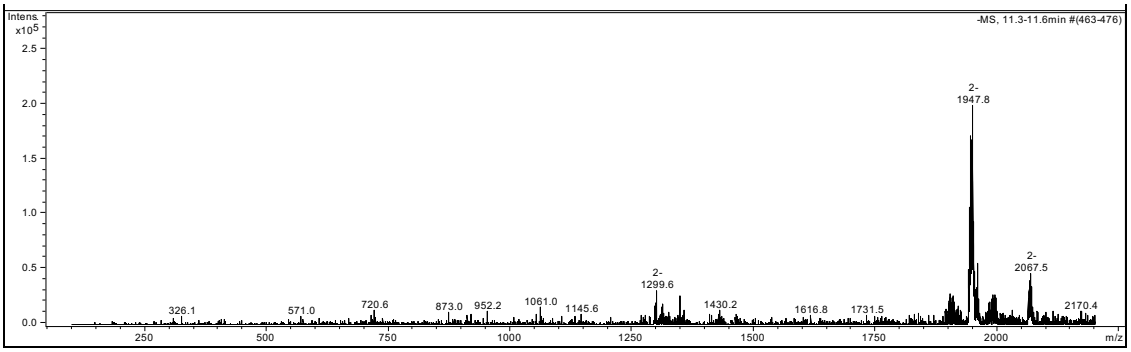

Figure 5.36 FT-IR spectrum of the reagent POM-NHS (in purple) and the final coupling product (in red).

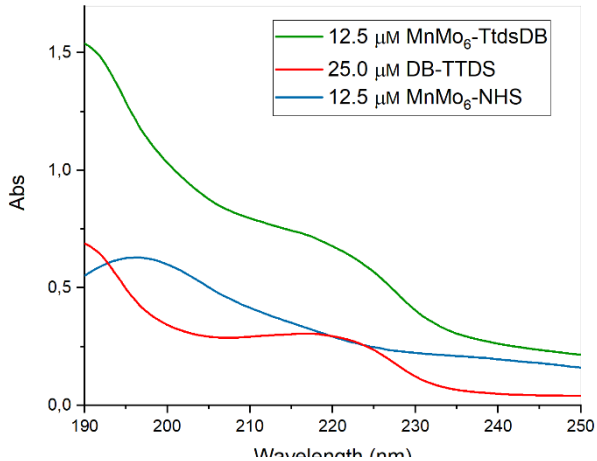

Figure 5.37 UV spectra of the product MnMo6-TtdsDB and the two (organic and inorganic) precursors. The solvent used was TFE/H2O 1:10.

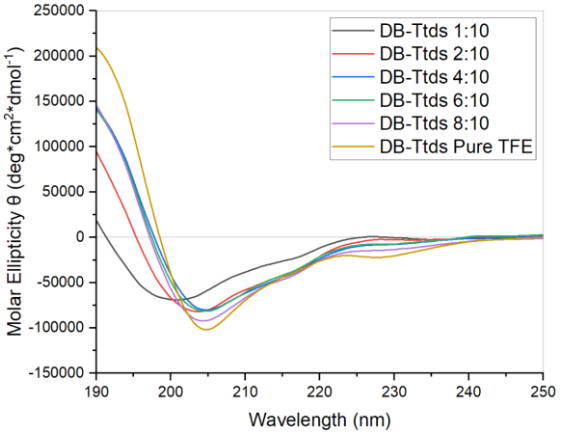

Figure 5.38 Molar ellipticity of 25μM DB-Ttds at different ratio of TFE/Water: 1:10, 2:20, 4:10, 6:10, 8:10, and pure

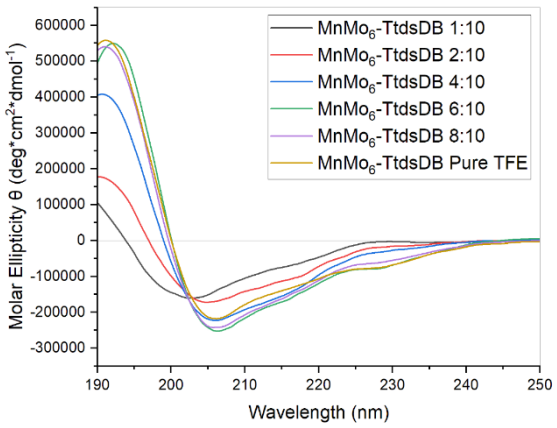

Figure 5.39 Molar ellipticity of 12.5 μM MnMo₆-TtdsDB at different ratio of TFE/Water: 1:10, 2:20, 4:10, 6:10,

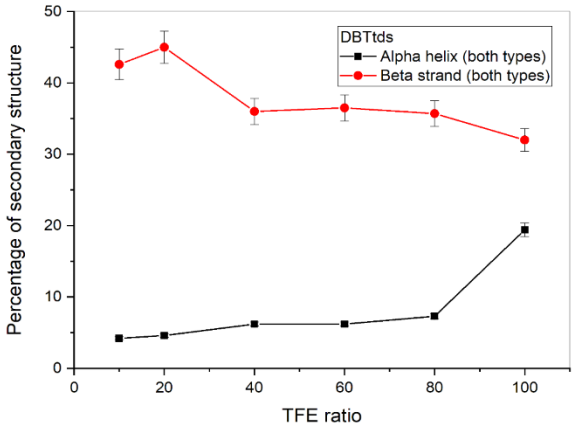

Figure 5.40 Percentage of α-helix and β-strand for the peptide DB-Ttds at different TFE/H₂O percentages: 1:10,

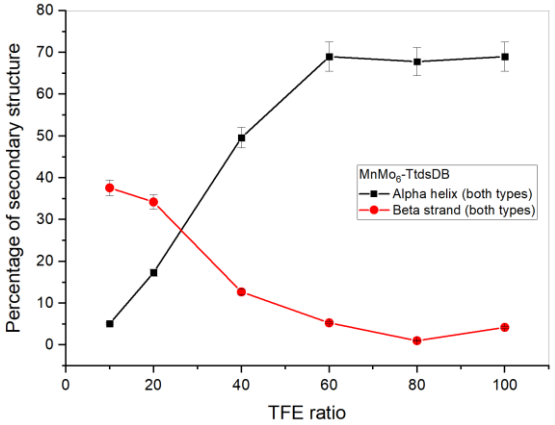

Figure 5.41 Percentage of α-helix and β-strand for the POM-peptide DB-Ttds at different TFE/H₂O percentages:

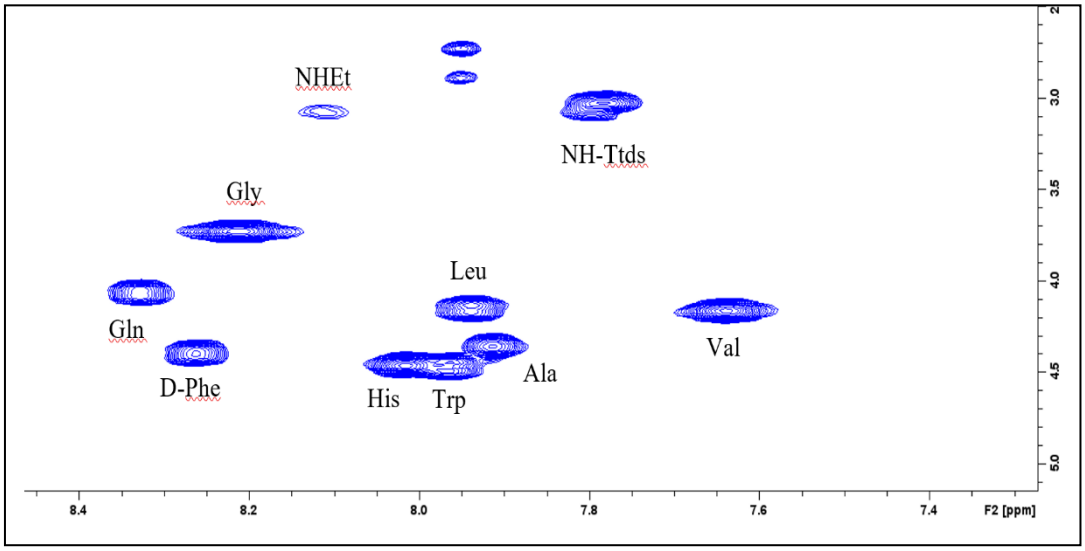

Figure 5.42 COSY signals for POM-TtdsDB

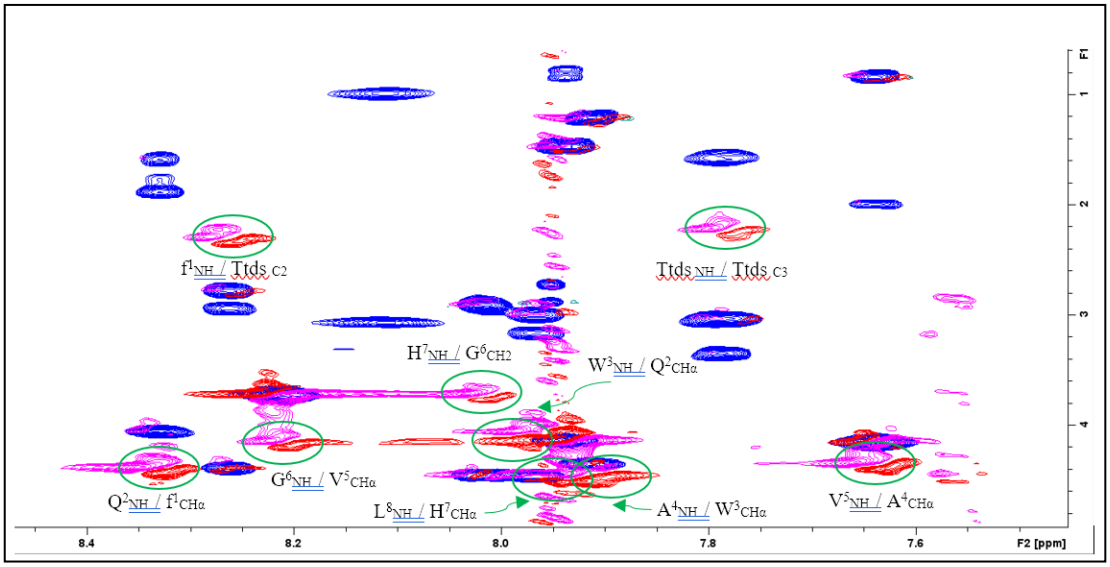

Figure 5.43 TOCSY (blue) and ROESY (red) of POM-TtdsDB

Table 5.7 Chemical shift of each amino acid in the DB-Ttds alone and linked to the POM. Additionally, the side chains of each amino acid in the hybrid were identified.

	MnMo6-TtdsDB			DBTtds	
AA	NH (ppm)	CHα (ppm)	Rest of the chain (ppm)	NH (ppm)	CHα (ppm)
D-Phe	8.26	4.39	-CH2β (diastereotopic) 2.78, 2.94 Aromatics not observed	8.25	4.41
Gln	8.33	4.06	-CH2β (diastereotopic) 1.78, 1.89 -CH2γ 1.59	8.34	4.07
Trp	7.97	4.47	-CH2β (diastereotopic) 3.00, 3.17	7.98	4.46

			Aromatics not assigned		
Ala	7.91	4.35	-CH3 1.21	7.90	4.35
Val	7.64	4.16	-CHβ 2.00 (-CH3γ)2 0.84	7.61	4.13
Gly	8.21	-CH2α 3.73	/	8.22	-CH2α 3.70, 3.76
His	8.02	4.46	-CH2β 2.91 -NH aromatic not observed -CH aromatics not assigned	8.08	4.60
Leu	7.94	4.15	-CH2β 1.48 -CHγ 0.81 (-CH3δ)2 not observed	8.06	4.20
NH-Ttds	7.79	-CH2α 3.03	-CH2β 1.58 -CH2γ 3.35	7.79	-CH2α 3.03
NHEt	8.11	-CH2α 3.07	-CH3β 1.00	8.02	-CH2α 3.06

SYNTHESIS 13A:

Synthesis of "V_6-OH" Compounds 9

$[(C_4H_9)_4N]_2[V_6O_{13}\{(OCH_2)_3CCH_2OH\}_2]$

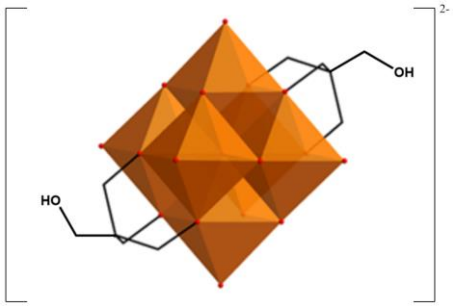

Reaction:

$$6NaVO_3 + 4HCl + 2(C_4H_9)_4BrN + 2(HOCH_2)_3CCH_2OH \xrightarrow[H_2O,\ 80°C,\ 48\ hours]{} [(C_4H_9)_4N]_2[V_6O_{13}\{(OCH_2)_3CCH_2OH\}_2] + 5H_2O + 4NaCl + 2NaBr$$

Procedure:

In a round-bottom flask $NaVO_3 \cdot H_2O$ (5.00g, 0.036mol) was dissolved in 120 mL of H_2O under mild heating (≈50°C) and vigorous stirring until a clear almost colorless solution was obtained. The solution was cooled to room temperature and a 3.8375M solution of HCl (8.65 mL, 0.033 mol) was added dropwise with a burette, monitoring the pH level with a universal indicator until it reached pH=3. During the titration experiment the solution passed from being colorless to yellow, then orange, then red, till when it stabilized on a bright orange coloration. $(HOCH_2)_3CCH_2OH$ (3.75g, 0.028 mol) was added to the solution and the mixture was heated to 80°C for 48 hours using a reflux condenser attached to it. The final brown/dark orange mixture was cooled to room temperature and added dropwise to a previously prepared TBA-Br solution (10g, 0.031 mol in 20 mL H_2O) under powerful

stirring until a red-orange solid was formed. The crude product was filtered on a fitted funnel and washed with 50 mL of H_2O, 80 mL of diethyl ether, monitoring its purity by ESI-MS and FT-IR, then it was dried under vacuum. A light orange powder was obtained (5.07g, 67% yield).

Analysis & Characterization:

FTIR (KBr, cm^{-1}): 3376 (m, br), 2962 (s), 2943 (s), 2873 (s), 1640 (m), 1481 (s), 1383 (m), 1263 (w), 1123 (s), 1074 (m), 1034 (s), 951 (s), 884 (w), 810 (s), 794 (s), 713 (s), 650 (m), 580 (s), 513 (w), 490 (w), 420 (s).

ESI-MS (-) CH_3CN: 1022 ($[M\text{-}TBA]^-$), 780.6 ($[M\text{-}2TBA+H]^-$).

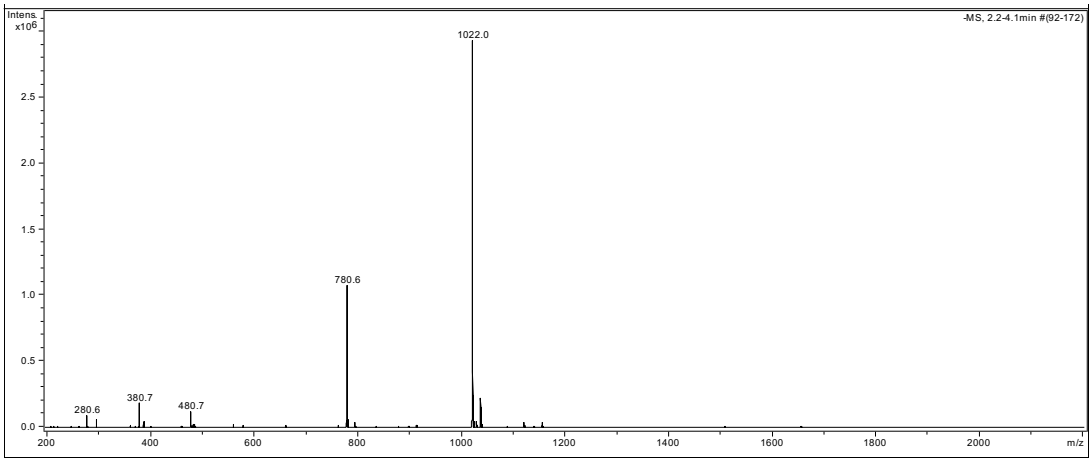

Figure 5.44 ESI-MS (-) (CH3CN) spectrum of V6-OH in CH3CN.

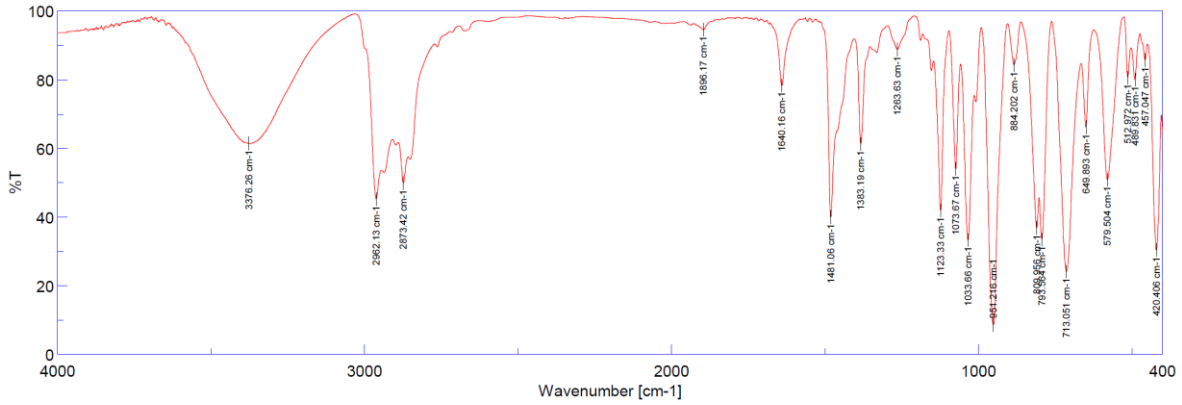

Figure 5.55 FT-IR spectrum of V6-OH.

SYNTHESIS 14A:

Synthesis of "V_6O-Succinate"

$[(C_4H_9)_4N]_2[V_6O_{13}\{(OCH_2)_3CCH_2OOCCH_2CH_2COOH\}_2]$

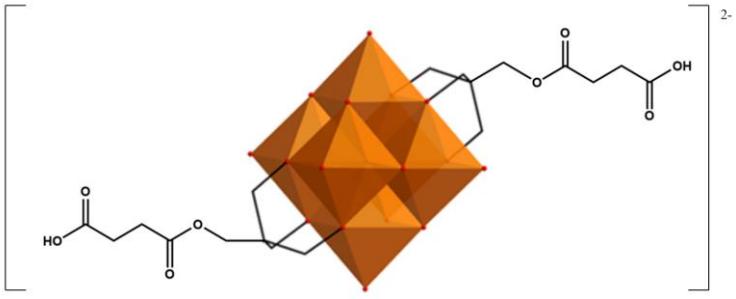

Reaction:

$$[(C_4H_9)_4N]_2[V_6O_{13}\{(OCH_2)_3CCH_2OH\}_2] + 2C_4H_4O_3 \xrightarrow[ACN,\ 50°C,\ 48\ hours]{DMAP,\ TEA} [(C_4H_9)_4N]_2[V_6O_{13}\{(OCH_2)_3CCH_2OOCCH_2CH_2COOH\}_2]$$

Procedure:

An amount of $[(C_4H_9)_4N]_2[V_6O_{13}\{(OCH_2)_3CCH_2OH\}_2]$ (1.11962g, $8.85x10^{-4}$ mol) was dissolved in 40 mL of acetonitrile in a round-bottom flask to obtain a clear orange solution. TEA (0.34 mL, ρ=0.726 g/mL, $2.44x10^{-3}$ mol) and DMAP (0.06, $4.91x10^{-4}$ mol) were added to the solution, causing a color change from orange to red-orange. The mixture was then refluxed for 48 hours at 50°C, and the resulting turbid orange solution was filtered to remove an orange precipitate. The solution was subsequently subjected to rotary evaporation under vacuum to evaporate the solvent, yielding a white precipitate that was filtered out. The resulting dark red solution was transferred to a beaker of cold water, and the red powder that formed was collected using a fitted funnel, washed with cold water, and finally dried under vacuum to yield 0.68g (52% yield).

Analysis & Characterization:

FTIR (KBr, cm^{-1}): 3444 (m, br), 2960 (s), 2932 (m), 2872 (m), 1738 (s), 1649 (w), 1469 (s), 1396 (w), 1380 (w), 1336 (w), 1265 (m), 1247 (m), 1224 (m), 1191 (m), 1161 (m), 1132 (s), 1061 (s), 1036 (m), 1000 (m), 950 (s), 933 (s), 879 (w), 810 (s), 723 (s), 582 (m), 417 (s).

ESI-MS (-) CH_3CN: 1221.9 ($[M\text{-}TBA]^-$), 980.8 ($[M\text{-}2TBA+H]^-$).

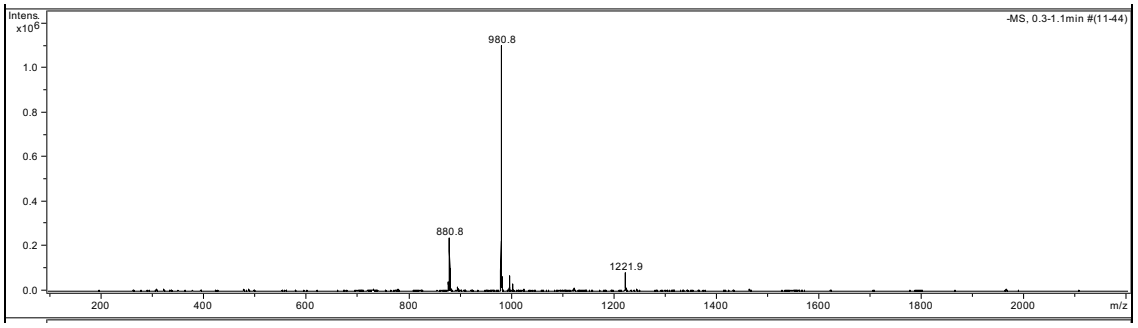

Figure 5.56 ESI-MS (-) Spectrum of V_6O-Succinate in CH_3CN.

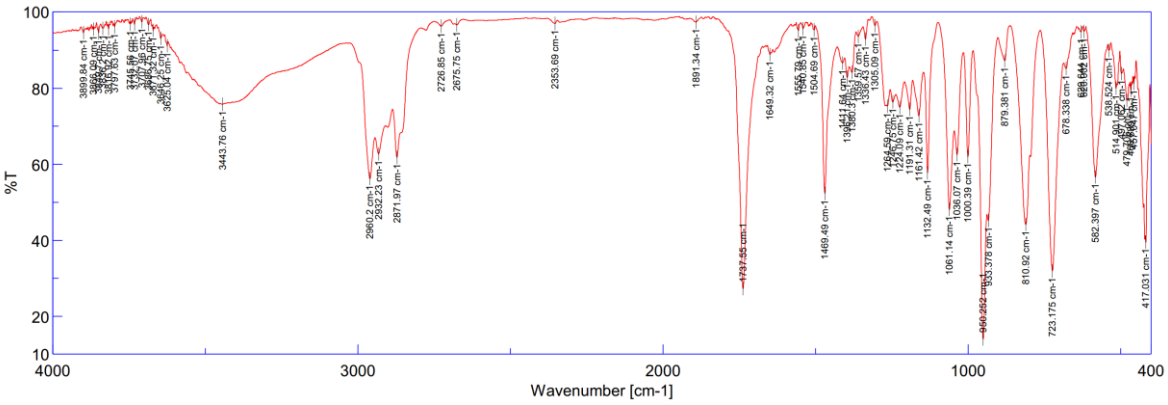

Figure 5.57FT-TR Spectrum of V_6O-Succinate.

SYNTHESIS 15A:

Synthesis of "V_6O-NHS" Compounds 10

$[(C_4H_9)_4N]_2[V_6O_{13}\{(OCH_2)_3CCH_2OOCCH_2CH_2CO(C_4H_4NO_3)\}_2]$

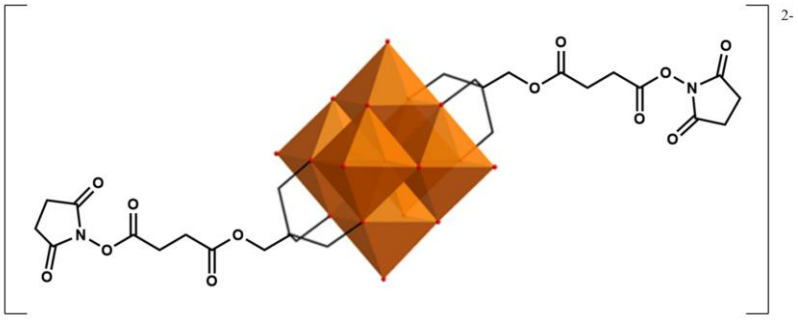

Reaction:

$$[(C_4H_9)_4N]_2[V_6O_{13}\{(OCH_2)_3CCH_2OOCCH_2CH_2COOH\}_2] + 2C_4H_5NO_3 \xrightarrow[DMF\ R.T.]{DCC}$$

$$[(C_4H_9)_4N]_2[V_6O_{13}\{(OCH_2)_3CCH_2OOCCH_2CH_2CO(C_4H_4NO_3)\}_2]$$

Procedure:

V_6O-Succinate (95.28mg, $6.50x10^{-2}$ mmol) was dissolved in a vial containing 2 mL of DMF, producing a clear red-orange solution. NHS (34.26mg, 0.26 mmol) was then added to the solution, and no noticeable color change was observed. Next, DCC (85.01mg, 0.39 mmol) was added to the mixture, causing a color change to a darker red shade. The solution was stirred for 24 hours at room temperature. The resulting brown mixture was subjected to diethyl ether for 5 days, leading to the formation of red needle-shaped crystals. These crystals were collected, washed multiple times with diethyl ether, and finally dried under vacuum to yield 53.89 mg (50%).

Analysis & Characterization:

FTIR (KBr, cm^{-1}): 3444 (m, br), 2962 (s), 2937 (m), 2875 (m), 1814 (w), 1783 (w), 1739 (s), 1667 (w), 1482 (w), 1383 (w), 1252 (w), 1205 (w), 1132 (w), 1085 (m), 954 (s), 883 (w), 809 (s), 719 (s), 648 (w), 582 (m), 422 (m).

ESI-MS (-) CH_3CN: 1415.5 ($[M\text{-}TBA]^-$), 1174.7 ($[M\text{-}2TBA+H]^-$), 1196 ($[M\text{-}2TBA+Na]^-$).

^1H NMR (300MHz, CD_3CN, δ, ppm): 0.96 (t, $^+N(CH_2CH_2CH_2CH_3)_4$ TBA, 24H), 1.35 (s, $^+N(CH_2CH_2CH_2CH_3)_4$ TBA, 16H), 1.60 (m, $^+N(CH_2CH_2CH_2CH_3)_4$ TBA, 16H), 2.66 (t, -$OCCH_2CH_2CO$-, 4H), 2.77 (s, DMF solvent impurities, overlapped with -CH_2- from NHS, (3+4)H), 2.85 (m, -$OCCH_2CH_2CO$-, 4H), 3.10 (m, $^+N(CH_2CH_2CH_2CH_3)_4$ TBA, 16H), 3.95 (s, -CCH_2O- TRIS, 4H), 5.01 (s, -$C(CH_2O\text{-})_3$, 12H).

UV-Vis (ACN): Maximum at 195 nm (ε_{195} = 38400 $cm^{-1}M^{-1}$), and shoulder at 221 nm (ε_{221}=44800 $cm^{-1}M^{-1}$).

Elemental Analysis: Calculated for $C_{50}H_{96}V_6O_{25}N_4$: C 41.16%, H 6.63%, N 3.84%. Experimental: C 42.18%, H 6.55%, N 4.10%.

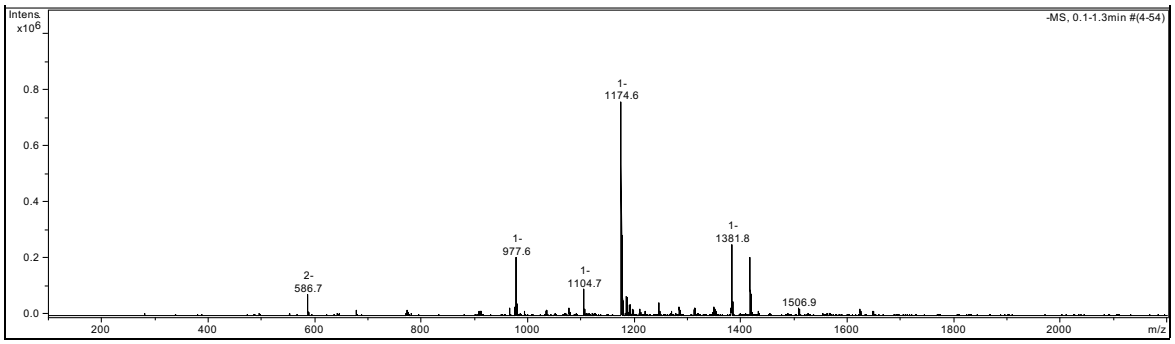

Figure 5.58 ESI-MS (-) Spectrum of V_6O-NHS in CH_3CN.

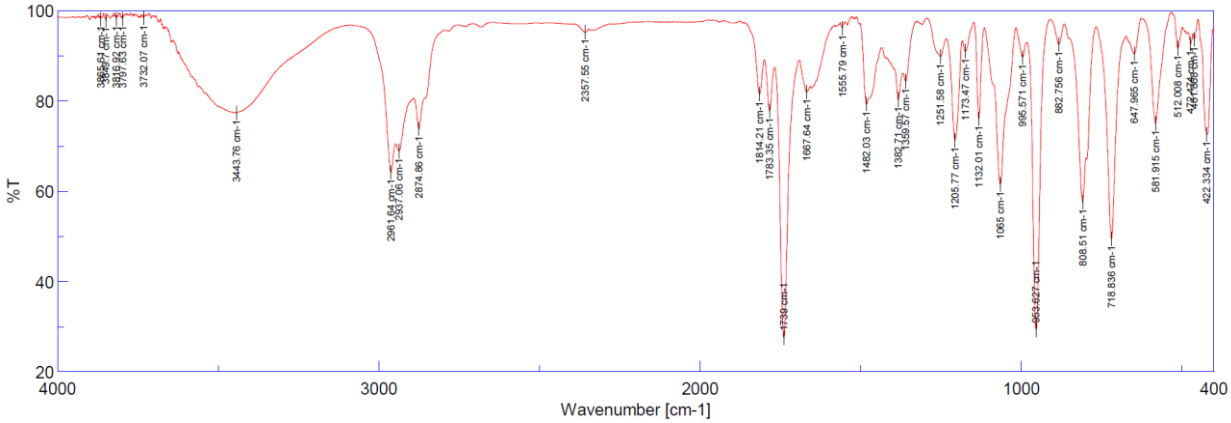

Figure 5.59 FT-IR spectrum of V6O-NHS.

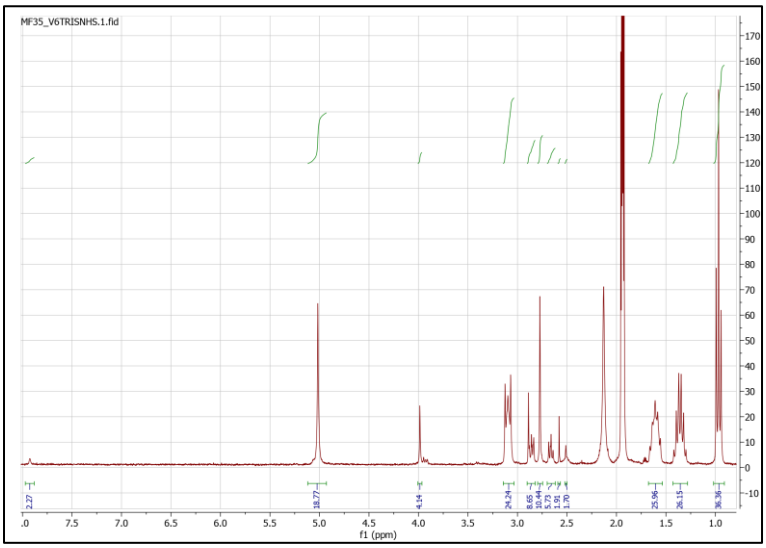

Figure 5.60 ^1H NMR (300MHz, CD_3CN, δ, ppm) of V_6O-NHS.

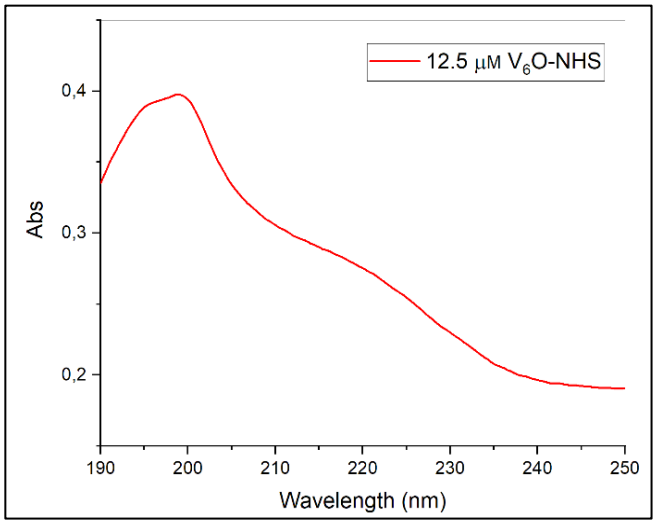

Figure 5.61 UV spectrum of V_6O-NHS in CH_3CN.

UNIVERSITA' DEGLI STUDI DI PADOVA
Dipartimento di Scienze Chimiche
LABORATORIO MICROANALISI
Tel. (049)8275194 Fax (049)8275161

Richiesta : C ☒, H ☒, N ☒, S ☐ Richiedente… MATTIA FRIGO (CARRARO)

N°…249/22… Contrassegno Campione …V6NHS MATTIA FRIGO

Data richiesta …01/09/2022.. Formula Campione……$C_{50}H_{36}N_4O_{26}V_6$

Caratteristiche del campione : SENSIBILE ALL'ARIA ☐ IGROSCOPICO ☐

Altre caratteristiche……..

% calcoli approssimativi	% trovato
C : 41,16	C : 42,18
H : 6,63	H : 6,55
N : 3,84	N : 4,10
S :	S : /

Data consegna …19/09/2022……

Il Direttore

Il Responsabile
(Dr. L. CALORE)

Figure 5.62 Elemental analysis of V_6O-NHS. analyzed for C, H and N gave the following results. C = 42.18 %, H = 6.55 %, N = 4.1 % by wt.

Synthesis 16A

Synthesis of "V_6O-L-Phe" Compounds 11

$[(C_4H_9)_4N]_2[V_6O_{13}\{(OCH_2)_3CCH_2OOCCH_2CH_2COPheOMe\}_2]$

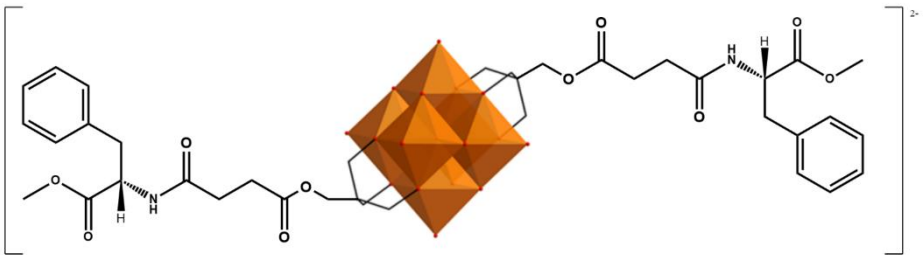

Reaction:

$[(C_4H_9)_4N]_2[V_6O_{13}\{(OCH_2)_3CCH_2OOCCH_2CH_2CO(C_4H_4NO_3)\}_2]$ + 2L-PheOMe·HCl

$\xrightarrow[DMF\ R.T.]{DIPEA}$ $[(C_4H_9)_4N]_2[V_6O_{13}\{(OCH_2)_3CCH_2OOCCH_2CH_2COPheOMe\}_2]$

Procedure:

V_6O-NHS (40.50 mg; 0.0244 mmol) was dissolved in 2.0 mL of DMF in a vial. L-PheOMe·HCl (14.70 mg, 0.068 mmol) and DIPEA (13 mg, 18 µL, 0.1 mmol) were added to the reaction mixture, and the reaction system was stirred for 24 hours at room temperature. Then the vial was crystallized under diethyl ether atmosphere. After one day, the dark orange greasy product was collected and washed with approximately diethyl ether for four times and dried under vacuum, finally weighted the product (MM = 1787.42 g/mol, 0.03810 g, 86% yield).

Analysis & Characterization:

FTIR (KBr, cm^{-1}): 3435 (m, br), 2961 (s), 2936 (m), 2874 (m), 1740 (s), 1668 (s), 1539 (m), 1465 (m), 1386 (m), 1212 (w), 1161 (m), 1131 (s), 1058 (s), 953 (s), 809 (s), 719 (s), 583 (s), 420 (s).

ESI-MS (-) CH_3CN: 1544.2 ($[M\text{-}TBA]^-$), 1302.9 ($[M\text{-}2TBA+H]^-$), 650.9 ($[M\text{-}2TBA]^{2-}$)

^1H NMR (300MHz, CD_3CN; δ, ppm): 0.97 (t, $^+N(CH_2CH_2CH_2CH_3)_4$ TBA, 24H), 1.37 (m, $^+N(CH_2CH_2CH_2CH_3)_4$ TBA, 18H), 1.62 (m, $^+N(CH_2CH_2CH_2CH_3)_4$ TBA, 16H), 3.11 (t, $^+N(CH_2CH_2CH_2CH_3)_4$ TBA, 18H), 3.63 (s, $-OCH_3$, 6H), 5.03 (s, $-C(CH_2O-)_3$, 12H), 3.91 (s, $-CCH_2O-$, 4H), 6.66 (d, -C=ONH-, 2H), 7.16-7.36 (m, aromatic ring Phe, 10H).

^{51}V NMR (78.9MHz, CD_3CN; δ, ppm): -499.75 (s, br)

UV (CH_3CN): Maximum at 191 nm (ε_{191}=150400 $cm^{-1}M^{-1}$), shoulder at 209 nm (ε_{209}=69600 $cm^{-1}M^{-1}$).

CD (CH_3CN): Maximum at 195 nm ([θ]=122438 $deg*cm^2*dmol^{-1}$) and approximately 216 nm ([θ]=35933 $deg*cm^2*dmol^{-1}$).

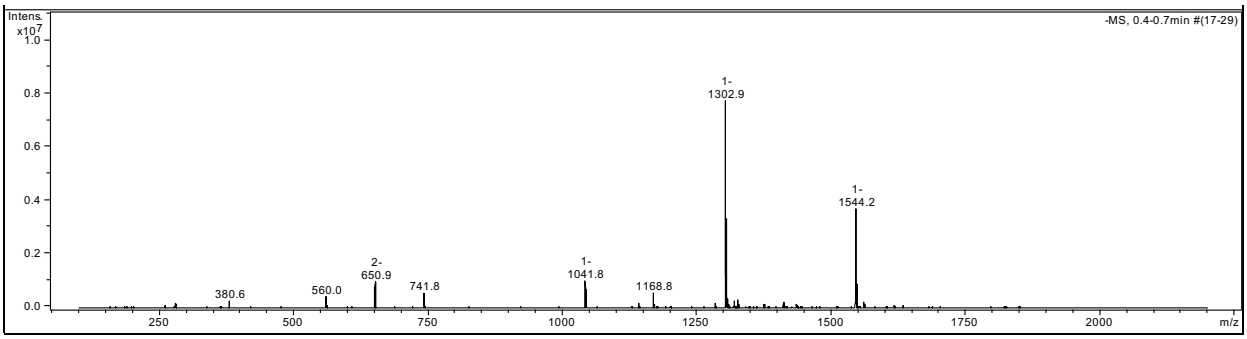

Figure 5.63 ESI-MS (-) spectrum of V6O-L-Phe in CH3CN.

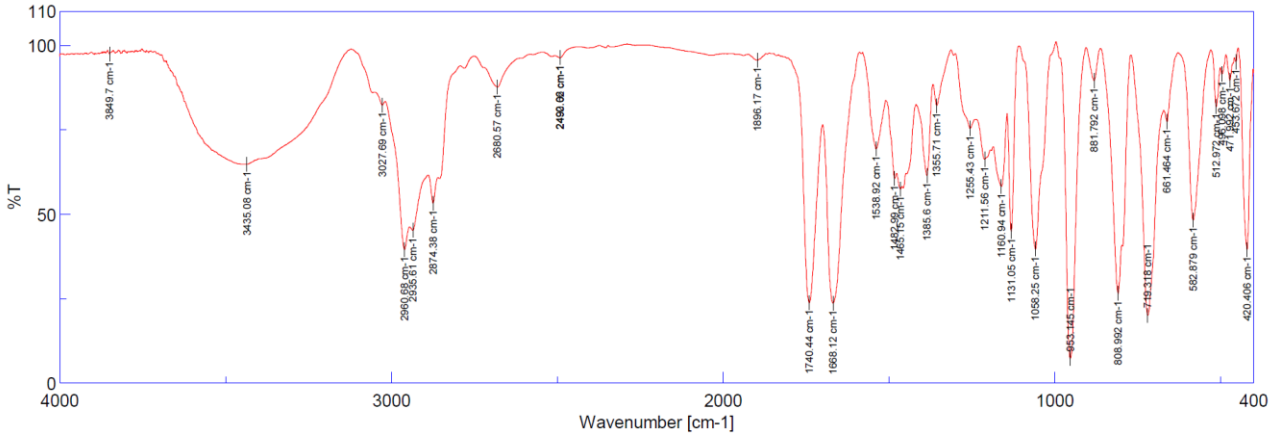

Figure 5.64 The FT-IR spectrum of V_6O- L-Phe.

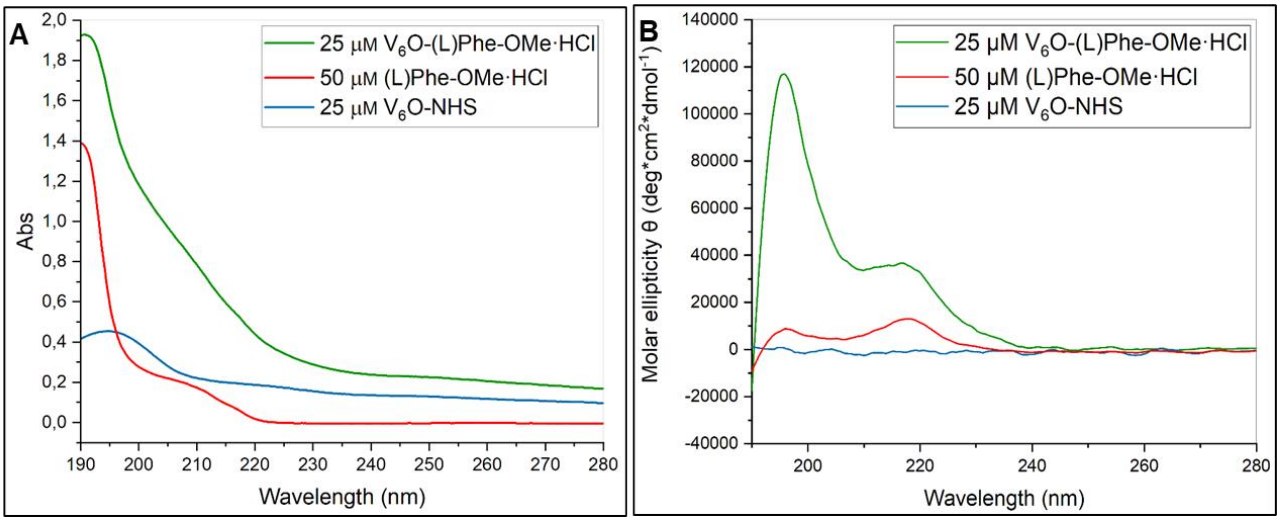

Figure 5.65 A) UV spectra of V6O-PheOMe, and the single precursors at tied concentrations (double for the amino acid). B) Molar ellipticity of V6O-NHS, V6O-Phe (coupling product), and the single amino acid phenylalanine (Phe).

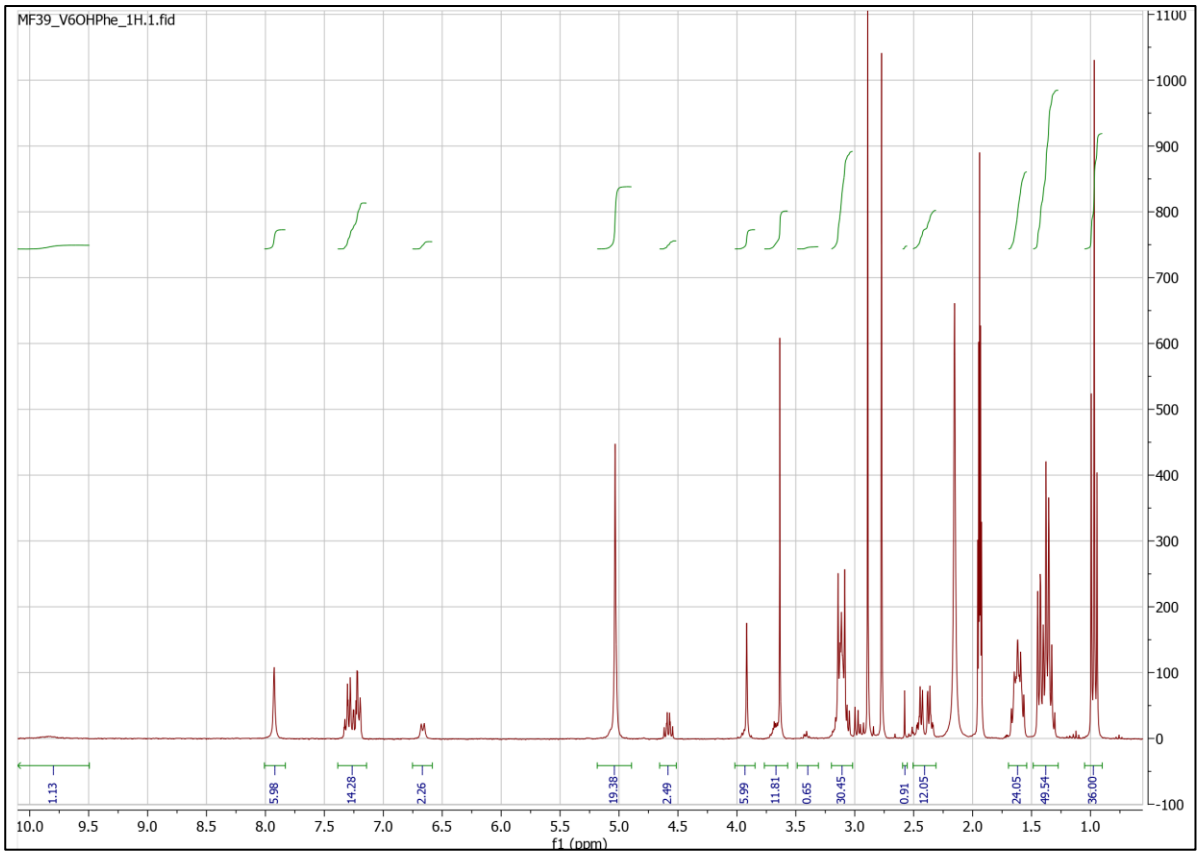

Figure 5.66 The 1H NMR 300 (CD3CN) of V6O-L-Phe.

Synthesis 17A

Synthesis of "V_6O-DB" Compounds 12

$[(C_4H_9)_4N]_2[V_6O_{13}\{(OCH_2)_3CCH_2OOCCH_2CH_2CO(C_{49}H_{68}N_{13}O_9)\}_2]$

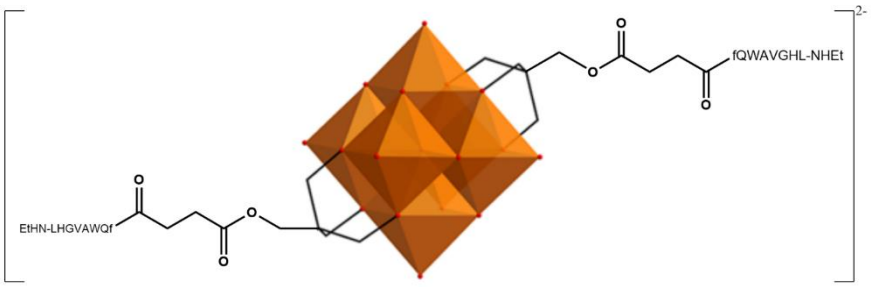

Reaction:

$[(C_4H_9)_4N]_2[V_6O_{13}\{(OCH_2)_3CCH_2OOCCH_2CH_2CO(C_4H_4NO_3)\}_2] + 2\ C_{49}H_{68}N_{13}O_9 \xrightarrow[DMF\ R.T.]{DIPEA} [(C_4H_9)_4N]_2[V_6O_{13}\{(OCH_2)_3CCH_2OOCCH_2CH_2CO(C_{49}H_{68}N_{13}O_9)\}_2]$

Procedure:

V_6O-NHS (8.17 mg; 0.0049 mmol) was dissolved in 0.8 mL of DMF in a vial. Dembesin-1 (10.05 mg, 0.010 mmol) and DIPEA (9.6 mg, 13 μL, 0.075 mmol) were added to the reaction mixture in order, and the orange solution has been stirred for 24 hours at room temperature. Then the vial was transferred into diethyl ether atmosphere to crystallize. After a few hours, the white powder was recovered and washed with diethyl ether for four times and then dried under vacuum, finally weighted the product (MM = 3395.3 g/mol, 0.01217 g, 73% yield).

Analysis & Characterization:

FTIR (KBr, cm^{-1}): 3291 (s, br), 3061 (w), 2962 (m), 2933 (m), 2872 (m), 1738 (m), 1647 (s, br), 1533 (s, br), 1452 (w), 1389 (w), 1233 (w), 1160 (w), 1130 (w), 1055 (m), 955 (s), 880 (w), 809 (m), 716 (m), 586 (m), 420 (m).

ESI-MS (-) CH_3CN: 1455.9 ($[M-2TBA]^{2-}$)

UV (TFE/H_2O) 1:10: Maximum at 191.5 nm (ε_{191}=169600 $cm^{-1}M^{-1}$) and a shoulder at 218 nm (ε_{212}=112800 $cm^{-1}M^{-1}$).

CD (TFE/H_2O) 1:10: Minimum located at 207 nm ([θ]=-102122 deg*cm^2*$dmol^{-1}$), and the maximum at 192 nm ([θ]=114616 deg*cm^2*$dmol^{-1}$).

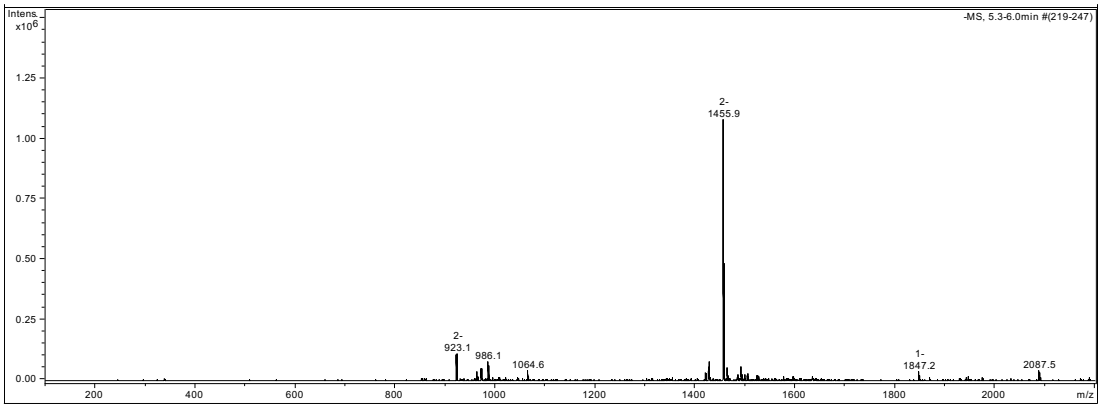

Figure 5.67 ESI-MS (-) spectrum of V6O-DB in CH3CN.

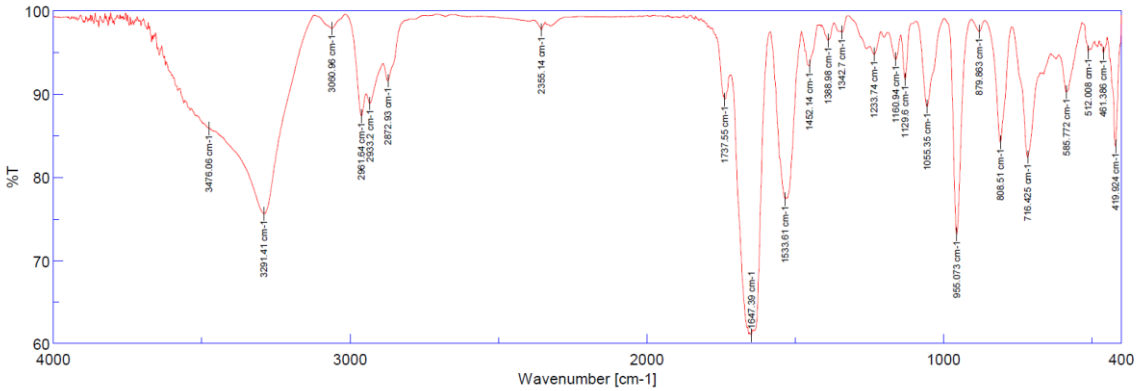

Figure 5.68 FT-IR spectrum of V6O-DB.

Table 5.7 Proton resonances of V_6O-DB.

AA	NH (ppm)	CHα (ppm)	Rest of the chain(ppm)
Gln	8.32	4.05	-CH2β (diastereotopico) 1.75, 1.85 -CH2γ 1.55 -NH2 not detected
D-Phe	8.28	4.43	-CH2β (diastereotopico) 2.79, 2.90 Unassigned aromatics
Trp	7.94	4.49	-CH2β (diastereotopico) 2.98, 3.15 Unassigned aromatics
Ala	7.93	4.35	-CH3 1.20
Val	7.63	4.15	-CHβ 2.00 (-CH3γ)2 0.85
Gly	8.22	-CH2α 3.73	/
His	8.02	4.48	-CH2β 2.93 -NH aromatic not detected -CH Unassigned aromatics
Leu	7.94	4.15	-CH2β 1.47 -CHγ 0.81 (-CH3δ)2 not detected
NHEt	8.08	-CH2α 3.07	-CH3β 0.99

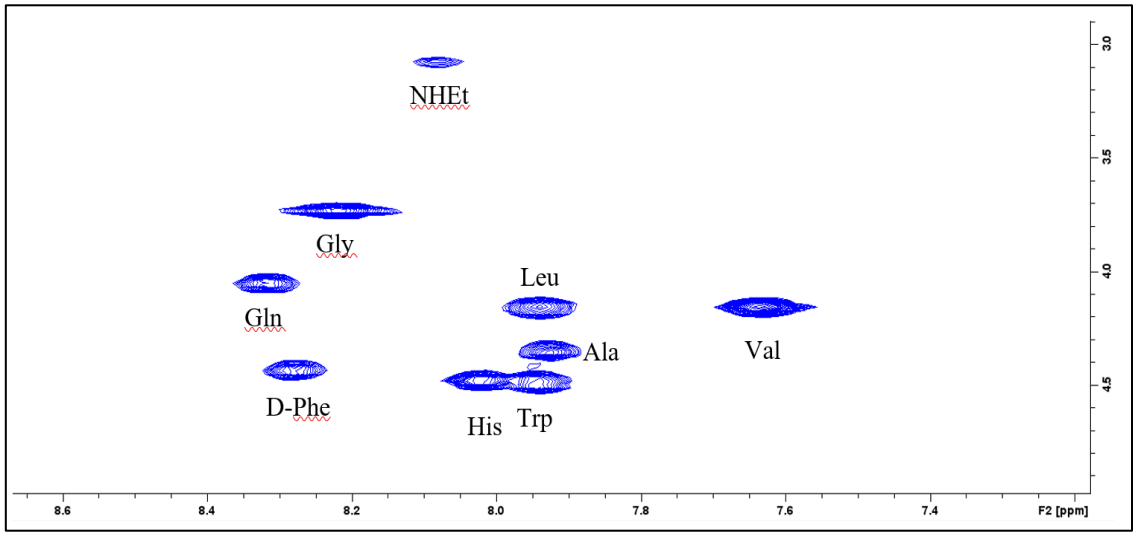

Figure 5.69 COSY spectrum, 2D ^{1}H-NMR of V_6O-DB (150 µM) in d6-DMSO.

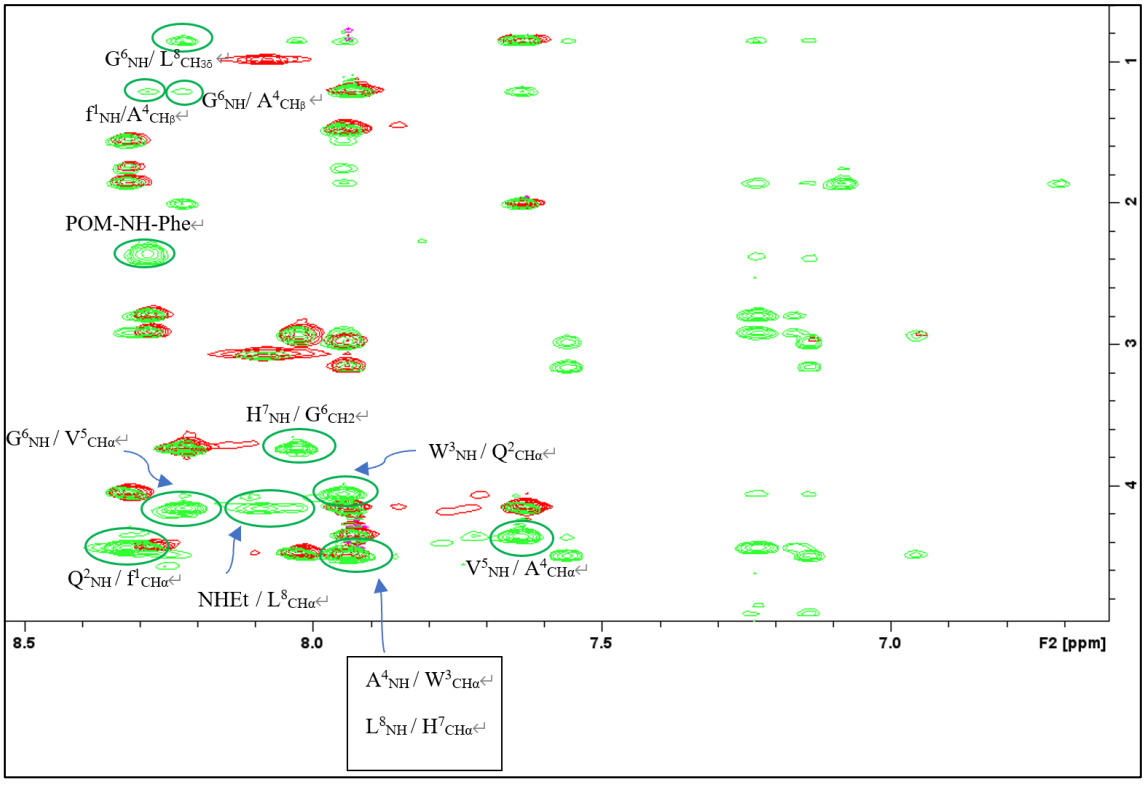

Figure 5.70 1H ROESY of V_6O-DB (in green) overlapped with TOCSY (in red) in d_6-DMSO.

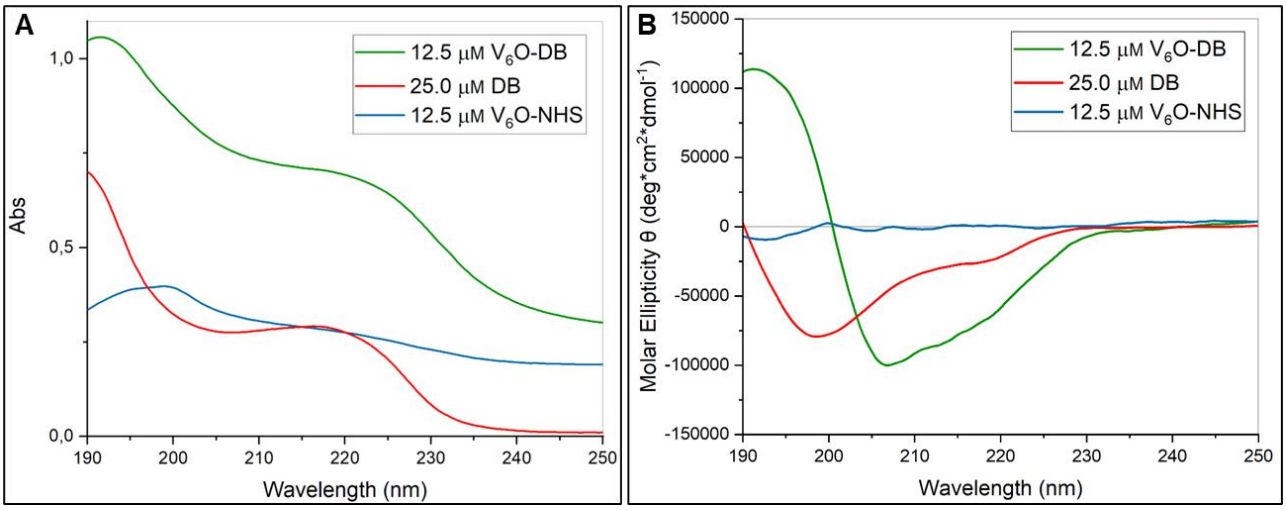

Figure 5.71 A) UV spectrum of V_6O-DB, V_6O-NHS and Demobesin-1 in TFE/H_2O 1:10. B) Molar Ellipticity graph of V_6O-DB, V_6O-NHS and Demobesin-1 in TFE/H_2O 1:10.

Synthesis 18A

Synthesis of "V_6O- EEEEβAla-fQWAVGHL-NHEt" Compounds 13

$[(C_4H_9)_4N]_2[V_6O_{13}\{(OCH_2)_3CCH_2OOCCH_2CH_2CO(C_{72}H_{101}N_{18}O_{22})\}_2]$

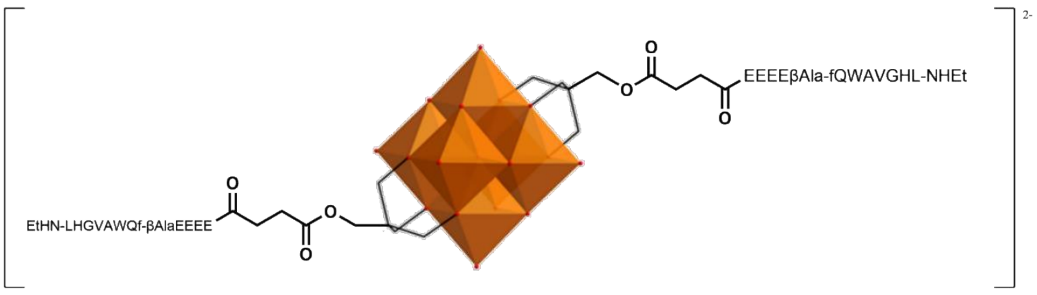

Reaction:

$[(C_4H_9)_4N]_2[V_6O_{13}\{(OCH_2)_3CCH_2OOCCH_2CH_2CO(C_4H_4NO_3)\}_2] + 2\ C_{72}H_{101}N_{18}O_{22} \xrightarrow[DMF\ R.T.]{DIPEA} [(C_4H_9)_4N]_2[V_6O_{13}\{(OCH_2)_3CCH_2OOCCH_2CH_2CO(C_{72}H_{101}N_{18}O_{22})\}_2]$

Procedure:

V_6O-NHS (13.64 mg; 0.00823 mmol) was dissolved in 1 mL of DMF in a vial. In order, EEEEβAla-fQWAVGHL-NHEt (29.93 mg, 0.019 mmol) and DIPEA (14.8 mg, 20 μL, 0.11 mmol) were added to the reaction mixture, and the orange solution was stirred for 24 hours at room temperature. Then the vial was put under diethyl ether atmosphere to crystallize. After 72 hours the light orange product was recovered and washed with approximately diethyl ether for three times and then dried under vacuum and finally weighted (MM = 4571 g/mol, 0.04277 g, 92% yield).

Analysis & Characterization:

FTIR (KBr, cm^{-1}): 3440 (m, br), 3289 (s), 3056 (w), 2955 (m), 2934 (m), 2879 (w), 1659 (s), 1539 (m), 1387 (m), 1255 (m), 1130 (w), 1052 (w), 958 (s), 808 (m), 718 (w), 578 (w), 473 (w), 426 (w).

ESI-MS (-) CH_3CN: 2163 ($[M\text{-}TBA\text{-}H]^{2-}$), 2043 ($[M\text{-}2TBA]^{2-}$), 1362 ($[M\text{-}2TBA\text{-}H]^{3-}$)

UV (TFE/H_2O 1:10): Maximum <190 nm (ε_{190}=289600 $cm^{-1}M^{-1}$) and a shoulder at 214 nm (ε_{214}=137600 $cm^{-1}M^{-1}$).

CD (Pure TFE): Minimum located at 206 nm ([θ]=-338766 deg*cm^2*$dmol^{-1}$), while the maximum is at 192 nm ([θ]=756593 deg*cm^2*$dmol^{-1}$).

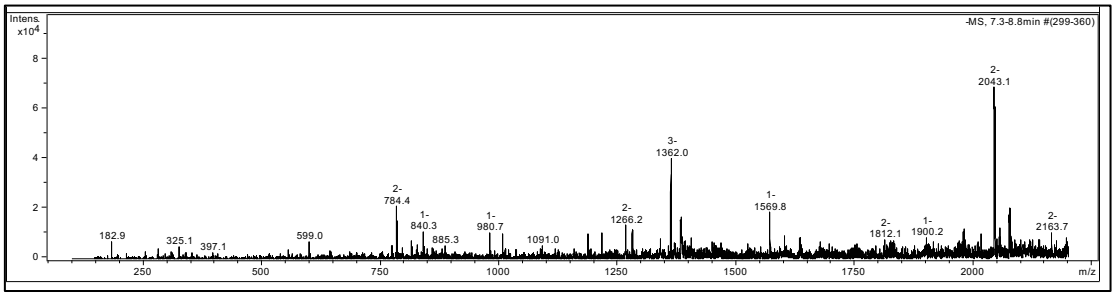

Figure 5.72 ESI-MS spectrum of V6O-NHS.

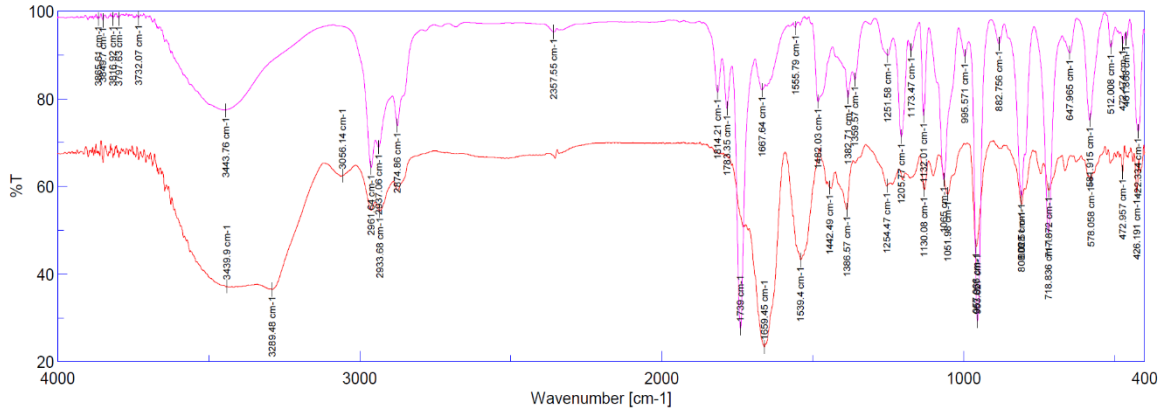

Figure 5.73 *FT-IR spectrum of the reagent V6O-NHS (in purple) and the final coupling product V6O-EEEEβAlaDB (in red).*

Table 5.8. Proton resonances of "V6O-EEEEβAla-fQWAVGHL-NHEt"

AA	NH (ppm)	CHα (ppm)	Rest of the chain(ppm)
Glu1	8.14	4.23	-CH2β 2.24 -CH2γ (diastereotopico) 1.72, 1.87
Glu2	8.06	4.19	-CH2β 2.25 -CH2γ (diastereotopico)

			1.77, 1.90
Glu3	7.97	4.21	-CH2β 2.24 -CH2γ (diastereotopico) 1.75, 1.90
Glu4	7.90	4.14	-CH2β 2.20 -CH2γ (diastereotopico) 1.73, 1.86
βAla	7.84	-CH2α 3.16	-CH2β 2.27
D-Phe	8.29	4.45	-CH2β (diastereotopico) 2.94, 2.78 Aromatics not observed
Gln	8.34	4.10	-CH2β (diastereotopico) 1.78, 1.89 -CH2γ 1.59
Trp	8.03	4.48	-CH2β (diastereotopico) 3.00, 3.17 Unassigned aromatics
Ala	7.99	4.38	-CH3 1.21
Val	7.68	4.18	-CHβ 2.01 (-CH3γ)2 0.86
Gly	8.24	-CH2α 3.74	/
His	8.02	4.46	-CH2β 2.90 -NH aromatic not detected

			-CH Unassigned aromatics
Leu	7.93	4.14	-CH2β 1.48 -CHγ 0.81 (-CH3δ)2 not detected
NHEt	8.13	-CH2α 3.08	-CH3β 1.00

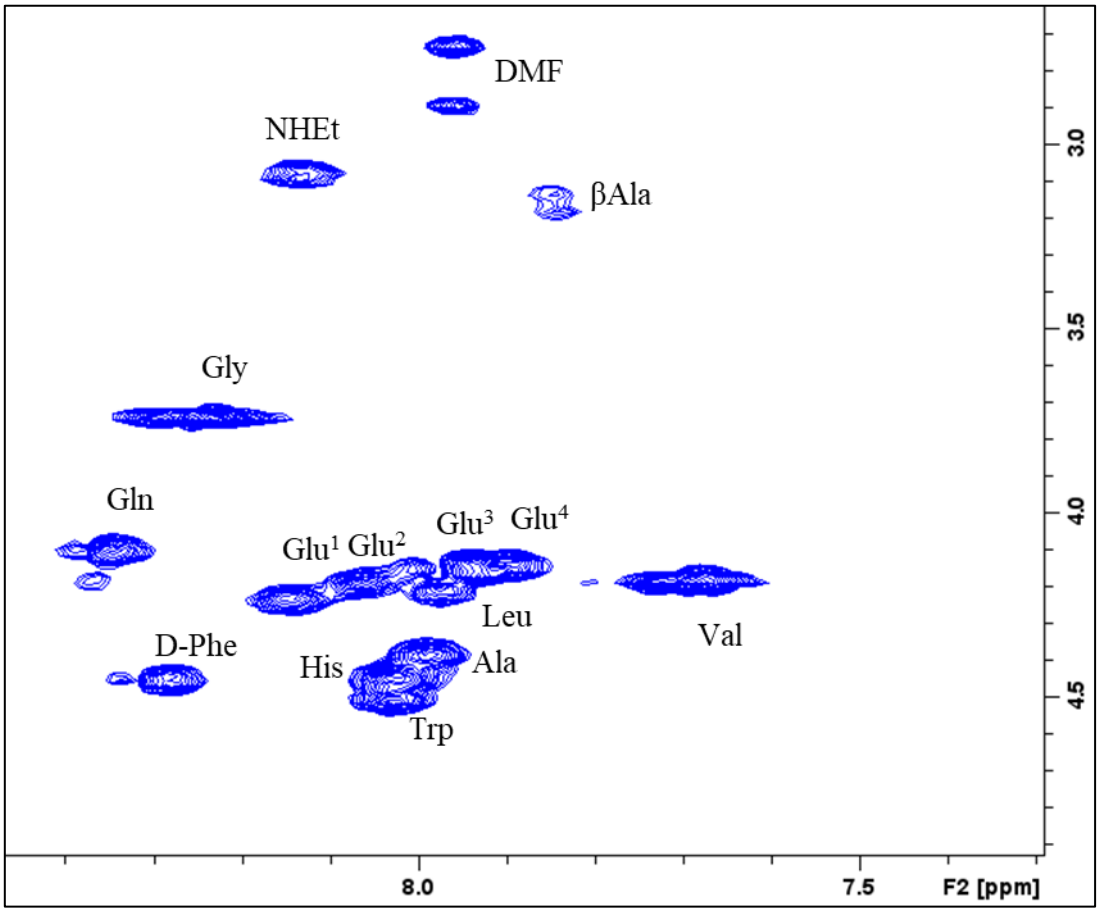

Figure 5.74 COSY spectrum, 2D 1H-NMR of V6O-EEEEβAlaDB (150 µM) in d6-DMSO.

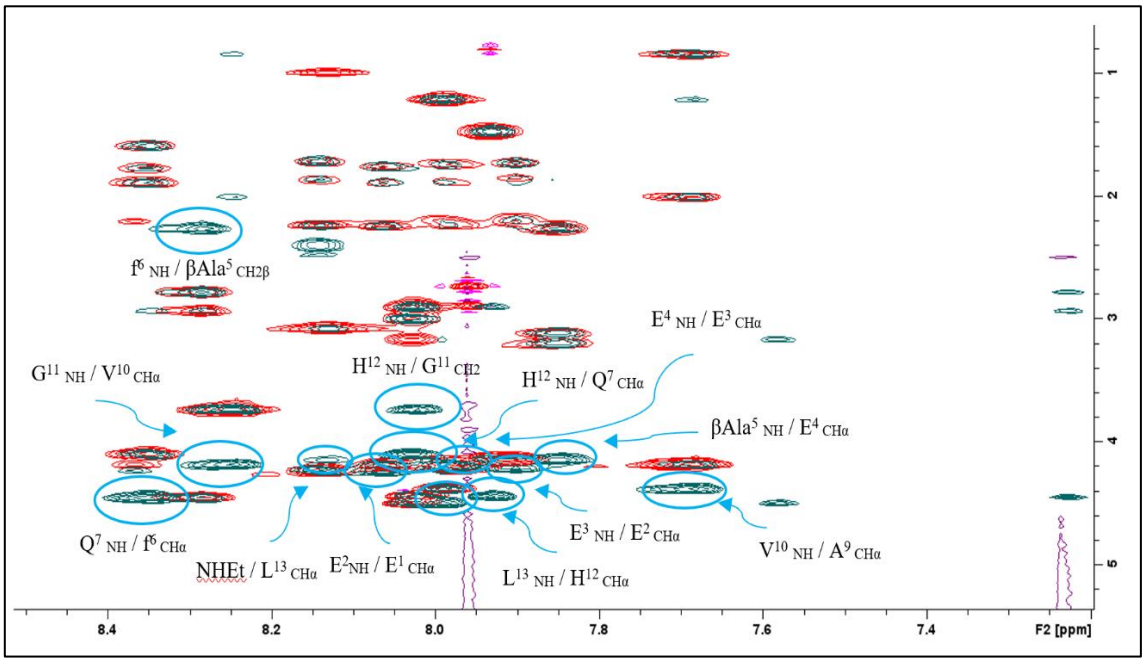

Figure 5.75 ^{1}H ROESY of V_6O-EEEEβAlaDB (in blue) overlapped with TOCSY (in red) in d6-DMSO. The special connection is between His and Gln.

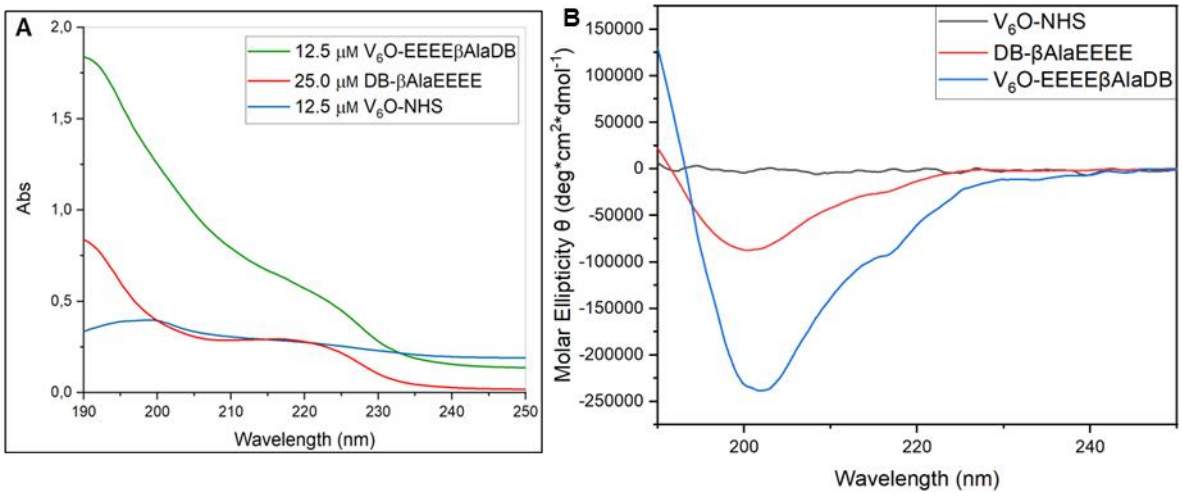

Figure 5.76 A) UV spectrum of V_6O-EEEEβAlaDB, V_6O-NHS and DB-βAlaEEEE in TFE/H2O 1:10. B) Molar Ellipticity graph of V6O-EEEEβAlaDB, V6O-NHS and DB-βAlaEEEE in TFE/H2O 1:10.

Synthesis 19A

Synthesis of "V_6O-TtdsDB" Compounds 14

$[(C_4H_9)_4N]_3[V_6O_{13}\{(OCH_2)_3CCH_2OOCCH_2CH_2CO(C_{63}H_{94}N_{15}O_{14})\}_2]$

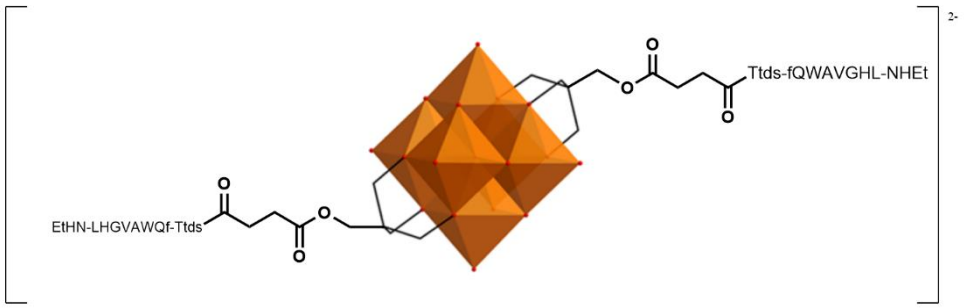

Reaction:

$[(C_4H_9)_4N]_2[V_6O_{13}\{(OCH_2)_3CCH_2OOCCH_2CH_2CO(C_4H_4NO_3)\}_2] + 2\ C_{63}H_{94}N_{15}O_{14}$

$\xrightarrow[DMF\ R.T.]{DIPEA} [(C_4H_9)_4N]_3[V_6O_{13}\{(OCH_2)_3CCH_2OOCCH_2CH_2CO(C_{63}H_{94}N_{15}O_{14})\}_2]$

Procedure:

V_6O-NHS (8.47 mg; 0.0051mmol) was dissolved in 0.8 mL of DMF in a vial. Ttds-fQWAVGHL-NHEt (15.15 mg, 0.012 mmol) and DIPEA (9.6 mg, 13 µL, 0.073 mmol) were added to the reaction mixture one by one, and the yellow-orange solution was stirred for 24 hours at room temperature. Then the vial was placed under diethyl ether atmosphere for the crystallization. After 96 h, the dark red product was recovered and washed with diethyl ether for four times and then dried under vacuum. finally weighted (MM = 4000.4 g/mol, 0.095 g, 46% yield).

Analysis & Characterization:

FTIR (KBr, cm^{-1}): 3429 (m, br), 3292 (s), 3071 (m), 2930 (m), 2874 (m), 1743 (m), 1664 (s), 1639 (s), 1541 (m), 1432 (w), 1386 (w), 1192 (w), 1139 (m), 1954 (m), 957 (s), 808 (m), 718 (m), 582 (m), 507 (w), 422 (m).

ESI-MS (-) CH_3CN: 1758.5 ($[M-2TBA]^{2-}$)

UV (TFE/H_2O 1:10): maximum at <190 nm (ε_{190}=289600 $cm^{-1}M^{-1}$) and shoulder at 218 nm (ε_{214}=120160 $cm^{-1}M^{-1}$).

CD (Pure TFE): The minimum for pure TFE is located at 206 nm ([θ]=-342728 $deg*cm^2*dmol^{-1}$), while the maximum is at 192 nm ([θ]=759366 $deg*cm^2*dmol^{-1}$)

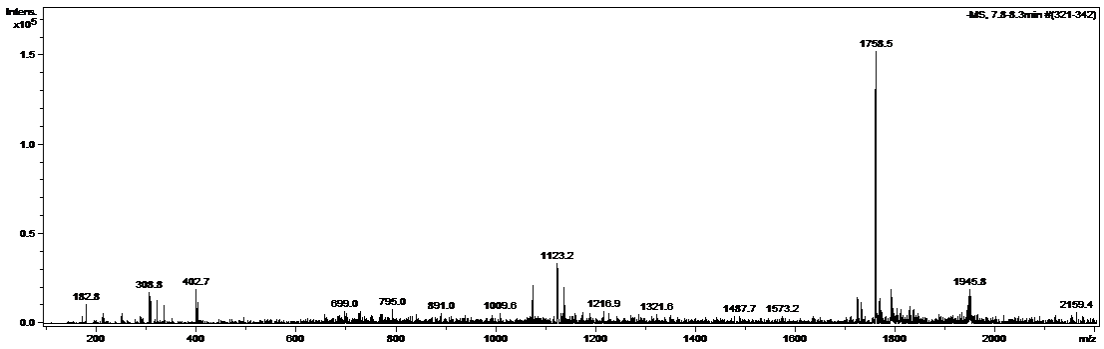

Figure 5.77 ESI-MS (-) spectrum of V6O-TtdsDB in CH3CN.

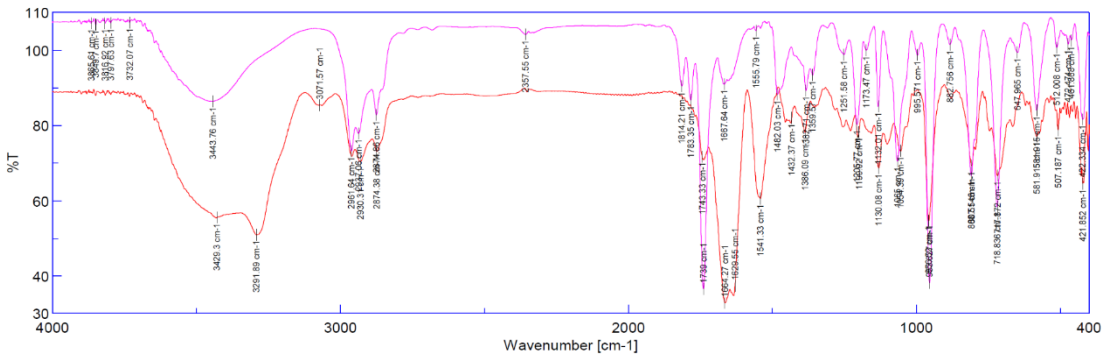

Figure 5.78 FT-IR spectrum of the reagent V6O-NHS (in purple) and the final coupling product V6O-TtdsDB (in red).

Table 5.9 Proton resonances of V6O-TtdsDB

AA	NH (ppm)	CHα (ppm)	Rest of the chain(ppm)
D-Phe	8.26	4.40	-CH2β (diastereotopico) 2.78, 2.94 Aromatics not observed
Gln	8.33	4.07	-CH2β (diastereotopico) 1.77, 1.89 -CH2γ 1.59
Trp	7.97	4.48	-CH2β (diastereotopico) 3.00, 3.17 Unassigned aromatics
Ala	7.92	4.36	-CH3 1.21
Val	7.65	4.17	-CHβ 2.00 (-CH3γ)2
Gly	8.22	-CH2α 3.73	/
			-CH2β 2.92

His	8.02	4.47	-NH aromatic not detected -CH Unassigned aromatics
Leu	7.95	4.13	-CH2β 1.47 -CHγ 0.81 (-CH3δ)2 not detected
NH-Ttds	7.79	-CH2α 3.04	-CH2β 1.58 -CH2γ 3.35
NHEt	8.11	-CH2α 3.08	-CH3β 1.00

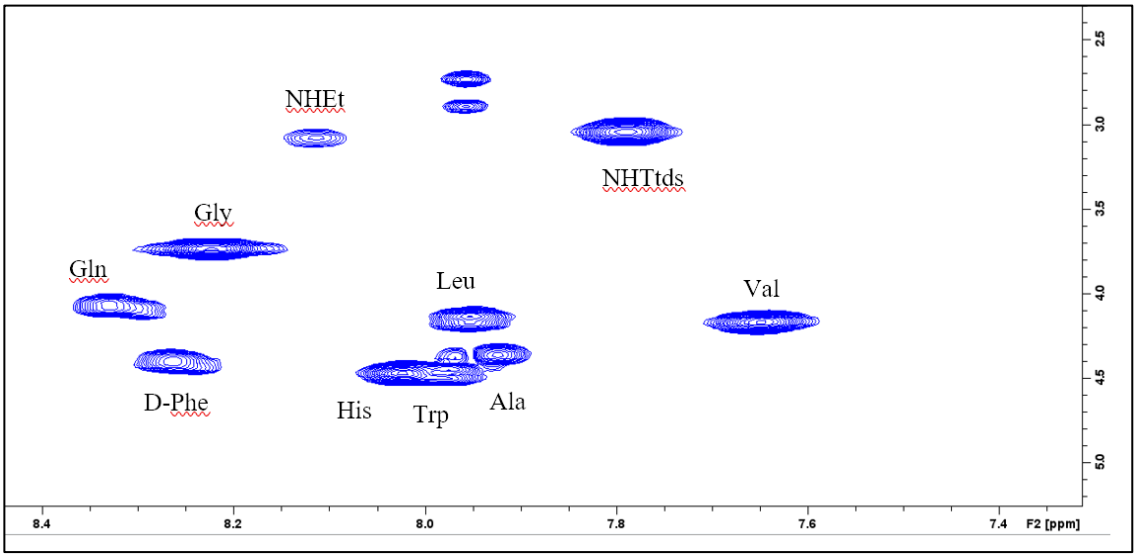

Figure 5.79 2D 1H NMR COSY of V6O-TtdsDB in d6-DMSO.

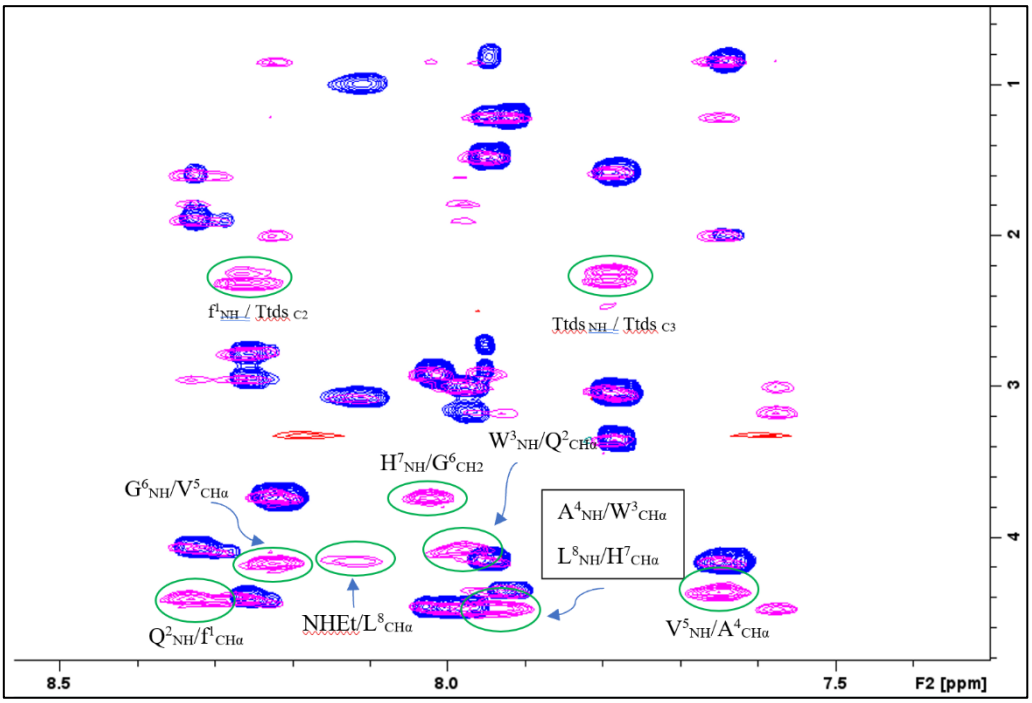

Figure 5.80 2D 1H NMR TOCSY (pink) and ROESY (blue) of V6O-TtdsDB.

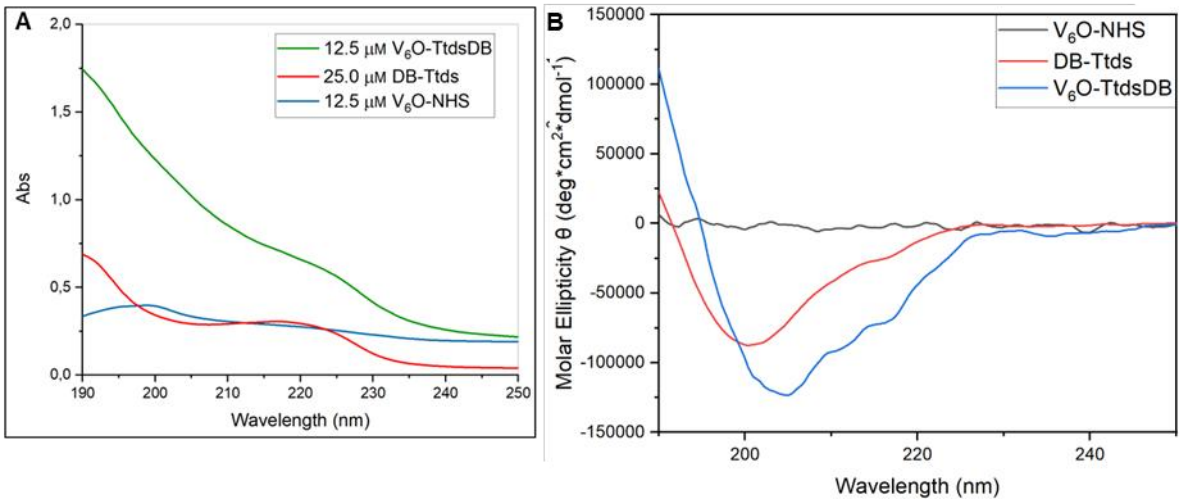

Figure 5.81 A) UV spectrum of V6O-TtdsDB, V6O-NHS and DB-Ttds in TFE/H2O 1:10. B) Molar Ellipticity graph of V6O-Ttds, V6O-NHS and DB-Ttds in TFE/H2O 1:10.

Synthesis 20A

Synthesis of "V_6O-EEEEβAlaTtdsDB" Compounds 15

$[(C_4H_9)_4N]_2[V_6O_{13}\{(OCH_2)_3CCH_2OOCCH_2CH_2CO(C_{86}H_{127}N_{20}O_{27})\}_2]$

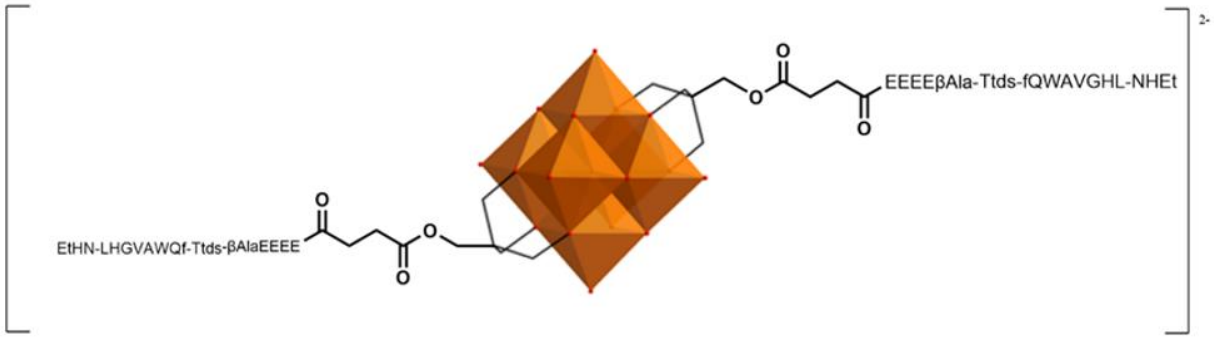

Reaction:

$[(C_4H_9)_4N]_2[V6\text{-}O\text{-}O_{13}\{(OCH_2)_3CCH_2OOCCH_2CH_2CO(C_4H_4NO_3)\}_2] + 2\ C_{86}H_{127}N_{20}O_{27}$

$\xrightarrow[DMF\ R.T.]{DIPEA} [(C_4H_9)_4N]_2[V_6O_{13}\{(OCH_2)_3CCH_2OOCCH_2CH_2CO(C_{86}H_{127}N_{20}O_{27})\}_2]$

Procedure:

V_6O-NHS (7.58mg; 0.00457 mmol) was dissolved in 0.8 mL of DMF in a vial. Ttds-EEEEβAla-fQWAVGHL-NHEt (6.72mg, 0.00358 mmol) and DIPEA (4.45 mg, 6 µL, 0.06 mmol) were added to the system. The mixture was stirred for 24 hours at room temperature. Then the vial was put under diethyl ether atmosphere to make the crystallization. 1 days later, the dark red product was observed and washed with diethyl ether and then dried under vacuum. (MM = 5175.7 g/mol, 6.75 g, 84% yield).

Analysis & Characterization:

FTIR (KBr, cm^{-1}): 3412 (m, br), 3287 (s), 3061(m), 2924 (m), 2873 (m), 1637 (s), 1536 (s), 1449 (w), 1390 (w), 1257 (w), 1057 (m), 956 (s), 879 808 (m), 713 (m), 626 (w) 588 (w), 507 (w), 423 (m).

ESI-MS (-) CH_3CN: ($[M-2TBA-2H_2O-7H+Na^+]^{7-}$ = 665.9)

UV (TFE/H_2O 1:10): maximum at <190 nm ($\varepsilon190=688700\ cm^{-1}M^{-1}$) and shoulder at 218 nm ($\varepsilon218=350635\ cm^{-1}M^{-1}$).

CD (Pure TFE): The minimum for pure TFE is located at 205 nm ($[\theta]= -699199\ deg*cm^2*dmol^{-1}$), while the maximum is at 193 nm ($[\theta]= 1540910\ deg*cm^2*dmol^{-1}$)

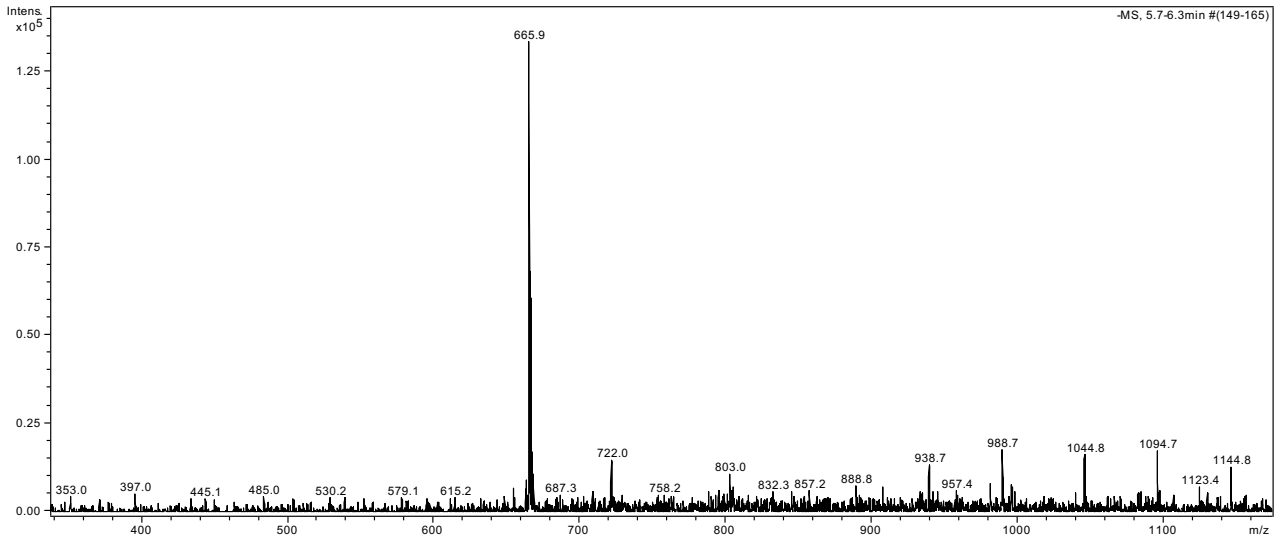

Figure 5.82 ESI-MS (-) spectrum of V6O-EEEEβAlaTtdsDB in CH3CN.

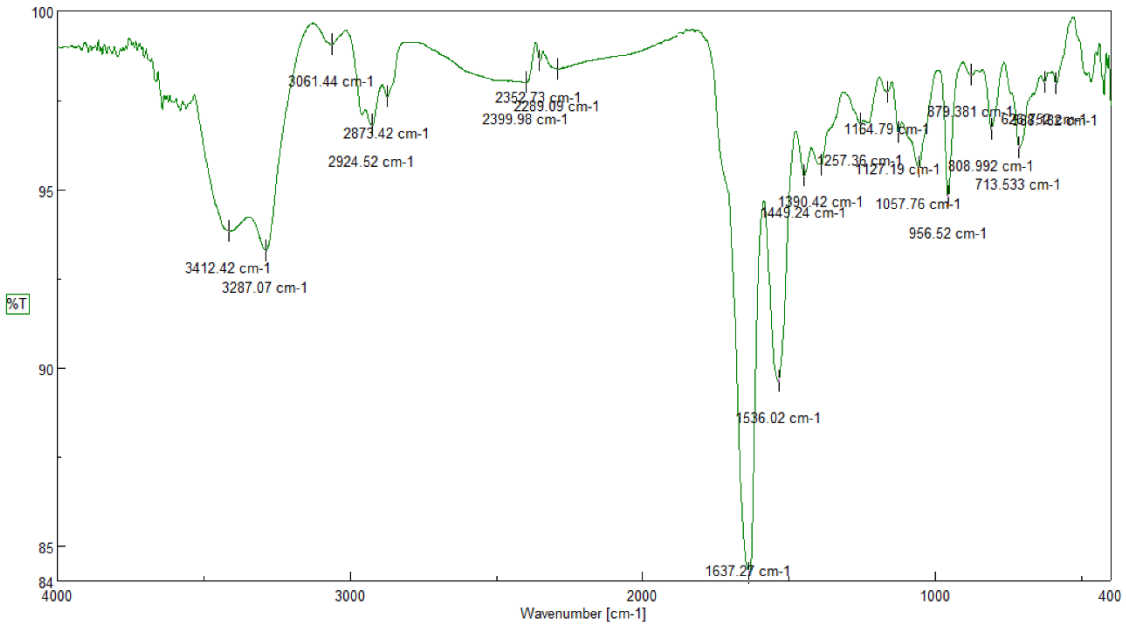

Figure 5.83 FT-IR spectrum of product V6O-TtdsEEEEβAlaDB.

Table 6.0 Proton resonances of V6O-EEEEβAlaTtdsDB.

AA	NH (ppm)	CHα (ppm)	Rest of the chain(ppm)
Glu1	8.27	4.14	-CH2β 2.25 -CH2γ 1.82
Glu2	8.20	4.16	-CH2β 2.25 -CH2γ 1.82
Glu3	7.87	4.17	-CH2β 2.21 -CH2γ 1.83
Glu4	7.78	4.12	-CH2β 2.20 -CH2γ 1.79
βAla	7.76	-CH2α 3.15	-CH2β 2.25
D-Phe	8.32	4.44	-CH2β (diastereotopic) 2.92, 2.77 Aromatics not observed
Gln	8.37	4.09	-CH2β (diastereotopic)

			1.76, 1.88 -CH2γ 1.56
Trp	8.02	4.51	-CH2β (diastereotopico) 2.99, 3.16 Unassigned aromatics
Ala	7.97	4.38	-CH3 1.20
Val	7.71	4.18	-CHβ 2.00 (-CH3γ)2 0.85
Gly	8.27	-CH2α 3.73	/
His	8.03	4.43	-CH2β 2.89 -NH aromatic not detected -CH Unassigned aromatics
Leu	7.93	4.14	-CH2β 1.47 -CHγ 0.80 (-CH3δ)2 not detected
NH-Ttds	7.93	3.05	-CH2β 1.59 -CH2γ 3.37
NH-V6-O-	7.80	-CH2α 3.05	-CH2β 1.59 -CH2γ 3.37
NHEt	8.12	-CH2α 3.07	-CH3β 0.99

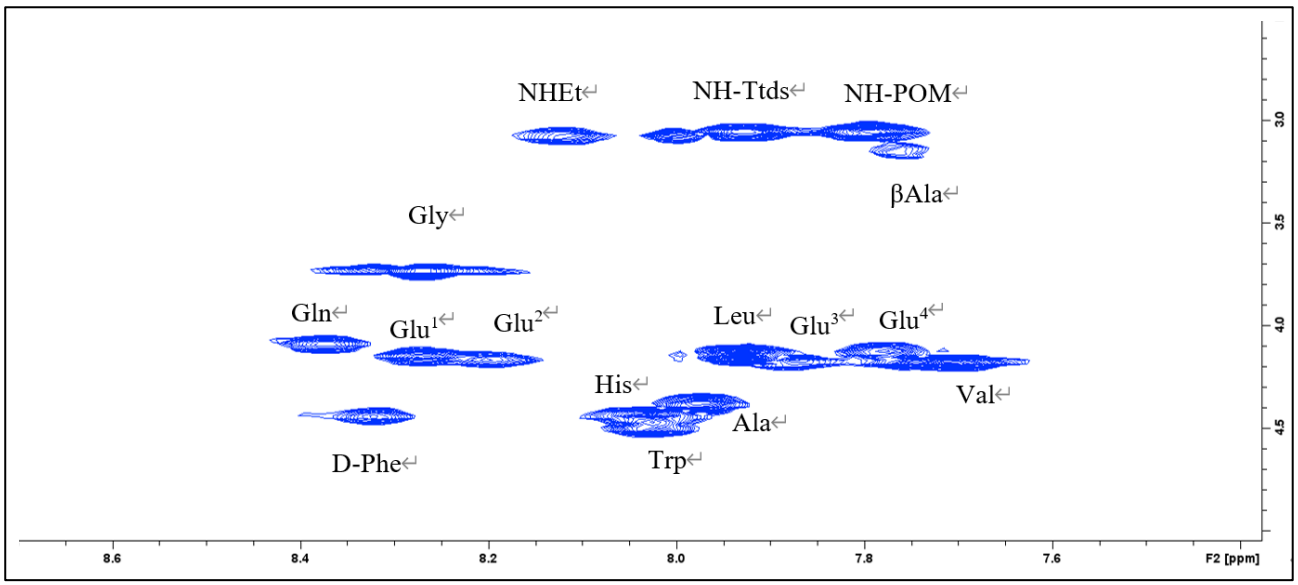

Figure 5.84 2D 1H NMR (COSY) of V6O-EEEEβAlaTtdsDB in d6-DMSO.

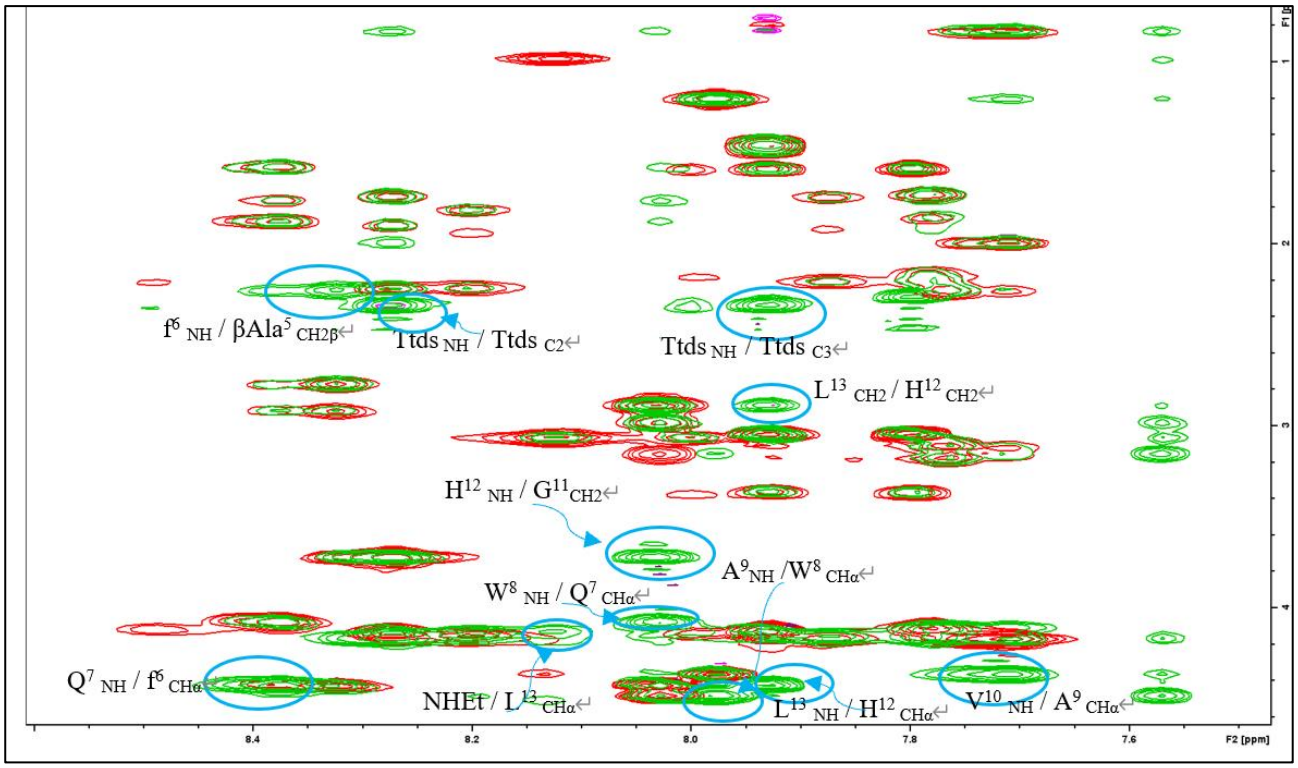

Figure 5.85 2D ^{1}H NMR (TOCSY and ROESY) of V6O-EEEEβAlaTtdsDB in d6-DMSO.

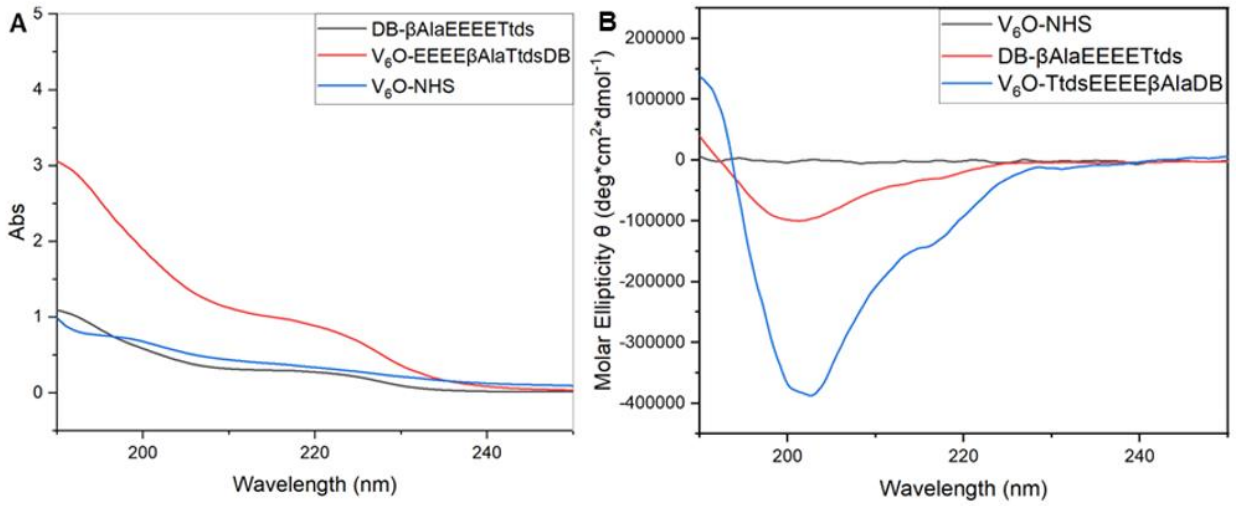

Figure 5.86 A) UV spectrum of V6O-TtdsEEEEβAlaDB, V6O-NHS and DB-βAlaEEEETtds in TFE/H2O 1:10. B)Molar Ellipticity graph of V6O-TtdsEEEEβAlaDB, V6O-NHS and DB-βAlaEEEETtds in TFE/H2O 1:10.

Circular Dichroism experiments

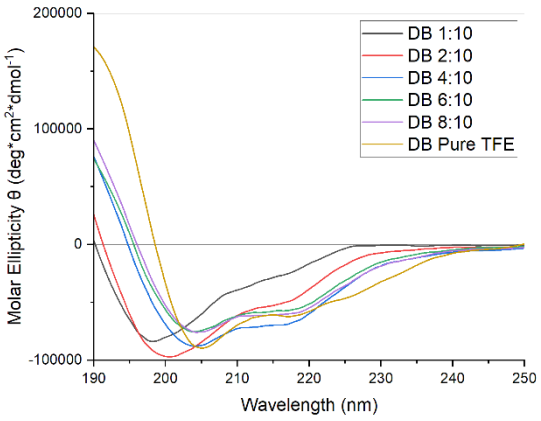

Figure 5.87 Far-UV CD spectra of peptide 1(25 μM) at variable % of trifluoroethanol in water.

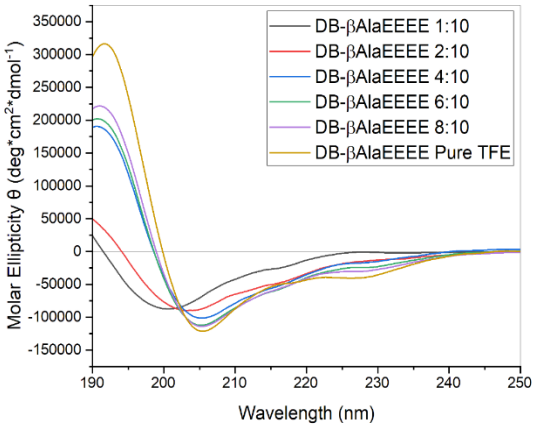

Figure 5.88 Far-UV CD spectra of peptide 2 (25 µM) at variable % of trifluoroethanol in water.

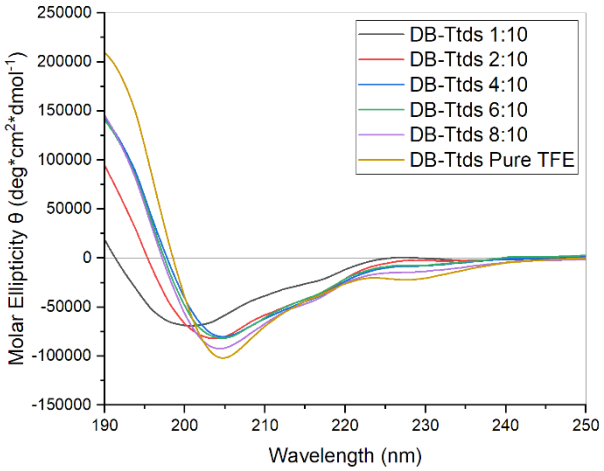

Figure 5.89 Far-UV CD spectra of peptide 3 (25 µM) at variable % of trifluoroethanol in water

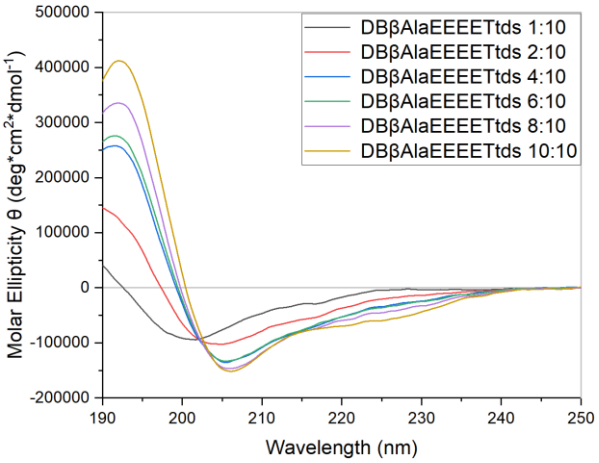

Figure 5.90 Far-UV CD spectra of peptide 4 (25 μM) at variable % of trifluoroethanol in water

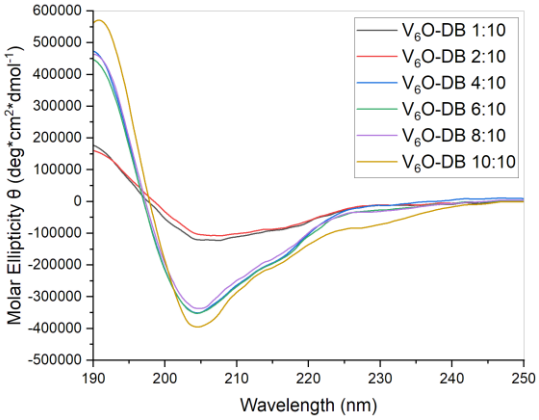

Figure 5.91 Far-UV CD spectra of V6O-DB (12.5 μM) at variable % of trifluoroethanol in water.

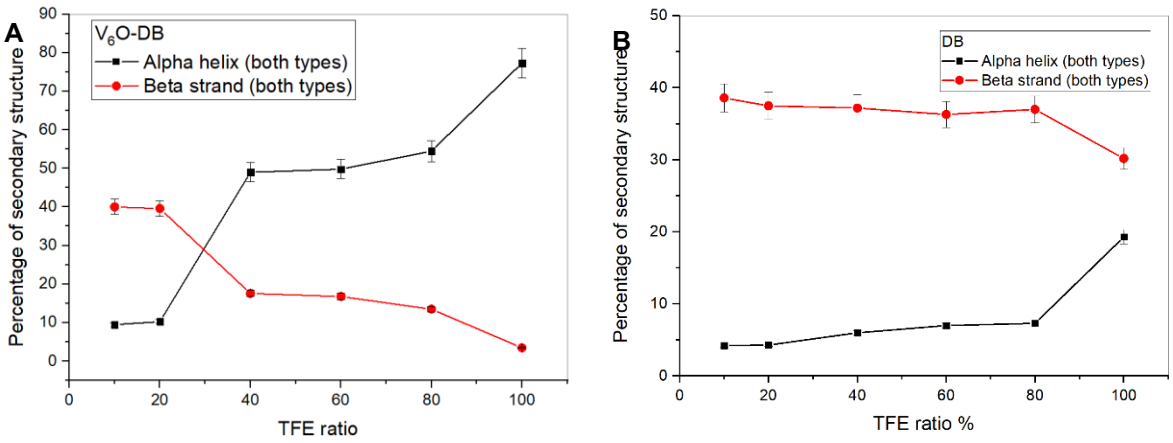

Figure 5.92 Percentage of α-helix and β-strand for the V6O-DB A) and DB B) at different TFE/H2O percentages: 1:10, 2:20, 4:10, 6:10, 8:10, TFE pure.

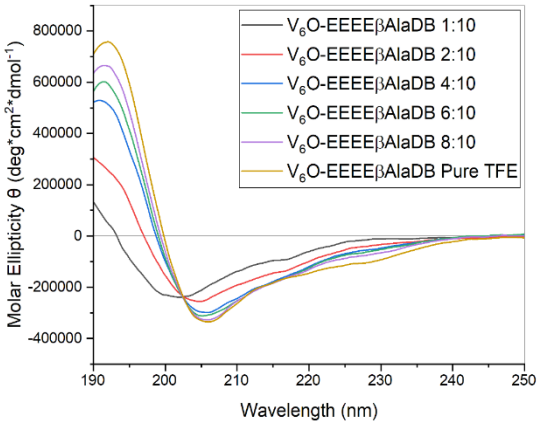

Figure 5.93 Far-UV CD spectra of V6O-EEEEβAlaDB (12.5 μM) at variable % of trifluoroethanol in water.

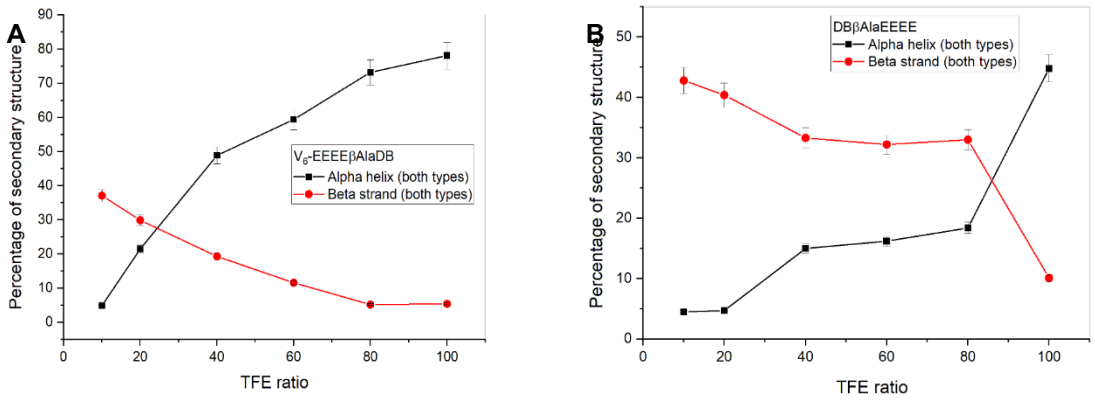

Figure 5.94 Percentage of α-helix and β-strand for the V6O-EEEEβAlaDB A) and peptide 2 B) at different TFE/H2O percentages: 1:10, 2:20, 4:10, 6:10, 8:10, TFE pure.

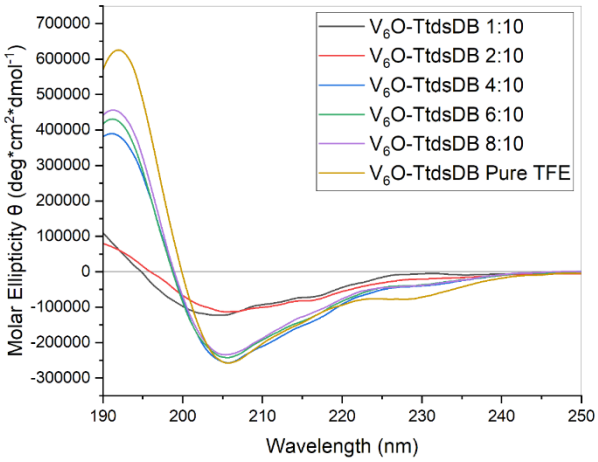

Figure 5.95 Far-UV CD spectra of V6O-TtdsDB (12.5 μM) at variable % of trifluoroethanol in water.

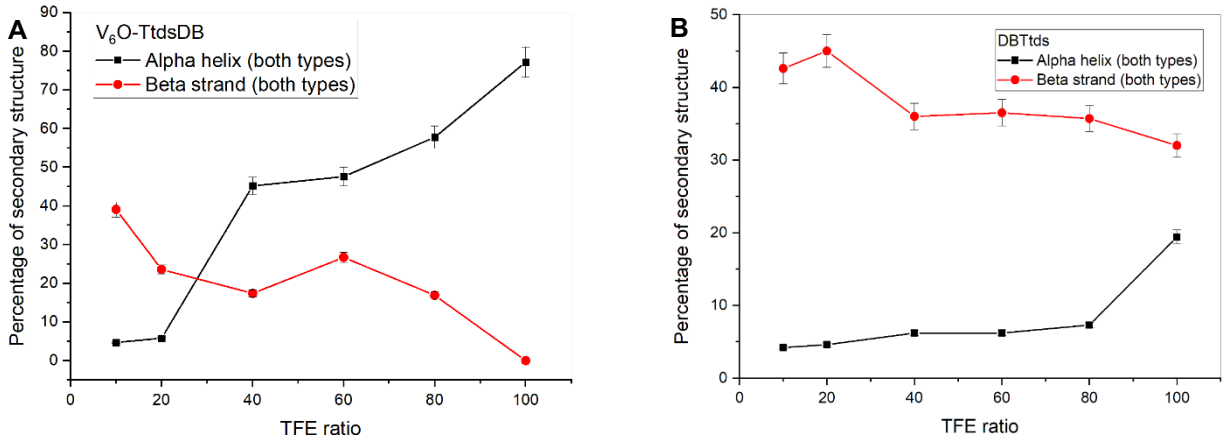

Figure 5.96 Percentage of α-helix and β-strand for the V6O-TtdsDB (A) and peptide 3 (B) at different TFE/H2O percentages: 1:10, 2:20, 4:10, 6:10, 8:10, TFE pure.

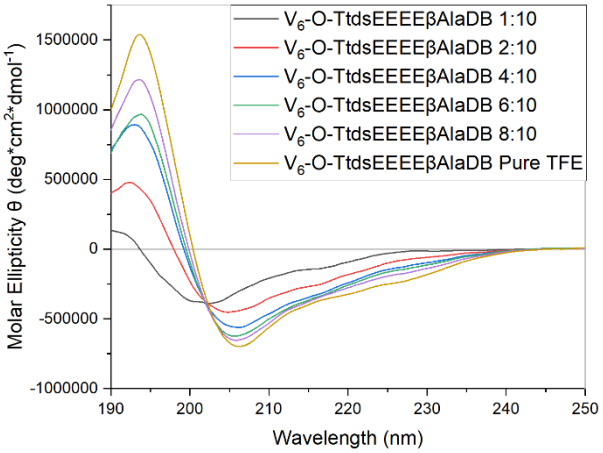

Figure 5.97 Far-UV CD spectra of V6O-EEEEβAlaTtdsDB (12.5 μM) at variable % of trifluoroethanol in water.

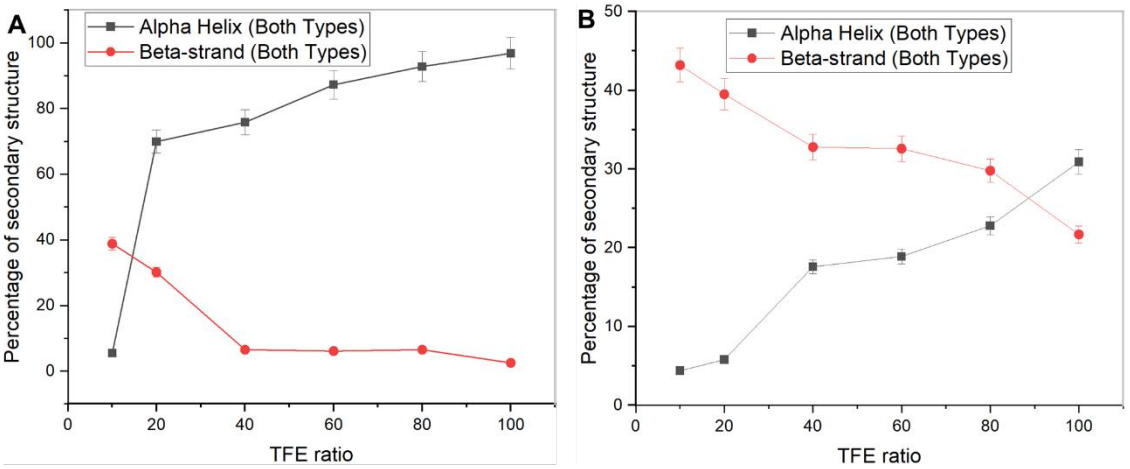

Figure 5.98 Percentage of α-helix and β-strand for the V6O-TtdsEEEEβAlaDB (A) and the Ttds DBβAlaEEEETtds (B) at different TFE/H2O percentages: 1:10, 2:20, 4:10, 6:10, 8:10, TFE pure.

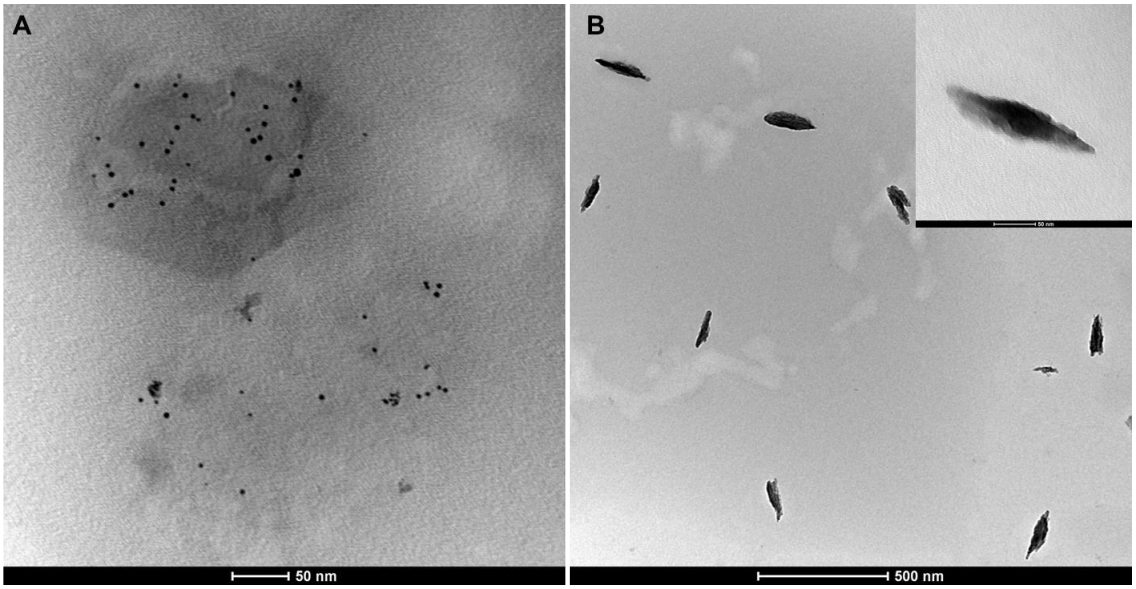

Figure 5.99 TEM measurements, 10^{-4} M solutions of A) V_6OH, B) V_6O-Phe in DMSO/water.

SYNTHESIS 21A:

Synthesis of the cyclic peptide 5 c(RGDfK)

The the cyclic peptide 5 was synthesized by coupling sequentially Fmoc-Gly-OH, Fmoc-Arg (Pbf)-OH, Fmoc-Lys (Boc)-OH and Fmoc-D-Phe -OH on the resin (H-Asp (OtBu)-2Cl-Trt with solid phase peptide synthesis methods (SPPS). The peptide was detached from the resin with 7 mL of a 1% TFA in CH_2Cl_2 solution for 15', then the liquid was collected and neutralized with 200 µL pyridine, that step was repeated 6 times. After evaporating all the solution under reduced pressure, the obtained white solid was dissolved in a little amount of EtOAc and precipitated by adding 30 mL petroleum ether. The crude product was then filtered on G4 fritted funnel and dried under vacuum.

The crude peptide was dissolved in 150 mL DMF,5 eq Na_2HPO_4 (222 mg) and 5 eq diphenylphosphoryl azide (163 µL) was added in the system. Subsequent additions of Na_2HPO4 and DIPEA (15.5 eq overall, N,N-Diisopropylethylamine) and DPPA (15 eq overall, Diphenylphosphoryl azide) was gradually done during the following 7 days. Later, PyBOP (233 mg, 3 eq), HOBt (67 mg, 3 eq) and DIPEA (156 µL, 6eq) were added to the reaction mixture, stirring for 3h. After repeating the last step for a second time, the mixture was concentrated and was precipitated by addition of 30 mL water, filtered on fritted funnel under vacuum and dried under vacuum. The waxy crude product was treated with 5 mL TFA, triisopropylsilane and water in 95:3:2 proportions for 4h. TFA was removed by gently fluxing N_2, and the peptide was subsequently precipitated by adding 50 mL Et_2O. After keeping the mixture at 0°C for 12h, the solid was separated by centrifugation, dissolved in a 1M acetic acid solution and freeze-dried. Finally, the peptide RGD was identified by ESI-MS. The solution was freeze-dried and purified by HPLC as shown in the Figure 5.
using a linear gradient from 5% to 25% of eluent B. 16 mg of peptide were obtained with a 18% .
yield. ESI-MS (+): $[M+H]^+_{calculated}$ = 604.3 Da, $[M+H]^+$found = 604.3 m/z

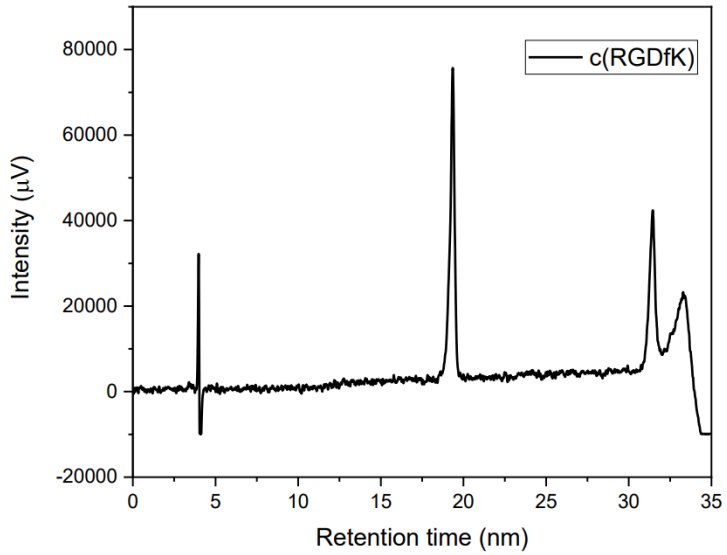

Figure 5.100 Analytical HPLC (C18, 300Å, 10 μm, 5-25% ACN/H2O 9:1, 0.05% TFA in 30 min) peptide 5.

SYNTHESIS 22A:

Synthesis of "$MnMo_6$-c(RGDfK)" Compounds 16

$[(C_4H_9)_4N]_3[MnMo_6O_{18}\{(OCH_2)_3CNHCO(CH_2)_2CO(C_{27}H_{40}N_9O_7)\}_2]$

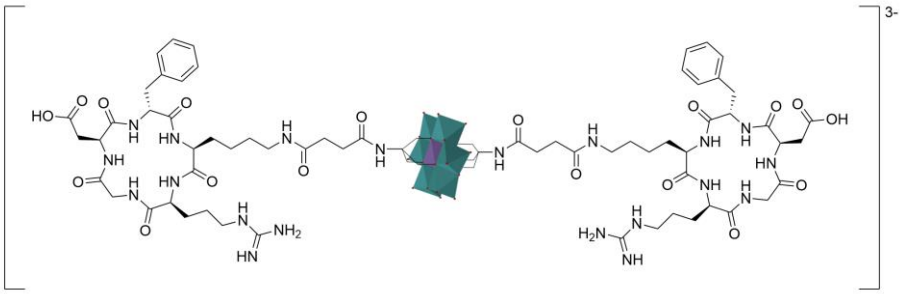

Reaction:

$[(C_4H_9)_4N]_3[MnMo_6O_{18}\{(OCH_2)_3CNHCO(CH_2)_2CO(C_4H_4NO_3)\}_2] + 2\ C_{27}H_{41}N_9O_7$

$\xrightarrow[DMF\ R.T.]{DIPEA} [(C_4H_9)_4N]_3[MnMo_6O_{18}\{(OCH_2)_3CNHCO(CH_2)_2CO(C_{27}H_{40}N_9O_7)\}_2]$

Procedure:

POM-NHS (20.92 mg; 0.0092 mmol) was dissolved in 0.6 mL of DMF in a vial. In c(RGDfK) (12.76 mg, 0.021 mmol) and DIPEA (16.4 mg, 22 µL, 0.12 mmol) were added to the reaction mixture, and the yellow solution has been stirred for 24 hours at room temperature. The day after the transparent solution was put under diethyl ether atmosphere for the crystallization. After 72 hours the pale orange colour product was recovered and washed with approximately 1.5 mL of diethyl ether for two times, then dried under vacuum, and finally weighted (MM = 3253.68g/mol, 0.023 g, 76% yield).

Analysis & Characterization:

FTIR (KBr, cm^{-1}): 3417 (s, br), 3057 (w), 2957 (w), 2935 (w), 2877 (w), 1660 (s), 1541 (m), 1377 (w), 1575 (w), 1107 (w), 1057 (w), 1021 (w), 943 (s), 921 (s), 915 (m), 670 (s), 570 (w).

ESI-MS (-) CH_3CN: 1386 ($[M-2TBA]^{2-}$), 1261.9 ($[M-3TBA+H]^{2-}$).

UV (TFE-H_2O 1:10): Maximum at <190 nm (ε_{190}=241600 $cm^{-1}M^{-1}$) and shoulder at 214 nm (ε_{214}=110400 $cm^{-1}M^{-1}$).

CD (TFE-H_2O 1:10): Minimum at 204 nm ([θ]=-163257 deg*cm^2*$dmol^{-1}$) and maximum under 190 nm ([θ]=78891 deg*cm^2*$dmol^{-1}$ at 190 nm).

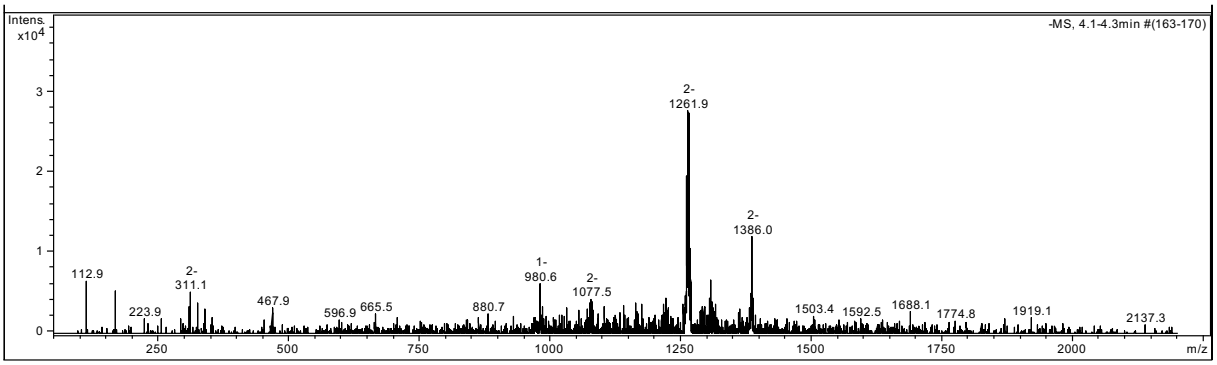

Figure 5.101 ESI-MS (-) of MnMo6-c(RGDfK) in CH3CN.

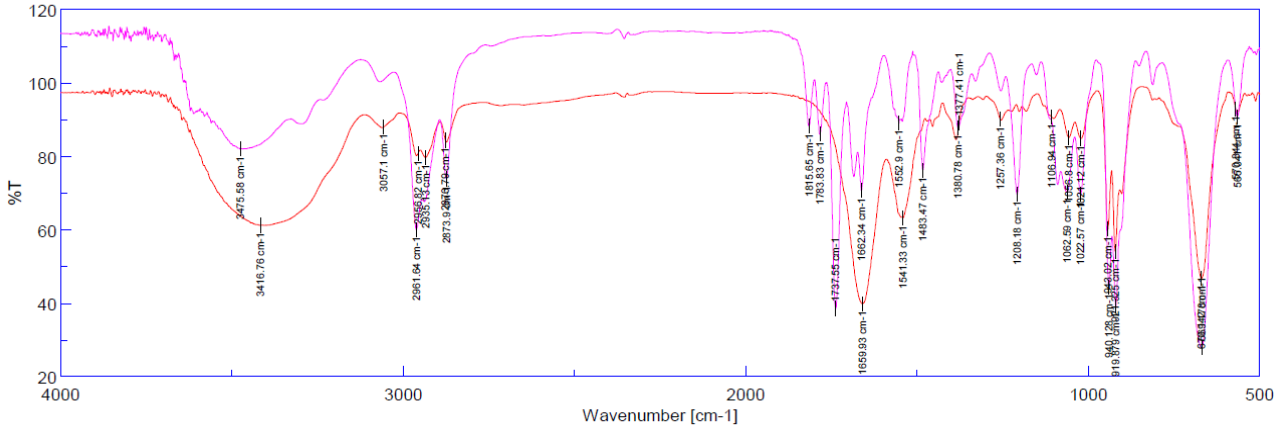

Figure 5.102 IR spectrum of MnMo6 POM-NHS and MnMo6 POM c(RGDfK).

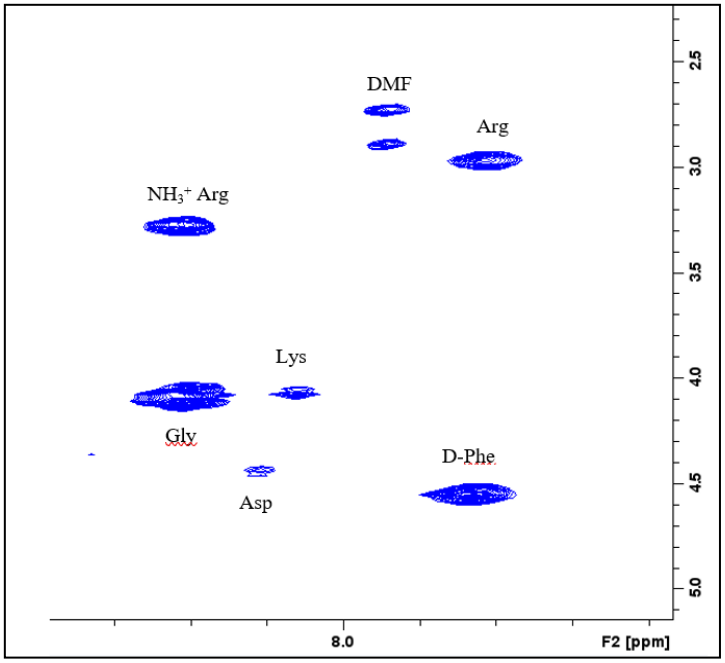

Figure 5.103 COSY signals for POM-TtdsDB.

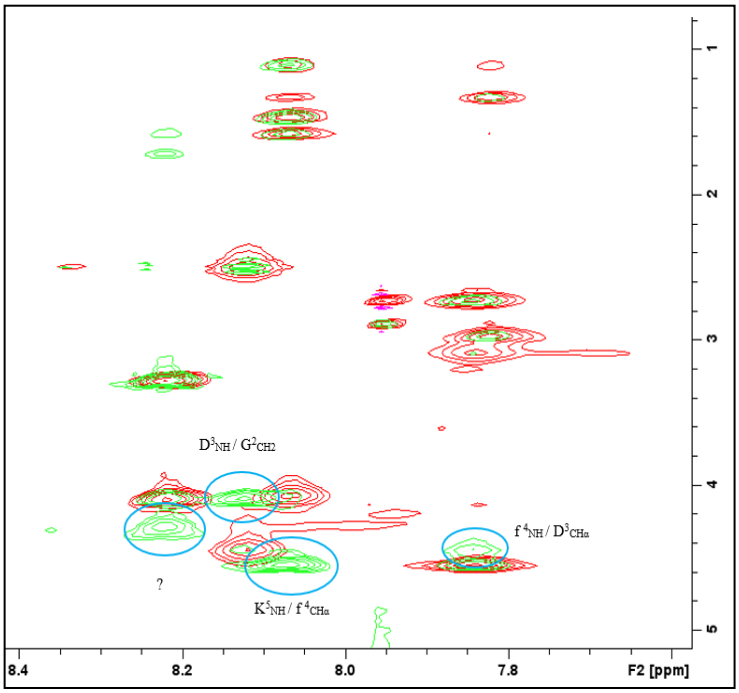

Figure 5.104 *TOCSY and ROESY of POM-c(RGDfK)*

SYNTHESIS 23A:

Synthesis of "V_6-O-c(RGDfK)" Compounds 17

$[(C_4H_9)_4N]_3[V_6O_{13}\{(OCH_2)_3CCH_2OOCCH_2CH_2CO(C_{27}H_{40}N_9O_7)\}_2]$

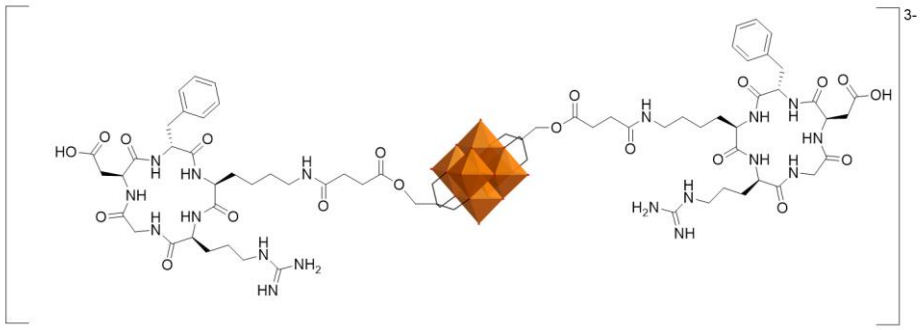

Reaction:

$[(C_4H_9)_4N]_2[V_6O_{13}\{(OCH_2)_3CCH_2OOCCH_2CH_2CO(C_4H_4NO_3)\}_2]$ + 2 $C_{27}H_{41}N_9O_7$

$\xrightarrow[DMF\ R.T.]{DIPEA}$ $[(C_4H_9)_4N]_3[V_6O_{13}\{(OCH_2)_3CCH_2OOCCH_2CH_2CO(C_{27}H_{40}N_9O_7)\}_2]$

Procedure:

V_6O-NHS (14.97 mg; 0.009 mmol) was dissolved in 0.8 mL of DMF in a vial. In order, c(RGDfK) (13.54 mg, 0.022 mmol) and DIPEA (17 mg, 23 µL, 0.13 mmol) were added to the reaction mixture, and the yellow-orange solution was stirred for 48 hours at room temperature. The day after the vial was put under diethyl ether atmosphere for the crystallization of the product. After 96 h, the greasy

dark red product was recovered and washed with approximately 1.5 mL of diethyl ether for two times and then dried under vacuum at the rotary evaporator and later under high vacuum pump for one week and finally weighted (MM = 2636.32 g/mol, 0.02250 g, 95% yield).

Analysis & Characterization:

FTIR (KBr, cm^{-1}): 3372 (s, br), 3061 (w, br), 2932 (m), 2859 (m), 1739 (m), 1660 (s), 1540 (m), 1438 (w), 1387 (m), 1253 (w), 1166 (w), 1131 (m), 1052 (m), 958 (s), 808 (m), 715 (m), 585 (w), 507 (w), 419 (m).

ESI-MS (-) CH_3CN: 2152.0 $([M-2TBA+H)^-$, 1075.7 $([M-2TBA]^{2-})$

UV (TFE-H_2O 1:10): Maximum at <190 nm (ε_{190}=211200 $cm^{-1}M^{-1}$) and shoulder at 211 nm (ε_{211}=164000 $cm^{-1}M^{-1}$),

CD (Pure TFE): The minimum for V_6O-c(RGDfK) in pure TFE is located at 207 nm ([θ]=-79633 deg*cm^2*$dmol^{-1}$) and the maximum noticeable value falls at 190 nm ([θ]=73026 deg*cm^2*$dmol^{-1}$).

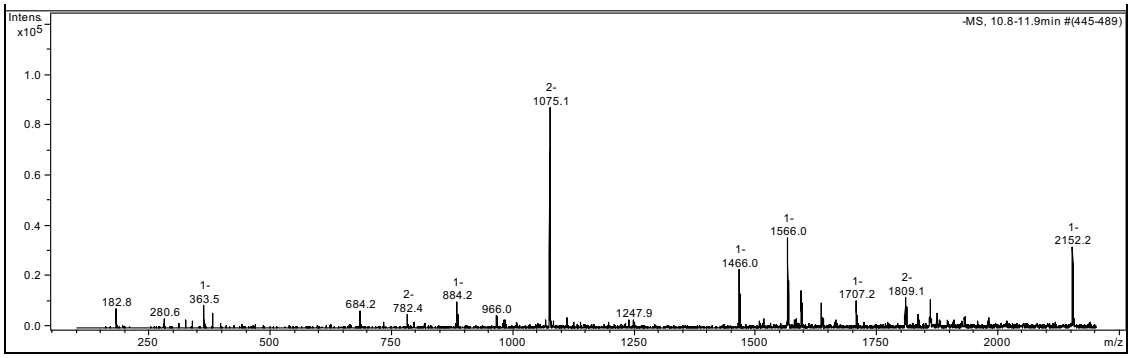

Figure 5.105 ESI-MS (-) of V_6O-c(RGDfK) in CH_3CN.

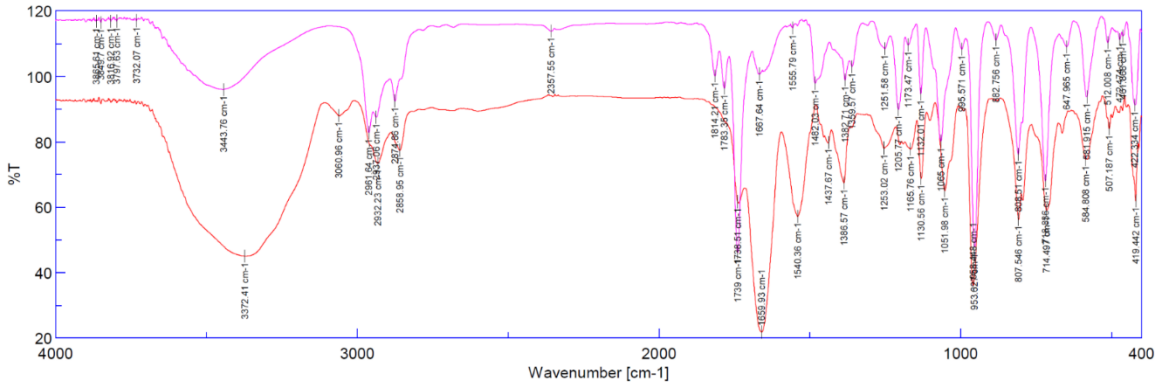

Figure 5.106 FT-IR spectrum of the reagent V_6-O-NHS (in purple) and the final coupling product V_6-O-c(RGDfK) (in red).

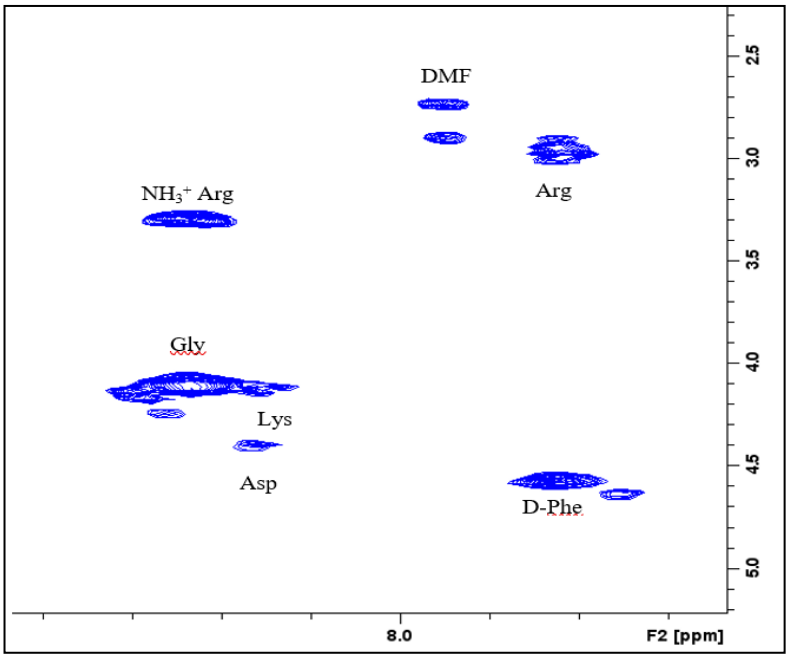

Figure 5.107 COSY of V_6O-c(RGDfK).

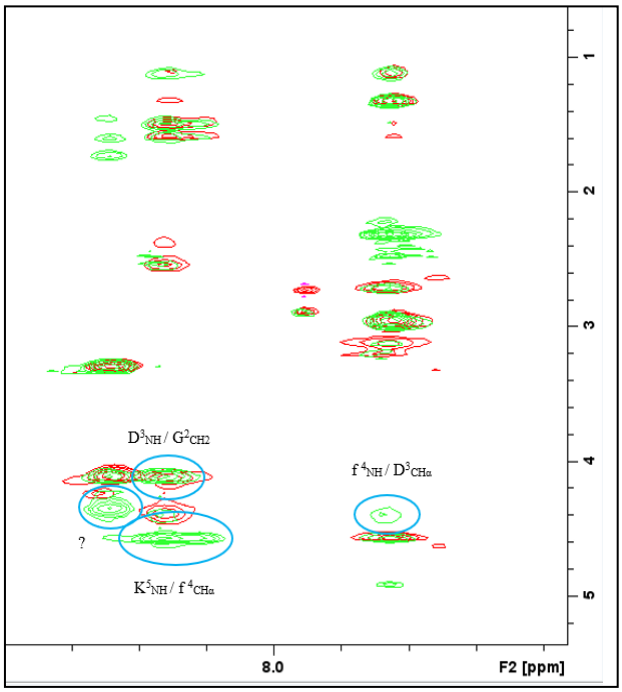

Figure 5.108 TOCSY and ROESY of V_6O-c(RGDfK)

SYNTHESIS 24A:

Synthesis of "Mn-Anderson *Hexyne*" Compounds 18

$[(C_4H_9)_4N]_3[MnMo_6O_{18}\{(OCH_2)_3CNHCOC_5H_7)_2]$

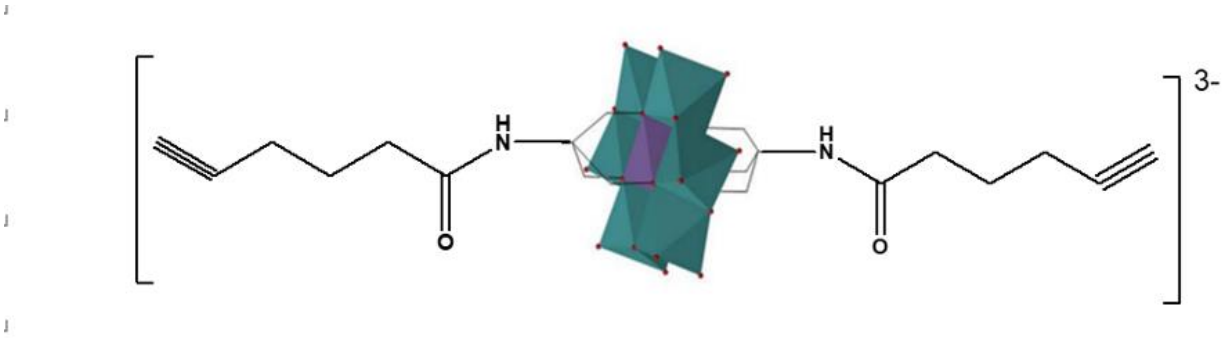

Reaction:

$$[(C_4H_9)_4N]_3[MnMo_6O_{18}\{(OCH_2)_3CNH_2)_2] + 2CH{\equiv}C(CH_2)_3CO_2H \xrightarrow[ACN,\ 50°C,\ 24\,h.]{DCC,\ DIPEA}$$

$$[(C_4H_9)_4N]_3[MnMo_6O_{18}\{(OCH_2)_3CNHCO(CH_2)_3C{\equiv}CH)_2] + 2H_2O$$

Procedure:

$[(C_4H_9)_4N]_3[MnMo_6O_{18}\{(OCH_2)_3CNH_2)_2]$ (200 mg, 0.106 mmol) and $CH{\equiv}C(CH_2)_3CO_2H$ (28.4 mg, 0.23 mmol) were dissolved in ACN (600 μL), in the presence of DCC in CH_3CN at 50°C. The day after the obtained solution was crystallized under diethyl ether atmosphere for a day. The pale orange was obtained. (MM = 2070.56 g/mol, 0.70440g, 86% yield).

Analysis & Characterization:

FTIR (KBr, cm^{-1}): 3441 (m, br), 2963 (s), 2935 (s), 2874 (s), 1680 (m), 1550 (m), 1480 (m), 1382 (m), 1027 (m), 940 (s), 920 (s), 905 (s), 803 (w), 667 (s), 594 (w), 565 (m), 462 (m), 415 (w).

ESI-MS (-) CH_3CN: m/z =1828.0 (m/z calcd. for $[M\text{-}TBA]^-$ = 1828.14) and 1585.8 (m/z calc. for $[M\text{-}2TBA]^{2-}$ = 1587.72).

SYNTHESIS 25A:

Synthesis of "Ala(N_3)-KLVFF-NH_2" peptide 6

Solid-phase peptide synthesis (SPPS) was performed in PTFE syringes endowed with porous filters. The steps of the peptide 6 synthesis is the following:

1. Swelling of the resin in DMF (30');

2. Fmoc deprotection of either the resin (Fmoc-Ethyl-Indole AM resin) or the

preloaded amino acids with a 20% v/v piperidine solution in DMF (5' x 2);

3. Washings with DMF (30'' x 5).

4. Activation of the carboxylic group on the free Fmoc-protected amino acid with

either HBTU/HOBt or HATU in the presence of DIPEA (5');

5. Coupling reaction (45');

6. Washings with DMF (30'' x 5).

Steps 2 through 6 were iteratively performed until the final amino acid condensation was achieved. Solvent removal was accomplished in each step through a filtration system connected to a vacuum pump. In the coupling reaction, a three-fold excess of Fmoc-AA-OH, activators, and a six-fold excess of DIPEA were employed. Upon completion of the synthesis, the resin was thoroughly rinsed with DCM and subsequently dried. the 5% piperidine/DMF and 2% DBU induced Fmoc deprotection. the peptide 6 was synthesized by conjugating of Fmoc-Phe-OH, Fmoc-Phe-OH, Fmoc-Val-OH and Fmoc-Leu-OH, Fmoc-Lys (Boc)-OH and Fmoc-*β*-azido-Ala-OH sequentially.

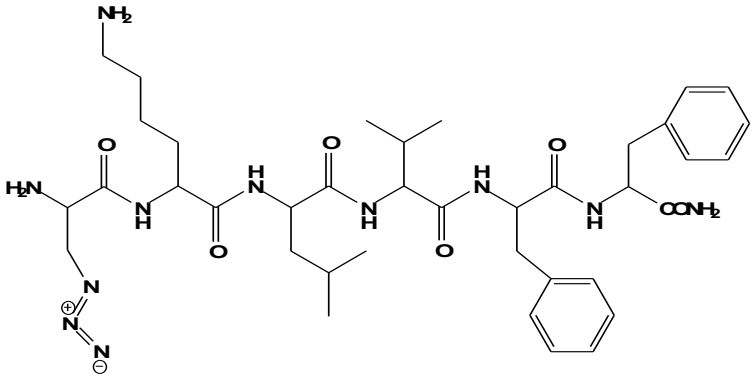

Figure 5.109 the structure of Ala(N_3)-KLVFF-NH_2

SYNTHESIS 26A:

"Mn-Anderson-Ala-KLVFFNH_2" Compounds 19

$[(C_4H_9)_4N]_3[MnMo_6O_{18}\{(OCH_2)_3CNHCO(C_{48}H_{68}N_{11})\}_2]$

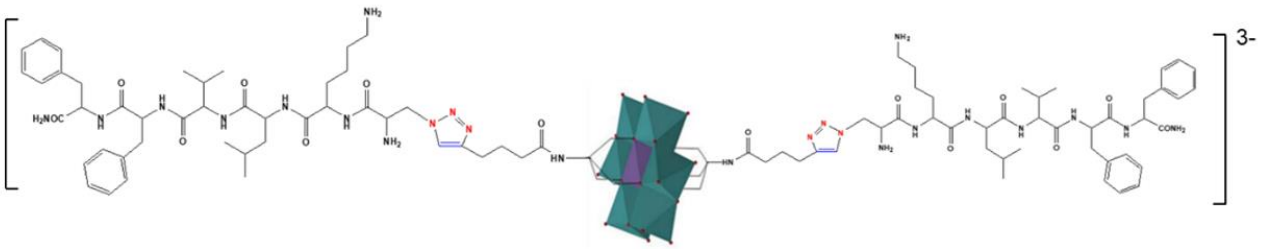

Reaction:

$$[(C_4H_9)_4N]_3[MnMo_6O_{18}\{(OCH_2)_3CNHCOC_5H_7)_2] + 2C_{18}H_{16}N_4O_4 \xrightarrow[DMF,\ 55°C,\ 24\,h.]{CuI,\ DIPEA}$$

$$[(C_4H_9)_4N]_3[MnMo_6O_{18}\{(OCH_2)_3CNHCO(C_{48}H_{68}N_{11})\}_2]$$

Procedure:

POM-hexyne (10.4mg, 0.050 mmol) and 0.9% CuI and DIPEA (0.080mmol) were dissolved in anhydrous DMF (400 μL). After stirring under N_2 flow for 30 min, peptide 6 (0.01mmol) was added in the mixture system. After 24h, the transparent orange solution was obtained upon centrifugation, then added 200 μL anhydrous ACN to remove the unreacted peptide then transferred liquid into diethyl ether atmosphere for two days and finally washed with ether. (MM=2163.26 g/mol, 10.1 mg, 56% yield

Analysis & Characterization:

FTIR (KBr, cm^{-1}): 3433 (m, br), 3294 (s), 3063(m), 2963 (m), 2874 (m), 1652 (s), 1541 (s), 1456 (w), 1386 (w), 1245 (w), 1027 (m), 943 (s), 923 (s) 905 (m), 668 (s), 567 (w).

ESI-MS (-) CH_3CN: 1435.1(m/z calcd. for $[M\text{-}TBA]^-$ = 1436.0)

UV (TFE/H_2O 1:10): maximum at <190 nm (ε190=1052600 $cm^{-1}M^{-1}$).

CD (Pure TFE): The minimum for pure TFE is located at 210 nm ([θ]= -121569 deg*cm^2*$dmol^{-1}$).

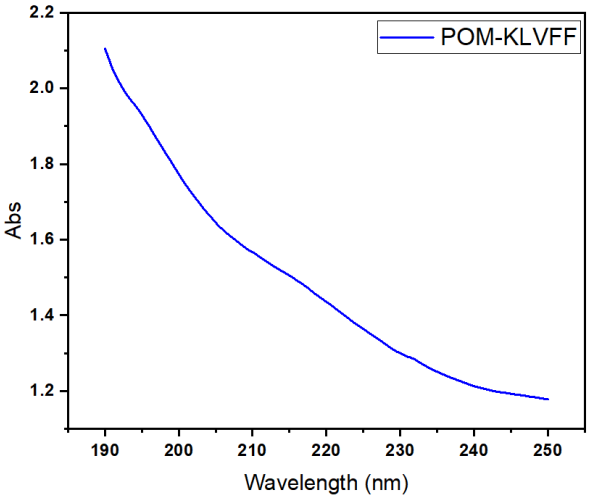

Figure 5.109UV spectrum of Mn-Anderson-Ala-KLVFFNH2 in TFE/H2O 1:10.

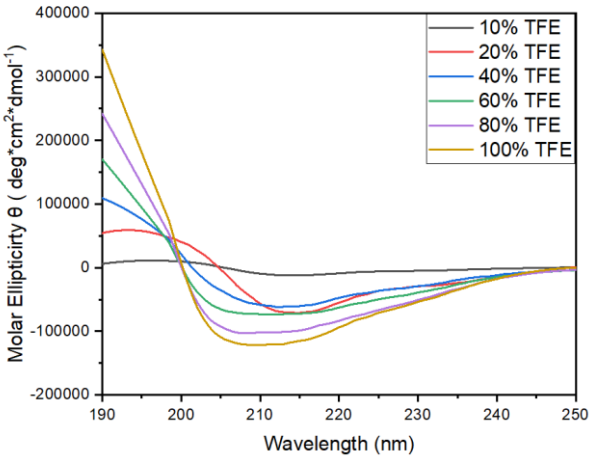

Figure 5.110 Far-UV CD spectra of Mn-Anderson-Ala-KLVFFNH2 (20μM) at variable % of trifluoroethanol in water.

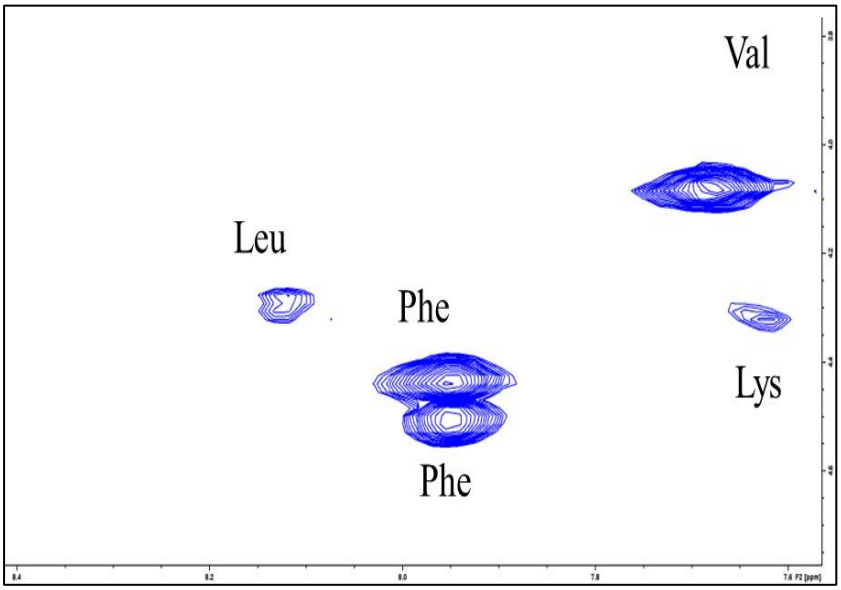

Figure 5.111 COSY spectrum of Mn-Anderson-Ala-KLVFFNH₂ (150 μM) in d6-DMSO.

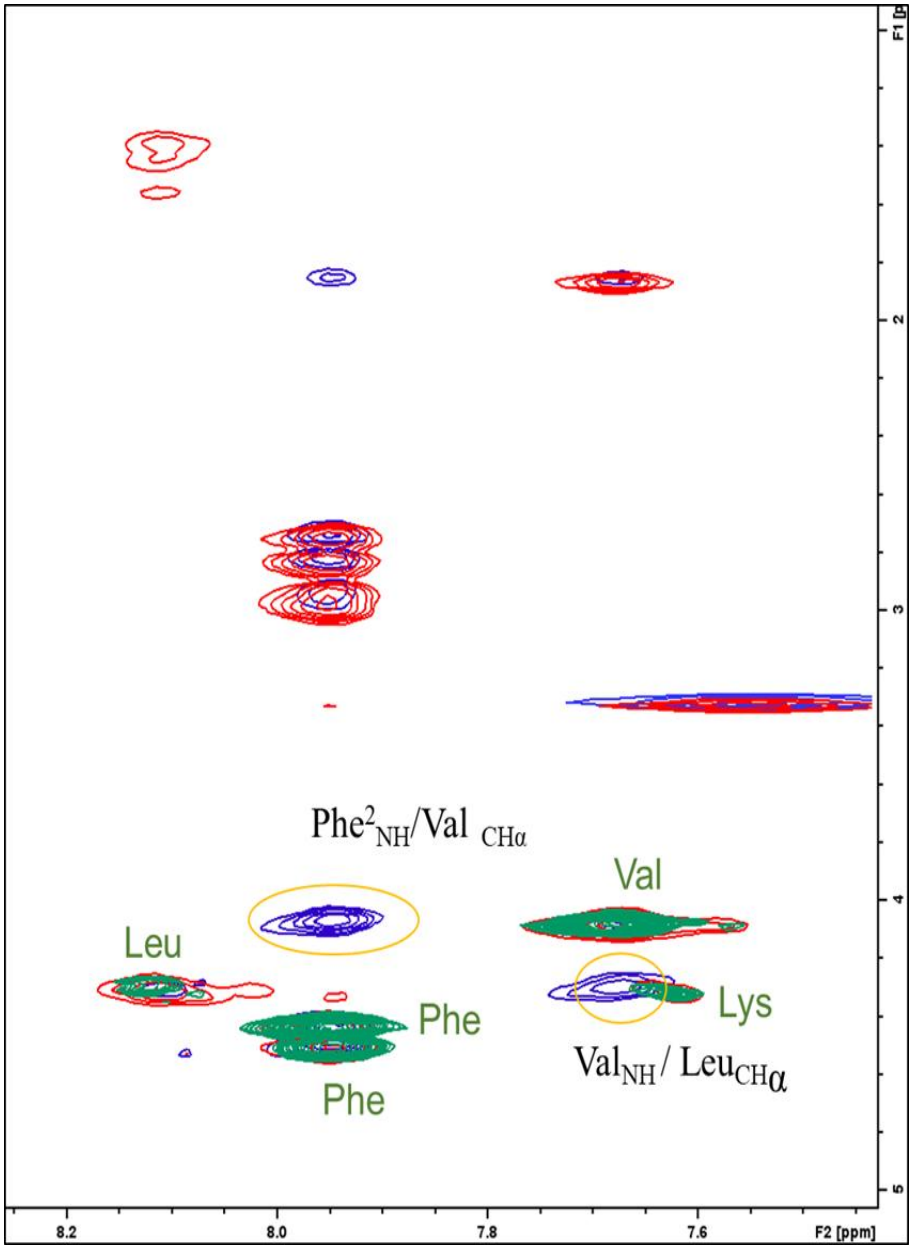

Figure 5.112 COSY spectrum of Mn-Anderson-Ala-KLVFFNH₂ (150 μM) in d6-DMSO.

Summary

This thesis pursues two primary objectives. The first objective is centered on the development of innovative POM-peptide hybrids designed to selectively target and eliminate tumor cells through their interaction with integrins and the GPRP receptor. The second objective revolves around the creation of POM-Ala-KLVFF hybrids, which hold promise in targeting Aβ and inhibiting its fibrillation process, thus potentially slowing the progression of Alzheimer's Disease (AD).

In the initial phase of this investigation, the primary objective was to evaluate whether the utilization of EEEE-βAlaDB or Ttds DB spacers could effectively impede the interactions between Mn Anderson POM and peptide DB, interactions that hinder DB's ability to engage with its receptor. Encouraged by promising results, and considering the distinct negative charge of V_6-POM, various spacers, namely EEEE-βAla spacer, Ttds spacer, and the Ttds-EEEE-βAla spacer, were employed to functionalize peptide DB. Following this, the spacers-DB constructs were subjected to conjugation with V_6O-NHS. This step was undertaken to gain a more profound understanding of the interaction between V_6-POM, peptide DB, and the spacer design. Among all spacers, Ttds-EEEE-βAla spacer displayed the most impressive impact. This approach holds the potential to offer a more cost-effective strategy for the future large-scale production of antitumor drugs. Furthermore, the study delved into the ramifications of covalently binding the cyclic peptide c(RGDfK) to molybdate to ascertain whether the presence of POM had any discernible impact on its ability to target integrin receptors. In the same time, the toxicity results of POM- c(RGDfK) showed cheering results (IC50 is around 3 μM). Additionally, successful design and synthesis of Ala(N_3)-KLVFF-NH_2 were carried out to facilitate the targeting of Aβ and enhance its penetration by conjugating it with molybdate.

Acknowledgements

Throughout my three years of thesis work, I had the privilege of encountering numerous brilliant individuals, and I wish to acknowledge a few of them here.

Foremost, I am deeply grateful to my supervisor, Prof. Carraro, for affording me the opportunity to participate in his research and become an integral part of his team. His unwavering support, willingness to clarify even the smallest of doubts, and constant readiness to assist at any hour have been invaluable. His commitment to ensuring my thorough understanding of every facet of my project has been truly commendable. I also extend my gratitude to Dr. Paolo Ruzza (ICB-CNR) for his insightful advice and for enabling me to view my project from an entirely different perspective, enriching my research experience.

I must acknowledge the entire "Nano and Molecular Catalysis" team, with special mentions for Mattia and Francesco, who have been wonderful companions throughout the numerous syntheses we undertook. I extend my heartfelt thanks to Dr. Claudia Honisch and Dr. Ruzza, along with Nicola and other members of the ICB-CNR research team, for guiding me through the intricate realm of peptides, serving as beacons of knowledge and support. I would be remiss not to express my appreciation for the technical and support staff who have been instrumental in facilitating my research journey. I also extend my thanks to prof. Monica Montopoli and her team for conducting the cytotoxicity tests on the hybrids in this study.

Lastly, my deepest gratitude goes to my family and relatives who have provided unwavering spiritual support, aiding me in completing my research.

Reference

1. Pope, M. T.; Jeannin, Y.; Fournier, M., *Heteropoly and isopoly oxometalates*. Springer: 1983; Vol. 8.
2. Long, D. L.; Burkholder, E.; Cronin, L., Polyoxometalate clusters, nanostructures and materials: From self assembly to designer materials and devices. *Chemical Society Reviews* **2007,** *36* (1), 105-121.
3. Wilson, E. F. Synthesis, structure and mechanism of polyoxometalate self-assembly: Towards designed nanoscale architectures. University of Glasgow, 2009.
4. Hasenknopf, B., Polyoxometalates: Introduction to a class of inorganic compounds and their biomedical applications. *Frontiers in Bioscience-Landmark* **2005,** *10*, 275-287.
5. Rakovský, E., *Isopolyoxometalate Functionalisation Facilitated by Transition Metal Complexes*. 2015.
6. Hagrman, D.; Haushalter, R. C.; Zubieta, J., Three-dimensional organic/inorganic hybrid materials constructed from one-dimensional copper diamine coordination polymers linked by bridging oxoanion tetrahedra:[Cu (dpe)(MoO4)] and [Cu (dpe)(SO4)(H2O)](dpe= 1, 2-trans-(4-pyridyl) ethene). *Chemistry of materials* **1998,** *10* (1), 361-365.
7. Proust, A.; Thouvenot, R.; Chaussade, M.; Robert, F.; Gouzerh, P., Phenylimido derivatives of [Mo6O19] 2−: syntheses, X-ray structures, vibrational, electrochemical, 95Mo and 14N NMR studies. *Inorganica chimica acta* **1994,** *224* (1-2), 81-95.
8. Xu, L.; Lu, M.; Xu, B.; Wei, Y.; Peng, Z.; Powell, D. R., Towards Main-Chain-Polyoxometalate-Containing Hybrid Polymers: A Highly Efficient Approach to Bifunctionalized Organoimido Derivatives of Hexamolybdates. *Angewandte Chemie* **2002,** *114* (21), 4303-4306.
9. Damian, H. A. Polyoxometalates and peptides: hybridisation and disulfide detection. University of Nottingham, 2022.
10. Nakamura, S.; Ozeki, T., Hydrogen-bonded aggregates of protonated decavanadate anions in their tetraalkylammonium salts. *Journal of the Chemical Society, Dalton Transactions* **2001,** (4), 472-480.
11. Paulat-Böschen, I., X-Ray crystallographic determination of the structure of the isopolyanion [Mo 36 O 112 (H 2 O) 16] 8–in the compound K 8 [Mo 36 O 112 (H 2 O) 16]· 36H 2 O. *Journal of the Chemical Society, Chemical Communications* **1979,** (17), 780-782.
12. Neumann, R.; Levin, M., Aerobic oxidative dehydrogenations catalyzed by the mixed-addenda heteropolyanion PV2Mo10O405-: a kinetic and mechanistic study. *Journal of the American Chemical Society* **1992,** *114* (18), 7278-7286.
13. Blazevic, A.; Rompel, A., The Anderson–Evans polyoxometalate: From inorganic building blocks via hybrid organic–inorganic structures to tomorrows "Bio-POM". *Coordination chemistry reviews* **2016,** *307*, 42-64.
14. Maestre, J. M.; Lopez, X.; Bo, C.; Poblet, J.-M.; Casan-Pastor, N., Electronic and magnetic

properties of α-keggin anions: A DFT Study of [XM12O40] n-,(M= W, Mo; X= AlIII, SiIV, PV, FeIII, CoII, CoIII) and [SiM11VO40] m-(M= Mo and W). *Journal of the American Chemical Society* **2001,** *123* (16), 3749-3758.
15. Lahnsteiner, M.; Kastner, A.; Mayr, J.; Roller, A.; Keppler, B. K.; Kowol, C. R., Improving the stability of maleimide–thiol conjugation for drug targeting. *Chemistry–A European Journal* **2020,** *26* (68), 15867-15870.
16. Fan, L.; Wang, E.; Li, Y.; An, H.; Xiao, D.; Wang, X., Wells–Dawson anion, a useful building block to construct one-dimensional chain as a chelate ligand coordinating with transition metal cations. *Journal of Molecular Structure* **2007,** *841* (1-3), 28-33.
17. Dablemont, C.; Hamaker, C. G.; Thouvenot, R.; Sojka, Z.; Che, M.; Maatta, E. A.; Proust, A., Functionalization of Heteropolyanions—Osmium and Rhenium Nitrido Derivatives of Keggin-and Dawson-Type Polyoxotungstates: Synthesis, Characterization and Multinuclear (183W, 15N) NMR, EPR, IR, and UV/Vis Fingerprints. *Chemistry–A European Journal* **2006,** *12* (36), 9150-9160.
18. Kibler, A. J.; Newton, G. N., Tuning the electronic structure of organic–inorganic hybrid polyoxometalates: The crucial role of the covalent linkage. *Polyhedron* **2018,** *154*, 1-20.
19. Anyushin, A. V.; Kondinski, A.; Parac-Vogt, T. N., Hybrid polyoxometalates as post-functionalization platforms: from fundamentals to emerging applications. *Chemical Society Reviews* **2020,** *49* (2), 382-432.
20. Cherevan, A. S.; Nandan, S. P.; Roger, I.; Liu, R.; Streb, C.; Eder, D., Polyoxometalates on functional substrates: concepts, synergies, and future perspectives. *Advanced Science* **2020,** *7* (8), 1903511.
21. Arefian, M.; Mirzaei, M.; Eshtiagh-Hosseini, H.; Frontera, A., A survey of the different roles of polyoxometalates in their interaction with amino acids, peptides and proteins. *Dalton Transactions* **2017,** *46* (21), 6812-6829.
22. Wang, X.; Wei, S.; Zhao, C.; Li, X.; Jin, J.; Shi, X.; Su, Z.; Li, J.; Wang, J., Promising application of polyoxometalates in the treatment of cancer, infectious diseases and Alzheimer's disease. *JBIC Journal of Biological Inorganic Chemistry* **2022,** *27* (4-5), 405-419.
23. Galani, A.; Tsitsias, V.; Stellas, D.; Psycharis, V.; Raptopoulou, C. P.; Karaliota, A., Two novel compounds of vanadium and molybdenum with carnitine exhibiting potential pharmacological use. *Journal of Inorganic Biochemistry* **2015,** *142*, 109-117.
24. Fraqueza, G.; Fuentes, J.; Krivosudský, L.; Dutta, S.; Mal, S. S.; Roller, A.; Giester, G.; Rompel, A.; Aureliano, M., Inhibition of Na+/K+-and Ca2+-ATPase activities by phosphotetradecavanadate. *Journal of Inorganic Biochemistry* **2019,** *197*, 110700.
25. Gao, N.; Sun, H.; Dong, K.; Ren, J.; Duan, T.; Xu, C.; Qu, X., Transition-metal-substituted polyoxometalate derivatives as functional anti-amyloid agents for Alzheimer's disease. *Nat Commun* **2014,** *5*, 3422.
26. Kareva, I., *Understanding Cancer from a Systems Biology Point of View: From Observation to Theory and Back*. Academic Press: 2018.
27. Lee, Y. T.; Tan, Y. J.; Oon, C. E., Molecular targeted therapy: Treating cancer with specificity. *European journal of pharmacology* **2018,** *834*, 188-196.
28. Torchilin, V. P., Passive and active drug targeting: drug delivery to tumors as an example. *Drug delivery* **2010**, 3-53.

29. Schwartz, R. S., Paul Ehrlich's magic bullets. *New England Journal of Medicine* **2004,** *350* (11), 1079-1080.
30. Svenson, S.; Prud'homme, R. K., *Multifunctional nanoparticles for drug delivery applications: imaging, targeting, and delivery*. Springer Science & Business Media: 2012.
31. Srinivasarao, M.; Low, P. S., Ligand-targeted drug delivery. *Chemical reviews* **2017,** *117* (19), 12133-12164.
32. Cerwenka, A.; Lanier, L. L., Ligands for natural killer cell receptors: redundancy or specificity. *Immunological reviews* **2001,** *181* (1), 158-169.
33. Wu, C.-H.; Liu, I. J.; Lu, R.-M.; Wu, H.-C., Advancement and applications of peptide phage display technology in biomedical science. *Journal of Biomedical Science* **2016,** *23* (1), 8.
34. Saw, P. E.; Song, E.-W., Phage display screening of therapeutic peptide for cancer targeting and therapy. *Protein & cell* **2019,** *10* (11), 787-807.
35. Cooper, B. M.; Iegre, J.; O'Donovan, D. H.; Halvarsson, M. Ö.; Spring, D. R., Peptides as a platform for targeted therapeutics for cancer: Peptide–drug conjugates (PDCs). *Chemical society reviews* **2021,** *50* (3), 1480-1494.
36. Vrettos, E. I.; Mező, G.; Tzakos, A. G., On the design principles of peptide–drug conjugates for targeted drug delivery to the malignant tumor site. *Beilstein journal of organic chemistry* **2018,** *14* (1), 930-954.
37. Fu, C.; Yu, L.; Miao, Y.; Liu, X.; Yu, Z.; Wei, M., Peptide–drug conjugates (PDCs): a novel trend of research and development on targeted therapy, hype or hope? *Acta Pharmaceutica Sinica B* **2023,** *13* (2), 498-516.
38. Poreba, M., Protease-activated prodrugs: strategies, challenges, and future directions. *The FEBS Journal* **2020,** *287* (10), 1936-1969.
39. Vadevoo, S. M. P.; Gurung, S.; Lee, H.-S.; Gunassekaran, G. R.; Lee, S.-M.; Yoon, J.-W.; Lee, Y.-K.; Lee, B., Peptides as multifunctional players in cancer therapy. *Experimental & Molecular Medicine* **2023**, 1-11.
40. Rigby, M.; Bennett, G.; Chen, L.; Mudd, G. E.; Harrison, H.; Beswick, P. J.; Van Rietschoten, K.; Watcham, S. M.; Scott, H. S.; Brown, A. N., BT8009; A Nectin-4 Targeting Bicycle Toxin Conjugate for Treatment of Solid Tumors. *Molecular Cancer Therapeutics* **2022,** *21* (12), 1747-1756.
41. Hruby, V. J., Designing peptide receptor agonists and antagonists. *Nature reviews Drug discovery* **2002,** *1* (11), 847-858.
42. Anastasi, A.; Erspamer, V.; Bucci, M., Isolation and structure of bombesin and alytesin, two analogous active peptides from the skin of the European amphibians Bombina and Alytes. *Experientia* **1971,** *27* (2), 166-167.
43. Reubi, J. C., Peptide receptors as molecular targets for cancer diagnosis and therapy. *Endocrine reviews* **2003,** *24* (4), 389-427.
44. Jensen, R.; Battey, J.; Spindel, E.; Benya, R., International Union of Pharmacology. LXVIII. Mammalian bombesin receptors: nomenclature, distribution, pharmacology, signaling, and functions in normal and disease states. *Pharmacological reviews* **2008,** *60* (1), 1-42.
45. Okarvi, S.; Al-Jammaz, I., Synthesis, radiolabelling and biological characteristics of a bombesin peptide analog as a tumor imaging agent. *Anticancer research* **2003,** *23* (3), 2745-2750.
46. Zhang, Y.; Holland, E.; Dinh, A.; Au, D.; Sun, L., Bombesin-drug conjugates in targeted therapy

for small cell lung cancer. *American Journal of Cancer Research* **2022,** *12* (3), 927.
47. Eble, J. A.; Haier, J., Integrins in cancer treatment. *Current cancer drug targets* **2006,** *6* (2), 89-105.
48. Danhier, F.; Le Breton, A.; Préat, V. r., RGD-based strategies to target alpha (v) beta (3) integrin in cancer therapy and diagnosis. *Molecular pharmaceutics* **2012,** *9* (11), 2961-2973.
49. Sani, S.; Messe, M.; Fuchs, Q.; Pierrevelcin, M.; Laquerriere, P.; Entz-Werle, N.; Reita, D.; Etienne-Selloum, N.; Bruban, V.; Choulier, L., Biological relevance of RGD-integrin subtype-specific ligands in cancer. *ChemBioChem* **2021,** *22* (7), 1151-1160.
50. Fu, S.; Xu, X.; Ma, Y.; Zhang, S.; Zhang, S., RGD peptide-based non-viral gene delivery vectors targeting integrin αvβ3 for cancer therapy. *Journal of drug targeting* **2019,** *27* (1), 1-11.
51. Selkoe, D. J.; Schenk, D., Alzheimer's disease: molecular understanding predicts amyloid-based therapeutics. *Annual review of pharmacology and toxicology* **2003,** *43* (1), 545-584.
52. Hippius, H.; Neundörfer, G., The discovery of Alzheimer's disease. *Dialogues in clinical neuroscience* **2022**.
53. Crowther, R.; Goedert, M., Abnormal tau-containing filaments in neurodegenerative diseases. *Journal of structural biology* **2000,** *130* (2-3), 271-279.
54. Armstrong, R. A., Alzheimer's disease and the eye. *Journal of Optometry* **2009,** *2* (3), 103-111.
55. Chow, V. W.; Mattson, M. P.; Wong, P. C.; Gleichmann, M., An overview of APP processing enzymes and products. *Neuromolecular medicine* **2010,** *12*, 1-12.
56. Zhang, Y.-w.; Thompson, R.; Zhang, H.; Xu, H., APP processing in Alzheimer's disease. *Molecular brain* **2011,** *4*, 1-13.
57. Lott, I. T.; Head, E., Dementia in Down syndrome: unique insights for Alzheimer disease research. *Nature Reviews Neurology* **2019,** *15* (3), 135-147.
58. Xi, Y.; Chen, Y.; Jin, Y.; Han, G.; Song, M.; Song, T.; Shi, Y.; Tao, L.; Huang, Z.; Zhou, J., Versatile nanomaterials for Alzheimer's disease: Pathogenesis inspired disease-modifying therapy. *Journal of Controlled Release* **2022,** *345*, 38-61.
59. Long, J. M.; Holtzman, D. M., Alzheimer disease: an update on pathobiology and treatment strategies. *Cell* **2019,** *179* (2), 312-339.
60. Kamenetz, F.; Tomita, T.; Hsieh, H.; Seabrook, G.; Borchelt, D.; Iwatsubo, T.; Sisodia, S.; Malinow, R., APP processing and synaptic function. *Neuron* **2003,** *37* (6), 925-937.
61. Reiss, A. B.; Arain, H. A.; Stecker, M. M.; Siegart, N. M.; Kasselman, L. J., Amyloid toxicity in Alzheimer's disease. *Reviews in the Neurosciences* **2018,** *29* (6), 613-627.
62. Furtado, D.; Björnmalm, M.; Ayton, S.; Bush, A. I.; Kempe, K.; Caruso, F., Overcoming the blood–brain barrier: the role of nanomaterials in treating neurological diseases. *Advanced materials* **2018,** *30* (46), 1801362.
63. Li, M.; Xu, C.; Wu, L.; Ren, J.; Wang, E.; Qu, X., Self-assembled peptide-polyoxometalate hybrid nanospheres: two in one enhances targeted inhibition of amyloid beta-peptide aggregation associated with Alzheimer's disease. *Small* **2013,** *9* (20), 3455-61.
64. Tjernberg, L. O.; Näslund, J.; Lindqvist, F.; Johansson, J.; Karlström, A. R.; Thyberg, J.; Terenius, L.; Nordstedt, C., Arrest of-Amyloid Fibril Formation by a Pentapeptide Ligand (∗). *Journal of Biological Chemistry* **1996,** *271* (15), 8545-8548.
65. Pallitto, M. M.; Ghanta, J.; Heinzelman, P.; Kiessling, L. L.; Murphy, R. M., Recognition

sequence design for peptidyl modulators of β-amyloid aggregation and toxicity. *Biochemistry* **1999,** *38* (12), 3570-3578.
66. Lührs, T.; Ritter, C.; Adrian, M.; Riek-Loher, D.; Bohrmann, B.; Döbeli, H.; Schubert, D.; Riek, R., 3D structure of Alzheimer's amyloid-β (1–42) fibrils. *Proceedings of the National Academy of Sciences* **2005,** *102* (48), 17342-17347.
67. Soria-Carrera, H.; Atrián-Blasco, E.; Martín-Rapún, R.; Mitchell, S. G., Polyoxometalate–peptide hybrid materials: from structure–property relationships to applications. *Chemical science* **2023,** *14* (1), 10-28.
68. Ventura, D.; Calderan, A.; Honisch, C.; Krol, S.; Serrati, S.; Bonchio, M.; Carraro, M.; Ruzza, P., Synthesis and biological activity of an Anderson polyoxometalate bis-functionalized with a Bombesin-analog peptide. *Peptide Science* **2018,** *110* (5).
69. Tagliavini, V.; Honisch, C.; Serratì, S.; Azzariti, A.; Bonchio, M.; Ruzza, P.; Carraro, M., Enhancing the biological activity of polyoxometalate–peptide nano-fibrils by spacer design. *RSC advances* **2021,** *11* (9), 4952-4957.
70. Luo, J. C.; Zhang, B. F.; Yvon, C.; Hutin, M.; Gerislioglu, S.; Wesdemiotis, C.; Cronin, L.; Liu, T. B., Self-Assembly of Polyoxometalate-Peptide Hybrids in Solution: Elucidating the Contributions of Multiple Possible Driving Forces. *European Journal of Inorganic Chemistry* **2019,** (3-4), 380-386.
71. Kulikov, V.; Johnson, N. A. B.; Surman, A. J.; Hutin, M.; Kelly, S. M.; Hezwani, M.; Long, D. L.; Meyer, G.; Cronin, L., Spontaneous Assembly of an Organic-Inorganic Nucleic Acid Z-DNA Double-Helix Structure. *Angewandte Chemie-International Edition* **2017,** *56* (4), 1141-1145.
72. Zhao, J.; Li, K.; Wan, K.; Sun, T.; Zheng, N.; Zhu, F.; Ma, J.; Jiao, J.; Li, T.; Ni, J.; Shi, X.; Wang, H.; Peng, Q.; Ai, J.; Xu, W.; Liu, S., Organoplatinum-Substituted Polyoxometalate Inhibits beta-amyloid Aggregation for Alzheimer's Therapy. *Angew Chem Int Ed Engl* **2019,** *58* (50), 18032-18039.
73. Huang, Y.; Chang, Y.; Liu, L.; Wang, J., Nanomaterials for Modulating the Aggregation of beta-Amyloid Peptides. *Molecules* **2021,** *26* (14).